2010-09-01

Sol-Gel Synthesis and Characterisation of Novel Metal Oxide Nanomaterials for Photocatalytic Applications

Nicholas T. Nolan
Technological University Dublin, nicholas.nolan@gmail.com

Sol-Gel Synthesis and Characterisation of Novel Metal Oxide Nanomaterials for Photocatalytic Applications

By

Nicholas T. Nolan BSc

A thesis submitted to the Dublin Institute of Technology for the award of Doctor of Philosophy.

Supervised by:

Dr. Michael K. Seery

Dr. Suresh C. Pillai

School of Chemical and Pharmaceutical Sciences,
Dublin Institute of Technology,
Kevin Street, Dublin 8.

September 2010

Abstract

This thesis presents a study of the effect of chemical modifiers and dopants on both the anatase to rutile transformation and also the photocatalytic efficiency of semiconductor nanomaterials. The main focus of the work is based on the crystallisation and phase transformation of the widely investigated semiconductor metal oxide, titanium dioxide (TiO_2)

Of the three polymorphs associated with titanium dioxide, anatase is widely regarded as the most effective photocatalyst. Typically anatase will transform to rutile in the temperature range 600 – 700 °C however, modification of a titanium precursor with a chelating agent can result in extended transformation temperature. The effect of employing various concentrations of formic acid and water on phase transition is systematically studied by XRD, FTIR and Raman spectroscopy (Chapter 3). Retention of anatase (41%) at increased temperatures (800 °C) and 10% at 900 °C is achieved at optimum conditions. On comparison, a control sample prepared without modification with formic acid show rutile formation at 600 °C. FTIR and Raman studies indicate that a bridging titanium-formate structure is formed upon addition of titanium isopropoxide to formic acid. It is proposed that under different reaction conditions, a *syn-syn* or *syn-anti* bridging structure is favoured. It is concluded that the *syn-anti* bridging structure hinders cross linking of the metal oxide oligomer network, resulting in a weakened structure, facilitating low temperature rutile formation when compared with the *syn-syn* binding mode which forms a more ordered network, stabilising anatase at increased temperatures.

Using the optimum formic acid, titanium isopropoxide molar ratios (TTIP:FA:H_2O, 1:4:4) obtained in chapter 3, silver (1, 3 and 5 mol %) was added to the system and the effects are reported (chapter 4). Through XRD it is shown that silver lowers the anatase to rutile transformation temperature. Samples calcined at 700 °C show that 5 mol % Ag-TiO_2 contains both anatase (46%) and rutile (54%), whereas the undoped TiO_2

consists primarily of anatase (95%). At 800 °C all silver containing samples transform to rutile but the undoped sample consists of both anatase (55%) and rutile (45%). XPS, FTIR and Raman spectroscopy show that incorporation of silver causes a reduction in the intensity of the COO^- stretches associated with the titanium formate bridging structure indicating that the metal oxide complex is weakened in the presence of silver. XPS analysis show that Ag^0 and Ag_2O had formed on the titania-formate surface prior to calcination (> 100 °C) indicating that photo-oxidation of silver has occurred. It is concluded that the presence of silver (Ag^0 and Ag_2O) hindered bridging ligands, resulting in a weakened gel network. This structurally weak network could easily collapse upon calcination to form rutile.

Titanium dioxide doped with aluminium also shows extended transformation temperatures. In chapter five, aluminium, silver, nitrogen, and sulfur are used to dope titanium dioxide powders. Addition of 1 mol % aluminium resulted in the retention of anatase (87%) at 900 °C and even at 1000 °C, anatase (20%) is still present as seen from XRD. Nitrogen doped titanium dioxide is synthesised using 1, 3-diaminopropane as a nitrogen source. Visible light absorption of nitrogen doped titanium dioxide is seen through diffuse reflectance spectroscopy and it is shown that increased amounts of nitrogen do not result in greater visible light absorbance. Addition of silver to N-TiO_2 result in increased photocatalytic activity for methylene blue degradation, 9.9 x 10^{-2} min^{-1} compared to N-TiO_2 without silver (9.6 x 10^{-2} min^{-1}) which is accredited to a reduction in recombination. Dimethysulfoxide and sodium thiosulfate are investigated as sources for sulfur doping of TiO_2. Sodium thiosulfate produces S-TiO_2 that is highly photoactive (43.1 x 10^{-2} min^{-1}) compared to S-TiO_2 synthesised from dimethylsulfoxide (8.4 x 10^{-2} min^{-1}). A combination of sodium thiosulfate and 1, 3 diaminopropane for N, S co-doped TiO_2 resulted in the formation of sodium titanates. Through FTIR and Raman spectroscopy it is shown that both nitrogen atoms from 1, 3-diaminopropane chelate to a single titanium metal centre. 1, 3-diaminopropane is also found to cause retention of sodium during the sol-gel synthesis leading to the formation sodium titanate.

TiO_2/ZnO hybrid materials show enhanced photocatalytic efficiency through the formation of heterojunctions where excited electrons migrate from TiO_2 to ZnO, delaying recombination. Chapter six describes a sol-gel synthesis of ZnO/TiO_2 hybrid. A number of molar ratios of zinc precursor to titanium precursor are investigated. Anatase, rutile and zinc oxide are formed from the sol-gel synthesis but it is found that zinc titanate phases dominated the material structures. Through XRD it is shown that when the titanium precursor is in excess over the zinc precursor, high percentages of anatase (at initial calcination temperatures 400 – 700 °C) and rutile are formed. Zinc metatitanate forms at ~ 600 °C. The samples with excess titanium precursor show high percentages of zinc metatitanate at temperatures 700 – 900 °C and at 1000 °C there is an almost 1:1 conversion of zinc metatitanate to zinc orthotitanate. For samples where zinc precursor is in excess, zinc oxide is the dominant phase at low calcination temperatures (400 – 600 °C) but at increased temperatures (> 700 °C), $Zn_2Ti_3O_8$ is formed. The $Zn_2Ti_3O_8$ undergoes ~1:1 phase transformation to form zinc orthotitanate at 1000 °C. Raman and FTIR show the formation of titanium oxalate and zinc oxalate coordinated structures. These are believed to form infinite chains that may combine during crystallisation to form zinc titanate structures.

In summary, the results shown in the current study have shown how strongly the synthesis conditions can affect the crystalline behaviour of metal oxide materials. A greater understanding of the synthesis of these materials can contribute to the wide area of semiconductor research.

Declaration

I certify that this thesis which I now submit for examination for the award of PhD, is entirely my own work and has not been taken from the work of others, save and to the extent that such work has been cited and acknowledged within the text of my work.

This thesis was prepared according to the regulations for postgraduate study by research of the Dublin Institute of Technology and has not been submitted in whole or in part for another award in any Institute.

The work reported on in this thesis conforms to the principles and requirements of the Institute's guidelines for ethics in research.

The Institute has permission to keep, lend or copy this thesis in whole or in part, on condition that any such use of the material of the thesis be duly acknowledged.

Signature

_____

Nicholas Nolan

Date _____

Acknowledgements

Where to start? For the past few years there have been several people that have been there for me that I wish to mention. An acknowledgement in my thesis is just a small gesture and doesn't truly represent how much I appreciate the influence that many people have had on my life.

Firstly I wish to thank my supervisors Suresh and Michael. Both of you were always ready to answer any question I had no matter how trivial, you replied to all my enquiries with great haste and you put a tremendous amount of effort into every aspect of my project both in the lab and in our many discussions. You were a constant source of ideas, knowledge and encouragement and without you I could not have achieved as much. I will always remember your efforts so thank you.

To my friends and companions in the lab and office; Gary, Mim, Damian, Luke, Anne, Mark, Zlata, Theresa, Reena, Vinod, Rav, Kieran and Crystal. You were (almost) all with me from the start and you've made the whole experience far more enjoyable so thank you. Thank you for the many pints, games of pool, poker and golf, I'll miss our tea breaks and chats. My PhD work is over but I'm sure our friendship will continue for many years. Luke, figure 4.15 is for you, thanks for the idea. However, the (non-existent) PL figures are also yours, thanks. Anne, thanks for your efforts on the SEM it's much appreciated even though the images are not included in this work. Andrew thanks for all your IT help, it's much appreciated.

I must also extend gratitude to all the CREST team who have given me plenty of ideas in our many discussions and whose constant expertise has been a great resource for me throughout my PhD.

To Hugh and Mary, thanks for Focas, it's a credit to you both from both scientific and social aspects. I've had a great time here.

For my friends from home, cheers for the constant inspiration regarding Bunsen burners and test tubes, although I never actually used either, I appreciate the sentiment.

I've been extremely lucky with my housemates for the past few years. Cathie, Yvonne, Nessa and Mandy it's been great to 'have the chat' after a long day in the lab, thanks.

To Melissa, you were a major part of my life at the start of this work. Although things didn't work out as planned it has been great to have you in my life again. You will always hold a special place in my thoughts and in my heart. I couldn't write an acknowledgement without mentioning you.

Finally for my family, Caroline, Sue and Liz thanks for everything, from your generosity to your many dinners and chats I'd be lost without you. It's great to have a PhD but it's better to have you three and although my nieces and nephews didn't contribute much to this work, it's great to have them all and it's always a pleasure to experience the innocence that surronds them at such a young age, every one of them has brought me great joy.

And last but certainly not least, Mam and Dad. I've no doubt that without your continued support and encouragement I would not have completed a degree let alone this. You truly are wonderful parents and I will forever be grateful for everything you've done for me throughout my life. This thesis is for both of you!

“Mystery is a very necessary ingredient in our lives. Mystery creates wonder, and wonder is the basis for man’s desire to understand. Who knows what mysteries will be solved in our lifetime and what new riddles will become the challenge of new generations?”

Neil Armstrong, Sept. 1969

Ad astra per aspera

Table of Contents

Abstract ... **iii**

Declaration ... **vi**

Acknowledgements ... **vii**

Abbreviations Used ... **xv**

List of Figures ... **xvii**

List of Tables and Schemes ... **xxii**

Tables ... xxii

Schemes ... xxiii

1 Introduction ... **1**

1.1 Overview ... 2

1.2 Applications of TiO_2 ... 4

1.2.1 Photocatalytic splitting of water ... 4

1.2.2 Self-cleaning surfaces ... 5

1.2.3 The dye sensitised solar cell ... 6

1.2.4 Photocatalytic degradation of pollutants ... 7

1.3 Electronic Structure of a Semiconductor ... 8

1.4 Physical Properties of TiO_2 ... 10

1.4.1 Anatase to rutile transformation ... 13

1.5 Mechanism of Photocatalysis ... 14

1.5.1 Electronic processes ... 14

1.5.2 Recombination ... 15

1.5.3 Physical effects ... 16

1.6 Superhydrophilicity ... 17

1.7 Improving Photocatalytic Materials ... 19

1.7.1 Decreasing the band gap (visible light activated TiO_2) ... 19

1.7.2 Reducing recombination ... 21

1.7.3 Deactivation of TiO_2 ... 24

1.8 Synthesis Techniques 24
1.8.1 Hydrothermal synthesis 25
1.8.2 Combustion 25
1.8.3 Gas phase methods 25
1.8.4 Microwave synthesis 26
1.9 Sol-Gel Processing 26
1.10 Mechanism of Sol-Gel Synthesis 27
1.10.1 Mechanism of hydrolysis 28
1.10.2 Mechanism of condensation 28
1.10.3 Role of the catalyst 31
1.10.4 Chemical modification 32
1.11 Overview of Thesis 35
1.12 Aims and Objectives 36
2 Experimental Procedures and Characterisation Techniques 39
2.1 Chemicals Used 40
2.2 Synthesis of Nanomaterials 40
2.2.1 Synthesis of titanium dioxide 40
2.2.2 Silver modified TiO_2 41
2.3 Ag, Al, N, S and co-doped (Al, N), (Al, S), (Al, N, S) and (Ag, Al, N, S) titania 42
2.3.1 Al-modified TiO_2 42
2.3.2 Synthesis of N-doped TiO_2 42
2.3.3 Synthesis of Al, N co-doped TiO_2 43
2.3.4 Synthesis of Ag, N-TiO_2 43
2.3.5 Synthesis of Al, S-doped TiO_2 43
2.3.6 Synthesis of Ag, N, S co-doped TiO_2 44
2.4 Synthesis of Zinc Titanates 45
2.4.1 Excess titanium precursor 45
2.4.2 Excess zinc precursor 46

2.5 Photocatalytic Studies 46
2.5.1 Metylene blue degradation 46
2.6 Characterisation Techniques 47
2.6.1 X-ray diffraction (XRD) 47
2.6.2 Fourier transform infrared spectroscopy (FTIR) 48
2.6.3 Raman spectroscopy 48
2.6.4 UV-visible absorption spectrometry (UV-vis) 48
2.6.5 UV-vis diffuse reflectance 49
2.6.6 Differential scanning calorimetry (DSC) 49
2.6.7 Field emission scanning electron microscopy (FESEM) 49
2.6.8 X-ray photoelectron spectroscopy 50
3 Formation of Titanium Formate Complexes; a Spectroscopic Study 51
3.1 Introduction 52
3.2 Results and Discussion 56
3.2.1 Effect of water 56
3.2.1.1 X-ray diffraction 56
3.2.1.2 Infrared spectroscopy 59
3.2.1.3 Raman spectroscopy 64
3.2.2 Effect of chelating agent 65
3.2.2.1 X-ray diffraction 65
3.2.2.2 Infrared spectroscopy 66
3.2.2.3 Raman spectroscopy 66
3.2.3 Photocatalytic studies 68
3.2.4 FESEM 70
3.3 Conclusions 74
4 Effect of Silver on the Chelation of Formic Acid to Titanium Isopropoxide .. 75
4.1 Introduction 76
4.2 Results and Discussion 78
4.2.1 X-ray diffraction 78

4.2.2 Infrared spectroscopy. 81
4.2.3 Raman spectroscopy 84
4.2.4 Differential scanning calorimetry 86
4.2.5 X-ray photoelectron spectroscopy 88
4.2.6 Proposed silver interaction 92
4.2.7 Diffuse reflectance spectroscopy 92
4.2.8 FESEM and EDX 96
4.3 Conclusions 98
5 Optimisation of a TiO_2 Photocatalyst through the Addition of Aluminium, Silver, Nitrogen and Sulfur 100
5.1 Introduction 101
5.2 Results and Discussion 104
5.2.1 Characterisation 104
5.2.1.1 Al-TiO_2 104
5.2.1.2 N-TiO_2 105
5.2.1.3 Al, N-TiO_2 107
5.2.1.4 Ag, N-TiO_2 112
5.2.1.5 Al, S-TiO_2 115
5.2.1.6 3% Ag, 1% Al, N, S-TiO_2 119
5.2.1.7 Sodium titanate 120
5.3 Conclusions 129
6 Sol-Gel Synthesis of Zinc Oxide/Titanium Dioxide Hybrid and the Resulting Formation of Zinc Titanates 131
6.1 Introduction 132
6.2 Results 133
6.2.1 Excess of titanium precursor 133
6.2.2 Excess of zinc precursor 136
6.2.3 Infrared spectroscopy 140
6.2.3.1 Excess titanium precursor 140

6.2.3.2 Excess zinc precursor 142
6.2.4 Raman spectroscopy 143
6.2.4.1 Excess titanium precursor 143
6.2.4.2 Excess zinc precursor 144
6.3 Discussion 146
6.4 Conclusions 151
7 Future Work 152
7.1 Investigate Alternative Carboxylate Chelating Agents 153
7.2 Incorporation of Powders into Thin Film Coatings 155
7.3 Synthesis of Visible Light Active, High Temperature Anatase 156
7.4 Antibacterial Testing 157
7.5 Nitric Oxide Degradation 157
7.6 Conclusions 159
References 160
Publications by the Author 169
Presentations by the Author 169
Appendices A-1
Appendix A: Gaussian fit of Ti2p XPS spectra with increasing amounts of silver A-1
Appendix B: EDX analysis of Ag-TiO_2 ..... A-3

Abbreviations Used

A	:	Anatase
A_N	:	Nucleophilic addition
ART	:	anatase to rutile transformation
BSE	:	Back-scattered electrons
CB	:	Conduction band
^{13}C NMR	:	Carbon^{13} nuclear magnetic resonance
CVD	:	Chemical vapour deposition
DMSO	:	Dimethylsulfoxide
DOS	:	Density of states
DSC	:	Differential scanning calorimetry
DSSC	:	Dye sensitised solar cell
EtOH	:	Ethanol
eV	:	electron volt
EXAFS	:	Extended X-ray absorption fine structure
e^-	:	excited electron
FA	:	Formic acid
FESEM	:	Field emission scanning electron microscopy
FT-IR	:	Fourier transform infrared spectroscopy
g	:	gram
h^+	:	positive hole
^{1}H NMR	:	Proton nuclear magnetic resonance
HOAc	:	Acetic acid
HOMO	:	Highest occupied molecular orbital
LUMO	:	Lowest unoccupied molecular orbital
mL	:	millilitre
MRSA	:	Methicillin-resistant *Staphylococcus aureus*
nm	:	nanometre

NO_x	:	Nitrogen oxides (NO and NO_2)
ns	:	nanosecond
OAm_t	:	Amyl alcohol
OBu	:	Butoxide
OEt	:	Ethoxide
OPr	:	Propoxide
OR	:	alkoxide
PL	:	Photoluminescence
ps	:	picosecond
PVD	:	Physical vapour deposition
R	:	Rutile
S_N	:	Nucleophilic substitution
SE	:	Secondary electrons
SEM	:	Scanning electron microscopy
STEM	:	Specimen current and transmitted electrons
TGA	:	Thermogravimetric analysis
TTIP	:	Titanium tetraisopropoxide
UV	:	Ultraviolet light
VB	:	Valence band
VOC	:	Volatile organic carbon
XANES	:	X-ray absorption near edge spectroscopy
XPS	:	X-ray photoelectron spectroscopy
XRD	:	X-ray diffraction

List of Figures

Figure 1.1. TiO_2 photocatalytic splitting of water[8,9] 4

Figure 1.2. Self cleaning windows from Pilkington Activ[10] 5

Figure 1.3. Pictures of DSSC[13,14] 6

Figure 1.4. Schematic of a DSSC showing energy levels and electronic transitions[15] ... 6

Figure 1.5. Change in the electronic structure of a semiconductor compound with increasing number of monomeric units *N*[19] 8

Figure 1.6. Band positions of various semiconductors and relevant redox couples[7] 9

Figure 1.7. Semiconductors, n-type (a), p-type (b) 10

Figure 1.8. Crystalline structures of titanium dioxide (a)-rutile, (b)-anatase, (c)-brookite[24] 11

Figure 1.9. Schematic of photocatalytic mechanism 14

Figure 1.10. Mechanism of photo-induced hydrophilicity 18

Figure 1.11. Schematic of N-doped TiO_2 photocatalysis 20

Figure 1.12. Mechanism for reduced recombination in the presence of silver 23

Figure 1.13. Proposed structure of titanium acetate[195] 35

Figure 3.1. Modes of carboxylate binding 54

Figure 3.2. The Carboxylate Functional Group 54

Figure 3.3. Percentage of anatase in the calcined TiO_2 samples, determined by XRD for materials heated to different temperatures (a) F_2W_4 – F_2W_{100}, (b) F_4W_4 – F_4W_{100}, (c) $F_{10}W_4$ – $F_{10}W_{100}$ (refer to P40 for table) 57

Figure 3.4. XRD of $F_{control}$ and F_4W_4 at 700 °C, A – anatase, R - rutile 58

Figure 3.5. IR spectra of TiO_2 precursor powders (a): F_2W_4 & (b): F_2W_8, where * = $\nu_{asym}(COO^-)$ and ‡ = $\nu_{sym}(COO^-)$ 59

Figure 3.6. Bidentate bridging modes of the formate group and TTIP, (a): *syn-syn* and (b): *syn-anti* 60

Figure 3.7. Bridging acetate ligands attached to TTIP 60

Figure 3.8. IR spectra of TiO_2 precursor powders (a): F_4W_4, (b): F_4W_8 and (c): F_4W_{10}, where * = $v_{asym}(COO^-)$ and ‡ = $v_{sym}(COO^-)$ 62

Figure 3.9. Raman spectra of TiO_2 precursor powders of F_4W_4 – F_4W_{10}..... 64

Figure 3.10. IR spectrum of TiO_2 precursor powders (a): $F_{control}$ and (b): F_4W_4, where * = $v_{asym}(COO^-)$ and ‡ = $v_{sym}(COO^-)$ 66

Figure 3.11. Raman spectra of $F_{control}$ 67

Figure 3.12. Photocatalytic degradation of methylene blue with F_4W_4 (700 °C), R^2 = 0.9981 68

Figure 3.13. FESEM image of $F_{10}W_4$ calcined at 700 °C..... 70

Figure 3.14. FESEM image of $F_{10}W_4$ calcined at 700 °C..... 71

Figure 3.15. FESEM image of $F_{control}$ calcined at 700 °C 72

Figure 3.16. FESEM image of $F_{control}$ calcined at 700 °C 73

Figure 4.1. XRD of 0 % and 5 % Ag-TiO_2 powders calcined at 700 °C 79

Figure 4.2. XRD of 0 % and 5 % Ag TiO_2 powders calcined at 800 °C 80

Figure 4.3. Variation in the nanocrystallite size (from XRD) as a function of increase in concentration of silver, at different calcination temperatures 80

Figure 4.4. IR spectra of TiO_2 powders with different mol % silver content after aging at 100 °C 82

Figure 4.5. IR spectra of TiO_2 powders with different mol % silver content before aging 83

Figure 4.6. IR spectra of TiO_2 powders with different mol % silver content after aging at 100 °C for 12 hr 83

Figure 4.7. Raman spectra of TiO_2 powders with different mol % silver content before calcination 84

Figure 4.8. DSC of 0 and 5 % Ag before ageing 86

Figure 4.9. DSC of 0 and 5 % Ag after ageing at 100 °C 86

Figure 4.10. XPS spectra of C 1s (a) and O 1s (b) of TiO_2 with and without silver before calcination 88

Figure 4.11. XPS spectra of Ti 2p (a) and Ag 3d (b) of 3 % Ag TiO_2 before calcination 89
Figure 4.12. O 1s XPS spectra of TiO_2 without silver calcined at 900 °C (a) and with 3 % silver calcined at 700 °C (b) 90
Figure 4.13. Ti 2p XPS spectra of TiO_2 without silver calcined at 900 °C (a) and with 3 % silver calcined at 700 °C (b) 90
Figure 4.14. Diffuse reflectance spectra of 0, 1, 3 and 5 % Ag TiO_2 calcined at 500 °C 93
Figure 4.15. Diffuse reflectance spectrum of silver nanoparticles (< 100 nm) 94
Figure 4.16. Mechanism for light absorption 94
Figure 4.17. Diffuse reflectance spectra of 0, 1, 3 and 5 % Ag TiO_2 calcined at 700 °C 95
Figure 4.18. Diffuse reflectance spectra of 0, 1, 3 and 5 % Ag TiO_2 calcined at 800 °C 96
Figure 4.19. FESEM image of 5 % Ag-TiO_2 calcined at 700 °C 97
Figure 4.20. FESEM image of 5 % Ag-TiO_2 calcined at 800 °C 97
Figure 5.1. Percentage anatase in Al – TiO_2 at various calcination temperatures 104
Figure 5.2. X-ray diffractogram of N doped TiO_2, 1:0.5 Ti:N 105
Figure 5.3. X-ray diffractogram of N doped TiO_2, 1:4 Ti:N 106
Figure 5.4. Diffuse reflectance spectra of TiO_2 and N-TiO_2 107
Figure 5.5. Schematic electronic structure for pure and N-doped anatase and rutile polymorphs of TiO_2[271] 108
Figure 5.6. X-ray diffractogram of 1 % Al, N doped TiO_2, 1:0.5 Ti:N 109
Figure 5.7. UV-vis absorption plot showing the degradation of methylene blue with N-TiO_2, Ti:N, 1:0.5 calcined at 600 °C (first order plot inset, R^2 = 0.9978) 110
Figure 5.8. X-ray diffractogram of 3 % Ag, N doped TiO_2, 1:0.5 Ti:N 112
Figure 5.9. Diffuse reflectance spectra of 3 % Ag, N-TiO_2 (Ti:N, 1:4) 113
Figure 5.10. X-ray diffractogram of 1 % Al, S doped TiO_2, 1:16 Ti:S (DMSO) 116
Figure 5.11. X-ray diffractogram of 1 % Al, S doped TiO_2, 1:1 Ti:S ($Na_2S_2O_3$) 116

Figure 5.12. Diffuse reflectance spectra of 1 % Al, S-TiO_2 (Ti:S, 1:1, DMSO) 117
Figure 5.13. X-ray diffractogram of 3 % Ag, 1 % Al, N, S co-doped TiO_2, 1:0.5:4 Ti:N:S 119
Figure 5.14. X-ray diffractogram of 3 % Ag, N, S co-doped TiO_2, 1:0.5:4 Ti:N:S 122
Figure 5.15. X-ray diffractogram of N, S co-doped TiO_2, 1:0.5:4 Ti:N:S..... 122
Figure 5.16. Diffuse reflectance spectra of 3 % Ag, 1 % Al, S, N-TiO_2 calcined at various temperatures..... 123
Figure 5.17. Diffuse reflectance spectra of S, N-TiO_2 calcined at various temperatures 124
Figure 5.18. Infrared spectrum of N-TiO_2 126
Figure 5.19. Diaminopropane chelated to titanium tetraisopropoxide 127
Figure 5.20. Infrared spectrum of N, S-TiO_2 128
Figure 6.1. Percentage phase composition of TZ-4:1 134
Figure 6.2. Percentage phase composition of TZ-4:2 134
Figure 6.3. Percentage phase composition of TZ-4:3 135
Figure 6.4. XRD of TZ-1:4, Z-ZnO and #-$TiZn_2O_4$ 137
Figure 6.5. XRD of TZ-3:4, R-rutile, Z-ZnO, +-$ZnTiO_3$ and #-$TiZn_2O_4$ 137
Figure 6.6. Phase composition of TZ-1:4 138
Figure 6.7. Phase composition of TZ-2:4 139
Figure 6.8. Phase composition of TZ-3:4 139
Figure 6.9. IR spectra of TZ-4:1 and TZ-4:3..... 140
Figure 6.10. IR spectra of TZ-1:4 and TZ-3:4..... 142
Figure 6.11. Raman spectra of TZ-4:1 and TZ-4:3..... 143
Figure 6.12. Raman spectra of TZ-1:4, TZ-2:4 and TZ-3:4 144
Figure 6.13. Molecular structure of zinc acetate dihydrate..... 146
Figure 6.14. Molecular structure of zinc oxalate dihydrate (a) and the infinite chain arrangement (b)..... 147
Figure 6.15. Molecular structure of titanium isopropoxide (a) and chelated titanium isopropoxide, titanium acetate (b) 147

Figure 6.16. Proposed structures of metal oxalate chains formed, zinc oxalate (a) and titanium oxalate (b) 148
Figure 7.1. Chemical structure of malic acid (a) and tartaric acid (b) 153
Figure 7.2. Possible structure of malic acid chelated to titanium isopropoxide 154
Figure 7.3. Chemical structure of 3-amino-2-(hydroxymethyl)propionic acid (a) and 4-amino-3-hydroxybutyric acid (b) 154
Figure 7.4. Scheme of the surface modification of the nanoparticulate TiO_2[320] 155
Figure 7.5. Proposed mechanism of the formation of thin film coating[320] 155
Figure 7.6. Scheme of photoactivation of the protective coating[320] 156
Figure 7.7. A schematic of the test equipment (dimensions in millimetres) 158
Figure A.1. Ti2p XPS spectrum of 0% Ag before calcination A-1
Figure A.2. Ti2p XPS spectrum of 1% Ag before calcination A-1
Figure A.3. Ti2p XPS spectrum of 3% Ag before calcination A-2
Figure A.4. Ti2p XPS spectrum of 5% Ag before calcination A-2
Figure A.5. Analysis area for EDX spectrum of 5% Ag-TiO_2 calcined at 700 °C A-3
Figure A.6. EDX spectrum of 5% Ag-TiO_2 calcined at 700 °C A-3
Figure A.7. Elemental mapping of 5% Ag-TiO_2 calcined at 700 °C, mapping area (a), oxygen profile (b), titanium profile (c) and silver profile (d) A-4
Figure A.8. Analysis area for EDX spectrum of 5% Ag-TiO_2 calcined at 800 °C A-5
Figure A.9. EDX spectrum of 5% Ag-TiO_2 calcined at 800 °C A-5
Figure A.10. Elemental mapping of 5% Ag-TiO_2 calcined at 800 °C, mapping area (a), oxygen profile (b), titanium profile (c) and silver profile (d) A-6

List of Tables and Schemes

Tables

Table 1.1. Physical and structural properties of anatase and rutile 12

Table 1.2. Oxidation potentials of various oxidants relative to NHE 15

Table 2.1. Molar ratios of TTIP:FA:H_2O 41

Table 2.2. Amounts used for excess titanium samples 45

Table 2.3. Amounts used for excess zinc samples 46

Table 3.1. Reaction rate constants (±0.01, k/min^{-1}) for the degradation of methylene blue 69

Table 5.1. First order rate constants for methylene blue degradation with N-TiO_2 110

Table 5.2. First order rate constants for methylene blue degradation with N-TiO_2 114

Table 5.3. First order rate constants for methylene blue degradation with S-TiO_2 118

Table 5.4. First order rate constants for methylene blue degradation with co doped TiO_2 125

Table 6.1. Assigned frequencies for IR spectra of TZ-4:1 and TZ-4:3. 141

Table A1. Atomic weight percentages calculated from EDX of 5% Ag-TiO_2 calcined at 700 °C A-4

Table A2. Atomic weight percentages calculated from EDX of 5% Ag-TiO_2 calcined at 800 °C A-6

Schemes

Scheme 1.1. $TiO_2 + hv \rightarrow h^+_{VB} + e^-_{CB}$ 14

Scheme 1.2. $e^-_{CB} + h^+_{VB} \rightarrow$ energy 16

Scheme 1.3. $TiO_2 + hv \rightarrow e^- + h^+$ 21

Scheme 1.4. Redox pathways of hydroxylated TiO_2 22

Scheme 1.5. Hydrolysis reaction 28

Scheme 1.6. Alcoxolation reaction 28

Scheme 1.7. Oxolation reaction 29

Scheme 1.8. Acid catalyst reaction 31

Scheme 1.9. Partially hydrolysed polymer 32

Scheme 3.1. Crystallisation of chelated titanium precursor 73

Scheme 3.2. Crystallisation of titanium isopropoxide without chelating agent 73

Scheme 4.1. Illustration of blocking mechanism of silver on titanium – formate bridge (suggested structure) 92

Scheme 7.1. Schematic showing the removal of organic modifier under heat action to leave edge sharing octahedra 154

1 Introduction

1.1 Overview

In 1972 Fujishima and Honda published an article in Nature[1] that propelled titanium dioxide (TiO_2) into the world of research. They demonstrated the powerful semiconductor capabilities of TiO_2 in the splitting of water in a photoelectrochemical cell. Their work ignited a revolution in the world of semiconductor research with Frank and Bard going on to demonstrate titanium dioxide's unique properties for environmental remediation through the reduction of CN^- in water[2,3] in 1977, and Ollis using TiO_2 for the mineralisation of organic pollutants in 1983.[4,5] In the 1990's, after Graetzel's paper on the dye sensitised solar cell,[6] TiO_2 became one of the most internationally researched semiconductor materials. The increase in TiO_2 publications per year demonstrates the growth in the area. In 1995 there were 700 TiO_2 publications, seven years later that number increased to over 2000 publications.[7] So why does TiO_2 attract such interest? There are many reasons why and they will be addressed throughout the introduction of this thesis but for the purpose of this body of work the important question is why has it attracted my interest?

The main focus of my research centres on two topics; one being the photocatalytic abilities of TiO_2, that is when light of energy greater than the band gap excites an electron from the valence band to the conduction band, hydroxyl radicals are formed that will oxidise organic materials to CO_2 and H_2O. Simple as this process appears, there are many factors which influence the efficiency of the photocatalytic materials. Many of which are investigated throughout this thesis.

My second area of interest regarding TiO_2 involves investigating the formation and transformation of the crystalline phases associated with titanium dioxide. The three main polymorphs of TiO_2 are anatase, rutile and brookite. Anatase and brookite are both metastable and rutile, found in nature, is the thermodynamically stable phase. All three phases can be readily synthesised in the laboratory. Typically, anatase will form at temperatures between 300 – 600 °C and at higher temperatures anatase to rutile transformation will occur. However, the synthesis conditions can have a strong

influence over the anatase to rutile transformation temperature, and in this study, a thorough investigation of the role that chemical modifiers have on the crystallisation properties of TiO_2 has been carried out.

One of the attractions of TiO_2 synthesis is its ease of preparation. Titanium alkoxides are readily available and inexpensive. Alkoxides stabilise titanium in its highest oxidation state but because of the low electronegativity of the metal they are very reactive towards nucleophilic attack. Addition of water to titanium alkoxide causes spontaneous proton transfer from the water to the metal as well as coordination expansion. Because of the reactivity of titanium alkoxides towards nucleophilic attack, this reaction is quite uncontrollable and precipitation of an amorphous powder will occur. This powder can be calcined to form anatase but will transform to rutile at a low temperature (~600 °C). However, the reaction can be controlled with the addition of a chelating agent which produces anatase that is stable at higher temperatures. Sanchez, Livage, Henry and Doeuff pioneered the chemical modification of alkoxide precursors during the late 1980's where they showed how chemical additives such as acetic acid or acetyl acetone react with alkoxide precursors and how the resulting reaction pathways become more controlled, resulting in increased stability of anatase.[8-11] Several researchers have since discussed the anatase to rutile transformation and how it may be affected by the addition of various metals or additives.[12-20] However, generally these authors discuss what happens during the crystallisation or transformation process.

The body of work presented here proposes that the anatase to rutile phase transformation is not only influenced by additives during the calcination process but that the transformation temperature may be influenced as early as the initial alkoxide reaction.

1.2 Applications of TiO_2

1.2.1 Photocatalytic splitting of water

Since Fujishima and Honda carried out the photocatalytic splitting of water using TiO_2 in 1972,[1] great effort has gone into maximising the potential of the process as it can provide clean renewable energy from sustainable sources.[8]

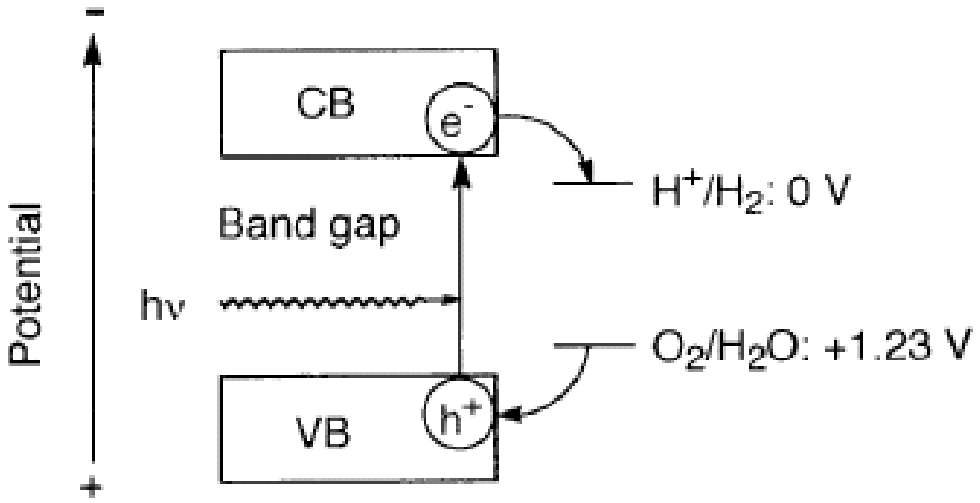

Figure 1.1. TiO_2 photocatalytic splitting of water[8,9]

Figure 1.1 shows a schematic presentation of the principle of water splitting using a TiO_2 photocatalyst. Light of energy grater than the band gap excites an electron from the valence band to the conduction band. The photogenerated electron/hole pair causes redox reactions. Water molecules are reduced by excited electrons to form H_2 and oxidised by holes to form O_2 leading to water splitting.[21,23-25]

1.2.2 Self-cleaning surfaces

Pilkington Glass have utilised titanium dioxide technology to develop a range of self cleaning windows known as Pilkington Activ.[10] Self-cleaning glass clearly displays the benefits of titanium dioxide's self-cleaning and super hydrophilic properties (figure 1.2).

Figure 1.2. Self cleaning windows from Pilkington Activ[10]

Titanium dioxide can be incorporated into concrete to produce photocatalyst-modified cement[7] It can be used to coat hospital surfaces and provide anti-bacterial protection against harmful bacteria such as *E. coli* and MRSA.[11] By applying TiO_2 to road side partitions and lights, the surfaces can be kept clean while having the added advantage of reducing harmful exhaust gases such as NO_x and VOCs.

Despite the great promise shown by the self-cleaning abilities of TiO_2 surfaces, there are certain limitations. Because TiO_2 is a wide band gap (3.2 eV) semiconductor material, the self-cleaning process can only be initiated by light of wavelength ~390 nm or less. This cause's substantial reduction in the efficiency of the product as light of such energy, ultraviolet light (UV), only makes up 3 – 5 % of the solar spectrum. Therefore, in order to improve the efficiency of these materials it is necessary to either reduce the band gap or to introduce mid-band gap energy levels that act as a stepping stone between the energy levels, facilitating visible light absorption.

1.2.3 The dye sensitised solar cell

The dye sensitised solar cell (DSSC) has shown great potential as the next generation of solar cells.[12] The DSSC has several advantages over current photovoltaic cells such as; low production costs, more consistent energy production from diffuse and direct sunlight, colour choice and transparency (figure 1.3).[6,12] Also, because the DSSC utilises TiO_2 nanoparticles, solar cells of much smaller sizes can be produced and they can even be flexible.

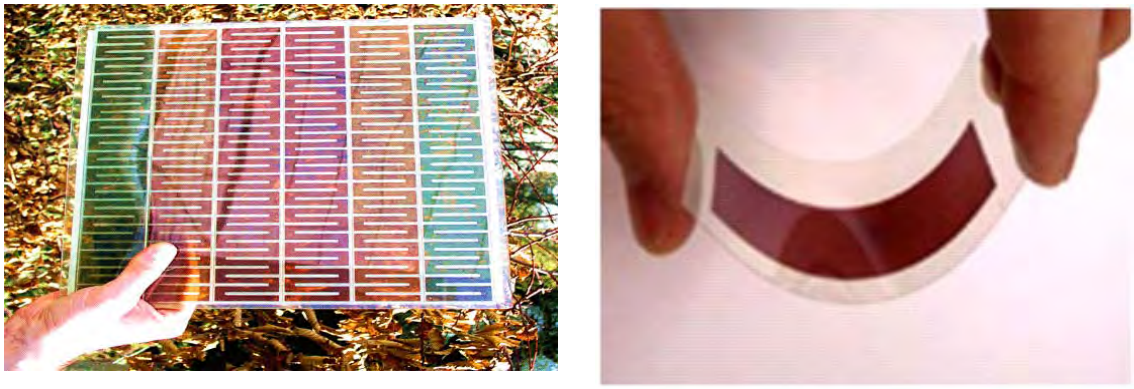

Figure 1.3. Pictures of DSSC[13,14]

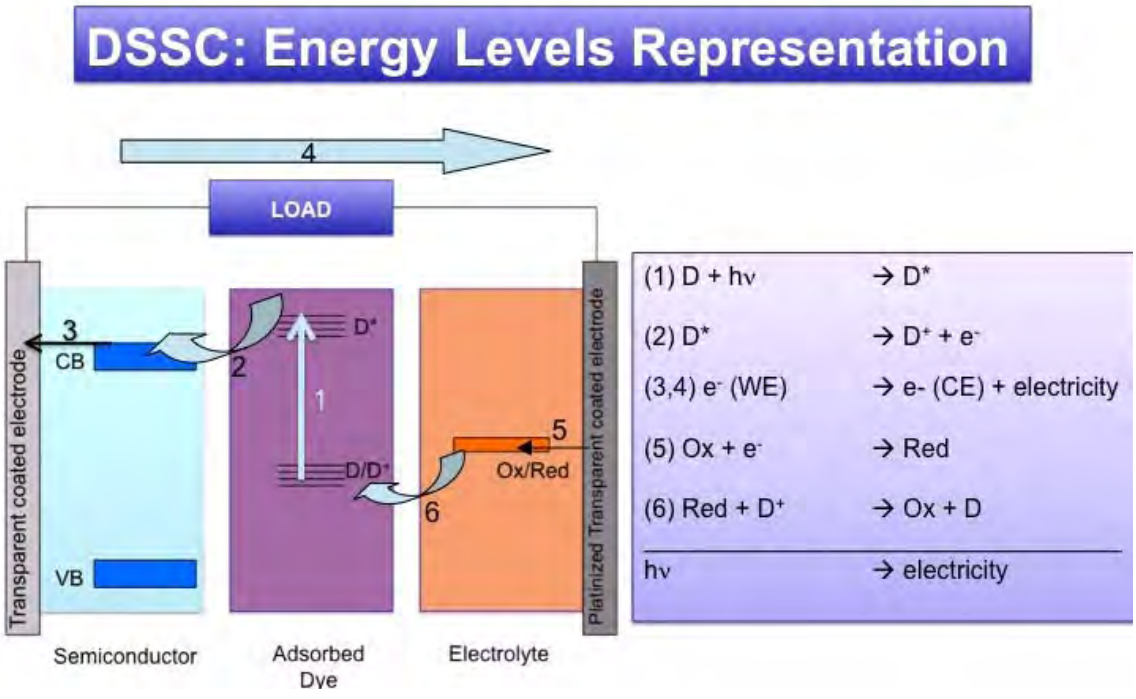

Figure 1.4. Schematic of a DSSC showing energy levels and electronic transitions[15]

The DSSC mimics nature's photosynthetic process of light absorption and electron injection. In the DSSC (figure 1.4), light is absorbed by a coloured dye (commonly

ruthenium based dye), to produce an excited singlet state. Excited electrons from the dye are then injected into the conduction band of the TiO_2 support. Following successful injection, the electron percolates through the oxide layer onto the working electrode. Once the electron reaches the electrode it will travel to the counter electrode, therefore generating an electrical current. The electrolyte contains a redox couple (1, 2-dimethyl-3-propylimidazolium iodide, iodine, N-methylbenzimidazole, I^-/I_3^-) which will regenerate the oxidised dye, allowing for the process to start again.[6,12]

A significant drawback of the DSSC is the electronic processes that compete with injection from the dye to the TiO_2 working electrode. The main competitive pathway is that of electron recombination in the dye. So instead of the dye excited electron transferring to the conduction band of the TiO_2, it will relax to the ground state of the dye. Therefore, for the full potential of DSSC energy production to be realised it is necessary for researchers to produce TiO_2 with enhanced electron collection abilities.[16] As TiO_2 synthesis reactions are better understood it may become possible to design synthesis techniques that will produce TiO_2 materials capable of enhanced electron capture properties.

1.2.4 Photocatalytic degradation of pollutants

Titanium dioxide has attracted great interest in the past decade due to its environmental applications such as air purification and water remediation.[1,17-25] The photocatalytic mechanism (which will be covered in greater detail later in section 1.5) is activated by light of energy greater than that of the semiconductor band gap. Upon photo-activation, an electron-hole pair is produced that reacts with adsorbed species to produce radical species. These radicals are powerful oxidising agents and will oxidise organic contaminants to CO_2 and H_2O.

1.3 Electronic Structure of a Semiconductor

When molecular orbitals are formed from two atoms, each type of atomic orbital gives rise to two molecular orbitals. When *N* atoms are used, *N* molecular orbitals are formed. In solids, *N* is very large, resulting in a large number of orbitals.[17] The overlap of a large number of orbitals leads to molecular orbitals that are closely spaced in energy and so form a virtually continuous band (figure 1.5).[18] The overlap of the lowest unoccupied molecular orbitals (LUMO) results in the formation of a conduction band and a valence band is formed from overlapping the highest occupied molecular orbitals (HOMO). The band separation is known as the band gap (E_g), a region devoid of energy levels. From the illustration shown in figure 1.5, the reduction in the band gap size with the formation of bands can clearly be seen.

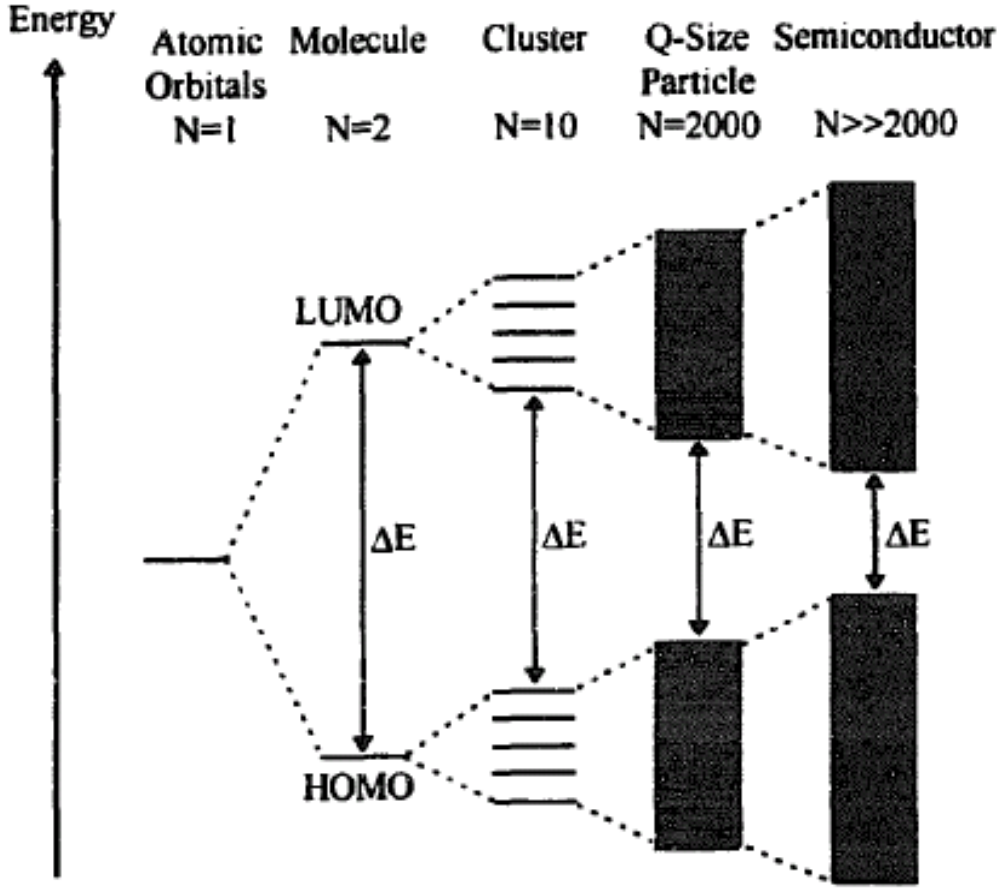

Figure 1.5. Change in the electronic structure of a semiconductor compound with increasing number of monomeric units *N*[19]

If a band is formed from the molecular overlap of *s* orbitals it is called an *s* band and likewise, an overlap of *p* orbitals, forms a *p* band and an overlap of *d* orbitals will give a *d* band. Typically, *p* orbitals have higher energy than *s* orbitals, resulting in a band gap. However, if the *s* and *p* bands are of similar energy, then the two bands overlap.[18] In titanium dioxide, the valence band consists of oxygen 2 p orbitals and the conduction band is made up from the titanium 3 d orbitals.[8,20]

The band gap of TiO_2 anatase is 3.2 eV and rutile is 3.0 eV corresponding to an absorbance threshold, λ = 388 and 415 nm respectively. Figure 1.6 shows the various band positions of different semiconductors. For a semiconductor to be capable of producing hydroxyl radicals, the potential of the valence band must be greater than the potential of OH•. From figure 1.6 it can be seen that ZnO, TiO_2, WO_3 and SnO_2 have the potential to produce hydroxyl radicals.

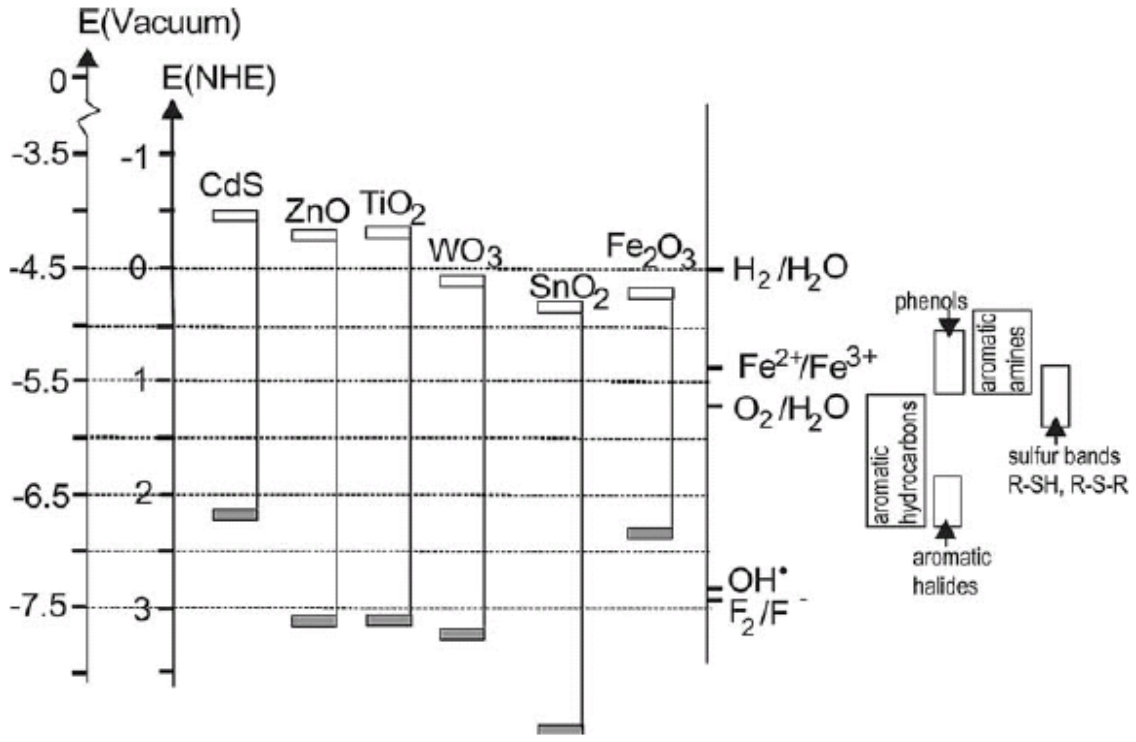

Figure 1.6. Band positions of various semiconductors and relevant redox couples[7]

Titanium dioxide is regarded as an n-type semiconductor due to the presence of oxygen vacancies in the lattice. These vacancies are formed upon the release of two electrons and molecular oxygen leaving a positive (+2) oxide ion vacancy.[7] When electrons of energy lower than the conduction band are present, the result is an n-type

semiconductor (figure 1.7a). Alternatively if a material is added with fewer electrons than the host, positive holes are added above the valence band resulting in a p-type semiconductor (figure 1.7b).

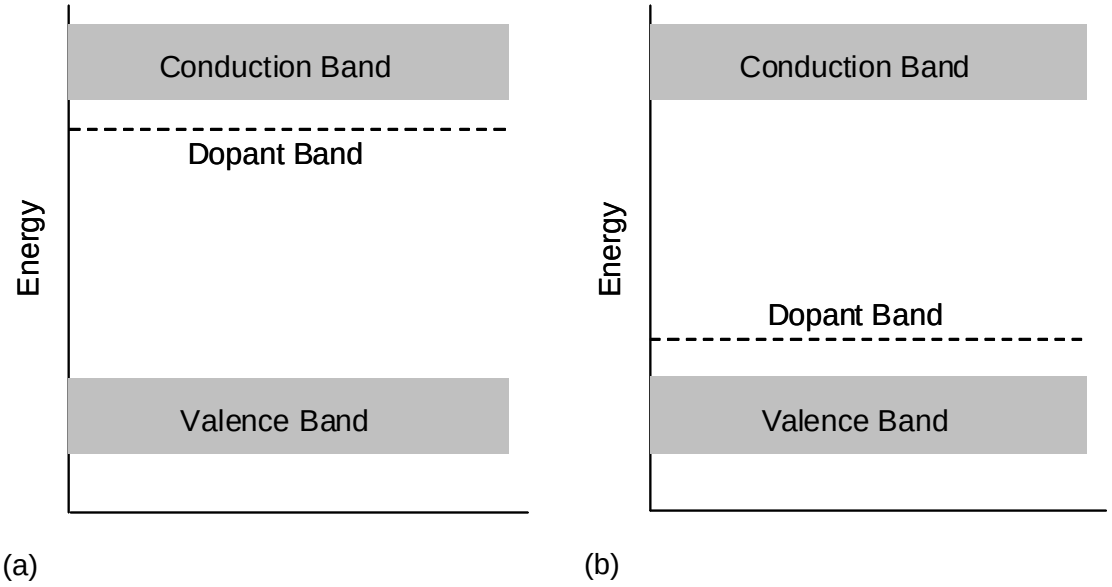

Figure 1.7. Semiconductors, n-type (a), p-type (b)

1.4 Physical Properties of TiO_2

Titanium is the world's fourth most abundant metal and ninth most abundant element. It was discovered in 1791 in England by Reverend William Gregor, who recognised the presence of a new element in ilmenite.[7] It was then rediscovered in rutile ore several years later by a German chemist, Heinrich Klaporth who named it after Titans, mythological first sons of the goddess Ge (earth in Greek mythology).[7]

Titanium is not found in its elemental state, it occurs mainly in minerals like rutile, ilmenite, leucoxene, anatase, brookite, perovskite and spene. It is also found in titanates and many iron ores.[7] The metal has been detected in meteorites and stars. In fact, samples brought back from the moon by Apollo 17 contained 12.1 % TiO_2.[7]

The primary source and the most stable form of titanium dioxide is rutile ore. It was discovered in Spain by Werner in 1803. Its name is derived from the Latin *rutilus*, red because of the deep colour observed in some specimens when the transmitted light is viewed.[7] Rutile is one of three main polymorphs of titanium dioxide (TiO_2), the other polymorphs being; anatase and brookite.[21-23] Brookite was discovered in 1825 by A.

Levy and was named after an English mineralogist, H. J. Brooke.[7] In 1801 anatase was named by R. J. Hauy from the Greek word *'anatasis'* meaning extension, due to its longer vertical axis compared to that of rutile.[7]

In all three forms, titanium (Ti^{4+}) atoms are co-ordinated to six oxygen (O^{2-}) atoms, forming TiO_6 octahedra.[23] All three forms differ only in the arrangement of these octahedra. The anatase structure, is made up of corner (vertice) sharing octahedra (figure 1.8b) resulting in a tetragonal structure.[7,8,21,22] In rutile the octahedra share edges to give a tetragonal structure (figure 1.8a)[7,8,21,22] and in brookite both edges and corners are shared to give an orthorhombic structure (figure 1.8c).[7,21,22]

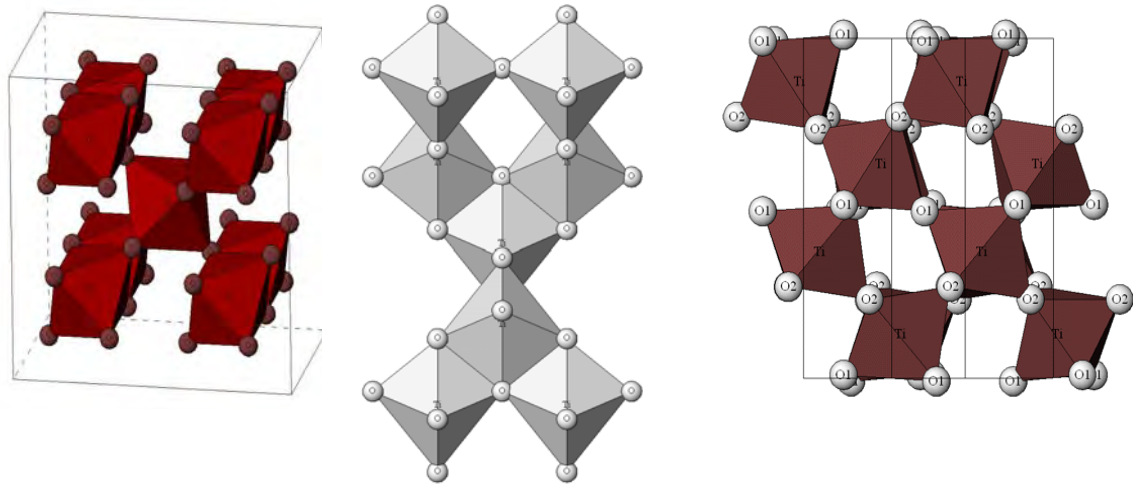

(a) **(b)** (c)

Figure 1.8. Crystalline structures of titanium dioxide (a)-rutile, (b)-anatase, (c)-brookite[24]

Titanium dioxide is an n-type semiconductor[25] that has a band gap of 3.2 eV for anatase,[26-29] 3.0 eV for rutile,[30-32] and ~3.2 eV for brookite.[33-35] Titanium dioxide (TiO_2) is the most widely investigated photocatalyst due to its strong oxidative properties, low cost, non toxicity, chemical and thermal stability.[36-38] Anatase and rutile are the most researched polymorphs. Their properties are summarised in table 1.1.

Table 1.1. Physical and structural properties of anatase and rutile

Property	Anatase	Rutile
Molecular Weight (g/mol)	79.88	79.88
Melting point (°C)	1825	1825
Boiling Point (°C)	2500 ~ 3000	2500 ~ 3000
Specific gravity	3.9	4.0
Light absorption (nm)	< 390	< 415
Mohr's Hardness	5.5	6.5 – 7.0
Refractive index	2.55	2.75
Dielectric constant	31	114
Crystal structure	Tetragonal	Tetragonal
Lattice constants (Å)	a = 3.78 c = 9.52	a = 4.59 c = 2.96
Density (g/cm^3)	3.79	4.13
Ti–O bond length (Å)	1.94 (4) 1.97 (2)	1.95 (4) 1.98 (2)

In the past few decades there have been several exciting breakthroughs with respect to titanium dioxide. The first major breakthrough was in 1972 when Fujishima and Honda reported the photoelectrochemical splitting of water ($2H_2O \rightarrow 2H_2 + O_2$) using a TiO_2 anode and a Pt counter electrode.[1] Titanium dioxide first showed promise for the remediation of environmental pollutants in 1977 when Frank and Bard investigated the reduction of CN^- in water.[2,3] This led into an increasingly well researched area of TiO_2 because of the potential implications for environmental water and air purification utilising solar energy.[36,39-46] In 1997 Wang *et al* reported TiO_2 surfaces with excellent anti-fogging and self-cleaning abilities which were attributed to the super hydrophilic attributes of the TiO_2 surfaces.[47] Nano sized titanium dioxide was employed to

excellent use in an efficient solar cell, the dye sensitised solar cell (DSSC) as reported by Graetzel and O'Regan in 1991.[6]

1.4.1 Anatase to rutile transformation

The anatase to rutile phase transformation in TiO_2 is an area of both scientific and technological interest.[48,49] The anatase to rutile transformation (ART) is kinetically defined and the reaction rate is determined by parameters such as particle shape/size,[50] purity,[51] source effects,[52] atmosphere[53] and reaction conditions.[54] It is agreed that the mechanism for phase transformation of titania is one of nucleation and growth.[55,56] Anatase nanocrystals coarsen, grow and then transform to rutile only when a critical size is reached.[57] Therefore, phase transformation is dominated by effects such as defect concentration,[40] grain boundary concentration,[58] and particle packing.[59] Rutile is the thermodynamically stable phase, while anatase and brookite are both metastable, transferring to rutile under heat treatment at temperatures typically ranging between 600 – 700 °C.[21] Anatase is widely regarded as the most photocatalytically active of the three crystalline structures.[7,60,61] The generally accepted theory of phase transformation is that two Ti–O bonds break in the anatase structure, allowing rearrangement of the Ti–O octahedra, which leads to a smaller volume, forming a dense rutile phase.[62,63] The removal of oxygen ions, which generate lattice vacancies, accelerates the transformation. The transition follows first order kinetics, with an activation energy of ~ 418 kJ mol^{-1}.[64] The breaking of these bonds can be affected by a number of factors, including the addition of dopants, synthesis method and thermal treatment.[57,62,63,65,66]

1.5 Mechanism of Photocatalysis

1.5.1 Electronic processes

The term photocatalysis implies that light is acting as a catalyst in a reaction which is not the case.[19,67] However, the term photocatalysis will always be used to describe the process that semi-conductor materials such as TiO_2 undergo when irradiated by light of a certain wavelength. It is a term that implies photon assisted generation of catalytically active species.

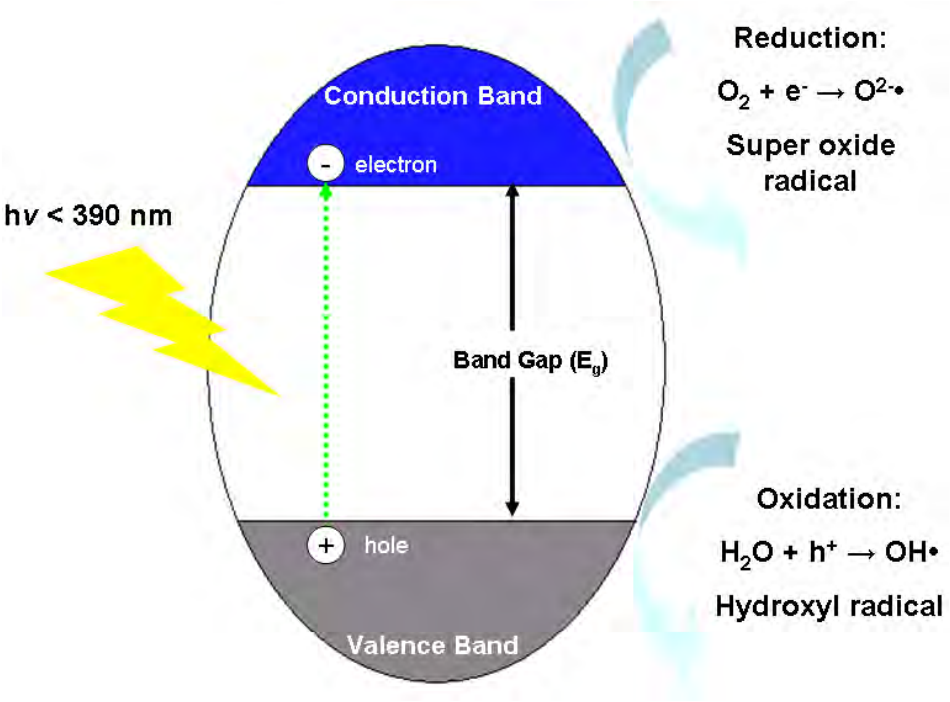

Figure 1.9. Schematic of photocatalytic mechanism

In photocatalysis, light of energy greater than the band gap of the semiconductor, excites an electron from the valence band to the conduction band (figure 1.9). In the case of anatase, the band gap is 3.2 eV, therefore UV light (< 390 nm) is required to initiate the photocatalytic process. Light (< 390 nm) excites an electron (e^-_{CB}) to the conduction band generating a positive hole (h^+_{VB}) in the valence band (Scheme 1.1). Charge carriers can be trapped as Ti^{3+} and O^- defect sites in the TiO_2 lattice, or they can recombine, dissipating energy.[68]

$TiO_2 + h\nu \rightarrow h^+_{VB} + e^-_{CB}$ Scheme 1.1

Alternatively the charge carriers can migrate to the catalyst surface and initiate redox reactions on the adsorbates.[69] Positive holes generated by light become trapped by surface adsorbed H_2O. The H_2O gets oxidised by h^+_{VB} producing H^+ and OH• radicals (Eqn. 1.1), which are extremely powerful oxidants (table 1.2). The hydroxyl radicals subsequently oxidise organic species from the surrounding environment to CO_2 and H_2O (Eqn. 1.3)[70] and in most cases these are the most important radicals formed in TiO_2 photocatalysis.

Table 1.2. Oxidation potentials of various oxidants relative to NHE

Oxidant	Oxidation Potential (V)
OH• (hydroxyl radical)	2.80
O_3 (Ozone)	2.07
H_2O_2 (hydrogen peroxide)	1.77
HClO (hypochlorous acid)	1.49
Cl (chlorine)	1.36

Electrons in the conduction band can be rapidly trapped by molecular oxygen adsorbed on the particle. Trapped molecular oxygen will be reduced by excited electrons to form superoxide (O^{2-}•) radicals (Eqn, 1.2) that may further react with H^+ (Eqn. 1.4), to generate peroxide radicals (•OOH) and H_2O_2 (Eqn. 1.5).[71,72]

1.5.2 Recombination

Recombination is a major limitation in semiconductor photocatalysis as it reduces the overall quantum efficiency of the photocatalyst because of the high recombination rate of photo-induced electron-hole pairs at the surface of the photocatalyst.[73] The photocatalytic efficiency can be significantly enhanced if recombination is reduced. Doping with ions,[74-76] heterojunction coupling[77-79] and nanosized crystals[80,81] have all been reported to promote separation of the electron-hole pair, reducing recombination and therefore improving the photocatlaytic activity of the semiconductor material.

When recombination occurs, the excited electron reverts to the valence band without reacting with adsorbed species (Scheme 1.2).[82] Radiation may be emitted when an excited electron recombines with the valence band. As such, photoluminescence may be successfully employed to monitor recombination and in general, low intensity photoluminescence signals indicate lower recombination rates.[73]

$e^-_{CB} + h^+_{VB} \rightarrow$ energy Scheme 1.2

$H_2O + h^+_{VB} \rightarrow \bullet OH + H^+$ Equation 1.1

$O_2 + e^-_{CB} \rightarrow O_2^-\bullet$ Equation 1.2

$\bullet OH + VOC \rightarrow H_2O + CO_2$ Equation 1.3

$O_2^-\bullet + H^+ \rightarrow \bullet OOH$ Equation 1.4

$\bullet OOH + \bullet OOH \rightarrow H_2O_2 + O_2$ Equation 1.5

$O_2^-\bullet + VOC \rightarrow CO_2 + H_2O$ Equation 1.6

$\bullet OOH + VOC \rightarrow CO_2 + H_2O$ Equation 1.7

Equations 1.1 – 1.7 schematise the whole process.[68,70,83] Hydroxyl radicals produced by the photocatalytic process will oxidise the majority of volatile organic compounds (VOC) until complete mineralization. Recombination competes strongly with the photocatalytic process. It may occur on the surface in the bulk and is in general catalysed by impurities, defects, or all factors which introduce bulk or surface imperfections into the crystal.[84] The fact that the process can only be initiated by UV light is also a limiting factor in the process. It is desirable to produce a photocatalyst that can be activated by visible light to make full use of the solar spectrum.

1.5.3 Physical effects

The photocatalytic efficiency of a TiO_2 photocatalyst depends not only on the electronic properties of the materials. The availability of active sites on the material surface also plays a major role in the ability of the photocatalytic material to degrade organic contaminants.[7] A photocatalyst can produce an infinite amount of oxidising species to no effect unless the resulting radicals migrate to the TiO_2 surface where they can initiate the oxidation of the organic species from the surrounding environment.

Therefore, properties such as crystal size and structure, pore size/volume, density of OH groups, surface charge, number and nature of trap sites and absorption/desorption characteristics all play an important factor in the photocatalytic activity of TiO_2.[7,85] Large surface areas will result in an increase in the number of active degradation sites available for degradation reactions. A delicate balance between surface area and recombination must be achieved in order to produce an effective photocatalyst. Smaller crystal sizes will result in larger surface areas but a spectral blue shift can be observed with crystal sizes below 10 nm. This is believed to be the result of the quantum size effect. The quantum size effect is believed to produce a blueshift in the absorbance band edge as a consequence of exciton confinement with decreasing particle size.[86]

Recombination is also promoted with larger surface areas. This is usually because increased amounts of crystal defects are present with larger surface areas. The surface defects will act as recombination centres for the photoinduced electron/hole pair.[7]

Surface hydroxyl groups also affect the photocatalytic efficiency of the materials. Surface hydroxyl groups participate in the photocatalytic process in a number of ways. They trap photoexcited electrons and produce OH• radicals and they can also act as active absorption sites for pollutants.[7] The high temperature calcination of TiO_2 will result in the removal of surface hydroxyl groups. Because rutile is produced from the high temperature calcination of anatase, rutile possesses fewer surface hydroxyl groups and as such this is considered as one of the reasons why rutile is a weaker photocatalyst than anatase.

1.6 Superhydrophilicity

It is known that titanium dioxide surfaces display excellent anti-fogging and self-cleaning abilities because of the super hydrophilic attributes the TiO_2 surfaces.[47] Wang *et al* have reported that the transition between the hydrophobic and hydrophilic states could possibly be connected to photoactive electronic transition across the energy gap, *i.e.*, the conversion of Ti^{4+} sites into Ti^{3+} on the surface under UV illumination.[87,88]

Therefore in terms of UV activation, there are common features between the photocatalytic mechanism and hydrophilicity.[89]

Recently however, there has been some consensus that the basic mechanism of these two phenomena may not be the same. According to Wanabe,[90] the existence of sodium ions in TiO_2 showed very different effects on these photoinduced reactions, suggesting two different photoinduced defect reaction mechanisms on the surface. The essential photocatalytic mechanism could be explained in terms of bulk properties, such as the charge transfer efficiency of a wide gap semiconductor. Therefore it seems photocatalysis of TiO_2 is more dependent on bulk properties, while the hydrophilicity of TiO_2 is an inherently interfacial property, limited to the interface between TiO_2 surface (solid) and water (liquid).[89]

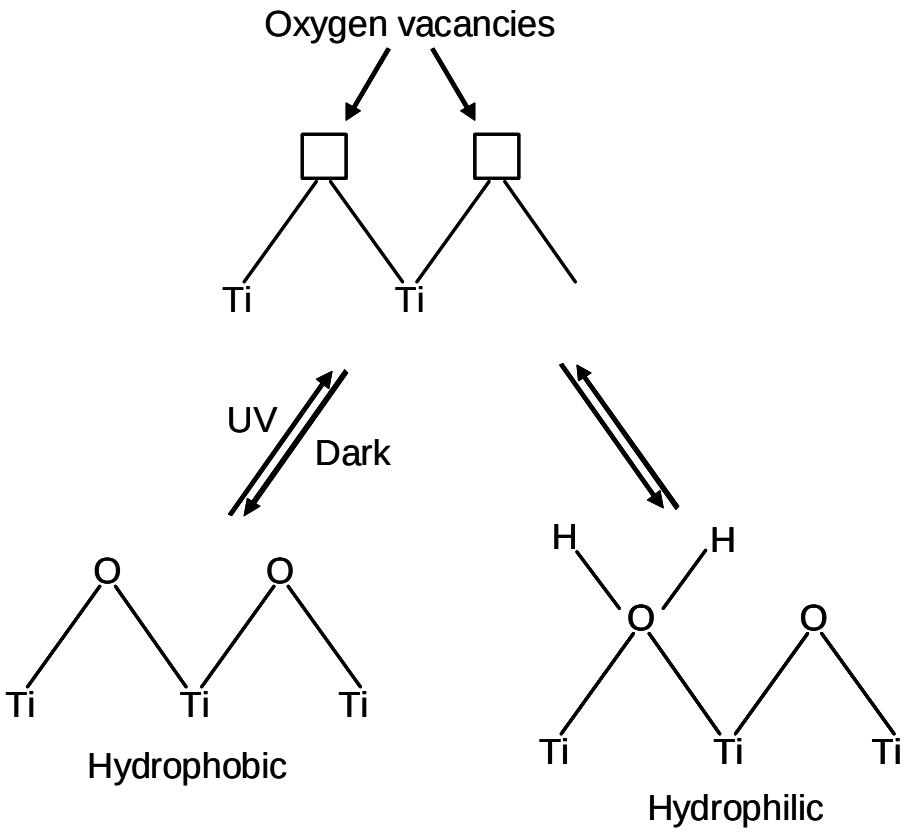

Figure 1.10. Mechanism of photo-induced hydrophilicity

The hydrophilic mechanism is believed to be as follows; electrons reduce the Ti (IV) cations to the Ti (III) state, and the holes oxidise the O^{2-} anions. In the process, oxygen atoms are ejected and oxygen vacancies are created (figure 1.10). Water molecules

can then occupy these oxygen vacancies, producing adsorbed OH groups, which tend to make the surface hydrophilic.[91]

1.7 Improving Photocatalytic Materials

1.7.1 Decreasing the band gap (visible light activated TiO_2)

A major drawback of TiO_2 photocatalysis is the large band gap. Titanium dioxide can only be activated upon irradiation with a photon of light <390 nm, limiting its use under solar irradiation.[92-94] Ultraviolet light makes up 3 – 5 % of the solar spectrum, whereas the spectrum consists of ~ 40 % visible light. Therefore, in order to utilise TiO_2 to its full potential it is necessary to decrease the band gap size facilitating visible light absorption. Non-metal doping has shown great promise in achieving visible light activated photocatalysis, with nitrogen being the most effective dopant. Asahi *et al* were the first to show visible light absorption through N doping. They reported nitrogen doped TiO_2 promoted photocatalytic activity up to λ = 520 nm.[95] The nitrogen substitutional doping of TiO_2 was early claimed as a method for narrowing the band gap by exclusively changing the valence band structure; fine electronic details of this are however under discussion. Asahi *et al* claimed that the presence of nitrogen narrows the band gap of TiO_2 thus making it capable of performing visible light driven photocatalysis.[95] However, Ihara *et al* suggested that it is the oxygen vacancies that contributed to the visible light activity, and the doped nitrogen only enhanced the stabilisation of these oxygen vacancies.[96] They also confirmed this role of oxygen vacancies in plasma-treated TiO_2 photocatalysts.[96] In addition the structural oxygen vacancy caused visible light photocatalytic activity was also reported by Martyanov *et al*.[97] Currently there appears to be some agreement on the mechanism of nitrogen doped visible light absorption explained by Irie and Nakamura.[98,99] They explained that TiO_2 oxygen lattice sites substituted by nitrogen atoms form an occupied midgap (N-2p) level above the (O-2p) valence band (figure 1.11). Irradiation with UV light excites

electrons in both the valence band and the narrow (N-2p) band, but irradiating with visible light only excites electrons in the narrow (N-2p) band.[98,99]

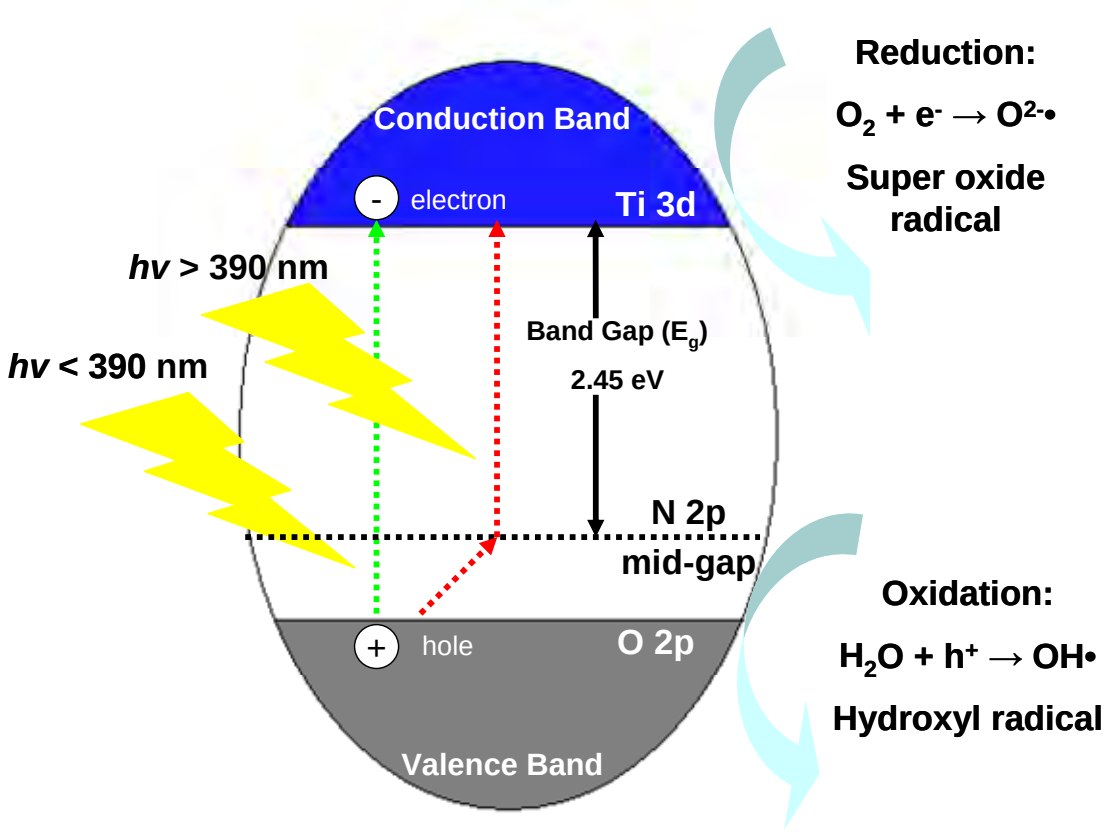

Figure 1.11. Schematic of N-doped TiO_2 photocatalysis

It has also been shown that F doping improves both UV and visible light photocatalytic activity. However, their mechanisms are still under discussion. Previous studies have shown that N-F-codoped TiO_2 powders demonstrated excellent photocatalytic activity no matter what kind of light source was used. This seems to be a consequence of the perfect combination of some beneficial effects induced by both N and F dopants.[100] Carbon, phosphorous and sulfur have also shown positive results for visible light responsive TiO_2.[101,102] The non-metal dopants effectively narrow the band gap of TiO_2 (< 3.2 eV).[103-105] Change of the lattice parameters and the presence of trap states within the conduction and valence bands from electronic perturbations give rise to band gap narrowing.[92] Not only does this allow for visible light absorption but the presence of trap sites within the TiO_2 bands increases the lifetime of photoinduced charge carriers.

Doping of TiO_2 with transition metals such as Cr, Co, V and Fe have extended the spectral response of TiO_2 well into the visible region also improving photocatalytic acitivity.[92,106-109] However, transition metals may also act as recombination sites for the photo induced charge carriers thus, lowering the quantum efficiency. Transition metals have also been found to cause thermal instability to the TiO_2 nanomaterials.[74] Kang argues that despite the fact that a decrease in band gap energy has been achieved by many groups through metal doping, photocatalytic activity has not been remarkably enhanced because the metals introduced were not incorporated into the TiO_2 framework. In addition, metals remaining on the TiO_2 surface cover photo reaction sites.[110]

1.7.2 Reducing recombination

When titanium dioxide absorbs photons of light with energy greater or equal to its band gap (3.2 eV for anatase), electrons are excited from the valence band to the conduction band.[8] Instead of the charge carriers migrating to the nanoparticle surface and undergoing redox reactions, the can recombine, nonradiatively or radiatively, dissipating the energy as light or heat.[8,73] The competition between recombination and redox processes determines the efficiency of the photocatalytic process. The processes can be summarised as follows:[8,111]

$TiO_2 + h\nu \rightarrow e^- + h^+$ Scheme 1.3

$e^- + Ti(IV)O–H \rightarrow Ti(III)O–H^-(X)$ Equation 1.8

$h^+ + Ti(IV)O–H \rightarrow Ti(IV)O\bullet–H^+(Y)$ Equation 1.9

$h^+ + ½O^{2-}_{lattice} \leftrightarrow ¼O_2(g) + vacancy$ Equation 1.10

$e^- + O_{2,s} \rightarrow O_{2,s}^-$ Equation 1.11

$O_{2,s}^- + H^+ \leftrightarrow HO_{2,s}$ Equation 1.12

$h^+ + Ti(III)O–H^- \rightarrow Ti(IV)O–H$ Equation 1.13

$e^- + Ti(IV)O\bullet–H^+ \rightarrow Ti(IV)O–H$ Equation 1.14

$O_{2,s} + Ti(IV)O\bullet–H^+ \rightarrow Ti(IV)O–H + O_{2,s}$ Equation 1.15

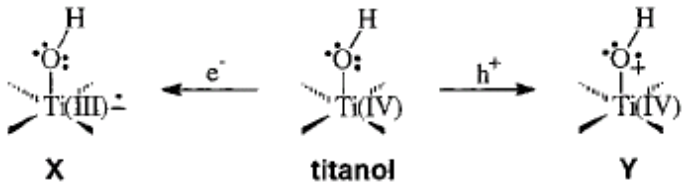

Scheme 1.4. Redox pathways of hydroxylated TiO_2

Scheme 1.1 shows the photon absorption process. Equations 1.8 – 1.12 are the photocatalytic redox pathways that compete with the recombination channels (Equations 1.13 – 1.15).[8,111] Serpone *et al* found that trapping excited electrons as Ti^{3+} species occurred on a time scale of ~ 30 ps and that about 90 % or more of the photogenerated electrons recombine within 10 ns.[112] Recombination is thus a process that must be overcome in order to improve the photocatalytic activity of TiO_2 nanomaterials.

Several researchers have modified TiO_2 with transition metals. Deposition of noble metals Ag, Au, Pt and Pd on the surface of TiO_2 enhance the photocatalytic efficiency by acting as an electron trap, promoting interfacial charge transfer and therefore delaying recombination of the electron-hole pair.[113-117]

Hwang *et al* showed that platinum deposits on TiO_2 trap photo-generated electrons, and subsequently increase the photo-induced electron transfer rate at the interface. They also provide catalytic sites where different mechanistic pathways from those on naked TiO_2 are enabled.[118] While Morikawa *et al* showed that doping TiO_2 with Cr was found to reduce photocatalytic activity, and that Cr and V ion implanted TiO_2 showed higher photocatalytic performances than bare TiO_2 did for the decomposition of NO under solar irradiation.[119]

Another technique involves TiO_2 doping with transition metals such as Fe, Cu, Co, Ni, Cr, V, Mn, Mo, Nb, W, Ru, Pt and Au.[115,120-128] The incorporation of transition metals in the titania crystal lattice may result in the formation of new energy levels between VB and CB, inducing a shift of light absorption towards the visible light region. Photocatalytic activity depends on the nature and the amount of doping agent. Possible limitations are photocorrosion and promoted charge recombination at metal sites.[120]

Many researchers have focused on modifying TiO_2 with silver. Silver has a Fermi-level or electron accepting region at an energy level just below the conduction band. Therefore, after light absorption and charge separation, the electron in the conduction band can be effectively trapped by silver, while the hole oxidises water and forms hydroxyl radicals, without the threat of recombination (figure 1.12). Chao *et al* reported the effect of Ag doping on the phase transformation and grain growth of sol-gel TiO_2 powder.[129] Kuo *et al* showed through X-ray diffraction (XRD) and X-ray photoelectron spectroscopy (XPS) that silver on TiO_2 surface coatings was easily oxidised into silver oxide (Ag_2O) and that the addition of silver causes a reduction in photoluminescence intensity as found by photoluminescence (PL) spectroscopy.[93] Seery *et al* previously showed enhanced visible light photocatalysis with Ag modified TiO_2.[130]

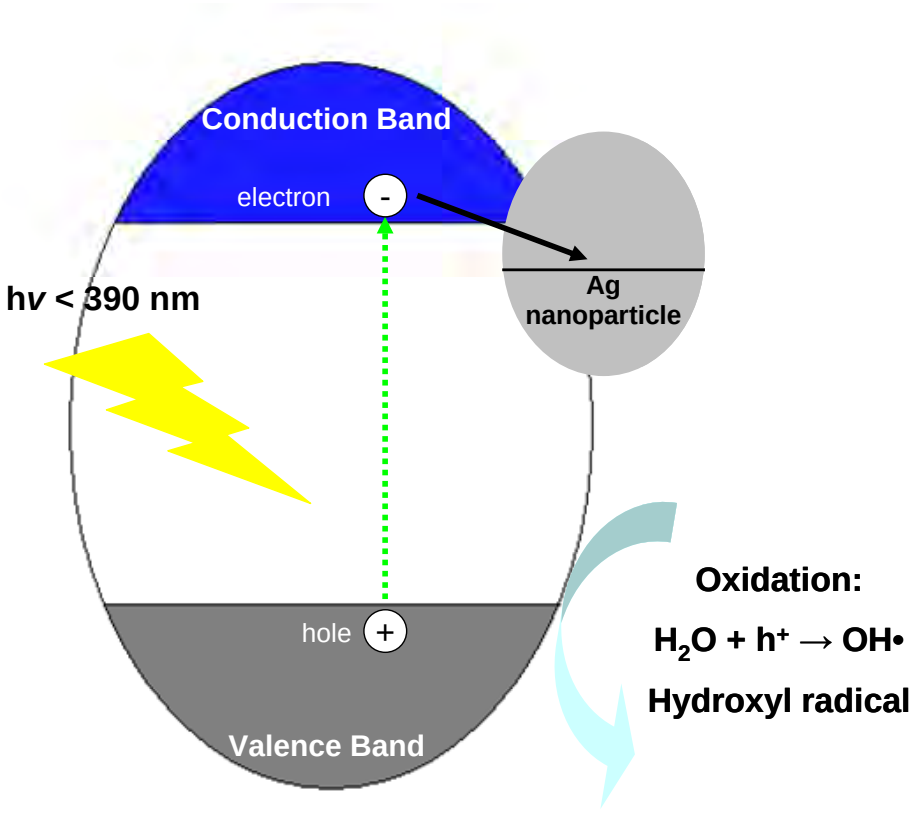

Figure 1.12. Mechanism for reduced recombination in the presence of silver

Another method of reducing recombination is to produce a heterojunction. Such is the case with the industrial TiO_2 photocatalyst Degussa P25 where a combination of anatase (~80 %) and rutile (~20 %) results in increased photocatalytic activity. The

intimate contact between two phases enhances the separation of photogenerated electrons and holes resulting in reduced recombination.[131]

1.7.3 Deactivation of TiO_2

Deactivation of TiO_2 photocatalysts has proved to be a major obstacle for commercial applications.[132] Deactivation occurs when partially oxidised intermediates block the active catalytic sites on the photocatalyst.[133] Gas phase deactivation is more predominant than the aqueous phase, because in the aqueous phase, water assists in the removal of reaction intermediates from the photocatalyst surface.[134] The photocatalytic degradation of many organic compounds generates unwanted byproducts.[19] Certain elements and functional groups contained in organic molecules have been found to strongly hinder the photocatalytic ability of TiO_2 through deactivation. Peral and Ollis found that N or Si containing molecules may cause irreversible deactivation through the deposition of species that inhibit photoactive sites on the catalyst surface.[135] Carboxylic acids formed from alcohol degradation are also believed to strongly adsorb to the active sites of a catalyst and cause deactivation.[19] Strongly adsorbed intermediate species appear to commonly cause deactivation of a photocatalyst and it is certainly an area where further improvement is essential before TiO_2 can be considered a viable option for continuous photocatalytic applications.

Several researchers have been studying regeneration methods for the TiO_2 photocatalyst. Potential regeneration methods investigated include; thermal treatment (< 400 °C) in air,[136] sonication with water and methanol,[137] irradiating the catalyst under UV light while passing humid air over the surface[138] and exposing the catalyst to air rich with H_2O_2, both with and without UV light.[134]

1.8 Synthesis Techniques

The choice of synthesis technique can be a key factor in determining the effectiveness of the photocatalyst as studies have shown that TiO_2 production and physical form are among the most important factors in determining the overall photocatalytic

efficiency.[3,139-146] There are many methods of synthesising titanium dioxide, such as hydrothermal,[147,148] combustion synthesis,[149] gas-phase methods,[150,151] microwave synthesis and sol-gel processing.[152] This research focuses on sol-gel processing techniques which will be discussed in great detail however, an overview of other much used techniques is also provided.

1.8.1 Hydrothermal synthesis

Hydrothermal synthesis is typically carried out in a pressurised vessel called an autoclave with the reaction in aqueous solution.[8] The temperature in the autoclave can be raised above the boiling point of water, reaching the pressure of vapour saturation. Hydrothermal synthesis is widely used for the preparation of TiO_2 nanoparticles which can easily be obtained through hydrothermal treatment of peptised precipitates of a titanium precursor with water.[8,153] The hydrothermal method can be useful to control grain size, particle morphology, crystalline phase and surface chemistry through regulation of the solution composition, reaction temperature, pressure, solvent properties, additives and aging time.[7]

1.8.2 Combustion

Combustion synthesis leads to highly crystalline particles with large surface areas.[104,149] The process involves a rapid heating of a solution containing redox groups.[7] During combustion, the temperature reaches approximately 650 °C for one or two minutes making the material crystalline. Since the time is so short, the transition from anatase to rutile is inhibited.[7]

1.8.3 Gas phase methods

Gas phase methods are ideal for the production of thin films. Gas phase can be carried out chemically or physically. Chemical vapour deposition (CVD) is a widely used industrial technique that can coat large areas in a short space of time.[7] During the procedure, titanium dioxide is formed from a chemical reaction or decomposition of a precursor in the gas phase.[150,154]

Physical vapour deposition (PVD) is another thin film deposition technique. Films are formed from the gas phase but without a chemical transition from precursor to product. For TiO_2 thin films, a focused beam of electrons heats the titanium dioxide material. The electrons are produced from a tungsten wire heated by a current. This is known as electron beam (E-beam) evaporation. Titanium dioxide films deposited with E-beam evaporation have superior characteristics over CVD grown films such as, smoothness, conductivity, presence of contaminations and crystallinity. Reduced TiO_2 powder (heated at 900 °C in a hydrogen atmosphere) is necessary for the required conductance needed to focus an electron beam on the TiO_2.[155]

1.8.4 Microwave synthesis

Various TiO_2 materials have been synthesised using microwave radiation. Microwave techniques eliminate the use of high temperature calcination for extended periods of time and allow for fast, reproducible synthesis of crystalline TiO_2 nanomaterials. Corradi *et al* prepared colloidal TiO_2 nanoparticle suspensions within 5 minutes using microwave radiation.[156] High quality rutile rods were developed combining hydrothermal and microwave synthesis,[157] while TiO_2 hollow, open ended nanotubes were synthesised through reacting anatase and rutile crystals in NaOH solution.[158]

1.9 Sol-Gel Processing

Sol-gel processing is a common chemical approach to produce high purity materials shaped as powders, thin film coatings, fibres, monoliths and self-supported bulk structures.[139,143,144,146] The sol-gel method has several advantages over other synthesis techniques such as purity, homogeneity, stoichiometric control, ease of preparation and ease of introducing dopants, composition and the ability to produce thin film coatings or porous powders. There are two possible routes for carrying out sol-gel synthesis, the non-alkoxide route and the alkoxide route. The non-alkoxide route uses inorganic salts ($TiCl_4$) as the starting material.[7,164-167] This requires the removal of the inorganic anion

to produce the required oxide (titanium dioxide). However, halides often remain in the final oxide material and are difficult to remove.

The alkoxide route involves hydrolysis of a metal alkoxide, followed by condensation. The hydrolysis/condensation reactions typically form a three dimensional polymeric structure, that, upon calcination will result in anatase or rutile titanium dioxide crystals depending on the calcination temperature. The alkoxide route is used throughout this thesis and it will be explained in greater detail in the following section.

1.10 Mechanism of Sol-Gel Synthesis

The past two decades have shown an increasing interest in the development of organic/inorganic materials prepared by the sol-gel process.[159-169] Although a lot of the research carried out on sol-gel science focuses on silicates[168,170,174,176-178] due to silicons ability to form stable organic frameworks through Si–C covalent bonds,[163] This thesis focuses on transition metal (mainly titanium) based sol-gel science. Transition metals can not form stable covalent bonds with carbon but can be linked to organic components through coordinative or ionic bonds.[163]

The sol-gel process involves hydrolysis and condensation of the metal alkoxide followed by heat treatment at elevated temperatures which induce polymerisation, producing a metal oxide network.[170] In general, transition metals have low electronegativities and their oxidation state is frequently lower than their coordination number in an oxide network. Therefore, coordination expansion occurs spontaneously upon reaction with water or other nucleophilic reagents to achieve their preferred coordination.[171] Metal alkoxides are in general very reactive due to the presence of highly electronegative OR groups (hard-π donors) that stabilise the metal in its highest oxidation state and render it very susceptible to nucleophilic attack. The lower electronegativity of transition metals causes them to be more electrophilic and thus less stable toward hydrolysis, condensation and other nucleophilic reactions. Controlling the conditions can be difficult but successful control of the reaction conditions has the potential to produce materials of consistent size, shape and structure.[139,143,144,146,171]

1.10.1 Mechanism of hydrolysis

As stated previously the sol-gel reaction involves hydrolysis of the metal alkoxide followed by condensation. Both hydrolysis and condensation is described in further detail in these sections.

Hydrolysis of titanium alkoxides occurs through a nucleophilic substitution (S_N) reaction. When a nucleophile, such as water is introduced to titanium alkoxide a rapid exothermic reaction proceeds. The nucleophilic addition (A_N) of water involves a proton from the attacking nucleophile (water) being transferred to the alkoxide group. The protonated species is then removed as either alcohol or water (scheme 1.5).[164,172]

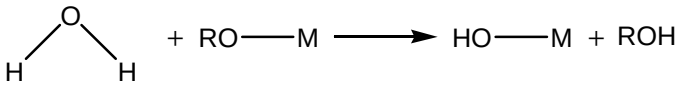

Scheme 1.5. Hydrolysis reaction

The nucleophilic substitution reaction that occurs during hydrolysis can be described as follows:[164]

1. Nucleophilic addition of the H_2O onto the positively charged metal atom.
2. Proton transfer, within the transition state from the entering molecule to the leaving alkoxy group.

1.10.2 Mechanism of condensation

Condensation reactions complete the sol-gel process. Condensation can proceed through either alcoxolation or through oxolation. In both processes an *oxo* bridge is formed between the metals (M–O–M) but the leaving group differs. During alcoxolation, two partially hydrolysed metal alkoxide molecules combine and an *oxo* bridge is formed between the two metals with alcohol departing as the leaving group (scheme 1.6).[164,172]

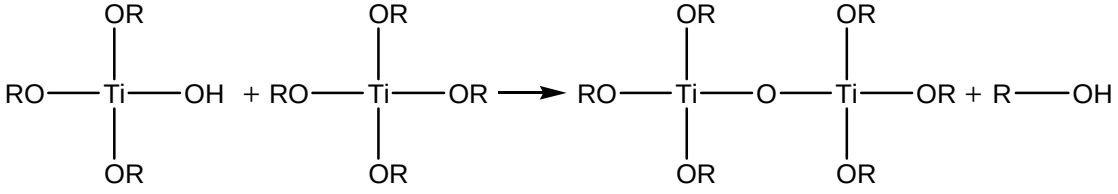

Scheme 1.6. Alcoxolation reaction

In oxolation (scheme 1.7) two partially hydrolysed metal alkides combine to form an *oxo* bridge between the metal centres but water is the leaving group.

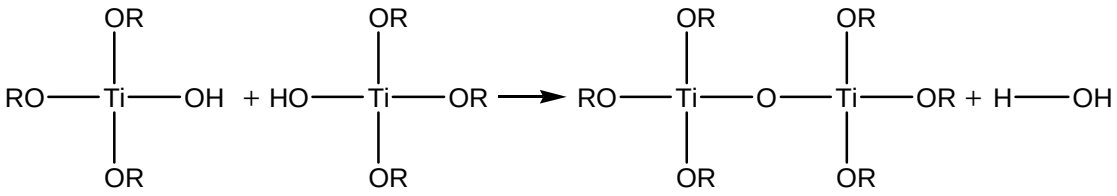

Scheme 1.7. Oxolation reaction

Condensation reactions can proceed to form large chains of molecules through polymerisation.

The electrophilicity of the metal, the strength of the entering nucleophile and the stability of the leaving group all have an influence over the thermodynamics of the hydrolysis and condensation reactions. To gain a better understanding of the reactions, Sanchez *et al* employed a 'partial charge model' which involves the principle of electronegativity equalisation.[164,173] This allowed them to calculate the charge distribution over the atoms involved in the reaction. The model allows the charge δ_i of each atom X_i in a given molecule to be calculated.[164] It was shown that hydrolysis, alcoxolation and oxolation reactions are favoured when $\delta(O) << 0$, $\delta(M) >> 0$, and $\delta(H_2O)$ or $\delta(ROH) > 0$.[174] Their charge distribution calculations showed that alcoxolation is the preferred condensation pathway for $Ti(OEt)_4$. Protonation of ethoxide (OEt), produced a more positively charged leaving group ($\delta(EtOH) = 0.02$) than OH protonation ($\delta(HOH) = -0.25$).[174] Therefore showing how alcoxolation is thermodynamically favoured over oxolation during the condensation of $[Ti_2(OEt)_6(OH)_2]$. These results indicated that alcoxolation may be the favoured condensation route for all titanium alkoxides.[164]

The extent of undersaturation of the metal, that is the coordination number, *N*, minus the charge, *z* ($N - z$), along with the ability of the leaving proton to be transferred, govern the kinetics of the reaction. The activation energy is reduced with high metal undersaturation values and greater proton acidity. Therefore enhancing the reaction kinetics.[172]

Transition metals are very electropositive. Livage *et al* calculated the partial charge values, δ(M) of 0.61 for $Ti(OPr)_4$ and 0.63 for $Ti(OEt)_4$, compared to δ(M) of 0.32 for $Si(OEt)_4$.[164] These values help explain why the hydrolysis and condensation kinetics of titanium alkoxides are so rapid compared to $Si(OR)_4$. A calculated rate constant value for $Ti(OR)_4$, 10^{-3} M^{-1} s^{-1},[172,175-177] is five orders of magnitude greater than the value calculated for $Si(OR)_4$, 5 x 10^{-9} M^{-1} s^{-1}. The calculated values show why the hydrolysis/condensation reactions occur at greater speed for titanium alkoxides than for silicon alkoxides.

Another major factor regarding sol-gel reaction kinetics is the extent of oligomerisation (molecular complexity) of the metal alkoxide. Molecular complexity varies depending on the nature of the metal atom. An increase in atomic size causes an increase in molecular complexity. [178,179] The alkoxide ligand also influences molecular complexity. As an example, $Ti(OEt)_4$ is an oligomer, but $Ti(OPr)_4$ is monomeric.[179] $Ti(OPr)_4$ is more susceptible to hydrolysis than $Ti(OEt)_4$ because terminal OR ligands are more reactive towards proton transfer than bridging ligands.

Employing a solvent may also influence the reaction kinetics as if a suitable solvent is chosen; it may be preferentially hydrolysed over the alkoxide ligands. This allows for greater control over the reaction kinetics through the correct use of solvent.[174] Kundu *et al* demonstrated how the correct choice of solvent can effect a sol-gel reaction through the hydrolysis of $Zr(OPr)_4$.[180] Dissolving $Zr(OPr)_4$ in the polar solvent isopropanol resulted in the formation of a precipitate but when the non-polar cyclohexane was used as a solvent, homogenous gels were formed.[180] It was believed that when cyclohexane was chosen, hydrolysis reactions were slow to occur and alkoxy bridges were formed resulting in the formation of a homogenous gel. However, with isopropoxide, partial hydrolysis occurs resulting in rapid hydrolysis and the formation of a precipitate.[180]

Hydrolysis and condensation kinetics are also affected by the organic ligand. The hydrolysis rate of titanium alkoxides decreases with increasing alkyl chain length.[177,181] This is mainly due to the steric effect which is expected for an associative S_N reaction mechanism. Another factor was shown by Livage *et* al where a trend of decreasing

partial charges of δ(Ti) and δ(H) was found with increasing alkyl chain length[174] and it was believed that this too would contribute to slower kinetics. Alkyl chain length also influences the condensation pathway, even under mild hydrolysis conditions, and several researchers have shown that with shorter alkyl ligand chains such as Et or Pr, precipitation occurs but a stable sol was obtained with butoxide as the alkyl group.[177,182,183] What is then observed in inorganic systems is that, the initial condensation products are oligomeric species that subsequently aggregate to form gels or precipitates. The oligomer size depends on the alkyl chain length (*R*), smaller oligomers occur with larger alkyl chain lengths. The *R* group also influences the morphology (particle size and surface area) and crystallisation behaviour of the resulting gel.[184,185] This may be caused by the altering size and structure of the primary oligomeric building blocks.[172]

1.10.3 Role of the catalyst

Acid and base catalysts can have a strong influence over hydrolysis and condensation rates as well as the structural properties of the final product. The addition of an acid will result in the preferential protonation of the negatively charged alkoxide group (scheme 1.8). Protonation of the alkoxide group produces good leaving groups which enhance the reaction kinetics, eliminating any proton transfer that occurs in the transition state and thus allowing hydrolysis to go to completion upon the addition of water.

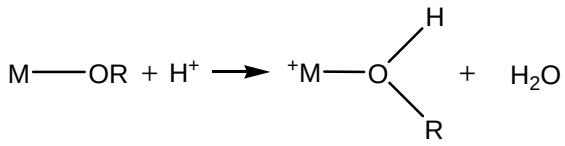

Scheme 1.8. Acid catalyst reaction

The condensation pathway can be influenced by the ease of protonation of the different alkoxide ligands (scheme 1.9).[174]

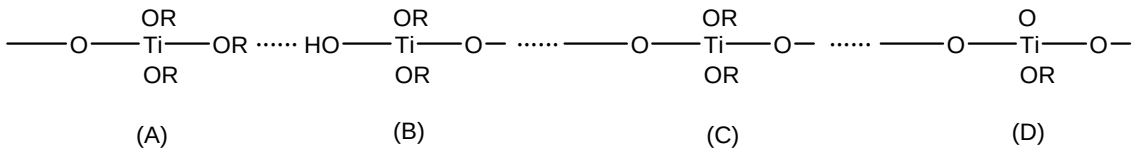

Scheme 1.9. Partially hydrolysed polymer

The ease of protonation decreases following, A > B > C > D, this reflects the electron providing power of the ligands, which decreases as alkoxy < hydroxo < oxo. Because of this, acid catalysed condensation occurs at the end of chains rather than the middle, resulting in longer polymer chains with little branching.[172] A combination of acid catalysts with low *r* values (water:metal ratio in alkoxide) result in monolithic gels[186,187] or sols.[188,189] The kinetics of the condensation reactions are severely retarded with high acid concentrations (H^+/Ti ≥ 1).[174]

In alkaline conditions, hydroxo ligands are deprotonated, producing strong nucelophiles:

$$L–OH + :B \rightarrow L–O^- + BH^+ \qquad \text{Equation 1.16}$$

where L = M or H and B = OH^- or NH_3. The hydrolysis rate of $Ti(OBu)_4$ was less in basic conditions than in acidic or neutral conditions. It was postulated that the nucleophilic addition of OH^- may reduce the partial charge of the titanium metal centre (δ(Ti)), making the hydrolysis reaction less favourable.[172,174,190]

While hydrolysis kinetics are retarded in basic conditions, the condensation kinetics of metal alkoxides are enhanced. Calculated partial charge values of δ(Ti) calculated for model sites A – D (scheme 1.9)[174] show a decrease in the order of reactivity toward nucleophilic attack in the order D > C > B > A. Therefore, base-catalysed condensation (and hydrolysis) should be directed toward the middle rather than the end of chains, resulting in the formation of compact, highly branched species.[172]

1.10.4 Chemical modification

The reaction rates of hydrolysis and condensation reactions associated with sol-gel synthesis can easily be altered. Chemical modification of titanium alkoxides will retard hydrolysis and condensation reactions, allowing for greater control over the reaction

and evolving polymeric species.[164,174] Modification typically occurs through a nucleophilic substitution (S_N) reaction. A new molecular precursor is produced upon the reaction of a nucleophilic reagent (XOH) with a metal alkoxide.[164]

$$XOH + M(OR)_z \rightarrow M(OR)_{z-x}(OX)_x + xROH \qquad \text{Equation 1.17}$$

If M is coordinatively unsaturated ($N - z > 1$) by nucleophilic addition (A_N), then:

$$XOH + M(OR)_z \rightarrow M(OR)_z(XOH)_{N-z} \qquad \text{Equation 1.18}$$

When δ(M) >>1, (N – z) > 1, and (XOH) is a strong nucleophile, the reactivity of the alkoxide towards this modification is increased.[174]

The hydrolysis and condensation behaviour of the modified precursor depends on the stability of the modifying ligands. In a typical modified synthesis, alkoxide ligands that are less electronegative are preferentially removed during hydrolysis. The modifying ligands which tend to be more electronegative will remain throughout the hydrolysis and are only removed during condensation.[172] In modified precursors, stable modifying ligands cause the effective functionality toward condensation to be reduced, altering the condensation pathway and resulting in less highly condensed products and promoting gelation.[172]

Alcohol exchange reactions can readily occur with metal alkoxide precursors:

$$M(OR)_z + xR'OH \rightarrow M(OR)_{z-x}(OR')_x + xROH \qquad \text{Equation 1.19}$$

therefore, alcohol exchange is known to be a common method of alkoxide synthesis.[179] When δ(M) >> 1 and when R' is less sterically bulky than R, alcohol exchange will proceed. Alcohol exchange rates decrease as alkoxy chain length increases, MeOH > EtOH > Pr^iOH > Bu^tOH.[174] As hydrolysis rates decrease with steric bulk of the alkoxy ligands, chemical modification of transition metal precursors may involve exchanging a bulky ligand for a less bulky one.[191]

The hydrolysis behaviour of transition metal alkoxides can be significantly altered through alcohol exchange. Precipitation occurs when relatively small alkoxy ligands such as $Ti(OEt)_4$ or $Ti(OPr^i)_4$ are hydrolysed with excess water (r > 2). Whereas stable sols are obtained with the bulky $Ti(OAm^t)_4$, (OAm^t = amyl alcohol, $C_5H_{11}OH$). In the mixed alkoxide, $Ti(OPr^i)_{4-x}(OAm^t)_x$, the (OAm^t) group is less electronegative than (OPr^i).

As hydrolysis preferentially occurs on less electronegative ligands, (OAm^t) is preferentially hydrolysed and rapid gelation occurs.[164]

Acetic acid (HOAc) is commonly used to modify titanium alkoxides. Reacting of (HOAc) with metal alkoxides leads to the formation of metal alkoxo-acetates.[192-194] The addition of HOAc increases the gel time for $Ti(OR)_4$ as explained below.[164] Livage and coworkers[195] have performed many experiments on acetic acid modified $Ti(OR)_4$. They have combined X-ray absorption near edge spectroscopy (XANES), ^{13}C NMR, IR and X-ray absorption fine structure (EXAFS) and have made several breakthroughs regarding the structure and behaviour of HOAc modified titanium alkoxides.

They have shown that $Ti(OPr^i)_4$ consists of monomeric units and the Ti atom exhibits a coordination number, N = 4. Upon addition of glacial acetic acid an exothermic reaction occurs. XANES experiments indicated that the coordination number of the central titanium atom, N, instantaneously increases to 6. ^{13}C NMR showed that the chemical environments of the carboxylic and methyl carbons in the HOAc were altered after the reaction with $Ti(OPr^i)_4$. It is believed that this is due to the HOAc bonding with the titanium and not the OPr^i groups. However, both bridged and terminal OPr^i ligands remain are present (figure 1.13). The IR spectrum of the reaction product exhibits absorption bands due to titanium alkoxide, acetic acid and the propyl acetate ester. Also, there are two strong bands at ~ 1500 cm^{-1} assigned to the symmetric and antisymmetric stretching vibrations of bridging carboxylic groups: $\nu_s(CO_2^-)$ = 1450 cm^{-1} and $\nu_a(CO_2^-)$ = 1580 cm^{-1}. The frequency difference ($\Delta\nu$ = 130 cm^{-1}) is typical of an acetate ion acting as a bidentate ligand. IR also confirms the presence of both terminal (1084 cm^{-1}) and bridging (1034 cm^1) OPr^i ligands. This evidence combined with a Ti-Ti correlation of 3.05 Å determined from EXAFS is consistent with a dimer composed of bridging and terminal OPr^i ligands and bridging CH_3COO^- ligands as shown in figure 1.13.[195]

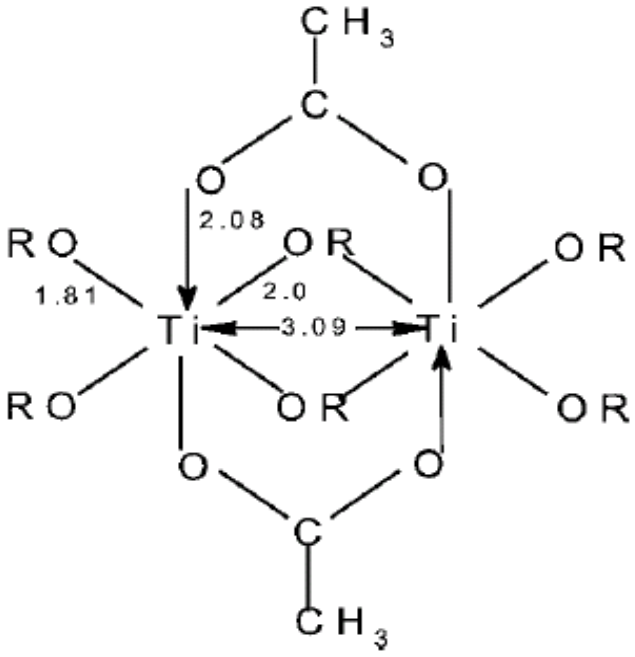

Figure 1.13. Proposed structure of titanium acetate[195]

During hydrolysis, ^{1}H and ^{13}C NMR and IR spectroscopy indicated that OPr^{i} groups are preferentially hydrolysed,[195] whereas the bridging acetate ligands remain bonded to titanium throughout much of the condensation process. Since the bridging CH_3COO^- ligands are not hydrolysed, they effectively alter the condensation pathway perhaps promoting the formation of linear polymers composed of edge shared octahedra.[172] The formation of the edge shared octahedra stabilise TiO_2 as anatase.[195,196]

1.11 Overview of Thesis

There is significant research being carried out on titanium dioxide semiconductors because of the wide amount of applications associated with the materials. Possibly the most investigated application of titanium dioxide is photocatalysis. Of the three common polymorphs of TiO_2, it is widely agreed that anatase has shown the most promise towards photocatalytic applications. As shown in the introduction, several techniques have been employed to synthesise TiO_2 nanomaterials. Of all the techniques mentioned in *section 1.8*, it is the sol-gel technique that this thesis will be based upon. The sol-gel technique is widely used for the synthesis of semiconductor nanomaterials. However, there is still much to be understood about the mechanism

from synthesis through to crystallisation and transformation. In the 80's and 90's, Livage, Sanchez and Doeuff carried out pioneering research on the sol-gel reactions of metal alkoxides. They also modified the metal alkoxides, thus, controlling the hydrolysis/condensation reactions associated with the sol-gel mechanism. The adapted materials were characterised through (XANES, EXAFS and FTIR) and structures of the modified metal alkoxides were proposed. Today, these proposed structures are still accepted and through their pioneering work the sol-gel synthesis of metal alkoxides is better understood.

In order for TiO_2 to be utilised in wider areas, it is necessary that anatase can be stable at temperatures exceeding 1000 °C. Greater anatase to rutile transformation temperatures have been achieved through the addition of various dopants and contradictory results have been found. In order to synthesise anatase that is stable at high temperatures it is necessary to understand how the metal alkoxide framework is arranged before crystallisation occurs and how modifying or doping the materials affects this framework. Why do different conditions cause anatase to transform to rutile at lower/higher temperatures? How do various dopants affect the band gap and photocatalytic mechanism and do different dopants affect the metal alkoxide framework in the early stages of synthesis? What happens when metal oxides are simultaneously synthesised? These are questions which are addressed in this thesis.

1.12 Aims and Objectives

The aims and objectives of this body of work are as follows:

- To understand how chemical modification of titanium alkoxide precursors influences the crystallisation behaviour and phase transition of TiO_2 materials. Structural determination of modified precursor materials can be investigated with IR and Raman and the crystalline phase can be found using XRD
- Addition of silver has been well reported to influence early phase transformation of anatase to rutile. Several researchers have reported that silver causes an increase in nucleation sites and oxygen vacancies which can all result in early phase

transformation. However, the effect of silver on the initial sol-gel reaction has not been investigated. The major objective of this study is to understand the effect of silver on the initial reaction before the heat treatment in order to gain a greater knowledge of how the crystal phase transformation can be affected after the annealing process.

- Anatase is widely reported as the most active crystalline phase for photocatalytic applications, however to utilise anatase for high temperature applications it is necessary to delay the anatase to rutile transformation temperature. This can be achieved through the addition of dopants. It is also necessary to develop visible light active TiO_2 in order to utilise the full solar spectrum. The objective of this work was to develop a high temperature stable visible light active anatase photocatalysts.
- A combination of semiconductor nanomaterials has shown improved photocatalytic properties, a simple sol-gel synthesis for the production of semiconductor hybrids is necessary for the development of such materials. This study aims at the development of sol gel ZnO/TiO_2 hybrids for potential photocatalytic applications.

The thesis is arranged into seven chapters as follows:

Chapter 1 introduces titanium dioxide and its applications as well as giving an overview of the photocatalytic and hydrophilic mechanisms and summarising different synthesis techniques, focusing on sol-gel synthesis and giving a detailed step by step description of the sol-gel process.

Chapter 2 presents the materials and experimental set-up used for the synthesis and phtocatalytic activity studies of the semiconductor nanomaterials. All characterisation techniques used are also presented.

Chapter 3 explains the effect of chelation on the anatase to rutile transformation. The effect of various molar ratios of formic acid and water are investigated and through XRD, FTIR and Raman a possible structural arrangement is proposed that may influence the anatase to rutile transformation.

Chapter 4 explains how the presence of silver retards the formation of chelation complexes, resulting in a lowering of the anatase to rutile transformation temperature. XPS, FTIR, Raman, XRD and DSC results support the proposed blocking effect of silver on titanium-formate chelation.

Chapter 5 provides a detailed study of TiO_2 modified and doped through various routes and shows the advantages and drawbacks of the various dopants from both a photocatalytic and a phase transformation viewpoint.

Chapter 6 proposes a novel sol-gel route for the synthesis of zinc orthotitanate, while discussing the stages of crystallisation of the various zinc titanate polymorphs and how different molar ratios favour different crystalline phases.

Chapter 7 provides some suggestions for future work based on the materials synthesised throughout the thesis and the direction of current interest within our group.

2 Experimental Procedures and Characterisation Techniques

2.1 Chemicals Used

Titanium tetraisopropoxide (97%), zinc acetate dihydrate (98 %), formic acid (98%), acetic acid (99.7%), oxalic acid dehydrate (98.5%), silver nitrate (99%) and aluminium nitrate nonahydrate (98%) were purchased from Sigma-Aldrich, ethanol (99.5%) was purchased from VWR international, 1, 3-diaminopropane was purchased from Fluka Chemika and methylene blue was purchased from Gurr company. All chemicals were used as received. Deionised water purified by a Millipore simplicity, water purification system was used in all experiments.

2.2 Synthesis of Nanomaterials

2.2.1 Synthesis of titanium dioxide

Titanium tetraisopropoxide (TTIP) was added to different amounts of formic acid (FA) under stirring (table 2.1). This resulted in a vigorous exothermic reaction producing a paste-like suspension. Water was then added in varying ratios to give total volumes in the range 10 – 50 mL. The molar ratios of TTIP:FA:H_2O were varied throughout the experiment.

After the addition of water, a white precipitate formed which was allowed to stir for two hours before being filtered, washed with deionised water and dried in air at 100 °C for 10 hr. Each powder was crushed into a fine white powder then calcined in air at temperatures ranging from 300 – 1000 °C for two hours at a ramp rate of 5 °C/min. A control sample was prepared without formic acid and labelled $F_{control}$.

Table 2.1. Molar ratios of TTIP:FA:H_2O

Sample Name	TTIP	Formic Acid	H_2O
F_2W_4	1	2	4
F_2W_8	1	2	8
F_2W_{10}	1	2	10
F_2W_{40}	1	2	40
F_2W_{80}	1	2	80
F_2W_{100}	1	2	100
F_4W_4	1	4	4
F_4W_8	1	4	8
F_4W_{10}	1	4	10
F_4W_{40}	1	4	40
F_4W_{80}	1	4	80
F_4W_{100}	1	4	100
$F_{10}W_4$	1	10	4
$F_{10}W_8$	1	10	8
$F_{10}W_{10}$	1	10	10
$F_{10}W_{40}$	1	10	40
$F_{10}W_{80}$	1	10	80
$F_{10}W_{100}$	1	10	100

2.2.2 Silver modified TiO_2

The method described above was used to synthesise silver modified TiO_2. The chosen TTIP:FA:H_2O ratio was 1:4:4 and varying amounts of silver nitrate were used to give 1, 3 and 5 mol % silver (0.102, 0.308 and 0.514 g respectively). The silver was introduced to the mixture by dissolving silver nitrate powder into the water immediately before

adding it to the titanium tetraisopropoxide-formic acid paste. The resulting powders were filtered, washed and dried in air at 100 °C for 10 hr, samples were labelled 0 % Ag-TiO_2, 1 % Ag-TiO_2, 3 % Ag-TiO_2 and 5 % Ag-TiO_2. The dried powders were then calcined at temperatures ranging from 300 – 1000 °C for two hours at a ramp rate of 5 °C/min. A control sample containing no silver was also prepared.

2.3 Ag, Al, N, S and co-doped (Al, N), (Al, S), (Al, N, S) and (Ag, Al, N, S) titania

2.3.1 Al-modified TiO_2

Titanium tetraisopropoxide (25 mL) was added to glacial acetic acid (48 mL) under stirring. After an initial exothermic reaction, a clear, yellow, titanium-acetate solution was formed. Water (151 mL) was then added, resulting in a solid gel which was dissolved upon stirring to give a clear titanium tetraisopropoxide-acetate solution. The final ratio was TTIP:HOAc:H_2O, 1:10:100. Aluminium nitrate ($AlNO_3$) 1, 3, 5 and 10 mol % Al (0.31, 0.95, 1.57 and 3.15 g respectively) was dissolved in water before the water was added to the sol. This incorporated aluminium into the solution. The solution was then allowed to stir for two hours before being aged in air at 100 ° C for 10 hr. The resulting substance was crushed with a mortar and pestle to give a fine, white powder which was calcined at temperatures ranging from 300 – 1000 °C for two hours at a ramp rate of 5 °C/min. A control solution was prepared in the same manner but without the use of $AlNO_3$.

2.3.2 Synthesis of N-doped TiO_2

Titanium tetraisopropoxide (10 mL) was added to varying amounts of 1, 3-diaminopropane (DAP) under stirring resulting in the formation of a white liquid-gel substance. Water (59.4 mL) was added to the gel to give a white paste. The paste suspension was allowed to stir for two hours before the liquid was filtered off leaving a white powder which was then dried in air at 100 °C for 24 hr. The dried powder was ground into a fine, white powder with mortar and pestle before being calcined at

temperatures ranging from 300 – 1000 °C for two hours at a ramp rate of 5 °C/min. Final TTIP:DAP ratios were 1:0.5 and 1:4 (1.39 and 10.7 mL DAP respectively).

2.3.3 Synthesis of Al, N co-doped TiO_2

Titanium tetraisopropoxide (10 mL) was added to varying amounts of 1, 3 diaminopropane (DAP) under stirring resulting in the formation of a white liquid-gel substance. In a separate beaker, aluminium nitrate (1 mol %, 0.31 g) was dissolved in water (59.4 mL). The aluminium nitrate solution was added to the titanium-nitrogen gel precipitate. Final TTIP:DAP ratios were 1:0.5 and 1:4 relating to 1.39 and 10.7 mL DAP respectively and all suspensions contained 1 mol % Al. The white precipitate was then separated from the liquid by vacuum filtration. The resulting white solid was dried in air at 100 °C for 24 hr. The dried powder was ground to a fine powder with a mortar and pestle and calcined at 400, 500, 600, 700, 800, 900 and 1000 °C at a ramp rate of 5 °C/min.

2.3.4 Synthesis of Ag, N-TiO_2

1, 3-diaminopropane (1.39 mL) was allowed to stir in a beaker. TTIP (10 mL) was slowly added. The resulting suspension was allowed to stir for 1 min before water (59.4 mL) containing dissolved $AgNO_3$ (0.17 g) was added. This resulted in a suspension with a molar ratio of 1:0.5:100, TTIP:DAP:H_2O and containing 3 mol % Ag. The suspension was allowed to stir for 2 hr before being filtered, washed with DI water and dried in air at 100 °C for 48 hours. The step was repeated using 10.7 mL DAP to give a molar ratio of 1:4:100, TTIP:DAP:H_2O and containing 3 mol % Ag. All samples were crushed into a fine powder and calcined at 400, 500, 600, 700, 800, 900 and 1000 °C at a ramp rate of 5 °C/min.

2.3.5 Synthesis of Al, S-doped TiO_2

Dimethylsulfoxide (DMSO, 2.34 mL) was stirred in a beaker, TTIP (10 mL) was added. The suspension was allowed to stir for 1 min. $AlNO_3$ (0.12 g) was dissolved in water (59.4 mL) and added to the suspension to give molar ratio of TTIP:DMSO:H_2O, 1:1:100

with 1 mol % Al. It was left to stir for 2 hr before being filtered and dried in air at 100 °C for 48 hr. The resulting white powder was crushed into a fine powder and calcined at 400, 500, 600, 700, 800, 900 and 1000 °C at a ramp rate of 5 °C/min. This was repeated to give TTIP:DMSO:H_2O, 1:16:100 by using 37.5 mL DMSO.

Sodium thiosulfate was chosen as second sulfur source to achieve S-doped TiO_2. Sodium thiosulfate (5.21 g) was dissolved in water (59. 4 mL) and added to titanium tetraisopropoxide (10.0 mL) under stirring. This resulted in a white suspension with a Ti:S molar ratio of 1:1. A Ti:S molar ratio of 1:4 was also synthesised by dissolving 20.84 g of sodium thiosulfate in water. The suspension was allowed to stir for two hours. The white precipitate was then separated from the liquid by vacuum filtration and was washed several times with deionised water to remove any remaining ions. The resulting white solid was dried in air at 100 °C for 24 hr. The dried powder was ground to a fine powder with a mortar and pestle before being calcined at 400, 500, 600, 700, 800, 900 and 1000 °C at a ramp rate of 5 °C/min.

2.3.6 Synthesis of Ag, N, S co-doped TiO_2

Titanium dioxide powder with 3 mol % Ag, and Ti:N:S molar ratios of 1:0.5:4 was synthesised as follows. Silver nitrate (0.168 g) and sodium thiosulfate (20.87 g) was dissolved in water. In a separate beaker, titanium tetraisopropxide (10.0 mL) was added to 1, 3-diaminopropane (1.39 mL) under stirring to give a white paste. The Ag^+/Na^+ aqueous solution was immediately added to the white titanium paste. The milky white suspension was allowed to stir for two hours before filtering off the white solid. The filtrate was washed with deionised water and dried in air at 100 °C for 24 hr. The dried powder was crushed with a mortar and pestle and calcined at temperatures from 300 – 1000 °C.

2.4 Synthesis of Zinc Titanates

A variety of zinc titanate powders were synthesised. The powders can be separated into two subsets. In one subset, the titanium precursor is in excess over the zinc precursor and in the other, the zinc precursor is in excess over the titanium precursor.

2.4.1 Excess titanium precursor

Zinc acetate (2.29 g) was dissolved in ethanol (EtOH, 125 mL) at 60 °C, oxalic acid (3.15 g) dissolved in ethanol (50 mL) was added slowly to the zinc acetate solution under stirring at 60 °C, giving a white, cloudy, zinc oxalate suspension. Titanium isopropoxide (TTIP, 14.80 mL) was then added to the cloudy zinc oxalate suspension followed by water (90 mL), resulting in a molar ratio of Ti:Zn, 4:1. The suspension was stirred for 2 hr before being aged in an oven in air at 100 °C for 48 hr, allowing the excess solvent to evaporate. The resulting white xerogel was then calcined at 400, 500, 600, 700, 800, 900 and 1000 °C for 2 hr at a ramp rate of 5 °C/min. Three different Ti/Zn powders (table 2.2) were synthesised to give ratios of Ti:Zn, 4:1, 4:2 and 4:3 and the samples were labelled TZ-4:1, TZ-4:2 and TZ-4:3 respectively.

Table 2.2. Amounts used for excess titanium samples

Sample	Ti:Zn	ZnAcOH (g)	EtOH (mL)	Oxalic Acid (g)	EtOH (mL)	TTIP (mL)	H_2O (mL)
TZ-4:1	0.05:0.0125	2.29	125	3.15	50	14.80	90
TZ-4:2	0.05:0.0250	4.59	250	6.30	100	14.80	90
TZ-4:3	0.05:0.0375	6.88	375	9.45	150	14.80	90

2.4.2 Excess zinc precursor

Samples with excess zinc over titanium were prepared as shown previously with the amounts used shown in table 2.3.

Table 2.3. Amounts used for excess zinc samples

Sample	Ti:Zn	ZnAcOH (g)	EtOH (mL)	Oxalic Acid (g)	EtOH (mL)	TTIP (mL)	H_2O (mL)
TZ-1:4	0.0125:0.05	9.17	500	12.60	200	3.70	22.50
TZ-2:4	0.0250:0.05	9.17	500	12.60	200	7.40	45.00
TZ-3:4	0.0375:0.05	9.17	500	12.60	200	11.10	67.50

2.5 Photocatalytic Studies

2.5.1 Metylene blue degradation

Photocatalytic studies were carried out on selected powders. The photocatalytic activity of the materials was investigated by degrading an organic pollutant (methylene blue). Methylene blue is one of the generally accepted organic pollutants for degradation studies and is used as an industrial standard (Japanese standard, JIS R 1703-2:2007). The standard protocol in our laboratory is as follows; in a typical experiment, TiO_2 powder (60 mg) was added to methylene blue (50 mL, 10^{-5} M). The suspension was allowed to stir in the dark for 30 min to obtain adsorption-desorption equilibrium, eliminating any error caused by initial adsorption. An initial 5 mL aliquot was then removed. The suspension (under continuous stirring) was then irradiated by light in a Q-sun Xenon solar simulation chamber (0.68 W/m^2 at 340 nm). Aliquots (5 mL) were removed at timed intervals and the visible absorption spectra were recorded using a Perkin-Elmer Lambda 900 UV-vis spectrometer.

The rate of degradation was found to obey (pseudo) first order kinetics and hence the rate constant for degradation, *k*, was obtained from the first-order plot of kinetic analysis according to equation 2.1.

$$\ln\left(\frac{A_0}{A}\right) = kt$$ Equation 2.1

where, A_0 is the initial absorbance, A is the absorbance after a time (t) of the methylene blue dye degradation, and *k* is the psuedo first order rate constant (min^{-1}). The rate constant, *k* can be derived from a plot of $ln(A_0/A)$ versus time. All photocatalytic degradation experiments were carried out twice, and an average error of ± 10% was calculated.

2.6 Characterisation Techniques

2.6.1 X-ray diffraction (XRD)

X-ray diffraction is a non-destructive technique that reveals the crystal structure of the material under analysis. XRD was used to determine the crystalline phase of all synthesised materials. Fine powdered samples were spread onto a glass slide using double sided sticky tape and X-ray diffractograms were collected using a Siemens D 500 X-ray diffractometer, with a diffraction angle range 2Θ = 20–80° using Cu Kα radiation. From the resulting diffractogram the crystallite size (*T,* nm) was estimated using the Scherrer equation (equation 2.2).[197]

$$T = \frac{0.9\lambda}{\beta\cos\theta}$$ Equation 2.2

where λ is the X-ray wavelength (1.54 Å), Θ is the Bragg angle of the peak of interest (peaks of interest are located at 2Θ = 25.2° for anatase (101) and 2Θ = 27.4° for rutile (110)) and β is the line broadening measured from the increased peak width at half height through a Gaussian fit obtained from Origin plotting software.

The mass fraction of rutile (X_R) was determined by the Spurr equation (equation 2.3).[198]

$$X_R = \frac{1}{1+0.8\left[I_A(101)/I_R(110)\right]}$$ Equation 2.3

where I_A is the intensity of the 101 peak and I_R is the intensity of the 110 peak.

2.6.2 Fourier transform infrared spectroscopy (FTIR)

Infrared radiation interacts with chemical bonds to cause stretches, bends and various other atomic vibrations. For a vibration to give rise to absorption of infrared radiation, it must cause a change in the dipole moment of the molecule. The larger this change the more intense the absorption band will be.

All IR spectra were recorded using a Perkin-Elmer GX FTIR. Samples were recorded as a KBr disc (1:10, sample/KBr), using 16 scans per sample at a resolution of 4 cm^{-1} over the range 4000 – 400 cm^{-1}.

2.6.3 Raman spectroscopy

IR absorption is caused by infrared light causing a change in the dipole moment of a molecule. Raman spectroscopy, although similar to IR (both measure the vibrational energies of molecules) does not cause a change in the dipole moment of a molecule. For a vibration to be Raman active, the polarisability of the molecule must change with the vibrational mode. All Raman spectra were collected with an ISA Labram using an argon ion laser (514.5 nm) as excitation source. Typically, a small amount of powdered sample was mounted on a glass slide using a spatula tip. Using the attached microscope and camera, the instrument was focused on the powder sample through the objective lens (x10). One scan was recorded with a detector exposure time of 1 sec.

2.6.4 UV-visible absorption spectrometry (UV-vis)

A Perkin-Elmer Lambda 900 UV–vis spectrometer was used to record absorption spectra of the organic dyes under investigation for photo-degradation studies. Spectra were recorded in the region 500 – 750 nm. The absorption at maximum wavelength (λ_{max}) of methylene blue (660 nm) was used to calculate degradation rates as a function of irradiation time.

2.6.5 UV-vis diffuse reflectance

Diffuse reflectance spectra were recorded on a Perkin-Elmer Lambda 900 UV–vis spectrometer. Sample preparation involved mixing the powdered sample with KBr (1:20) and pressing into a pellet of uniform thickness. From the resulting diffuse reflectance spectra, the band gap of the semi-conductor sample could be recorded by placing the pellet into the reflection sphere where it reflects light directly from the source.

2.6.6 Differential scanning calorimetry (DSC)

Approximately 5 mg of sample was placed into an aluminium sample pan for DSC using an empty aluminium pan as a reference. All DSC were recorded on a Shimadzu DSC-60 between 25 °C and 600 °C at the default ramp rate of 20 °C/min. The instrument measures the difference in heat flow between the sample and the reference material. A graph of heat flow versus temperature was plotted to show the exothermic and endothermic events associated with the material.

2.6.7 Field emission scanning electron microscopy (FESEM)

Electron micrograph images were taken on a Hitachi SU 70 FESEM with a Schottky electron gun. Measurements were carried out at an accelerating voltage range of 5 – 15 kV. Powdered samples were evenly distributed on a mounted carbon tape surface. Loose powdered sample was removed with canned air spray.

The field emission scanning electron microscope (FESEM) is a type of electron microscope that images the sample surface by scanning it with a high-energy beam of electrons in a raster scan pattern. The electrons interact with the shells in atoms that make up the sample producing signals that contain information about the sample's surface topography, composition and other properties such as electrical conductivity.

The types of signals produced by an SEM include secondary electrons (SE), back-scattered electrons (BSE), characteristic X-rays, light (cathodoluminescence), specimen current and transmitted electrons (STEM). Generally the most common or

standard detection mode is SE imaging. The spot size in a Field Emission SEM is smaller than in conventional SEM and can therefore produce very high-resolution images, revealing details in the range of 1 to 5 nm in size.

2.6.8 X-ray photoelectron spectroscopy

X-ray photoelectron spectroscopy (XPS) was carried out on a Thermo VG Scientific (East Grinstead, UK) Sigma Probe spectrometer by Dr. S. J. Hinder of the University of Surrey. The instrument operates as 140 W employing a monochromated Al Kα X-ray source ($h\nu$ = 1486.6 eV). The analysis area was ~ 500 μm in diameter. For survey spectra, a pass energy of 100 eV and a 0.4 eV step size was used. Charge compensation was achieved using a low energy electron flood gun. Quantitative surface chemical analyses were calculated from the high resolution core level spectra, following the removal of a non-linear Shirley background. The manufacturer's Avantage software was used to plot results. The software incorporates the appropriate sensitivity factors and corrects for the electron energy analyser transmission function.

3 Formation of Titanium Formate Complexes; a Spectroscopic Study

3.1 Introduction

In this chapter an alternative chemical modifier, formic acid is employed as a chelating agent for the synthesis of titanium dioxide using titanium isopropoxide. Formic acid was chosen because it is the simplest carboxylate species and because of its similar structural properties to acetic acid. Initially it was assumed that titanium dioxide may be synthesised with formic acid in a similar manner to that of acetic acid and as such it was decided that the same synthesis route will be employed but with varying ratios of precursor:formic acid:water. In order to synthesise anatase TiO_2 that is stable at higher temperatures than existing materials it is necessary to have a greater understanding of the reaction dynamics and how the early stages of the reaction conditions may affect the eventual crystalline behaviour of the material. The chapter results are divided into two sections, firstly the influence of increasing amounts of water on the sol-gel synthesis is investigated and secondly the effect of the chelating agent is examined.

Sol-gel synthesis of TiO_2 is regarded as a relatively straight forward synthesis technique and is thus of great interest and use to researchers.[172] Titanium alkoxides are readily hydrolysed by water due to their susceptibility to nucleophilic attack.[199] Rates of hydrolysis and condensation may be controlled by using organic chelating agents such as acetyl acetone,[200] alkanolamines,[201] diols[202] and acetic acid[203] to replace alkoxide groups on the central metal atom. This stability improves control over the reaction conditions.[204] Suresh *et al* concluded that the pH of the precursor influences the chelation effect of acetic acid and that the extent of chelation of the acetate group decreases with an increase in pH causing weakened gel structures resulting in decreased anatase to rutile transformation temperatures.[48]

Previous work studying anatase to rutile transformation (ART) temperatures has been carried out grouping our laboratories where acetic acid was chelated to the titanium alkoxide precursor.[205] It is widely accepted that acetic acid forms a bridging complex to titanium alkoxides.[172,206,207] Titanium dioxide sol gel materials synthesised using titanium alkoxides (without chemical additives), typically transform from anatase to

rutile at ~600 °C. In order to determine whether varying ratios of a chelating species alters the ART temperature, the simplest carboxylic acid – formic acid – and titanium isopropoxide in various ratios were used to synthesise a wide range of TiO_2 powders. The formate carboxylate group was chosen because of its versatile coordination behaviour.[208] The carboxylate coordinations include: ionic, monodentate, bidentate chelating and bridging.[208] From FTIR and Raman spectroscopy, the role of the chelating agent in the synthesis was examined. Ivanda *et al* carried out spectroscopic studies on powders synthesised from an esterfication reaction to find bridging of various carboxylates. However, the paper focused mainly on particle size as opposed to relating oligomeric structure and ART temperatures.[209]

FTIR and Raman spectroscopy can be used to determine the mode of the carboxylate binding (figure 3.1). The frequency of the asymmetric carboxylate vibration in the IR spectra, $\nu_{as}(COO^-)$, and the magnitude of the separation between the carboxylate stretches, $\Delta = \nu_{as}(COO^-) - \nu_s(COO^-)$, are often used as spectroscopic criteria to determine the mode of the carboxylate binding.[208]

Generally the following order is proposed for divalent metal carboxylates:

Δ (chelating) < Δ (bridging) < Δ (ionic) < Δ (monodentate)[208]

Δ ionic is reported as 160 – 170 cm^{-1} for acetates and 200 – 210 cm^{-1} for formates.[210]

In the monodentate coordination electron density redistribution occurs and the shift of $\nu_{as}(COO^-)$ to higher wavenumbers is observed in comparison with the ionic group, increasing the value of Δ. The chelating coordination, however, shifts the position of the asymmetric carboxylate stretch to lower wavenumbers in comparison with the ionic group and thus lowers the value of Δ. In the bridging coordination, one divalent metal cation is bound to one of the oxygen atoms of the COO^- group and another divalent metal cation to the other oxygen, the asymmetric stretch is located at the same position as that of the ionic group.[208,211] The range 200 – 210 cm^{-1} was derived for ionic formates and in general the comparison of the Δ value of the respective complex with the Δ value of the sodium salt should be used for the assignment following the guidelines: (i) bidentate chelating coordination: $\Delta(COO^-)_{studied\ complex} << \Delta(COO^-)_{sodium\ salt}$;

(ii) bidentate bridging carboxylate: $\Delta(COO^-)_{studied\ complex} \leq \Delta(COO^-)_{sodium\ salt}$; (iii) monodentate coordination: $\Delta(COO^-)_{studied\ complex} >> \Delta(COO^-)_{sodium\ salt}$.[208,210,212-215]

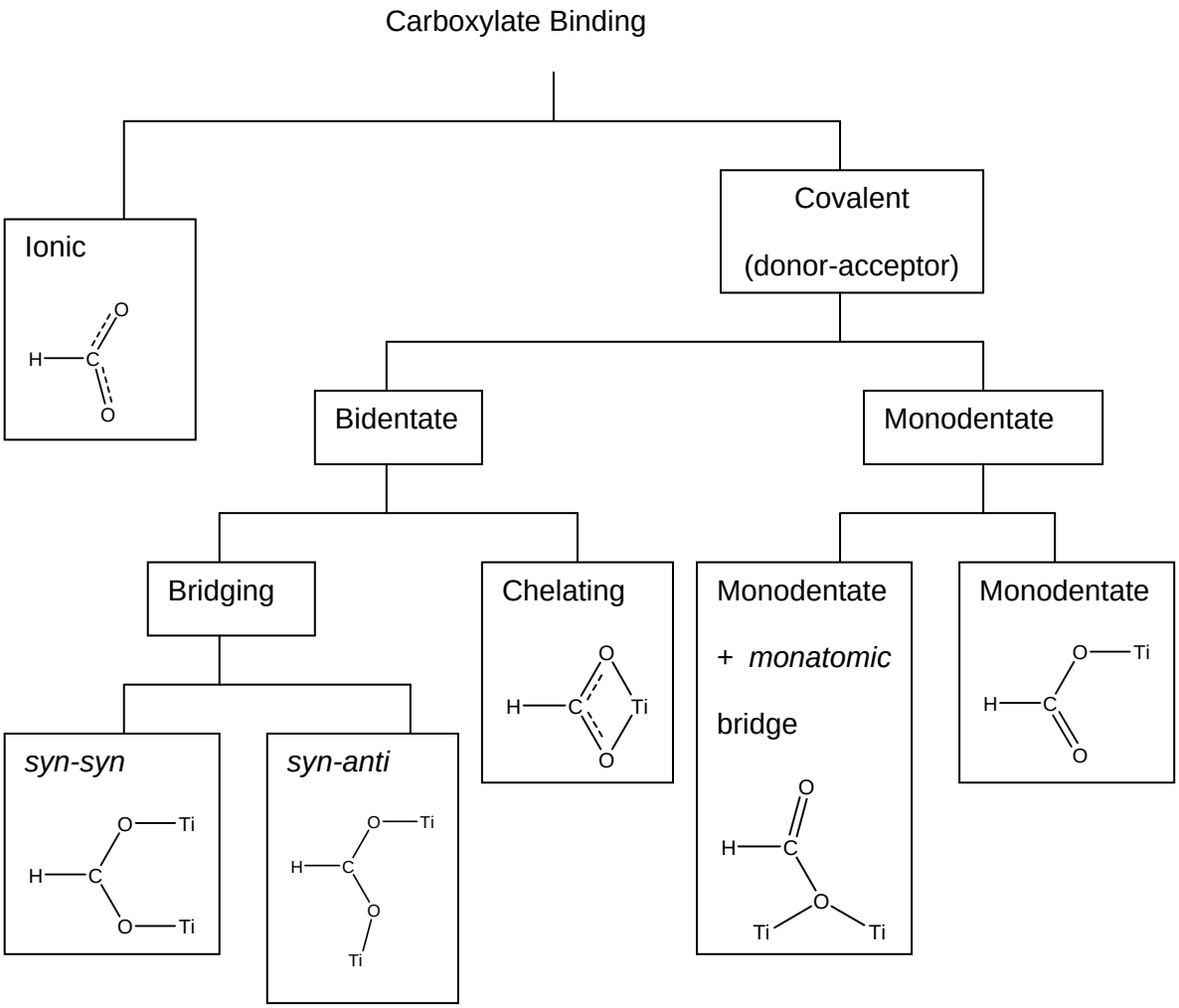

Figure 3.1. Modes of carboxylate binding

The carboxylate functional group (figure 3.2) has four lone pairs of electrons available for coordination to a metal. These lone pairs subtend to an angle of 120 ° and are referred to as the *syn* and *anti*-lone pairs. On the basis of stereoelectronic arguments it has been suggested that the *syn*-lone pairs are more basic than those in the *anti* position.[216]

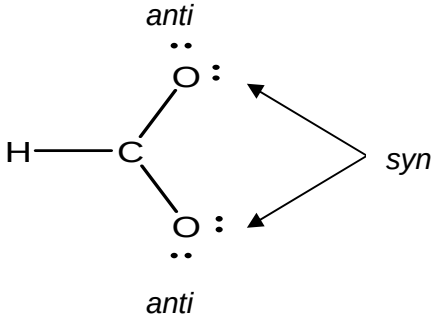

Figure 3.2. The Carboxylate Functional Group

From FTIR and Raman spectroscopy, the role of the chelating agent in the synthesis is examined. These are practical, efficient and useful techniques for gaining information on modes of binding. In order to understand why anatase transforms to rutile at different temperatures these spectroscopic techniques were employed to investigate how the formate group binds to the titanium. Anatase and rutile percentages and transformation temperatures are examined using XRD.

3.2 Results and Discussion

In order to investigate the influence of chelation on anatase to rutile transition, the effect of various concentrations of water and formic acid on the titania precursor were investigated.

3.2.1 Effect of water

3.2.1.1 X-ray diffraction

XRD was employed to determine the phase analysis of each powder calcined at increasing temperatures. The percentage of anatase in the calcined sample is shown in figure 3.3. All samples were 100 % anatase at temperatures 300 – 500 °C. From figure 3.3 it is apparent that for each series of powders (F_2W_4 – F_2W_{100}, F_4W_4 – F_4W_{100} and $F_{10}W_4$ – $F_{10}W_{100}$) where the TTIP:FA ratio remains constant, that the increase in water promotes the formation of rutile. For the powders F_2W_4 – F_2W_{100}, F_2W_4 has the lowest water ratio and it is the only powder with anatase at 700 °C, but the remaining powders have all underwent complete phase transformation to a more thermodynamically stable rutile.

The formic acid ratio was increased for powders F_4W_4 – F_4W_{100} causing improved chelation. This is reflected throughout the 6 powders as most retain anatase at 700 °C. Anatase is predominant for F_4W_4 at 700 °C (86 %) (figure 3.4) but the increase in water along the series causes increased rutile formation for the remaining powders. At 800 °C anatase is still dominant for the powder F_4W_4 (61 %) and is even present in F_4W_8 (5 %), however, the other powders in the series are rutile.

From these results it is clear that an increase in the amount of water used for hydrolysis has an adverse effect on ART temperatures resulting in the lowering of the anatase to rutile transformation. This increase in water reduces the acidity of the sol resulting in a decrease in the chelation effect of the formate group.[206,213,214,224] This decrease in chelation results in a weakened gel network and consequently a lowering of ART temperature was observed.[217] Sahni *et al* reported that increasing water content

causes increased hydrolysis which results in the formation of larger particles that thermodynamically favour phase transformation to rutile.[218]

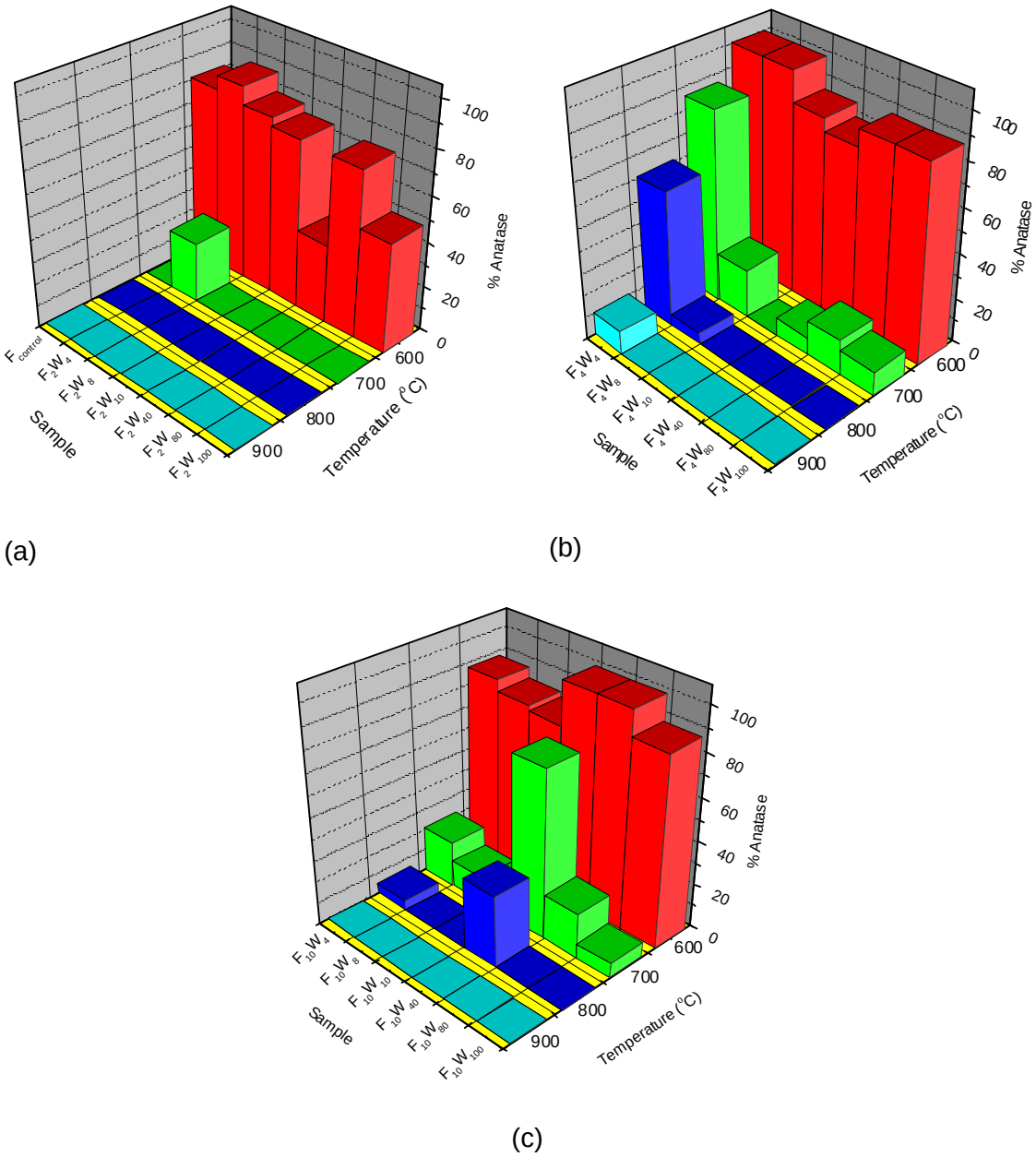

Figure 3.3. Percentage of anatase in the calcined TiO_2 samples, determined by XRD for materials heated to different temperatures (a) F_2W_4 – F_2W_{100}, (b) F_4W_4 – F_4W_{100}, (c) $F_{10}W_4$ – $F_{10}W_{100}$ (refer to P40 for table)

For powders $F_{10}W_4$ – $F_{10}W_{100}$, the sample with the lowest water ratio, $F_{10}W_4$, is one of only two samples where anatase is present at 800 °C. The other is $F_{10}W_{40}$ and the reason why anatase is present in $F_{10}W_{40}$ is unclear as it has an increased amount of

water whereas powders $F_{10}W_8$, $F_{10}W_{10}$, $F_{10}W_{80}$ and $F_{10}W_{100}$ follow the theory that increased amounts of water cause a reduction in ART temperatures.

From figure 3.3, F_4W_4 was found to maintain anatase at temperatures as high as 900 °C. All powders synthesised (except $F_{10}W_{40}$) showed that as water ratio is increased rutile forms at lower temperatures.

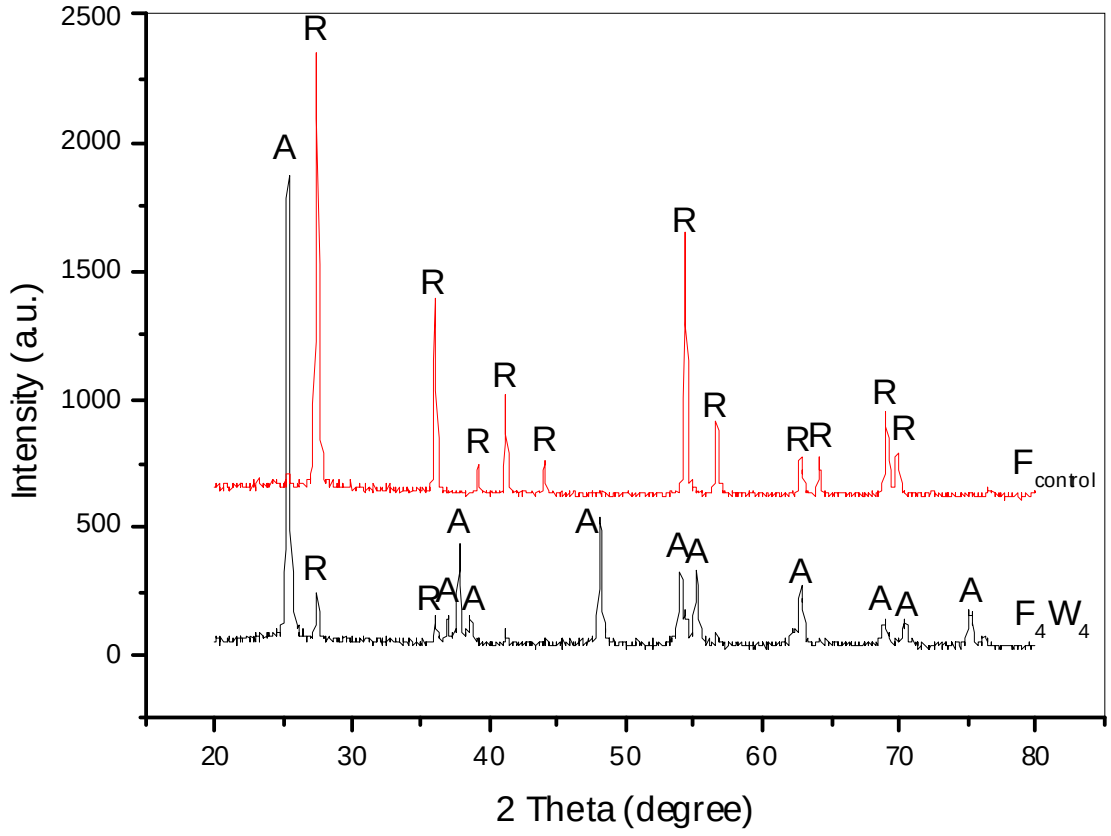

Figure 3.4. XRD of $F_{control}$ and F_4W_4 at 700 °C, A – anatase, R - rutile

As the carboxylate group may coordinate to Ti in a number of different arrangements [199,206-208,210,219] spectroscopic (Raman and IR) studies were carried out on all pre-calcined samples in order to determine if an increase in water influences the way that the carboxylate group binds to Ti, which in turn affects the anatase to rutile transformation temperature.

3.2.1.2 Infrared spectroscopy

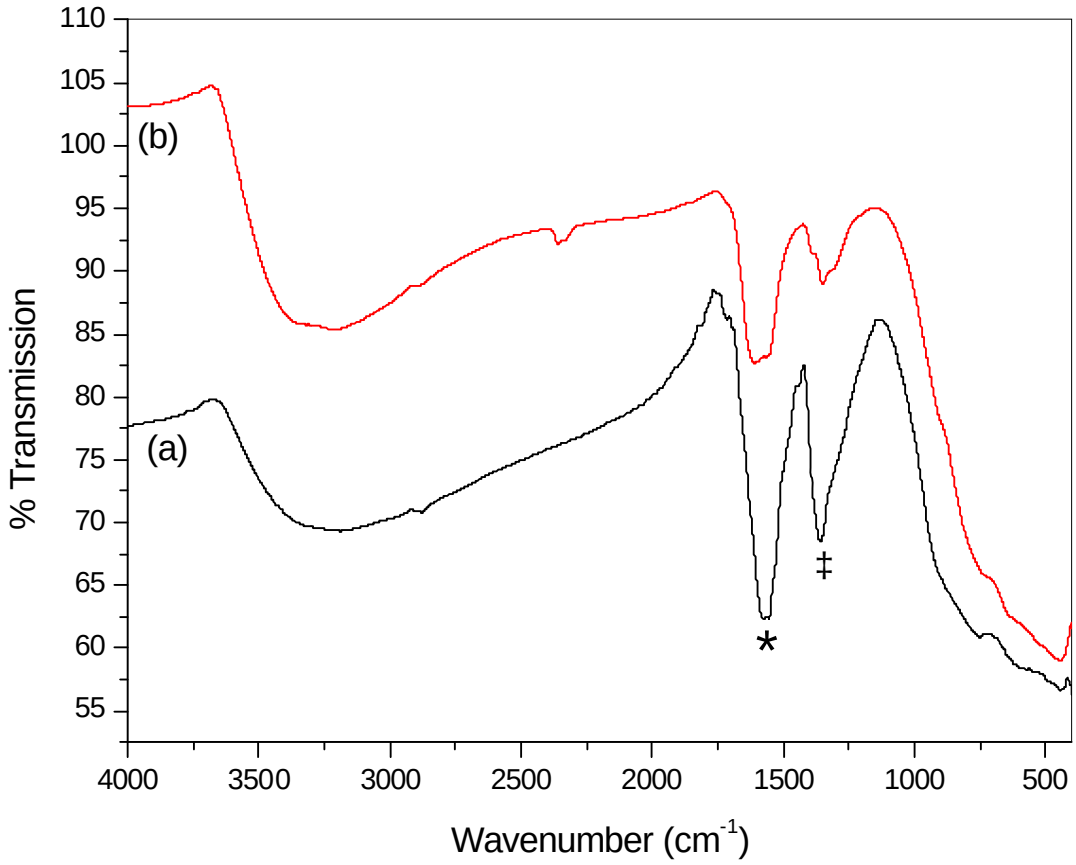

Figure 3.5. IR spectra of TiO_2 precursor powders (a): F_2W_4 & (b): F_2W_8, where * = $\nu_{asym}(COO^-)$ and ‡ = $\nu_{sym}(COO^-)$

Figure 3.5 shows the IR spectra of powdered samples F_2W_4 and F_2W_8 (F_2W_8 – F_2W_{100} give near identical spectra). At ~450 cm^{-1} there is a broad peak due to the formation of Ti – O bonds. Peaks at 1350 and 1550 cm^{-1} represent $\nu(COO^-)_{sym}$ and $\nu(COO^-)_{asym}$ respectively. Zalenak *et al* determined the mode of bonding of the carboxylate group to the metal atom by calculating Δ, where $\Delta = \nu_{as}(COO^-) - \nu_s(COO^-)$.[208] From the spectra obtained for F_2W_4 and F_2W_8 (Figure 4), Δ = ~ 200 cm^{-1}. This value is consistent with the literature value for ionic formate ($HCOO^-$) = ~201 cm^{-1}.[210]

Figure 3.6. Bidentate bridging modes of the formate group and TTIP, (a): *syn-syn* and (b): *syn-anti*

As has been reported elsewhere; the bidentate bridging carboxylate exists when $\Delta(COO^-)_{\text{formate complex}} \leq \Delta(COO^-)_{\text{sodium salt}}$.[210,212-215] Therefore it is proposed that the formate group binds to the Ti centre in bidentate bridging mode such as *syn-syn* or *syn-anti* (Figure 3.6).

It has been reported that metal alkoxo-acetates are formed by the reaction of acetic acid (HOAc) with metal alkoxide, in which OPr^i (OR) groups on the central titanium atom are preferentially hydrolysed, whereas bridging acetate ligands remain bonded to titanium throughout much of the condensation process (Figure 3.7).[172,207]

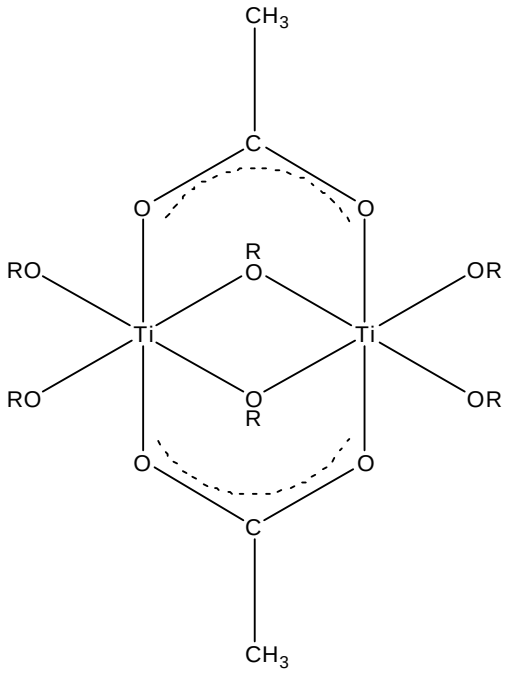

Figure 3.7. Bridging acetate ligands attached to TTIP

Since the bridging acetate ligands are not hydrolysed, the chelated ligands effectively alter the condensation pathway toward promoting the formation of linear polymers composed of edge sharing octahedra.[207,220] The addition of excess water destabilises the system by altering the highly cross-linked network structure. The gels having polymeric chains with little branching and cross-linking, and also a smaller void region, are structurally weak and thus collapse rapidly on calcination forming rutile at lower temperatures.[217]

This can clearly be seen from both the rutile percentage results (Figure 3.3) and also from the IR spectra (Figure 3.8) where bands corresponding to the chelated formate group become weaker. From the IR spectra of samples F_4W_4 – F_4W_{10} (Figure 3.8), it can be seen that there is a strong OH peak at ~2800 – 3500 cm^{-1}. As the ratio of water is increased in each series (F_2W_4 – F_2W_{100}, F_4W_4 – F_4W_{100}, $F_{10}W_4$ – $F_{10}W_{100}$), the intensity of both ν_{sym}(COO) and ν_{asym}(COO) decrease in relation to both the Ti – O and the OH peaks. F_4W_4 shows the strongest COO stretches and the weakest Ti – O and OH signal when compared with the other samples. It is believed that this is due to an increase in the molar ratio of water which alters the pH of the system as well as increasing hydrolysis and weakening the gel network.[48] This, as has been reported previously, weakens the chelation of the carboxylate group, which will cause weakened COO stretches, facilitating increased hydrolysis, therefore increasing OH stretches and causing a reduction in the anatase to rutile transformation temperature.[48,217,218]

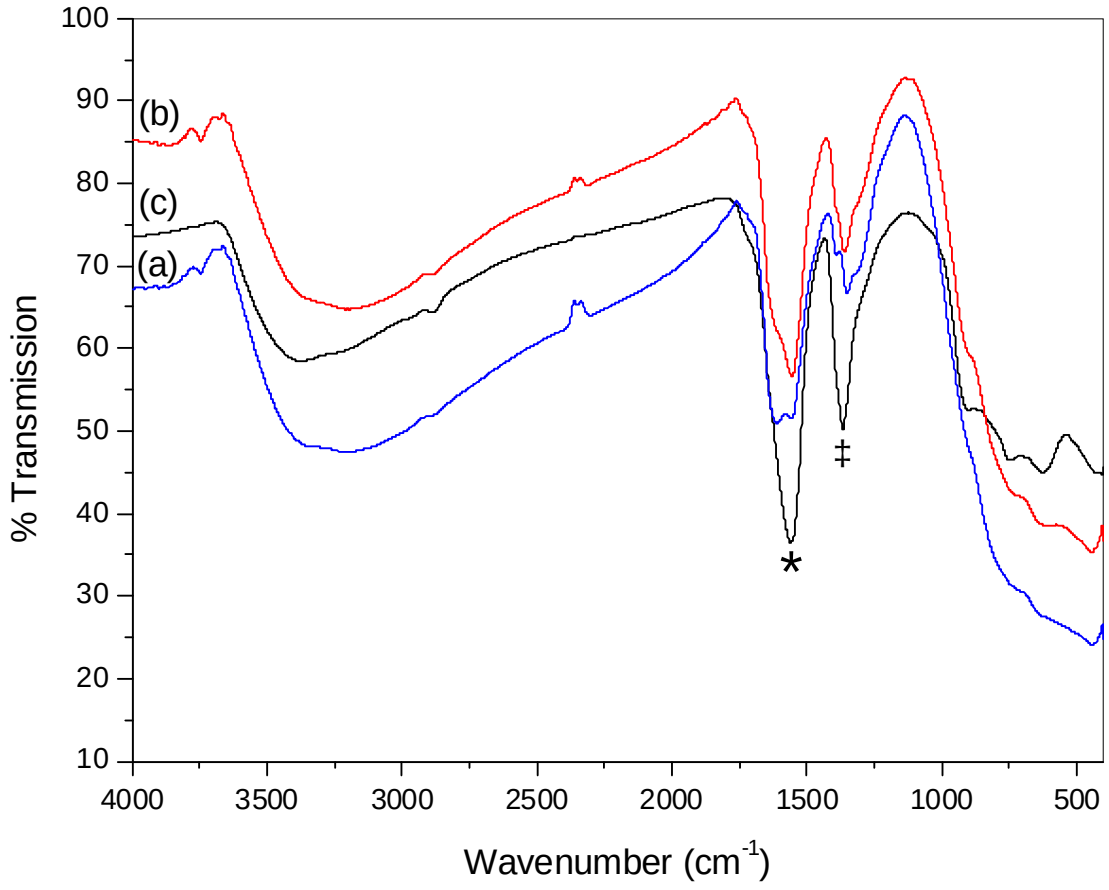

Figure 3.8. IR spectra of TiO_2 precursor powders (a): F_4W_4, (b): F_4W_8 and (c): F_4W_{10}, where * = $\nu_{asym}(COO^-)$ and ‡ = $\nu_{sym}(COO^-)$

The IR spectra (Fig 3.5 and Fig 3.8) show that for samples F_2W_8 and F_4W_{10} two asymmetric (1600 and 1550 cm^{-1}) and two symmetric (1382 and 1340 cm^{-1}) carboxylate stretches were observed. For sample F_4W_4 one asymmetric (1550 cm^{-1}) and one symmetric (1362 cm^{-1}) carboxylate stretch were observed in the IR spectra. The spectra of sample F_4W_8 showed that secondary asymmetric and symmetric stretches were beginning to form. The presence of two carboxylate stretches indicates the presence of two different modes of carboxylate binding.[208] The frequency of asymmetric and symmetric vibrations depends on the electronic charge density of C – O bonds and C – O bond lengths, the higher is the frequency of the asymmetric vibration and the lower is the frequency of the symmetric vibration. Hence for compounds F_2W_4, F_4W_4, F_4W_8 and $F_{10}W_{40}$ the asymmetric vibration at 1550 cm^{-1} appertains to the symmetric vibration at 1350 cm^{-1}. Similarly the stretches at 1600 and

1380 cm^{-1} are related. The respective experimental values are, Δ_{exp} = ~210 cm^{-1} for samples F_2W_4, F_4W_4 and F_4W_{10}, and Δ_{exp} = ~220 cm^{-1} for the remaining samples. Both Δ_{exp} values are similar and indicate the bridging chelation. However, the formation of secondary peaks indicates a different binding mode. As stated above the carboxylate functional group has two lone pairs of electrons on each oxygen atom available for binding, the *syn*-lone pair and the *anti*-lone pair. It has been suggested that the *syn*-lone pair is more basic than those in the *anti* position.[216] It may be possible that a *syn-anti* (Figure 3.6b) mode of binding occurs when the water ratio is increased due to the altering pH and the increased hydrolysis of the system. This would explain the appearance of secondary peaks in the IR spectra.

Zelenak *et al* observed singlet peaks for both the v_{as} and v_s (COO^-) stretches for bridging complexes that follow *syn-syn* binding and they observed doublet peaks at similar wavenumbers for *syn-anti* binding with zinc carboxylate complexes,[208] while Ishioka *et al* reported similar values of separation for *syn-anti* bridge in zinc (II) acetate.[221] The result of *syn-anti* bridging may produce a polymeric network with little branching and cross linking that is structurally weak, therefore, forming rutile at lower calcination temperatures than that of a typical *syn-syn* mode of bidentate bridging.

3.2.1.3 Raman spectroscopy

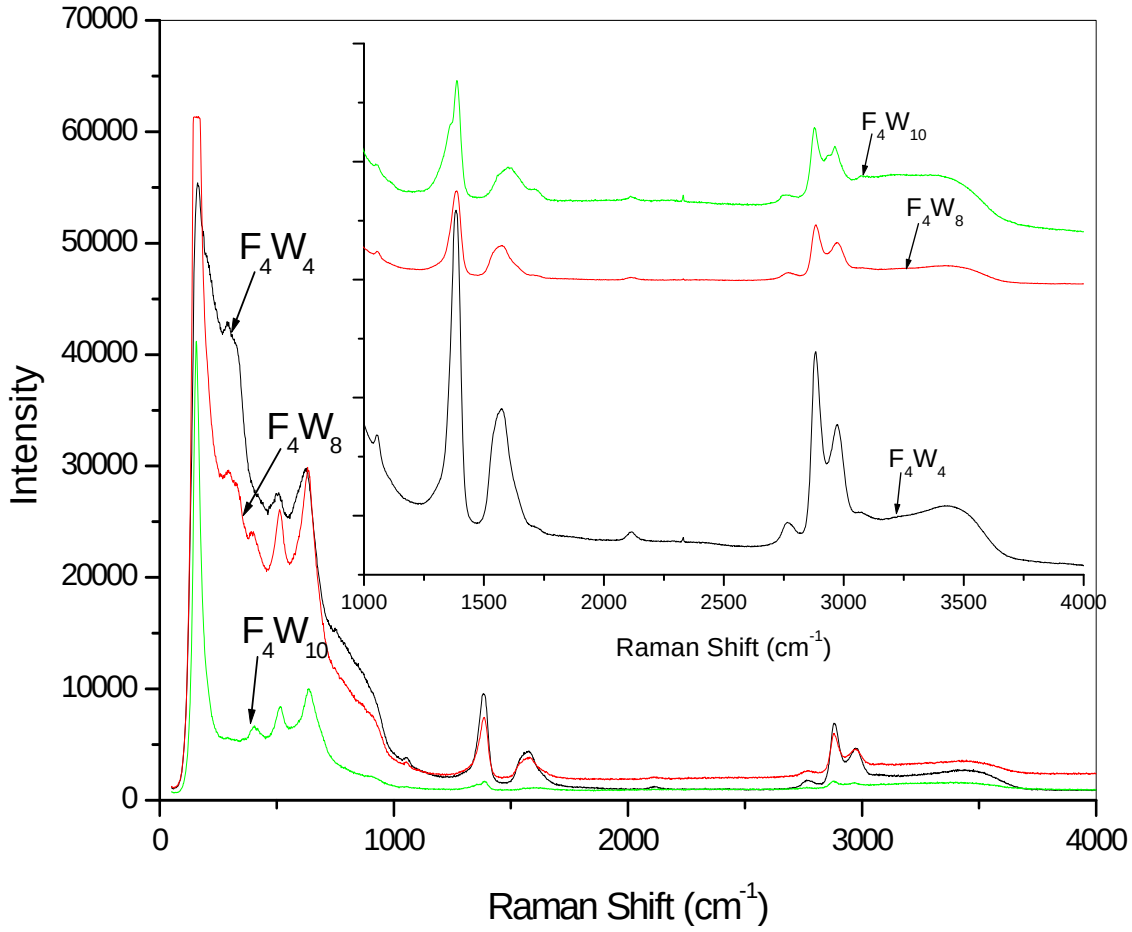

Figure 3.9. Raman spectra of TiO_2 precursor powders of F_4W_4 – F_4W_{10}

Raman spectroscopy was employed as a secondary technique to IR in order to confirm the above results.

Figure 3.9 shows the Raman spectra of the pre-calcined TiO_2 powders. Although the powders have not been calcined, the Raman spectra display clear signs of the anatase phase four-peak pattern with peaks at 160, 405, 515 and 635 cm^{-1} for powders F_4W_{10} – F_4W_{100}. However, for the powders F_4W_4 and F_4W_8 (like with IR spectra) the appearance of a peak at ~290 cm^{-1} indicates that the Ti – O structure is different than the other samples and contains a pattern similar to that of an anatase/rutile mixture. The formation of rutile like structures during the course of crystallisation of titania hydrolysate into anatase has been confirmed by several research groups.[222-224] It has been suggested that the structures which provide the anatase and rutile Raman spectral patterns disappear just before the crystallisation into anatase.[224] It is apparent

that the presence of the anatase/rutile like structure for samples F_4W_4 and F_4W_8 cause an increase in the ART temperature. From Figure 3.9 it can also be seen that the presence of intense peaks at 1393, 1580, 2890 and 2980 cm^{-1} are only present in samples F_4W_4 and F_4W_8. In order to investigate further, all Raman spectra were repeated but scans were only carried out in the region 800 – 4000 cm^{-1} (the organic region) to further confirm binding modes of the formate group.

Figure 3.9 (inset) shows the Raman spectra of the formate group binding with the titanium. Peaks from ~2800 – 3500 cm^{-1} are due to OH stretches.[210] As seen with the IR spectra the intensity of the OH peak increases in comparison with the COO^- stretches (1392 and 1567 cm^{-1}) in F_4W_4 and F_4W_8 when compared with F_4W_{10} – F_4W_{100}. The appearance of secondary peaks also appears beside the main COO^- peaks (1392 and 1567 cm^{-1}) at 1370 and 1720 cm^{-1}. The peak at 1567 cm^{-1} is also shifted to a higher energy. The formation of secondary peaks in the Raman spectra are for the same samples as those of the IR which again indicates the presence of an alternative mode of binding such as *syn-anti* as was proposed previously (Figure 3.6b).

3.2.2 Effect of chelating agent

Sample $F_{control}$ was synthesised using water only to determine what effect formic acid had on the structure of the Ti – O network both before and after calcination.

3.2.2.1 X-ray diffraction

Without the presence of a chelating agent ($F_{control}$), rutile begins to form at a temperature as low as 600 °C (20%) and total transformation has occurred at 700 °C. Samples F_2W_{10}, F_2W_{40}, F_2W_{80} and F_2W_{100} have a higher rutile content at 600 °C. This may be due to the chelating agent having an adverse effect on the initial TiO_2 structure whereby a *syn-anti* bridging mode is dominant throughout the structure thus forming a structure without cross linking that upon calcination, forms a larger percentage of rutile at 600 °C.

3.2.2.2 *Infrared spectroscopy*

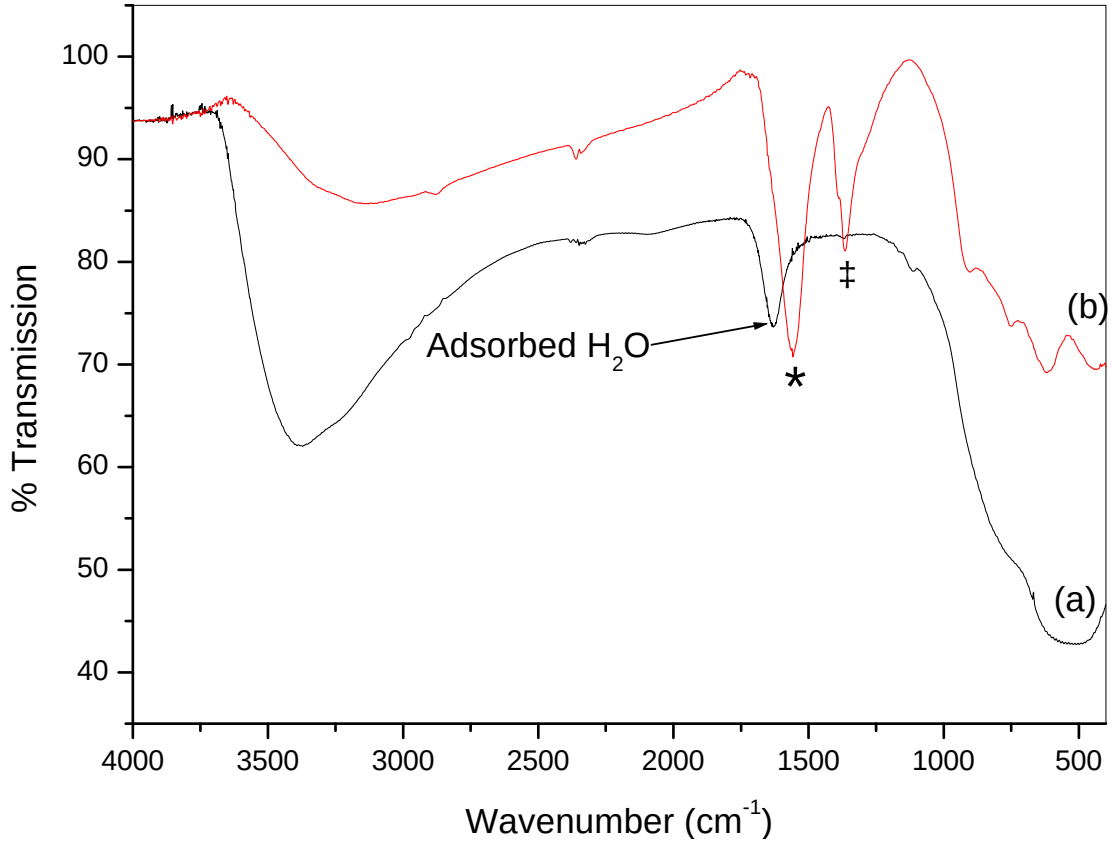

Figure 3.10. IR spectrum of TiO_2 precursor powders (a): $F_{control}$ and (b): F_4W_4, where * = $\nu_{asym}(COO^-)$ and ‡ = $\nu_{sym}(COO^-)$

In figure 3.10 there is an OH stretch (2800 – 3600 cm^{-1}), a Ti-O stretch (400 – 1000 cm^{-1}) and also a signal at 1610 cm^{-1} due to the bending vibrations of adsorbed water. There is a clear difference in the IR spectra of $F_{control}$ and F_4W_4. This was expected and is due to the carboxylate group – Ti bridging structure. Also in the region 400 – 1000 cm^{-1}, F_4W_4 gives more defined peaks as opposed to the broad peak given by $F_{control}$. This is due to a more ordered Ti – O framework.[199,204,209]

3.2.2.3 *Raman spectroscopy*

The Raman spectrum of $F_{control}$ gives no peaks of distinction. This indicates that without the presence of formic acid, Ti – O atoms randomly arrange as opposed to the more ordered structure shown in figure 3.9 where formic acid was employed as a chelating agent. Comparing the Raman spectra of $F_{control}$ with figure 3.9, where the samples were chelated, it becomes clear that the presence of the formic acid as a chelating agent

enables the metal – oxygen atoms to form a defined, crystalline like structure which is apparent in figure 3.9 (0 – 1000 cm^{-1}).

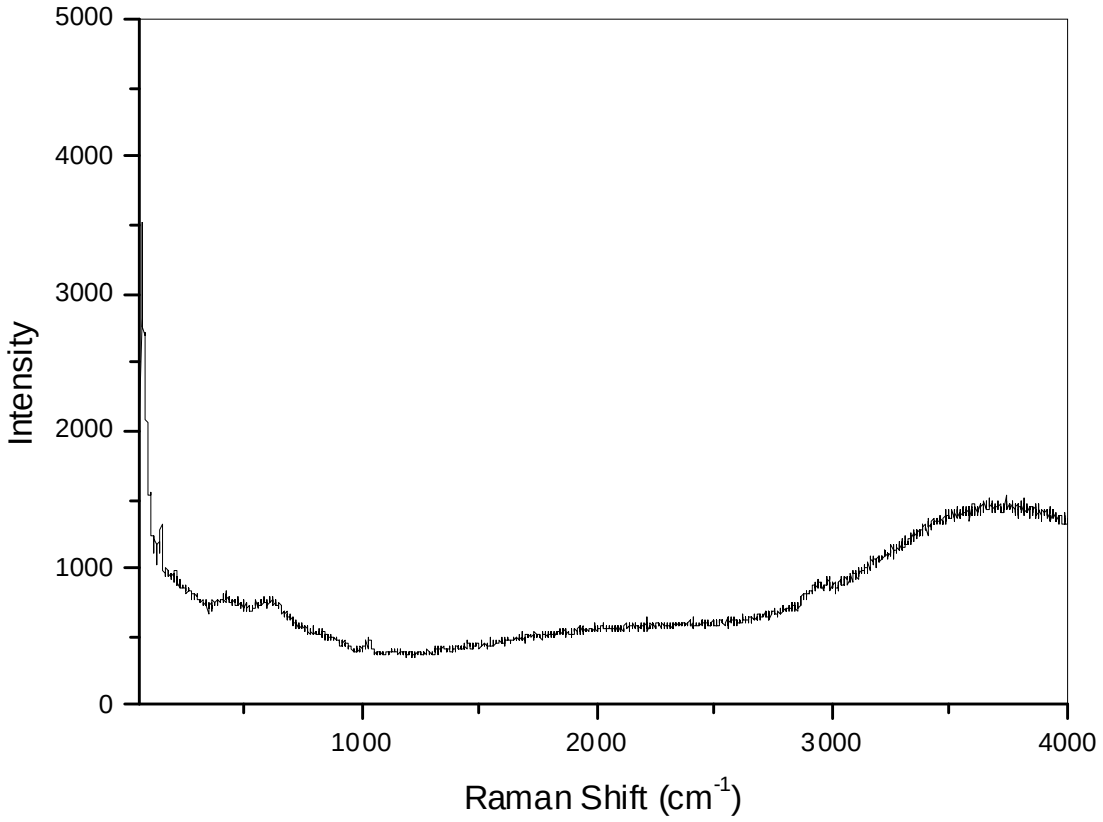

Figure 3.11. Raman spectra of $F_{control}$

The Raman spectra of $F_{control}$ (figure 3.11), as expected also lacks the presence of the bridging peaks present in figure 3.9 at 1390 and 1570 cm^{-1}. It is the presence of this C – O – Ti bridge that allows a controlled arrangement of the Ti – O atoms. Without the bridge there is uncontrolled hydrolysis leading to a random arrangement of Ti – O atoms. The Raman spectra of $F_{control}$ compares favourably to the IR spectrum of the same sample shown in figure 3.10.

3.2.3 Photocatalytic studies

Photocatalytic studies were carried out on selected powders ($F_{control}$, F_2W_4, F_4W_4 and $F_{10}W_4$) at calcination temperatures (600, 700 and 800 °C) and were compared with the commercial photocatalyst, Degussa P25. Powder F_4W_4 calcined at 700 °C was found to be the most photocatalytically active (figure 3.12). The methylene blue was completely degraded after 6 minutes.

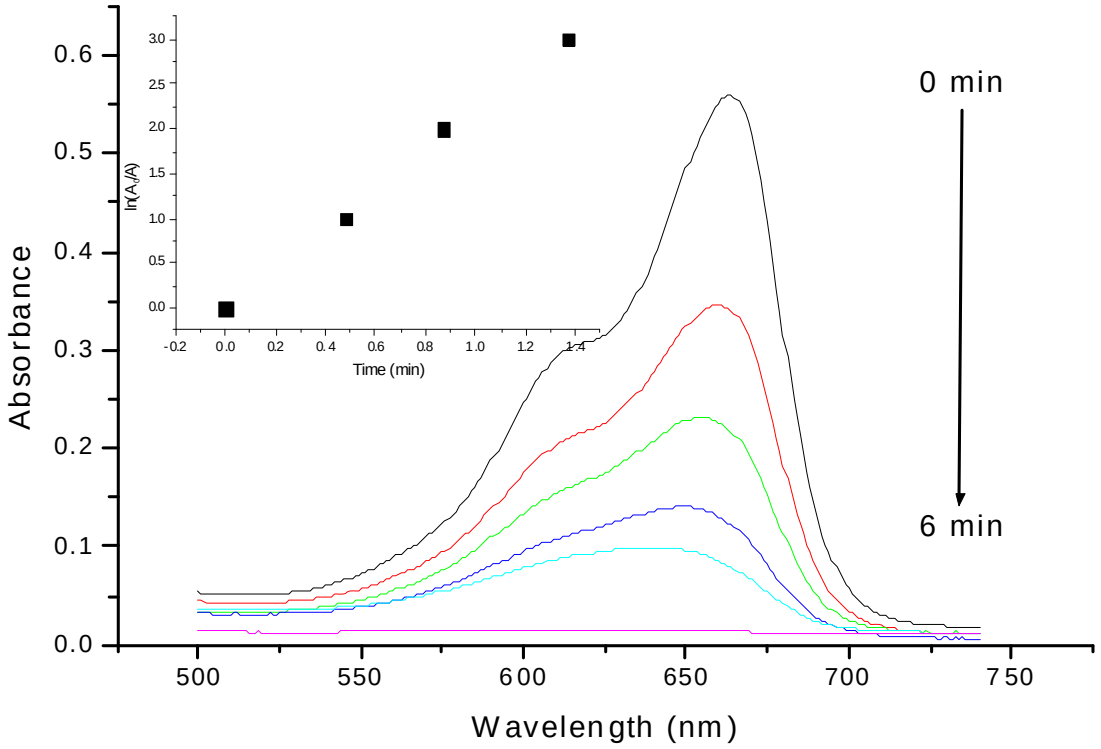

Figure 3.12. Photocatalytic degradation of methylene blue with F_4W_4 (700 °C), R^2 = 0.9981

Improved photocatalytic activity has been previously found with anatase/rutile interactions, due to enhanced electron – hole seperation.[225-227] A mixture of both phases has given rise to the most efficient photocatalyst out of the powders synthesised. It has been suggested that an intimate contact between anatase and rutile phases may enhance the separation of photogenerated electrons and holes resulting in excellent photocatalytic efficiency.[228] It is believed that the anatase/rutile mixture present in Degussa P25 is one of the reasons why it is the one of the most investigated photocatalysts.[227] First order degradation plots of powders $F_{control}$, F_2W_4, F_4W_4 (figure

3.11 inset) and $F_{10}W_4$ at calcination temperatures 600, 700 and 800 °C were used to calculate the reaction rate constant, k (min^{-1}) (table 3.1).

Table 3.1. Reaction rate constants (±0.01, k/min^{-1}) for the degradation of methylene blue

Sample	600 °C	700 °C	800 °C
$F_{control}$	0.12	0.12	0.05
F_2W_4	0.17	0.20	0.17
F_4W_4	0.13	0.45	0.38
$F_{10}W_4$	0.26	0.13	0.08

Sample F_4W_4 calcined at 700 °C had the largest rate constant at 0.45 min^{-1}, the rate constant for Degussa P25 was found to be 0.29 min^{-1} for the same reaction conditions. Sample F_4W_4 calcined at 700 °C consists of 87 % anatase and 13 % rutile to give an ideal mixture for photocatalytic efficiency for the degradation of methylene blue as a model pollutant. Sample F_2W_4 has an identical anatase/rutile mixture at 600 °C but is not as photoactive as F_4W_4. At 700 °C F_2W_4 consists of mainly rutile (72 %) which results in a reduction of photocatalytic activity. At 600 and 800 °C, F_4W_4 has 0 and 32 % rutile respectively. This reduces the photocatalytic activity of F_4W_4. $F_{control}$, the sample prepared without any chelating agent was the poorest photocatalyic performer, even at 600 °C where it consisted of an anatase/rutile mixture (90/10 %), giving a reaction rate of 0.12 min^{-1}. As shown through IR and Raman spectroscopy, the absence of a chelating agent causes complete disorder among the Ti – O bonds upon hydrolysis resulting in an unorganised network of TiO_2 particles when compared with those where a chelating agent was present. $F_{10}W_4$ consisted of 77 % rutile at 600 °C and 95 % rutile at 700 °C. As reported previously[225-228] a mixture of anatase and rutile has greater photoactivity than either phase alone.

3.2.4 FESEM

FESEM microscopy was used in order to determine the shape and morphology of the calcined materials.

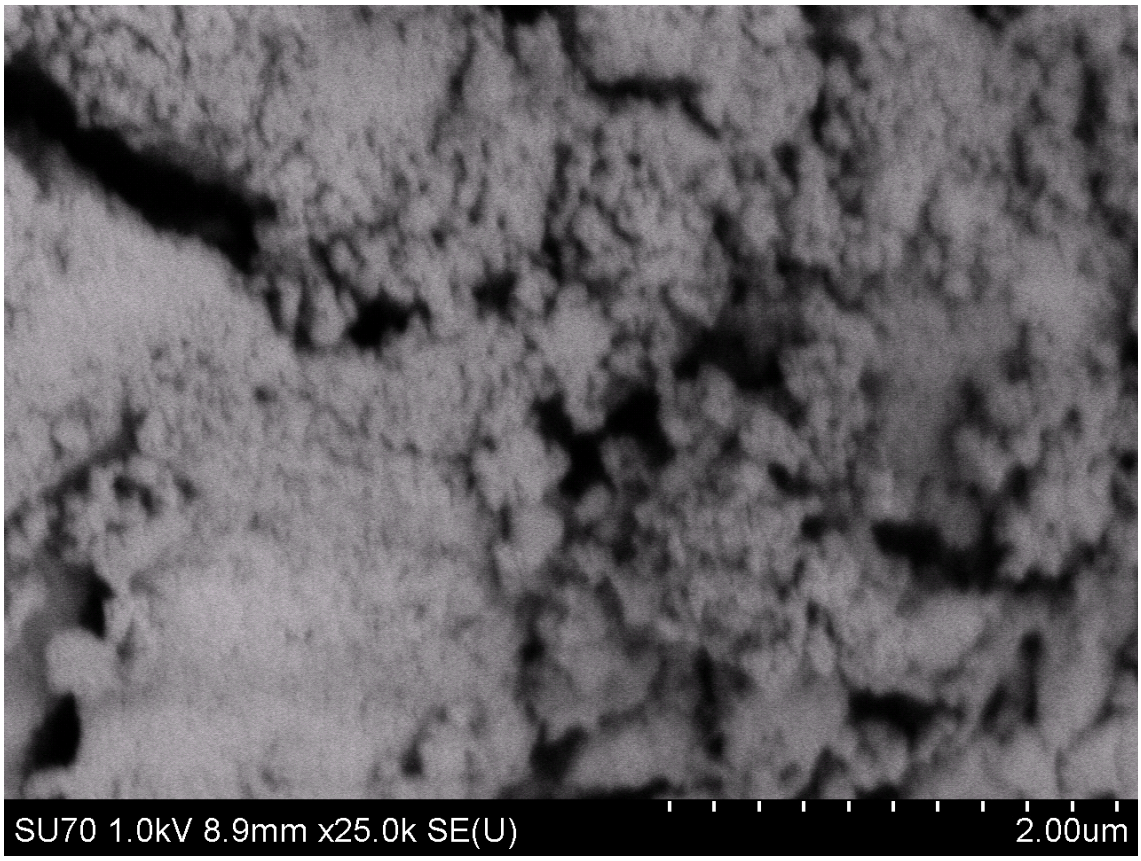

Figure 3.13. FESEM image of $F_{10}W_4$ calcined at 700 °C

From the image shown in figure 3.13 it is clear that the particles are highly agglomerated and no definite shape or morphology can be seen.

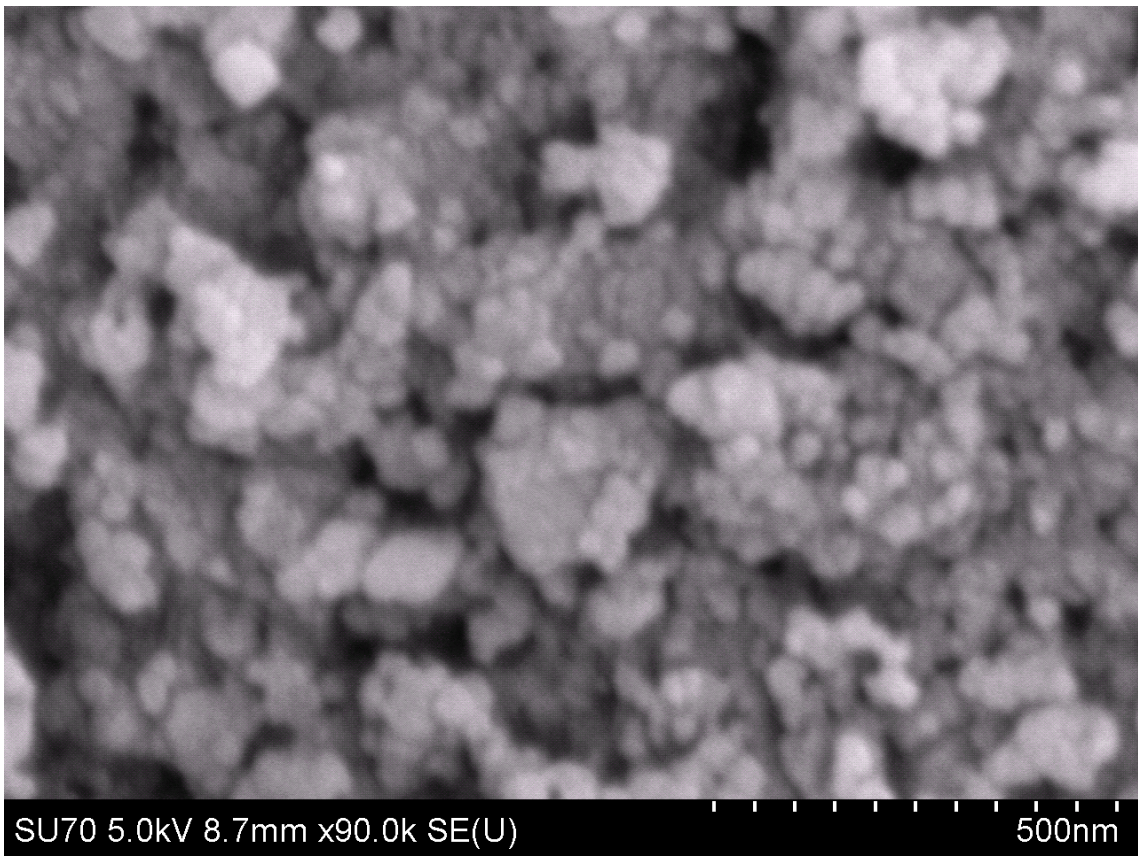

Figure 3.14. FESEM image of $F_{10}W_4$ calcined at 700 °C

Higher magnification images of the sample (figure 3.14) clearly show the presence of individual particles grouping up to form large agglomerated, rugged structures. From the image shown in figure 3.14 it appears that individual crystals < 50 nm agglomerate and form larger particles > 150 nm. The material forms relatively flat surfaces with poor porosity. It is possible that in the presence of a chelating agent, titanium formate can evolve and form polymeric structures.[172] The presence of polymeric titanium formate chains can then form crystals with increased agglomeration. This is further shown through FESEM imaging of $F_{control}$ where no chelating agent was used.

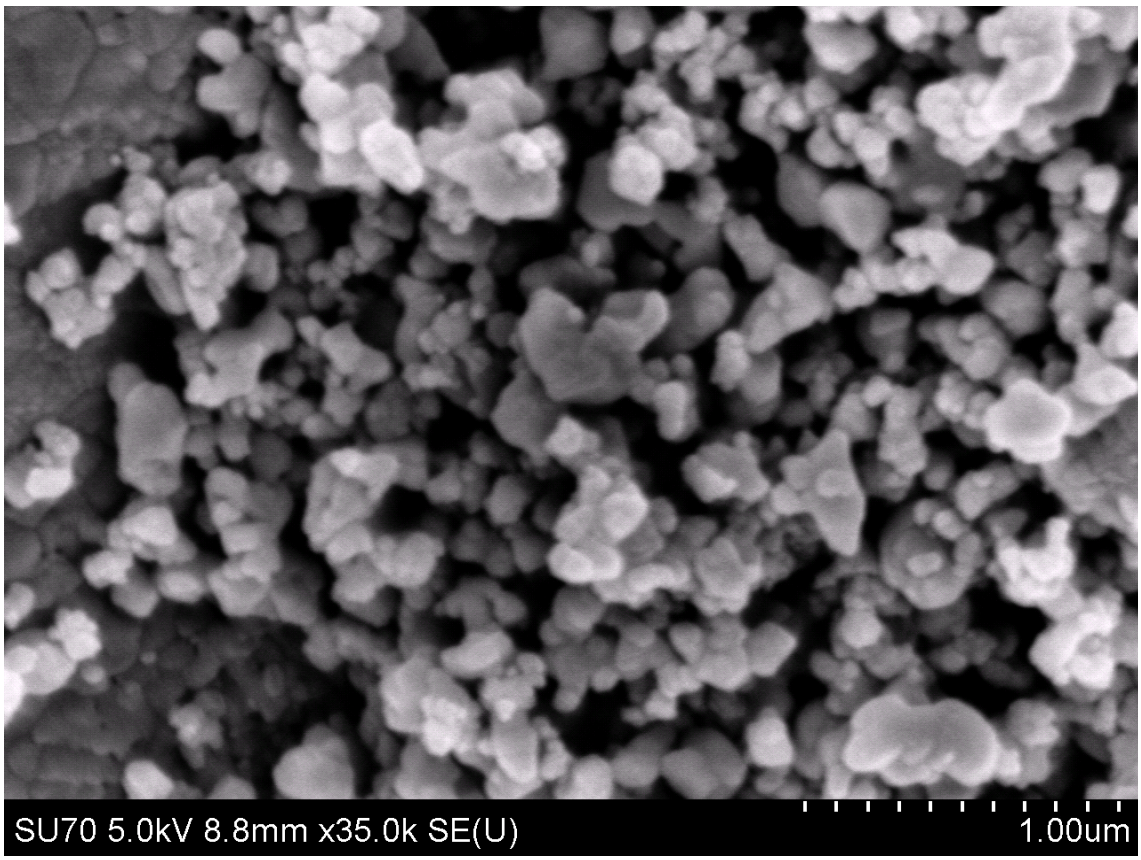

Figure 3.15. FESEM image of $F_{control}$ calcined at 700 °C

Figures 3.15 and 3.16 show materials of different size and morphology to those shown earlier. In figure 3.15 it can clearly be seen that the material has large open pores in comparison with $F_{10}W_4$ also upon closer magnification it can be seen that the individual crystals are much larger than those formed through the use of a chelating agent. Since no chelating agent was used for $F_{control}$, it is known that upon the addition of water to titanium isopropoxide, instantaneous, uncontrollable hydrolysis of the metal alkoxide occurs resulting in the formation of a metal disordered oxide network with randomly arranged octahedra that can easily agglomerate upon calcination to form particles in a range of different sizes as shown in scheme 3.1 and 3.2.

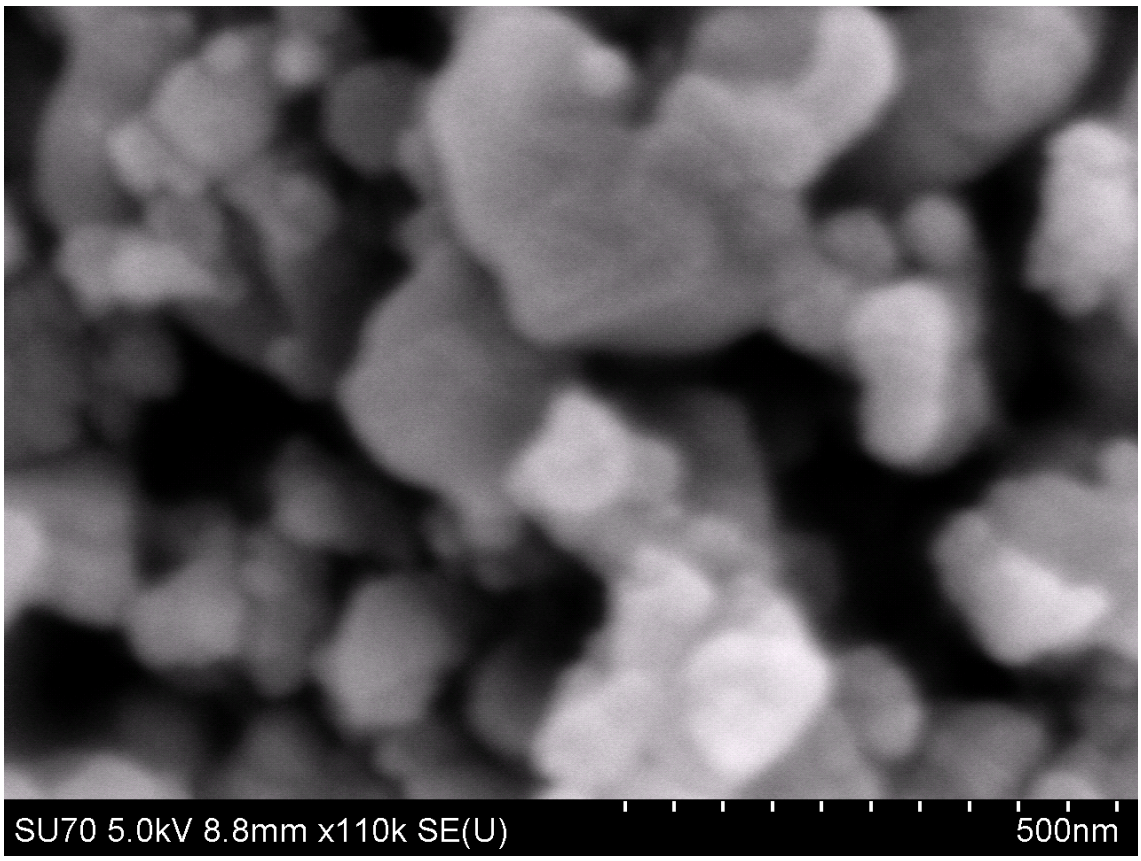

Figure 3.16. FESEM image of $F_{control}$ calcined at 700 °C

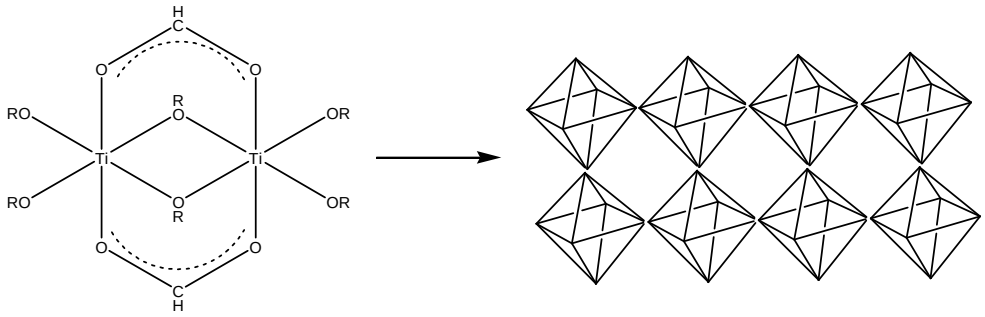

Scheme 3.1. Crystallisation of chelated titanium precursor

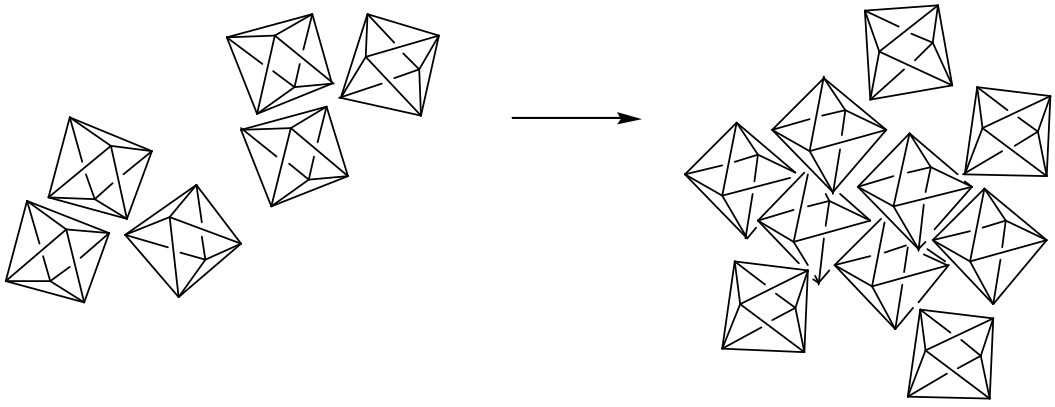

Scheme 3.2. Crystallisation of titanium isopropoxide without chelating agent

3.3 Conclusions

Anatase to rutile transition in a formic acid modified titania material has been studied using XRD, FTIR and Raman spectroscopy. Through Raman and IR it was possible to determine the mode of binding of the chelating agent, formic acid to the titanium precursor with the equation: $\Delta = \nu_{as}(COO^-) - \nu_s(COO^-)$. A value for $\nu_{as}(COO^-) - \nu_s(COO^-)$ of 210 cm^{-1} indicated that bidentate bridging is the mode of binding for the samples. However, for samples with increased water concentrations, spectroscopy results showed doublet peaks indicating alternate modes of bridged binding. It was postulated that for these samples *syn-anti* binding was occurring as well as *syn-syn* binding. It is believed that the resulting *syn-anti* binding hinders crosslinking of the oligomer network, resulting in a weakened structure and thus causing the anatase to rutile transformation temperature to occur at lower temperatures than with the *syn-syn* mode of binding where more ordered oligomer networks are believed to be formed.

Photocatalytic studies showed that the formic acid modified sample (calcined at 700 °C) with an anatase/rutile mixture of 86/14 % respectively was more effective for the degradation of methylene blue than the commercial titania sample Degussa P25, showing that an anatase/rutile mixture is more effective than either phase alone, which is consistent with previous literature results.

4 Effect of Silver on the Chelation of Formic Acid to Titanium Isopropoxide

4.1 Introduction

In the previous chapter, formic acid was used to modify titanium isopropoxide, it was found that a molar ratio of 1:4:4, TTIP:FA:H_2O was the best photocatalyst as well as retaining anatase at the highest temperature. This ratio was then chosen for further analysis. The effect of the addition of silver was investigated using similar techniques to those applied in the previous chapter and a mechanism was proposed showing that not only does silver promote the anatase to rutile transformation through the previously published methods (discussed later) but that the silver also affects the formation of a chelated structure, resulting in a disordered metal oxide structure that can easily transform to rutile upon calcination.

As highlighted in chapter 1, the photocatalytic mechanism of TiO_2 is based on the production of electron (e^-), hole (h^+) pairs upon irradiation with UV light.[74,229] The separated electron-hole pair may diffuse to the TiO_2 surface and react with water and oxygen absorbed on the TiO_2 surface, producing oxidising radicals such as OH• and O_2•$^-$. The produced radicals are powerful oxidising species and as such have the ability to further react with organic or inorganic compounds on the surface of the TiO_2 material, degrading them to CO_2 and H_2O.[69,70] There are three factors that in general, affect the photocatalytic efficiency of TiO_2; the ability of TiO_2 to create the electron hole pair, the electron hole charge transfer or the efficiency of the electron-hole pair in migrating to the catalyst surface and finally the lifetime of the excited electron, *ie* the extent of recombination.

There are two reasons why silver is believed to promote the photocatalytic activity of TiO_2. Silver may promote visible light absorption through surface plasmon resonance of silver nanoparticles[130] but silver also has the ability to reduce recombination due to the trapping excited electrons through the introduction of the Fermi level of silver which evidence suggests is located just below the conduction band of TiO_2.[230] Studies on the effect of silver on phase transformation and grain growth of TiO_2 have also been investigated by this group[130] and also by Chao *et al*.[129] This group previously reported a

delay in the anatase to rutile transformation of TiO_2 which was caused by silver.[130] However, Chao *et al* reported a lowering of the phase transformation temperature with silver addition[129] which is in agreement with the results shown in this chapter. There are believed to be a number of causes for enhanced anatase to rutile phase transformation from the inclusion of silver.

Firstly, the addition of silver causes a reduction in the anatase grain size.[129,130] With the anatase grain size reduced, the surface area of the materials increases, this leads to an increase in crystal defects at the surface of the anatase grains these surface defects act as nucleation sites for crystal transformation and growth. The main driving force for rutile formation is believed to be a mechanism of nucleation and growth.[55,56] Therefore, with an increased presence of nucleation sites the anatase to rutile transformation is enhanced, thus lowering the transformation temperature[129]

Secondly, the ionic radius of Ag^+ (126 pm) is much larger than that of Ti^{4+} (68 pm) and as such it is widely accepted that Ag does not enter the TiO_2 crystal lattice but exists on the surface of the crystal.[129,130,230] Silver particles on the TiO_2 surface will also act as nucleation sites, lowering the anatase to rutile transformation temperature. Also, silver modification of TiO_2 is reported to cause an increase in oxygen vacancies.[231,232] Silver was introduced as the Ag^+ ion but in the presence of heat the Ag^+ ions will be reduced to Ag^0. To facilitate the reduction of Ag charge compensation from the TiO_2 crystal occurs and oxygen vacancies are created. An increase in oxygen vacancies facilitates the atomic structural rearrangement associated with the anatase to rutile transformation through destabilisation of the metal oxide crystal structure by bond rupture and ionic movement.

Many researchers have focused on modifying TiO_2 with Ag. For example, Kuo *et al* showed through X-ray diffraction (XRD) and X-ray photoelectron spectroscopy (XPS) that silver on TiO_2 surface coatings was easily oxidised into silver oxide (Ag_2O) and that the addition of silver causes a reduction in photoluminescence intensity as found by photoluminescence (PL) spectroscopy.[93] Gunawan *et al* reported enhanced antimicrobial activity of Ag-TiO_2 and a reversible photoswitching between Ag^+ and Ag^0

depending on the excitation wavelength.[230] This group previously showed enhanced visible light photocatalysis with Ag modified TiO_2[130] and as mentioned previously, Chao *et al* discussed the effect of silver on TiO_2 phase transformation relative to the formation of silver on the crystal surface. However, this research focuses on the effect silver has on the early stages of the sol-gel TiO_2 synthesis. Similar to the previous chapter, the extent of chelation of the formate group to the titanium metal centre will be investigated.

The current chapter reports a systematic study on how the addition of increasing amounts of silver affects the extent of chelation of a formate group to a titanium precursor and how the resulting reduction in formate chelation causes early transformation of anatase to rutile. The effect of the addition of silver on structural changes is investigated by characterising the sample in its amorphous state (*i.e.* before it is calcined) with XPS, IR and Raman. X-ray diffraction (XRD) was used to determine the crystalline phase of the calcined samples and DSC was employed to examine the thermal events of the sample. The effect of silver on the electronic transitions of crystalline TiO_2 is shown through UV-vis spectroscopy.

4.2 Results and Discussion

4.2.1 X-ray diffraction

X-ray diffraction was carried out on the calcined samples in order to determine the crystalline phase of the samples. All samples calcined at 300 °C were amorphous. Crystalline anatase TiO_2 was present for all samples calcined at 500 and 600 °C. However, at 700 °C the diffractogram (figure 4.1) showed that 5 mol % Ag TiO_2 contained both anatase (46 %) and rutile (54 %), but TiO_2 without silver consisted mainly of anatase (95 %). This indicated that the presence of increased amounts of silver promotes the anatase to rutile transformation.

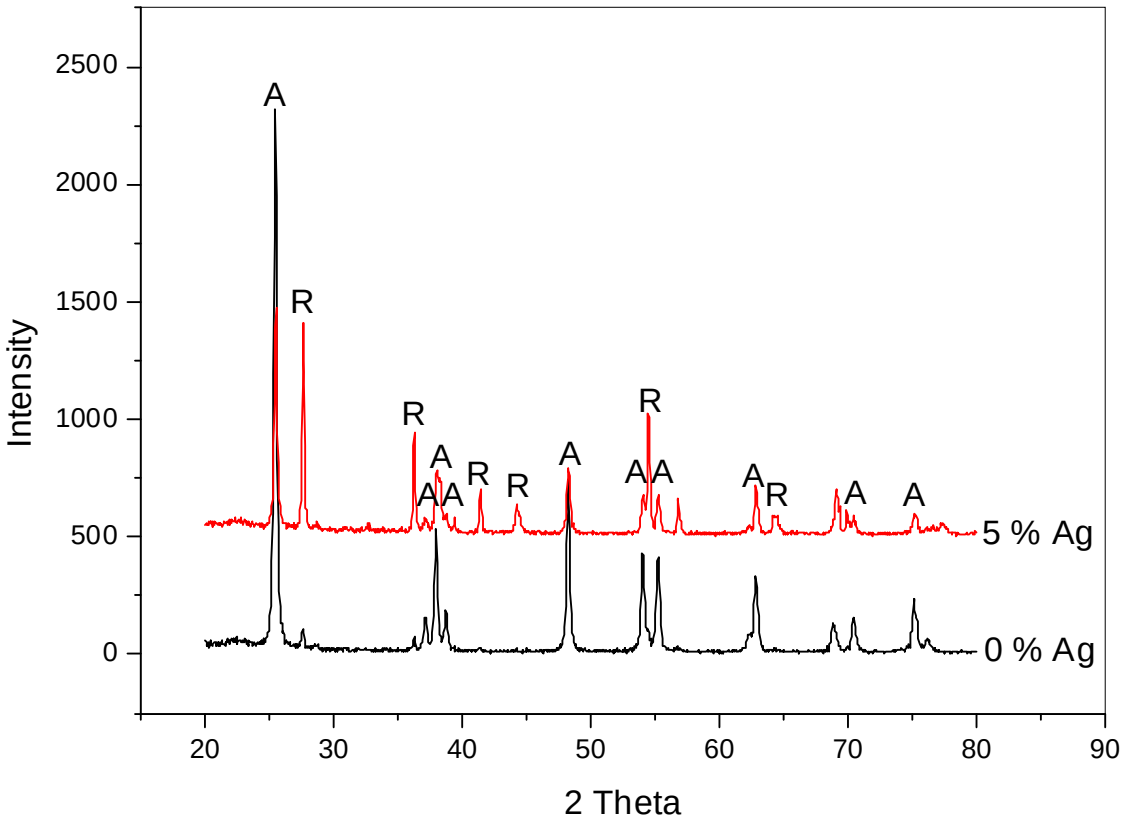

Figure 4.1. XRD of 0 % and 5 % Ag-TiO_2 powders calcined at 700 °C

At 800 °C the un-doped TiO_2 sample consisted of both anatase (55 %) and rutile (45 %), whereas the silver doped samples were all 100 % rutile (figure 4.2). A higher Ag concentration promotes earlier phase transformation. Figures 4.1 and 4.2 show that the presence of silver promotes the formation of rutile.[129]

Promotion of phase transformation by the addition of silver is believed to be caused by the following factors.[129] Decreasing anatase grain size (figure 4.3) results in an increase in the total boundary energy for the TiO_2 powder. The driving force for rutile grain growth is therefore increased, which promotes anatase to rutile phase transformation.[233] As the transformation of anatase to rutile is a mechanism of nucleation and growth,[55,56] an increased amount of nucleation sites would favour rutile formation. Phase transformation is also governed by such effects as defect concentration[40] and grain boundary concentration,[58] the presence of which can be expected to be increased with greater surface areas. Rutile nucleation is thus enhanced as the presence of defect sites is increased. Therefore, an increase in the

number of defect sites promotes anatase to rutile transformation at lower temperatures.[129]

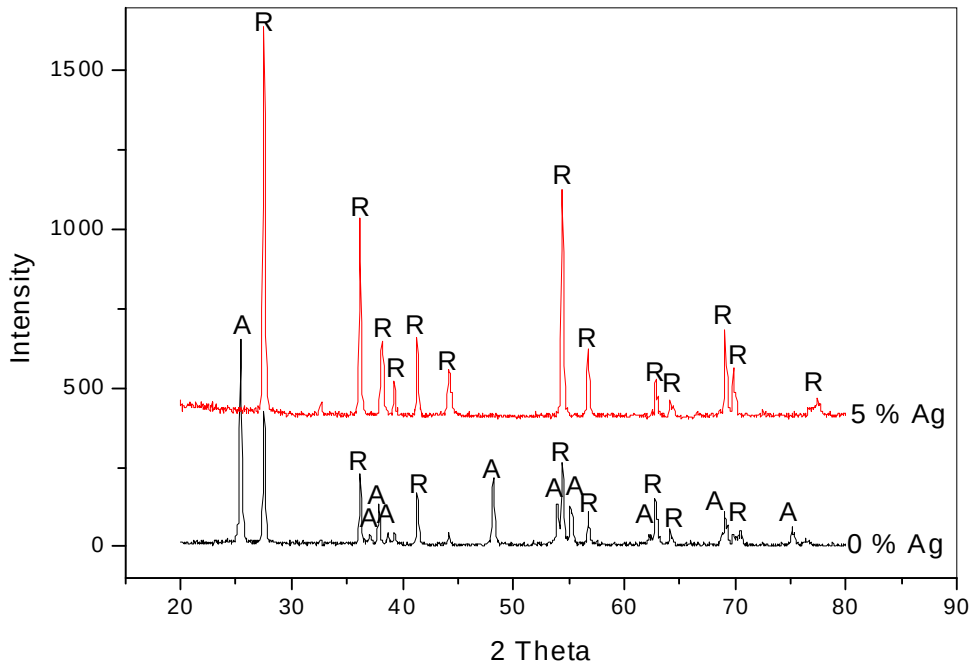

Figure 4.2. XRD of 0 % and 5 % Ag TiO_2 powders calcined at 800 °C

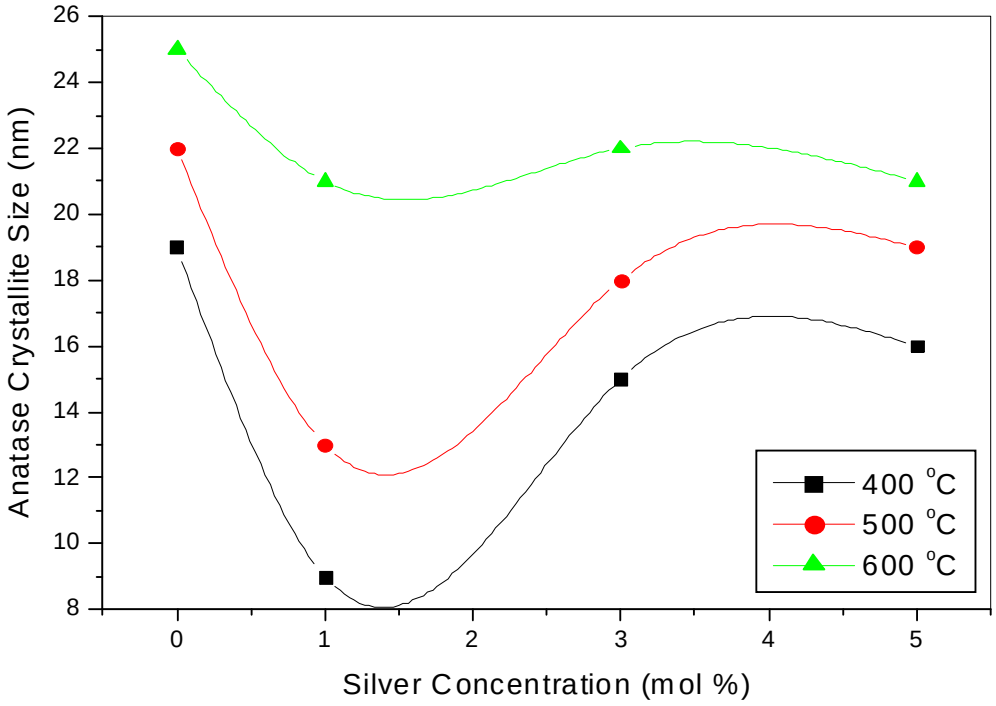

Figure 4.3. Variation in the nanocrystallite size (from XRD) as a function of increase in concentration of silver, at different calcination temperatures

The radius of Ag^+ ion (126 pm) is much larger than that of Ti^{4+} ion (68 pm) and so Ag^+ ions introduced during the sol-gel synthesis cannot enter the lattice of the anatase TiO_2

grains during crystallisation of the metal oxide network.[129,130] Migration of the Ag^+ ions to the crystal surface will also occur during calcination.[129,130] Metallic and ionic silver on the particle surface will serve as further sites where nucleation for rutile formation can occur. Oxygen vacancies may also influence the anatase to rutile transformation.[129,231,232] Previous reports[231,232] indicate that the concentration of oxygen vacancies at the surface of anatase increases with Ag doping. This favours the ionic rearrangement necessary for the structure changes associated with rutile phase formation.[129]

Ionic silver has a relatively high redox potential (-1.8 V NHE),[234,235] as such, the Ag^+ ion can be reduced to Ag^0 through both heat and possibly photo reduction. [236,237] To facilitate the reduction of Ag^+, oxygen vacancies will occur due to a charge compensation caused by Ag^+ reduction, again these oxygen vacancies are favoured for the formation of rutile.[129,231,232] To further investigate the role silver plays in altering the transformation temperature of TiO_2 in this study, it is necessary to understand the structure of the oligomer before calcination. In order to gain insight on this, DSC, IR, Raman and XPS were carried out on the powders before calcination.

4.2.2 Infrared spectroscopy.

The influence of silver on the structure of the Ti – O powders was investigated before calcination using IR and Raman spectroscopy. Figure 4.4 shows IR spectra of the doped and un-doped powders. Symmetric and asymmetric COO^- stretches at ~1360 and 1540 cm^{-1} respectively indicated that the formic acid forms a bidentate bridge with the titanium precursor.[178,214,217,239]

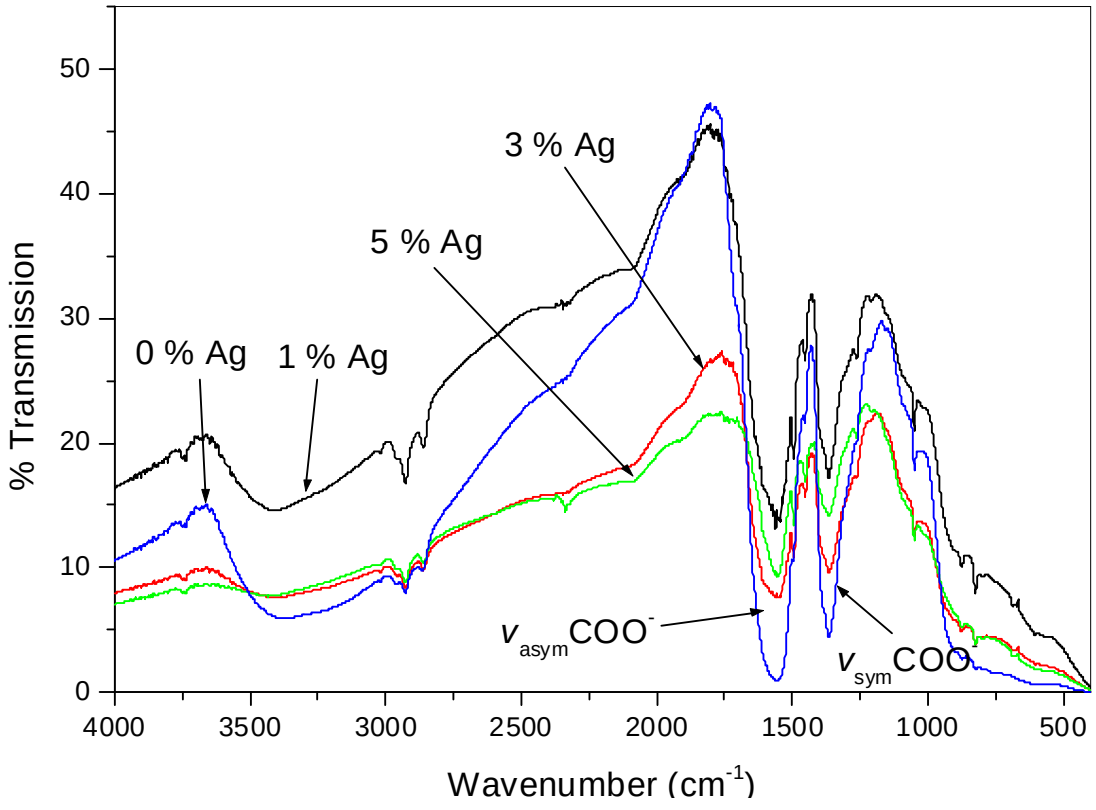

Figure 4.4. IR spectra of TiO_2 powders with different mol % silver content after aging at 100 °C

Figure 4.4 also shows that silver clearly reduces the intensity of the COO^- stretches as with each increase in Ag concentration there is a reduction in intensity of both the asymmetric and symmetric COO^- peaks. This result provides evidence for an alternative mechanism to those stated above, for early anatase to rutile transformation in the presence of silver as will be further discussed throughout the chapter. In fact, silver may influence the anatase to rutile transformation through interactions with the titanium precursor in the early stages of the sol-gel synthesis. These interactions may ultimately alter the condensation pathway, resulting in a weakened TiO_2 oligomer network.

To compare the effects of ageing at 100 °C, IR spectra of samples 0 and 5 mol % silver TiO_2 were recorded before and after aging (figures 4.5 & 4.6).

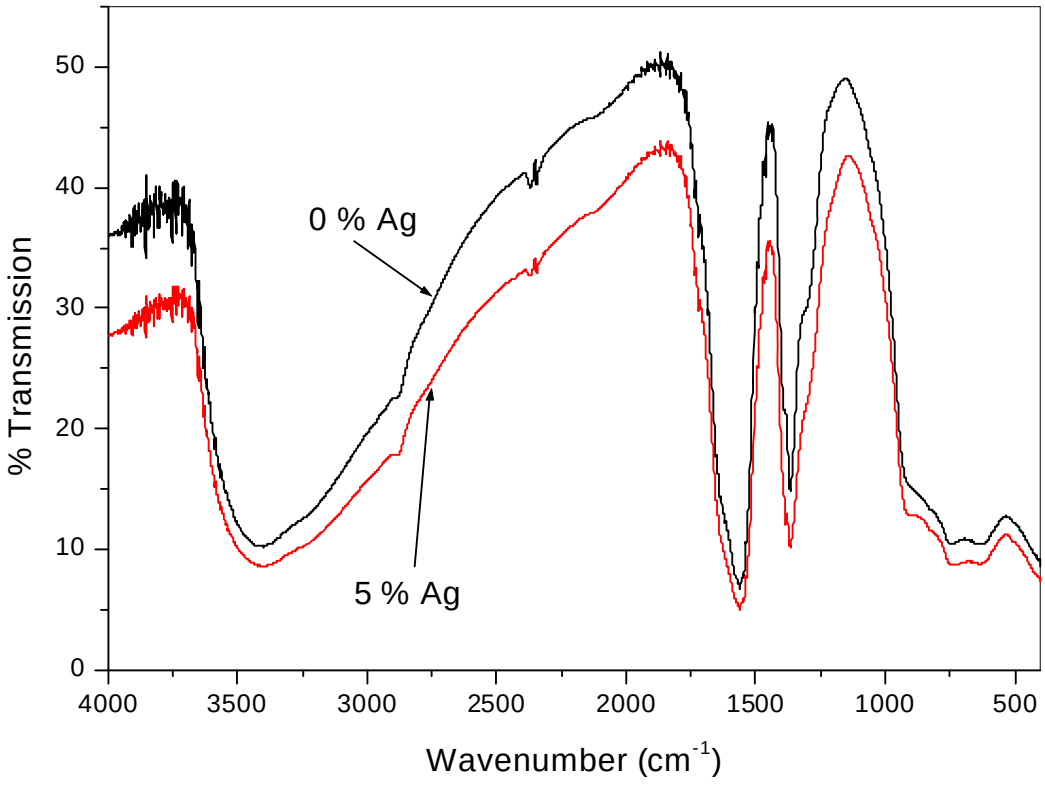

Figure 4.5. IR spectra of TiO_2 powders with different mol % silver content before aging

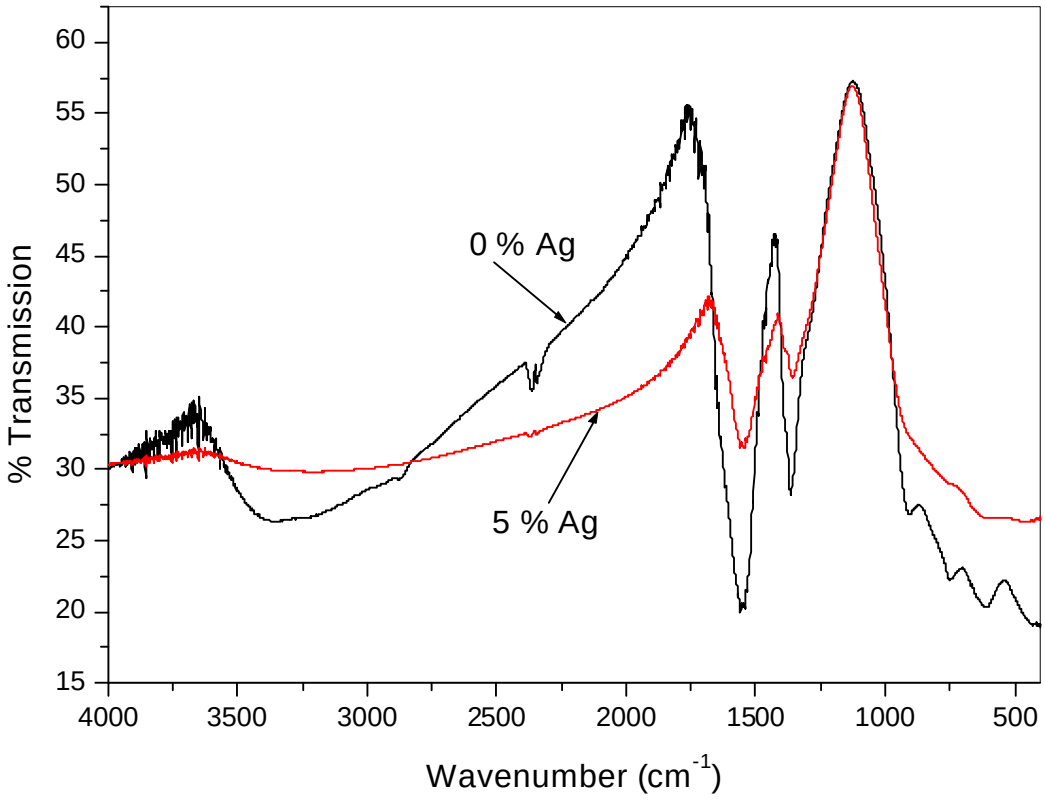

Figure 4.6. IR spectra of TiO_2 powders with different mol % silver content after aging at 100 °C for 12 hr

After both samples are aged at 100 °C for 12 hours there is a significant reduction in the bridging formate COO^- stretches of the 5 % silver doped sample whereas the TiO_2 sample without silver does not show a significant reduction in the carboxylate stretches. Since the boiling point of formic acid is 101 °C it is possible that the formic acid is displaced by the presence of silver and is then evaporated upon aging.

4.2.3 Raman spectroscopy

Raman spectroscopy analysis was carried out on the powders before they were calcined to support infrared spectroscopy results.

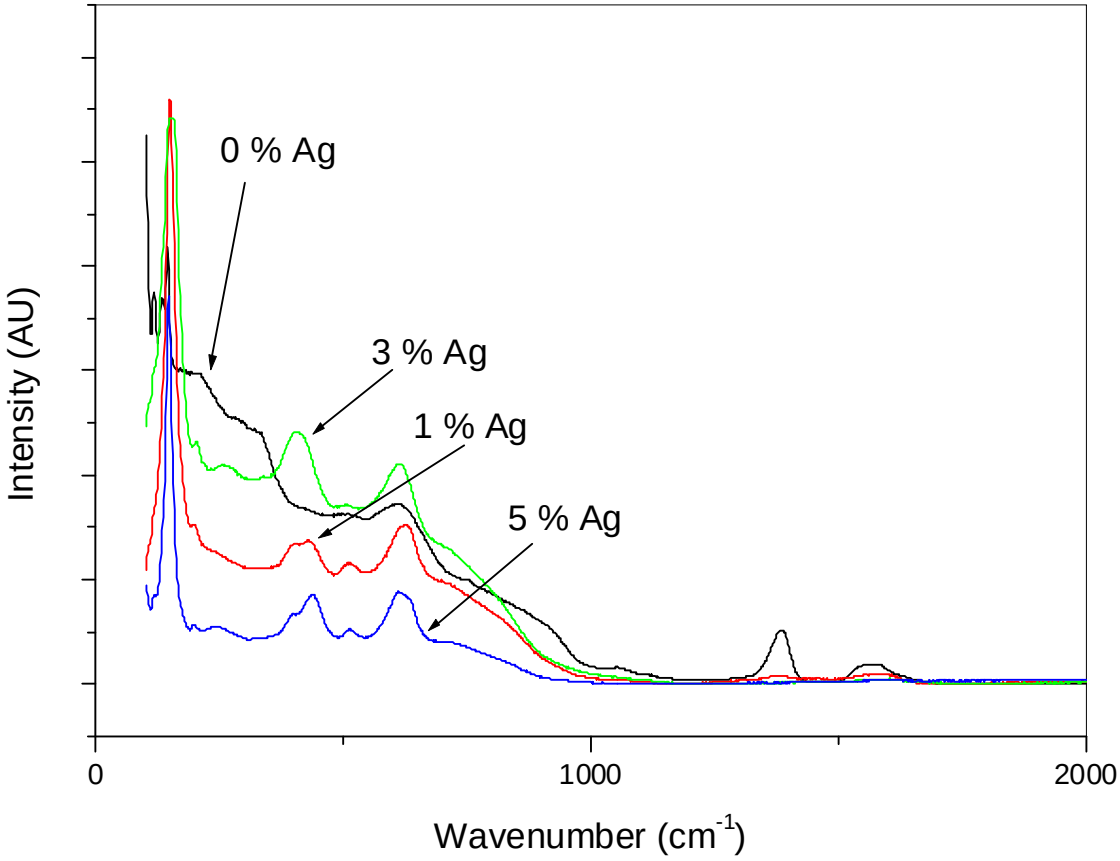

Figure 4.7. Raman spectra of TiO_2 powders with different mol % silver content before calcination

The Raman spectra of the doped and un-doped TiO_2 samples, (figure 4.7) support the observation deduced from the IR results. As the silver content is increased, the asymmetric and symmetric COO^- stretches (1570 and 1390 cm^{-1}) decrease accordingly. The addition of silver also causes significant changes in the Ti – O region

of the spectra (0 – 1000 cm^{-1}). The presence of peaks at 160, 420, 515 and 620 cm^{-1} in the Raman of the silver doped TiO_2 are indicative of the four peak pattern that would be expected for anatase.[222-224] However, without the presence of silver, this four peak pattern is not as distinctive. This provides further evidence that silver affects the titanium-formate complex before crystallisation has occurred.

It is agreed that the use of a chelating agent gives stability to the hydrolysis and condensation reactions associated with the sol-gel process in the production of TiO_2 from titanium alkoxides.[172,200-204] IR and Raman spectroscopy have shown that formic acid forms a bridging ligand with titania.[210,212-215] Previous reports have shown that similar chelating agents remain bound to the central titanium atom while the iso-propoxy (OR) groups are preferentially hydrolysed. The bridging ligands remain throughout much of the condensation process,[172,207] altering the condensation pathway and promoting the formation of linear polymers composed of edge sharing octahedral.[207,220] The system may be destabilised through the addition of water, which leads to a structurally weak network that can easily collapse upon calcination to form rutile.[48,217]

From the vibrational spectroscopy results it can be seen that the addition of silver causes a reduction in the intensity of the COO^- stretches indicating that the titania – formate bridging complex is becoming weaker in the presence of silver. This may lead to a structurally weak oligomer that upon calcination easily forms rutile at lower temperatures.

4.2.4 Differential scanning calorimetry

Differential scanning calorimetry was carried out to investigate the thermal events associated with the doped and undoped TiO_2 samples before and after aging.

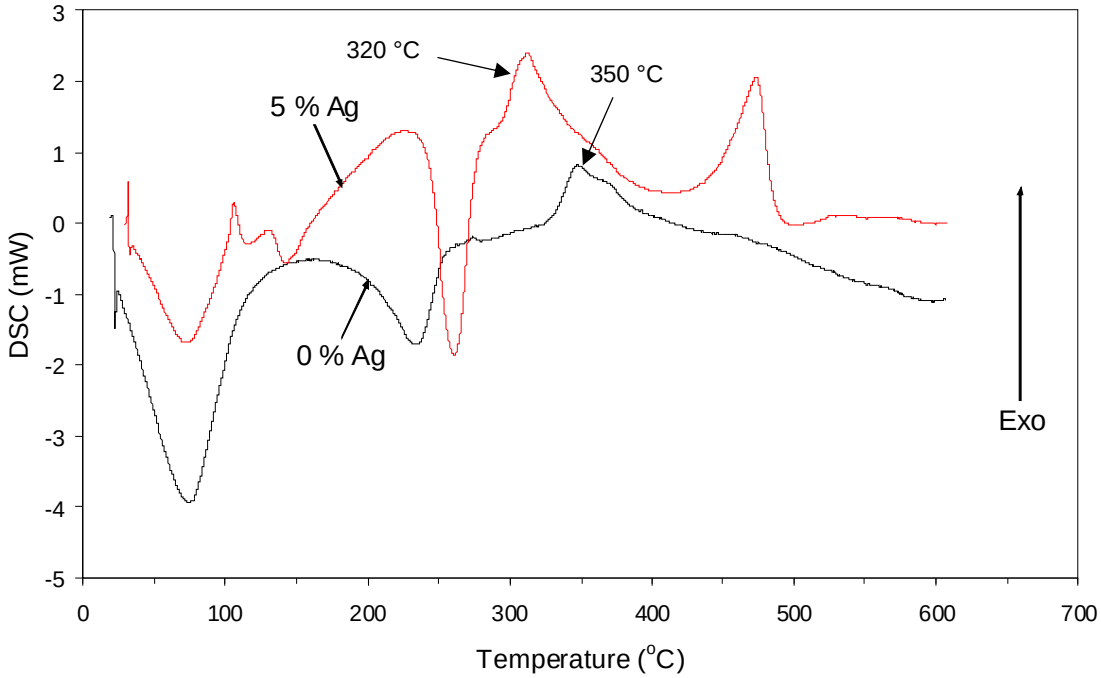

Figure 4.8. DSC of 0 and 5 % Ag before ageing

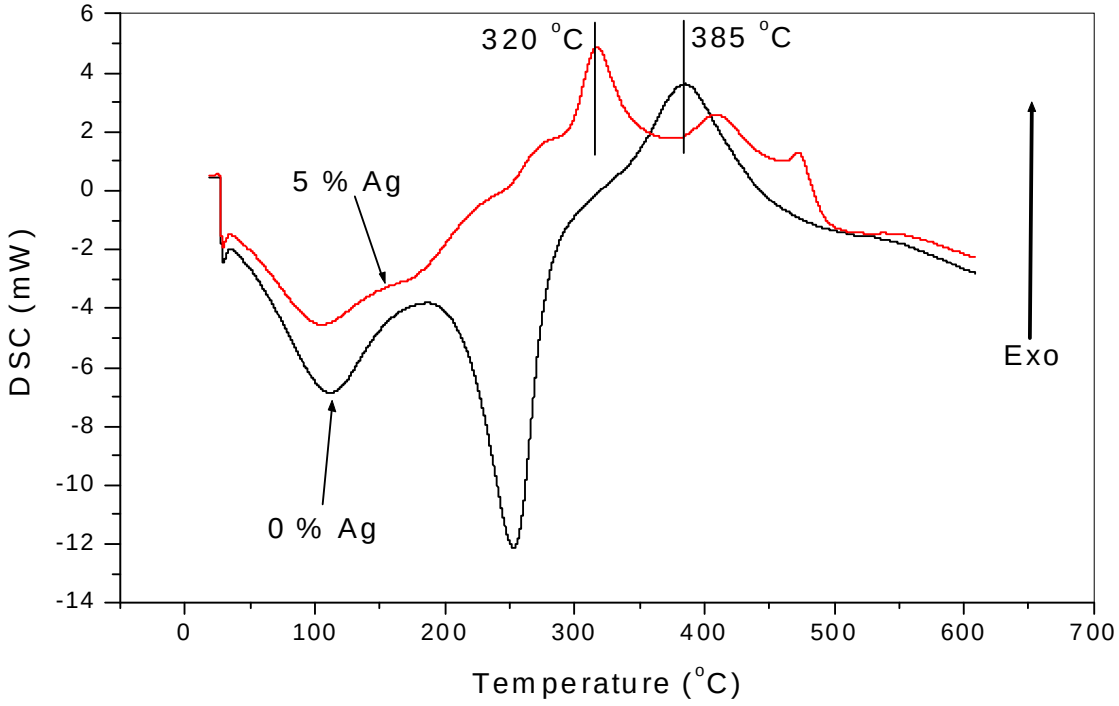

Figure 4.9. DSC of 0 and 5 % Ag after ageing at 100 °C

The DSC curve of the un-doped TiO_2 powder analysed before ageing (figure 4.8) is almost identical to the same sample after ageing (figure 4.9). It reveals an endothermic peak at ~ 100 °C attributed to the elimination of unbound water and formic acid from the surface of the TiO_2 powder. The same peak for the silver doped sample reveals, as expected, a smaller enthalpy of -420 J/g compared with -636 J/g for the undoped sample, indicating that formic acid is easier to remove in the presence of silver. This is in agreement with the previously proposed mechanism from the FTIR and Raman spectroscopy results, that silver inhibits formic acid and it is thus removed upon ageing at 100 °C therefore, allowing the oligomer structure to readily collapse and form rutile upon calcination.

In figures 4.8 and 4.9 an endothermic peak at ~ 250 °C is due to the removal of isopropanol formed through the condensation step. The removal of isopropanol indicates that the condensation step is complete. Comparing the DSC curves of the samples before (figure 4.8) and after (figure 4.9) aging shows that the endothermic isopropanol peak is present in both the 0 and 5 mol % silver sample before aging. But after aging the isopropanol peak at 250 °C is only present with 0 % Ag-TiO_2. This provides further explanation for the formation of rutile at lower temperatures, since when the condensation step is near completion, the crystallization temperature is lowered and then so too is the anatase to rutile transformation temperature.

The appearance of the first exothermic peak in all DSC curves is the transition from amorphous TiO_2 to crystalline anatase and as expected this peak occurs earlier with silver doped TiO_2 than with TiO_2 only. Figure 4.8 shows that crystallization occurs at 320 °C for 5 % Ag-TiO_2 but does not occur until 350 °C for the undoped sample. This can also be seen in figure 4.9 where crystallization of 5 % Ag-TiO_2 takes place at 320 °C but for the undoped sample crystallization does not occur until 385 °C.

4.2.5 X-ray photoelectron spectroscopy

To determine more information on exactly how silver is interacting with the titanium formate complex, XPS was carried out on the silver doped and undoped samples before calcination to establish the titanium structure, the chemical state of the silver particles and also for further evidence of the reduction in the carboxylate species. XPS spectra were recorded of the samples pre-calcination (as with IR and Raman) and XPS was also carried out on the crystalline titania after calcination. The spectra of C1s and O1s of TiO_2 without silver show the presence of the carboxylate group at 289.1[238] and 532.3 eV[238,239] respectively (figure 4.10 a & b). As the silver content is increased the intensity of these peaks decreases in a similar manner as those of the IR and Raman results, again indicating that with increased silver content, the formation of a titania-formate bridging complex becomes increasingly difficult to form.

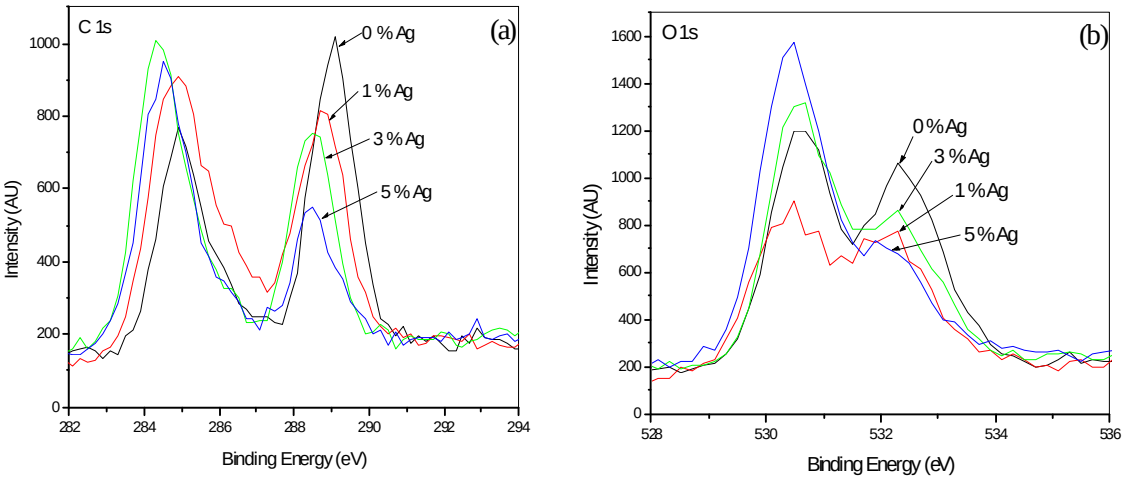

Figure 4.10. XPS spectra of C 1s (a) and O 1s (b) of TiO_2 with and without silver before calcination

Figure 4.11 shows the XPS narrow scans for Ti 2p and Ag 3d peaks. The XPS spectrum of Ti 2p is unchanged with increasing amounts of silver, the Ag 3d spectrum of 1 % silver TiO_2 gives a weaker signal than the 3 % shown in figure 4.11b and the Ag 3d scan of 5 % silver TiO_2 results in a spectrum similar to 3 % silver TiO_2. The fact that increasing amounts of silver does not affect the Ti 2p spectra indicates that central titanium atom has not been reduced. In figure 4.11a, a Ti 2p peak at 459.1 eV is

representative of Ti in its tetravalent state[240] in an octahedral environment.[241] The absence of a Ti^{3+} peak at 457.4 eV leads to the following observations.

Ti has not been reduced to Ti^{3+} which may indicate an absence of surface oxygen vacancies.[242] However, if TiO_n (n < 2) is formed it may not be present in detectable amounts.[243]

Ag_2O or Ag^0 incorporation into the TiO_2 lattice may give rise to a signal at 457.4 eV representative of Ti^{3+}.[93] From the XPS there was no evidence of Ag – TiO_2 bond formation, which can be expected due to the differences in atomic radius.

The Ag 3d scan (figure 4.11b) shows two large peaks. A Gaussian fit of the main peak (~368 eV) showed that it was made up of two signals at 367.9 and 368.2 eV, representing the chemical bonding states of Ag_2O and Ag^0 respectively.[93] Therefore, it has been shown that Ag^0 and Ag_2O have formed on the surface of the titania – formate complex, before heat treatment above 100 °C. Spectroscopic (FTIR, Raman and XPS) studies of the carbonyl species have shown a reduction in the titanium – formate bridging complex with increased amounts of silver.

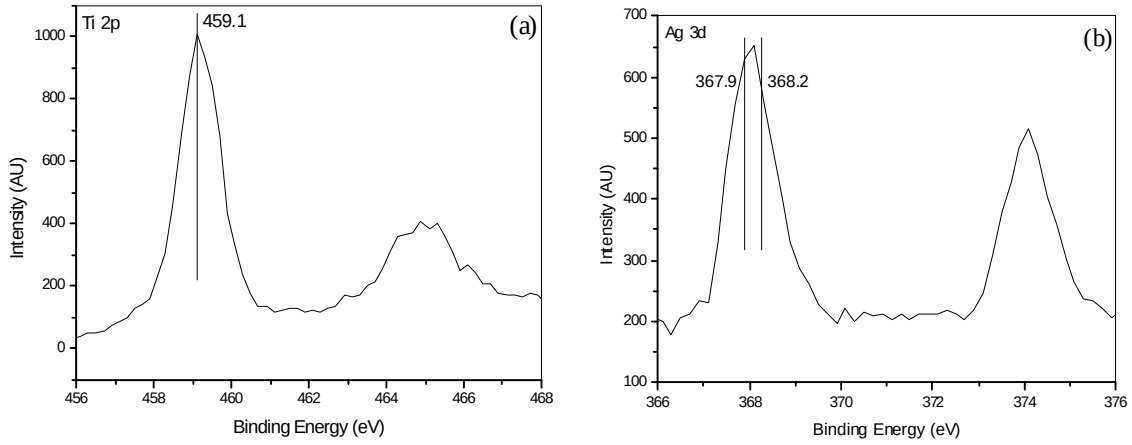

Figure 4.11. XPS spectra of Ti 2p (a) and Ag 3d (b) of 3 % Ag TiO_2 before calcination

The Ag 3d scan of a sample (before calcination) containing silver (figure 4.11b), shows the presence of Ag_2O (Ag^{2+}, 367.8eV) and Ag^0 (368.2 eV).[93] Therefore, the presence of Ag_2O and Ag^0 in the powders before calcination may be responsible for the reduction of the titanium – formate bridge as shown by IR, Raman and XPS. The presence of Ag_2O and Ag^0 may then restrict the formation of a titanium – formate bridging complex which

leads to an altered condensation pathway and therefore low temperature formation of rutile.

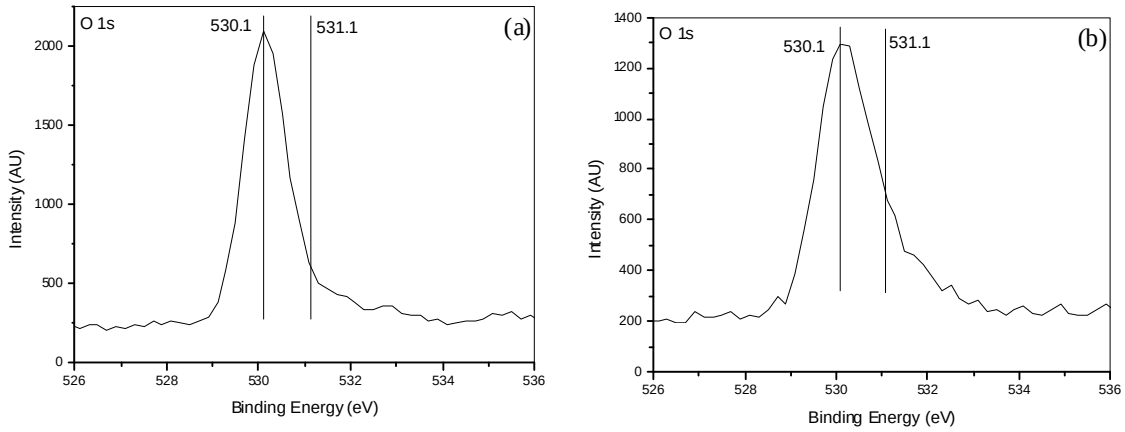

Figure 4.12. O 1s XPS spectra of TiO_2 without silver calcined at 900 °C (a) and with 3 % silver calcined at 700 °C (b)

Figure 4.12 shows the narrow scan XPS spectra for O 1s of TiO_2 only calcined at 900 °C and 3 % Ag TiO_2 calcined at 700 °C. Gaussian fits of both spectra give rise to two peaks at 530.1 and 531.1 eV for crystal lattice oxygen and hydroxy oxygen respectively.[241,244] The silver doped sample contains a greater amount of hydroxy oxygen. Chemisorbed surface hydroxyl groups can enhance photocatalysis by trapping photoinduced holes resulting in an increase in the formation of the highly oxidising $OH^{\bullet}$ radicals.[244,245]

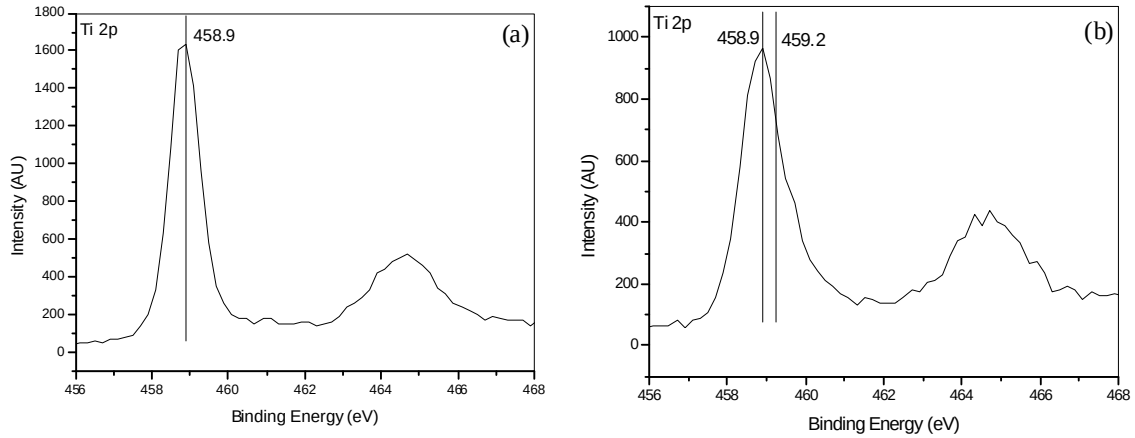

Figure 4.13. Ti 2p XPS spectra of TiO_2 without silver calcined at 900 °C (a) and with 3 % silver calcined at 700 °C (b)

It is well reported that silver retards the recombination of photogenerated electron hole pairs,[73,93,130] this may not only be due to the attraction of excited electrons to silver but also due to the presence of extra hydroxyl species to delay recombination through hole trapping.

There is an apparent difference between the Ti 2p spectra shown in figure 4.13. Unmodified TiO_2 gives a signal at 458.9 eV in the Ti 2p narrow scan. However, 3 % silver TiO_2 results in the presence of an additional signal at 459.2 eV. The un-doped sample after calcination at 900 °C gives a symmetrical peak at 458.9 eV (figure 4.13a) typical of tetravalent Ti-O bonds.[240] However, the Ti 2p narrow scan of the 3 % Ag TiO_2 sample calcined at 700 °C does not give a symmetrical peak. A Gaussian fit of the spectrum gives two signals at 458.9 and 459.2 eV both representing Ti-O[240] but the shift in the binding energy to 459.2 eV indicates that there may be an interaction between TiO_2 and silver.[230]

4.2.6 Proposed silver interaction

Through XPS, IR and Raman, it was shown that the addition of silver restricts the formation of a titanium – formate bridging complex. XPS also shows that silver exists as both Ag^0 and Ag_2O. Finally, XPS has shown that the presence of silver results in a peak being present at 459.2 eV in the Ti 2p scan (Figure 4.13b), which may be indicative of an interaction between TiO_2 and silver.[230] The combination of these results leads to the proposal of scheme 4.1. In scheme 4.1 it is proposed that Ag^0 and Ag_2O block the formation of the titanium – formate bridge. The resulting titanium complex can then collapse readily upon calcination to form rutile.

Scheme 4.1. Illustration of blocking mechanism of silver on titanium – formate bridge (suggested structure)

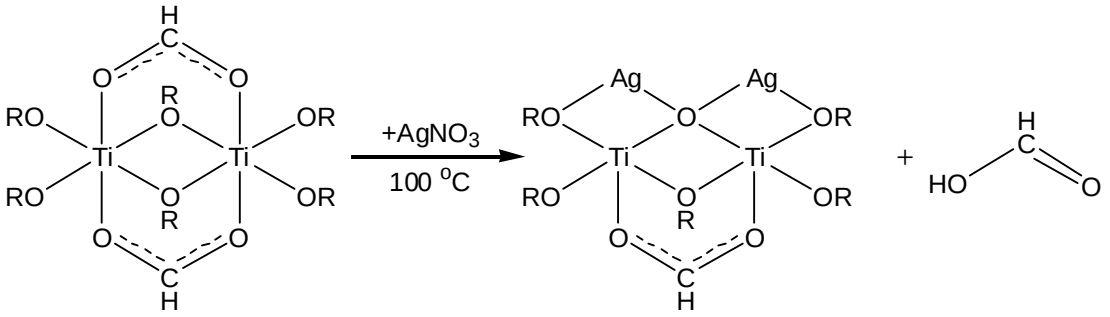

Gaussian fits of the narrow scan Ti 2p XPS spectra (appendix A) of all samples before calcination reveals two signals. The intensity of the signals accordingly varies with the increasing presence of silver, further indicating that Ag^0/AgO is interacting with titanium,[246] thus facilitating the removal of formate species and allowing for the collapse of the Ti-O gel framework upon calcination to form rutile at lower temperatures.

4.2.7 Diffuse reflectance spectroscopy

In order to estimate the band gap distance, UV-vis spectroscopy was employed. The results show that silver does improve visible light absorbance of TiO_2 due to silver plasmon absorption, moreover, a blue shift was observed for the band gap separation of the TiO_2 materials upon increased silver addition.

Figure 4.14 shows the diffuse reflectance spectra for 0, 1, 3 and 5 mol % Ag TiO_2. It can be seen that un-modified TiO_2 has a smaller band gap than the silver modified TiO_2. The blue shift of the silver modified materials can be attributed to the presence of additional silver.[247] The influence light absorption through silver is highlighted in the diffuse reflectance spectrum of silver (figure 4.15).

Figure 4.15 shows a diffuse reflectance spectrum of Ag nanoparticles (< 100 nm) where a strong absorbance is observed at ~335 nm. The band gap of the TiO_2 nanomaterials can therefore not be accurately determined because of the strong silver absorption.[248] It is also clear that the presence of increased amounts of silver (3 and 5 mol %) facilitates visible light absorbance. This can also be seen from figure 4.15 through strong visible light absorption of the silver nanoparticles. The proposed mechanism for the visible light absorbance of Ag – TiO_2 is shown in figure 4.16.[230]

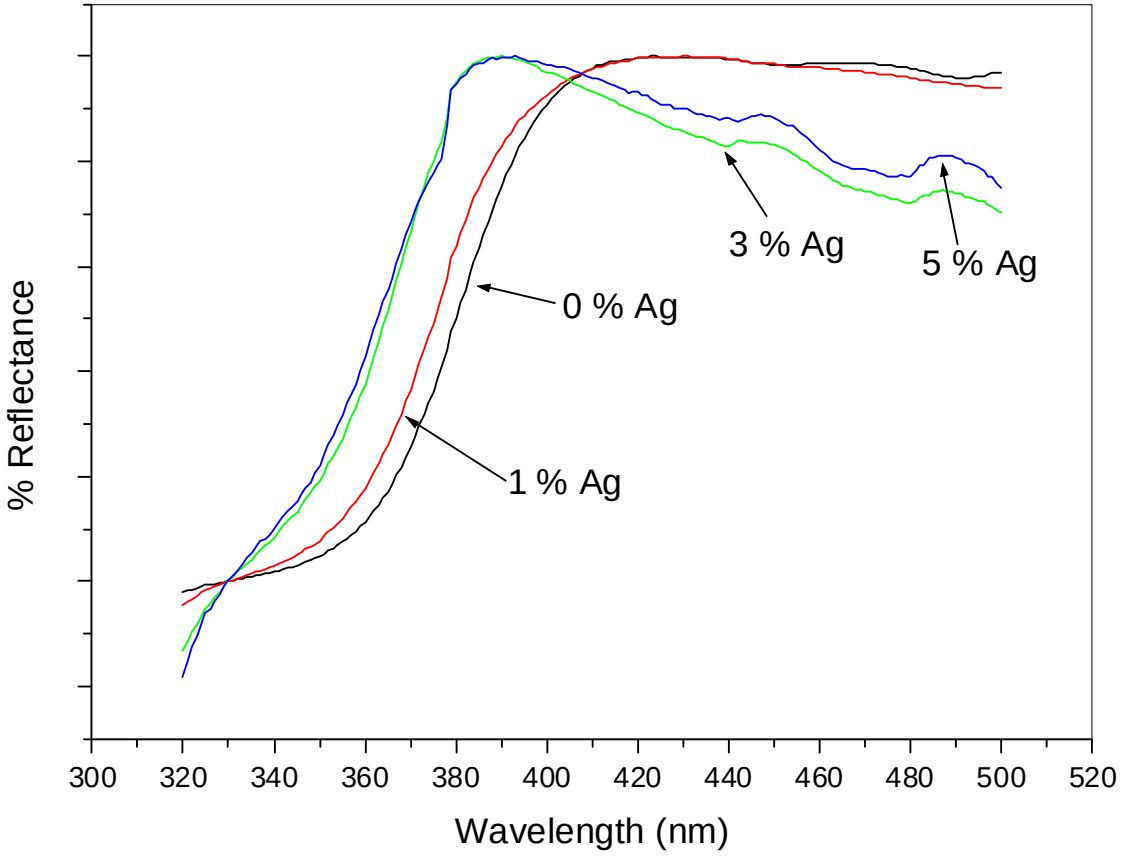

Figure 4.14. Diffuse reflectance spectra of 0, 1, 3 and 5 % Ag TiO_2 calcined at 500 °C

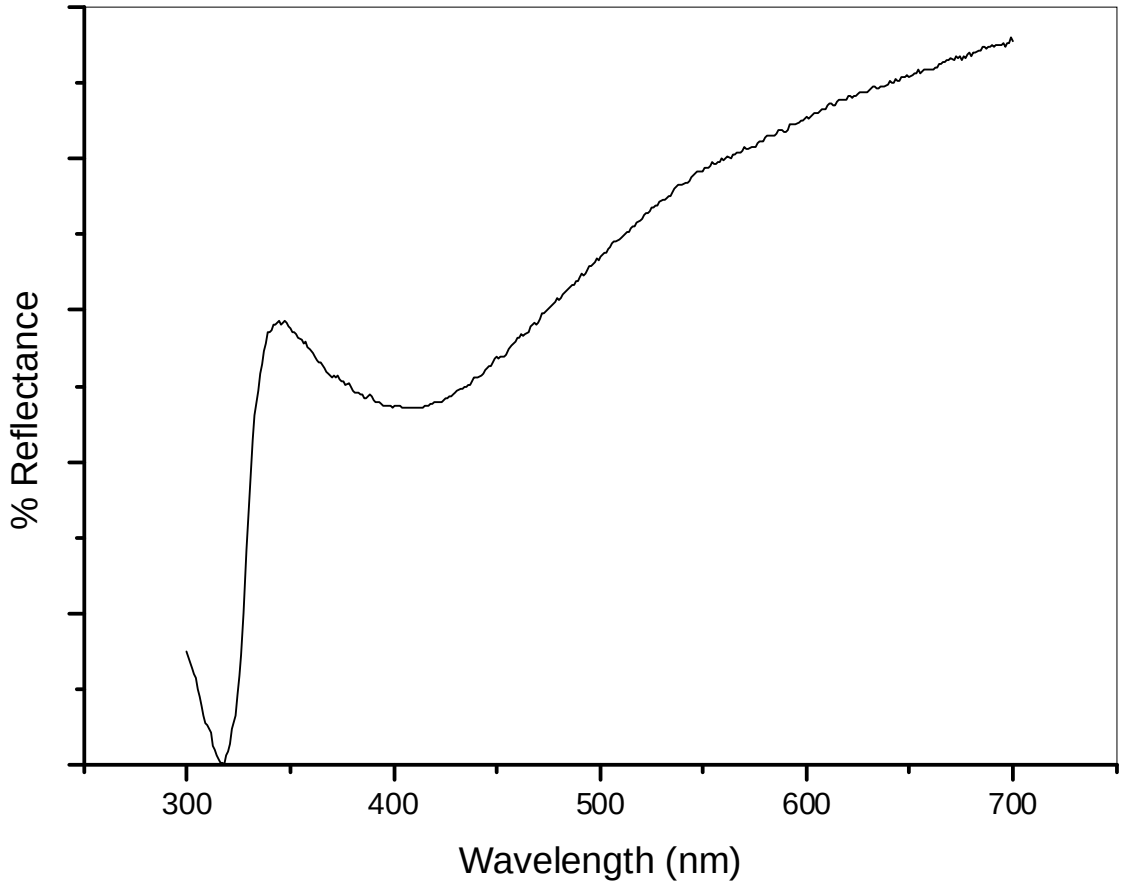

Figure 4.15. Diffuse reflectance spectrum of silver nanoparticles (< 100 nm)

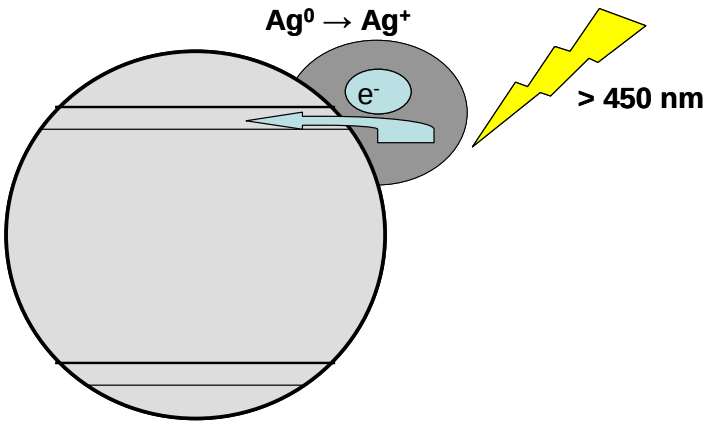

Figure 4.16. Mechanism for light absorption

It can also be seen in both figures 4.14 and 4.17 that 3 mol % silver TiO_2 has greater absorption than 5 mol % Ag in the visible region. This is because increased levels of silver act as a physical block against TiO_2 light absorption. This causes an increase in the diffuse light reflectance of the material. [130]

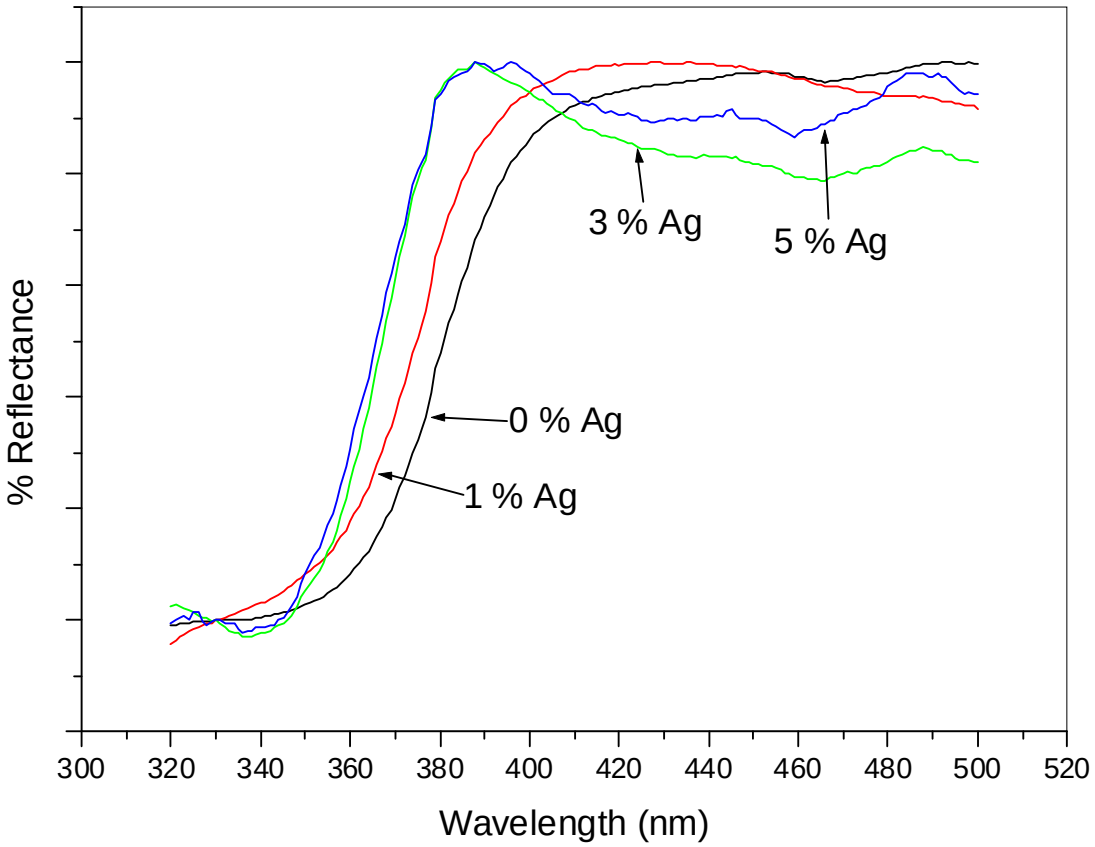

Figure 4.17. Diffuse reflectance spectra of 0, 1, 3 and 5 % Ag TiO_2 calcined at 700 °C

In figure 4.18 it is observed that the band gap of the modified TiO_2 is reduced, as seen by the red shift in the spectra of the 3 and 5 mol % Ag TiO_2 in comparison with figures 4.14 and 4.17. This is attributed to the formation of rutile. Rutile has a smaller band gap than anatase,[7] XRD results confirm that silver doped samples calcined at 800 °C have rutile structure (figure 4.3). Comparing figure 4.18 with figures 4.14 and 4.17, silver does not have the same influence in causing the blue shift. As discussed earlier, the mechanism of anatase to rutile transformation is one of nucleation and growth, [55,56] therefore, rutile particles are significantly larger than those of anatase. The larger particles may result in a significant reduction in the influence of silver on the band gap of the materials.

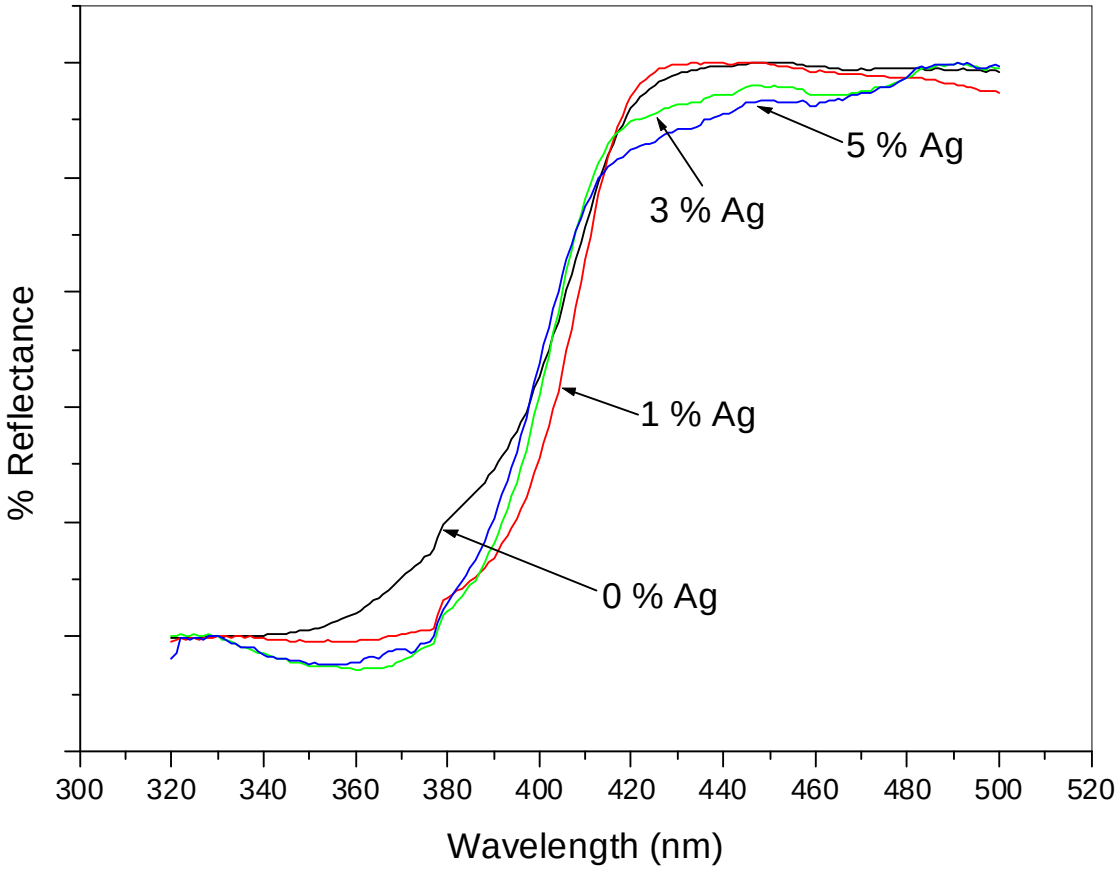

Figure 4.18. Diffuse reflectance spectra of 0, 1, 3 and 5 % Ag TiO_2 calcined at 800 °C

4.2.8 FESEM and EDX

Field emission scanning electron microscopy (FESEM) and energy dispersive X-ray spectroscopy (EDX) was carried out on the TiO_2 samples with 5 mol % silver loading calcined at 700 and 800 °C.

Figure 4.19 shows the electron micrograph of 5 % Ag-TiO_2 calcined at 700 °C. Combining EDX spectroscopy (appendix B) with the image shown in figure 4.19 it was determined that metallic silver is evenly dispersed on the surface of the TiO_2 particles. It was determined from XRD that the sample is a mixture of anatase (46 %) and rutile (54 %) and crystal sizes determined from XRD and the Scherrer equation were 35 nm for anatase and 52 nm for rutile. From the FESEM micrograph it is clear that both small (50 nm) and large particles (100 nm) are present in the sample area. The clusters (~ 10 nm) spread throughout the surface of the larger TiO_2 particles are believed to be metallic silver nanoparticles.

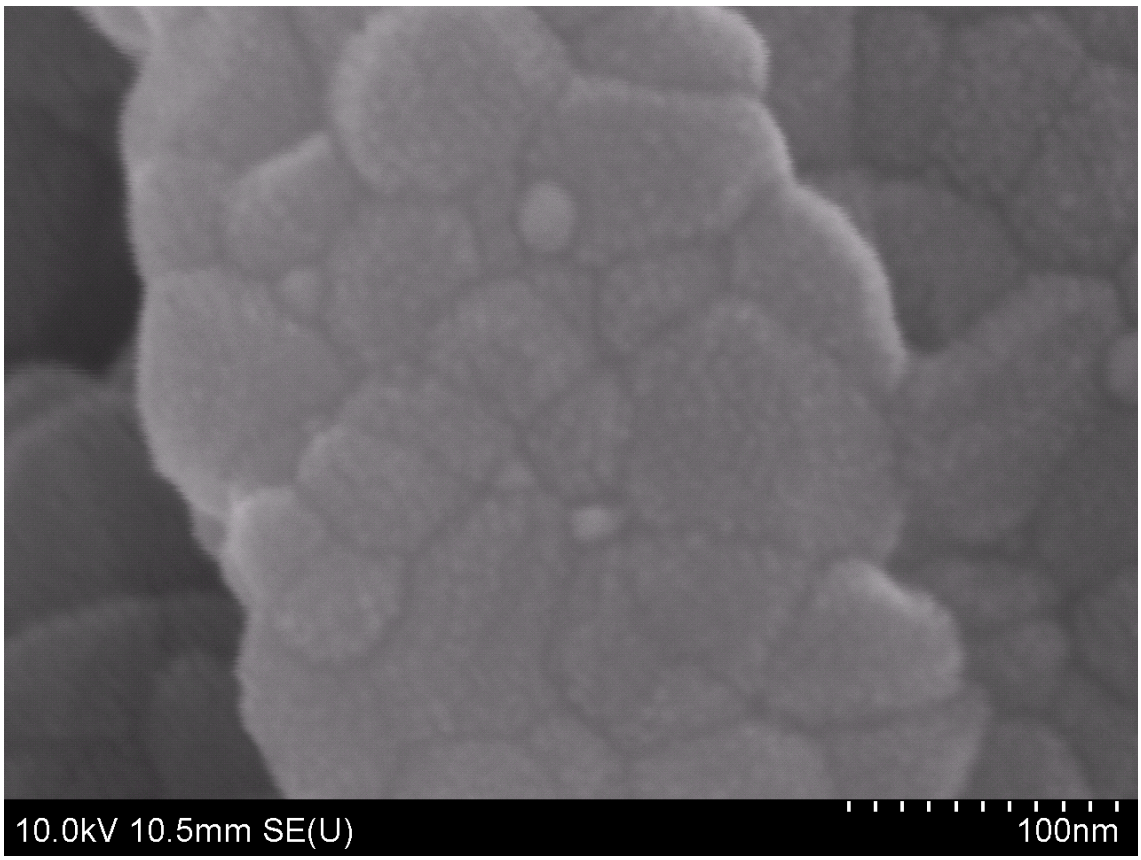

Figure 4.19. FESEM image of 5 % Ag-TiO_2 calcined at 700 °C

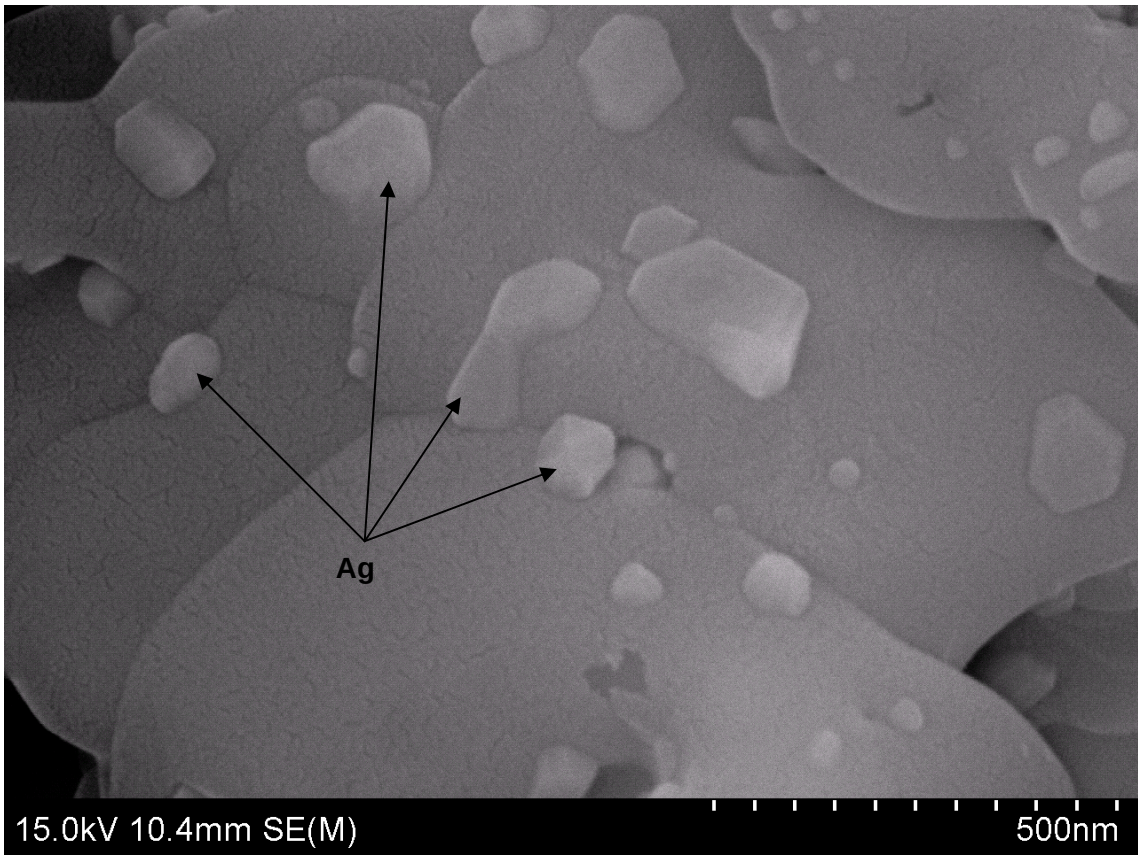

Figure 4.20. FESEM image of 5 % Ag-TiO_2 calcined at 800 °C

As the calcination temperature was increased to 800 °C, total transformation from anatase to rutile occurred. Rutile crystal sizes of ~ 50 nm were recorded using the Scherrer equation but the electron micrograph (figure 4.20) did not resolve single rutile crystals possibly due to increased agglomeration of the rutile crystals to form larger particles (200 nm – 1 μm) as seen from the FESEM analysis area. EDX analysis (appendix B) of the image shown in figure 4.20 revealed that agglomeration had not only occurred for the TiO_2 crystals but the silver nanoparticles had also combined to form larger silver particles (~ 50 – 200 nm) as highlighted in figure 4.20.

4.3 Conclusions

A systematic study of the effect of silver on the anatase to rutile transformation temperature of TiO_2 has been carried out. Using XRD, FTIR, Raman, DSC and XPS it was proposed that the addition of silver blocks the formation of a titanium – carboxylate bridging ligand. This was clearly shown by monitoring the carboxylate stretches in FTIR, Raman and XPS. Without the formation of this bridging ligand the condensation pathway is altered and the resulting titania polymer network is weakened. When calcined, this weakened structure can readily transform from anatase to rutile due to a greater atomic mobility. The sample with no silver present, maintained anatase at greater temperatures than those that contained silver. This was due to the formation of a strong carboxylate bridge that promoted a more organised structure throughout the condensation process. The more ordered oligomer network of the sample without silver consisted of anatase at greater temperatures than those where silver was present. This was clearly seen from the XRD diffractograms. Previous reports have indicated that oxygen vacancies contribute to the early formation of rutile, but through XPS, it was concluded that the presence of additional silver did not form extra oxygen vacancies. XPS also showed that Ag_2O and Ag^0 were present in the samples before high temperature calcination. It was also showed through XPS that there may be an interaction between Ag and Ti, which agrees with the proposed mechanism outlined in scheme 4.1.

Through diffuse reflectance spectra it could be seen that the addition of silver promotes visible light absorbance through surface plasmon resonance arising from light interactions with the silver nanoparticles.

An alternative mechanism has been proposed on how silver affects the anatase to rutile transition of TiO_2. In the proposed mechanism, silver blocks the formation of a bridging ligand with the titanium alkoxide precursor. This is clearly shown in FTIR, Raman and XPS spectra and the resulting lower formation of rutile is clear from XRD and DSC.

5 Optimisation of a TiO_2 Photocatalyst through the Addition of Aluminium, Silver, Nitrogen and Sulfur

5.1 Introduction

The work in this chapter began with the aim of synthesising visible light active anatase that is stable at increased temperatures. From the previous two chapters, the effect that the early synthesis conditions have on the anatase to rutile transformation temperature has clearly been shown through the chelation of formic acid. Using this knowledge as well as what is known from the literature, it may be possible to develop anatase that is stable at increased temperatures and is also photocatalytically active under visible light irradiation.

As well as having an understanding of how chelation affects the anatase to rutile transformation temperature, it is well understood that the addition of aluminium may stabilise TiO_2 as anatase at increased temperatures. It is necessary to synthesise TiO_2 anatase that remains stable at high temperatures for applications such as catalysis and ceramics.[249] The addition of aluminium has shown promising results by increasing the anatase to rutile transformation temperature above 1000 °C.[250,251] Despite the addition of aluminium extending the anatase to rutile transformation temperature, negative effects on photocatalytic activity have been widely reported.[89,110]

As mentioned previously, the photocatalytic efficiency of TiO_2 is limited by its wide band gap (3.2 eV). In order to improve the efficiency of the light absorbing molecule it is necessary to decrease the band gap to allow for absorption of photons from the visible light spectrum (> 400 nm). This can be achieved through a number of methods. Non-metal dopants have given the most promise and the best performers include N, F, C and S.[252-254] Asahi *et al* reported visible light activated TiO_2 through N-doping.[252] Although N-doped TiO_2 has clearly been shown to be visible light active; the mechanism through which the red shift occurs is still under debate. Asahi concluded that N atoms replaced O in the anatase crystal lattice and a mixture of N 2p and O 2p bands caused band gap reduction.[252,255] Oxygen vacancies were also believed to cause visible light absorption and Ihara *et al* believed that the addition of N stabilised these oxygen vacancies[256] which was also supported by Martyanov *et al*.[257] In

contrast, several authors have proposed that N doping results in the formation of localized N 2p energy levels, existing just above the valence band of the semiconductor[258-260] which seems to now be the accepted mechanism for N doped visible light photocatalysis.

Sulfur doped TiO_2 has also shown promising results in terms of visible light absorption. However, there is also some debate about the nature of how the S atoms interact with the TiO_2. For example Umebayashi *et al*[30-32] used ion implantation to produce S-TiO_2 photocatalyst. It was indicated that S is doped in TiO_2 as an anion and replaces lattice oxygen in TiO_2. However, Ohno *et al*[261-263] found that S is incorporated as S^{4+} cations and replaced Ti ions in TiO_2. Secondly, it was indicated that the photocatalytic activities of the cation doped TiO_2 photocatalyst decreased even in the UV region because the doped oxides suffer from a thermal instability or an increase in the carrier recombination centres. The non-metallic ion doping may destroy the electric charge balance of the system and an oxygen vacancy is produced in the crystal lattice. The oxygen vacancy can become an electron-hole recombination centre.[264,265] Recently, it was reported that using the different cation co-doping or anion-cation co-doping may further expand the photoabsorption region of the TiO_2 photocatalyst and enhance its activity. Wang *et al*[265] incorporated S into TiO_2 with a simple sol-gel method in mild conditions using tetrabutyl titanate as the Ti precursor and thiourea as the S precursor. They demonstrated that in the S-TiO_2 photocatalysts prepared, some of S atoms exist on the crystal surface as S^{4+} and S^{6+} cations, which replace the Ti ions on the crystal surface and other S atoms enter into the crystal lattice of TiO_2 as S^{2-}, which replace the lattice oxygen in the inner crystal lattice of TiO_2 giving higher photocatalytic activity than that of pure TiO_2.[265] Ohno *et al*[262] reports S cation doped TiO_2 that are expected to replace Ti ions. This S doped TiO_2 absorbs visible light more strongly than N, C and the S anion-doped TiO_2 to show visible light photocatalytic activity.

Improvements in photocatalytic activity have also been shown through the addition of transition metals. New energy levels between the valence and conduction bands were believed to be introduced through the addition of Fe^{3+}.[121,282-285] The noble metals (Ag,

Au, Pt and Pd) also show enhanced activity by acting as electron traps for light promoted electrons, thereby reducing recombination rates.[113-117]

Combinations of non metal atoms into TiO_2 has also attracted considerable interest of late. Li *et al* found that N-F-codoped TiO_2 was more effective than either N or F alone.[266] Improved visible light activity has also been reported with C-N-TiO_2,[267] C-S-TiO_2[268] and C-N-S-TiO_2.[37,269]

In this chapter, the effects of a combination of N, S, Al and Ag doped TiO_2 will be investigated both individually and combined. The individual effects on anatase to rutile transformation and photocatalysis will be investigated and the chapter layout is as follows.

1) Optimisation of Al-TiO_2 for the synthesis of high temperature anatase was carried out in order to determine the optimum Al mol % necessary to achieve high temperature stable anatase.
2) It was then necessary to achieve successful insertion of nitrogen into the TiO_2 crystal lattice, this was carried out using a novel sol-gel technique and with the ideal loadings of both nitrogen and aluminium found it was possible to synthesise co-doped Al, N-TiO_2 materials.
3) As N-doped TiO_2 causes visible light active TiO_2 it may be deduced that if electrons can be excited using less energy, they can also recombine at increase rates, reducing the photoactivity of the material. In an effort to counteract recombination, 3 mol % silver was added to create Ag, N-TiO_2 the value of 3 mol % was determined to be the optimum silver loading in previous work carried out in our laboratory.[130]

   It is well reported that sulfur doped TiO_2 is more difficult to achieve than N-TiO_2 because of sulfur's larger ionic radius.[95,270] Therefore, two separate sulfur sources were investigated for this synthesis. Dimethyl sulfoxide (DMS) and sodium thiosulfate ($Na_2S_2O_3$) were the sulfur sources chosen for this study.

4) With all synthesis conditions and dopant amounts optimised it was then possible to synthesise multi doped Al, Ag, N, S-TiO_2. This chapter presents the results and steps of each stage of the journey to achieve Al, Ag, N, S-TiO_2.

5.2 Results and Discussion

5.2.1 Characterisation

5.2.1.1 Al-TiO_2

It has been reported that the presence of aluminium with TiO_2 extends the anatase to rutile transformation temperature by up to 200 °C.[251] To determine what the optimum percentage of aluminium modification is, 1, 3, 5 and 10 mol % Al was added to TiO_2 and the samples were calcined at temperatures 400 – 1000 °C. X-ray diffraction was carried out on the calcined samples and the results are summarised in figure 5.1.

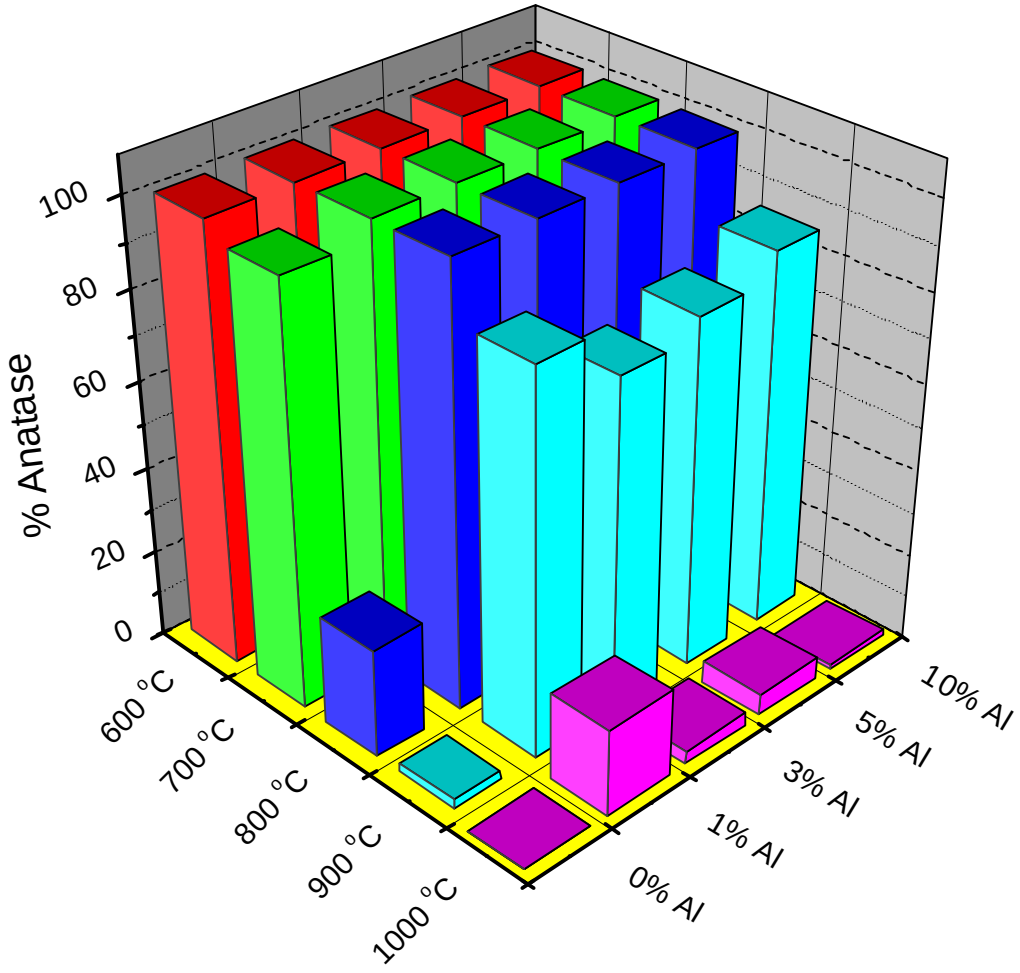

Figure 5.1. Percentage anatase in Al – TiO_2 at various calcination temperatures

From the results shown in figure 5.1, it is obvious that the presence of aluminium does stabilise TiO_2 as anatase at prolonged temperatures. Without the presence of aluminium, anatase begins to transforms to rutile at 700 °C and at 800 °C, rutile is the majority phase. However, aluminium delays the transformation at temperatures up to 900 °C, with anatase still present at 1000 °C. The maximum delay in the anatase to rutile transformation was achieved by the addition of 1 % Al. As the Al percentage increased, the effectiveness on delaying the formation of rutile was decreased. Also since Al has been reported to hinder photocatalytic activity[89] it was decided that 1 % Al-TiO_2 would be used for further investigations.

5.2.1.2 N-TiO_2

Nitrogen doped TiO_2 was synthesized from a novel sol-gel method using molar ratios of Ti:N, 1:0.5 and 1:4. The powders were calcined at temperatures 400 – 1000 °C. X-ray diffraction of the calcined powders (figures 5.2 and 5.3) showed that increased amounts of nitrogen stabilise TiO_2 as anatase at increased temperatures.

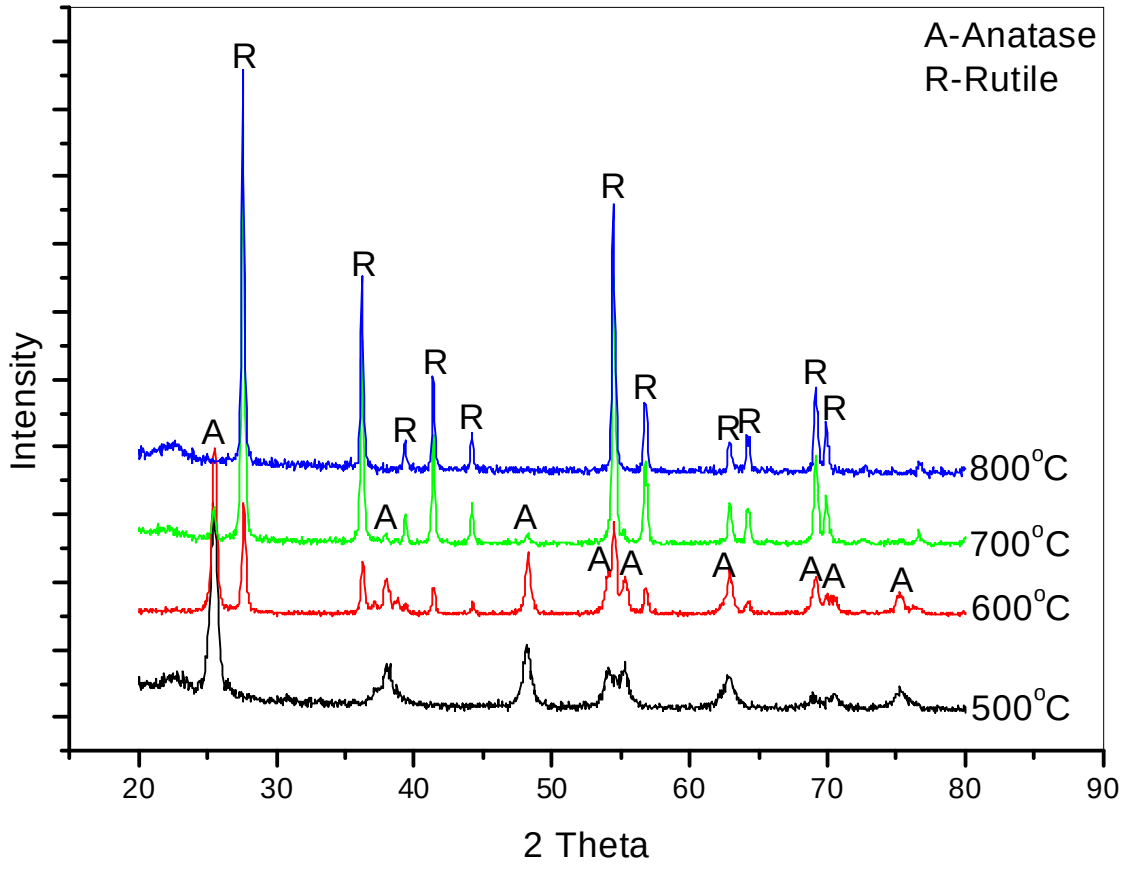

Figure 5.2. X-ray diffractogram of N doped TiO_2, 1:0.5 Ti:N

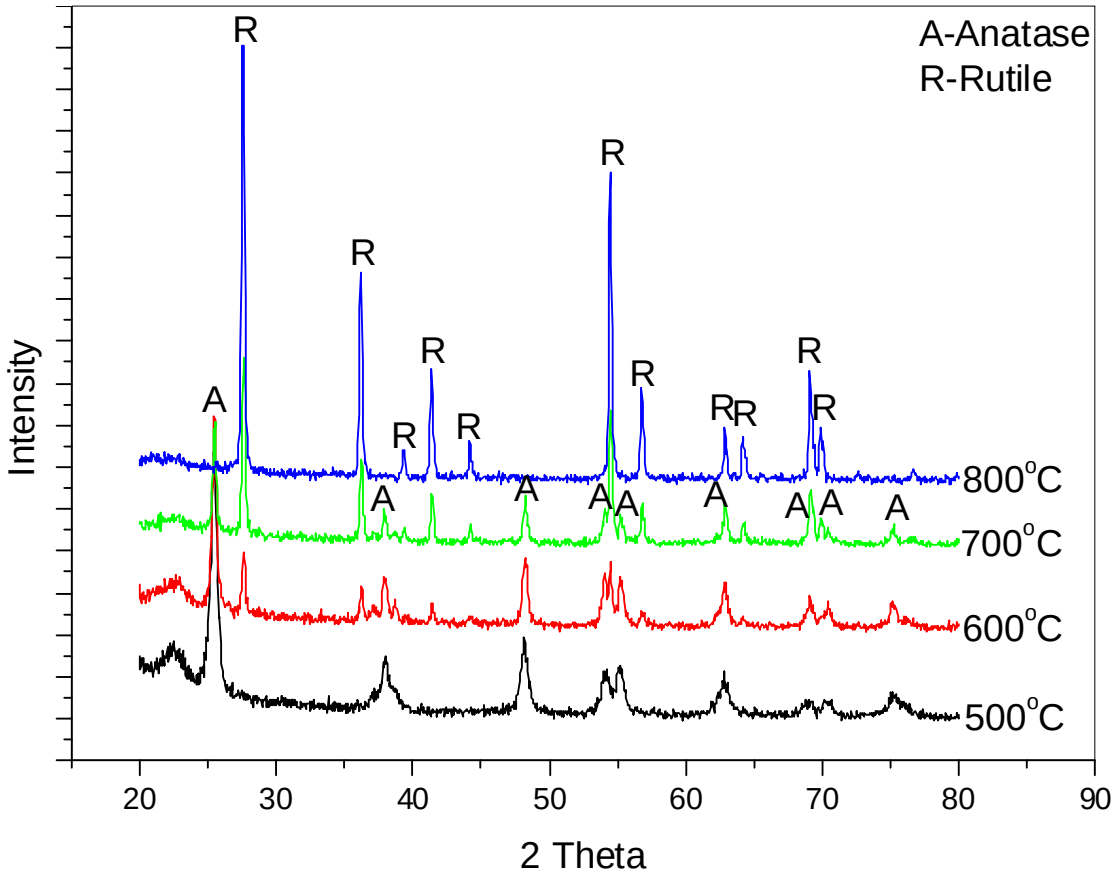

Figure 5.3. X-ray diffractogram of N doped TiO_2, 1:4 Ti:N

Molar ratios of Ti:N, 1:0.5 give anatase percentages of 54 and 7% at temperatures of 600 and 700 °C respectively, whereas molar ratios of 1:4, Ti:N result in anatase percentages of 68 and 35% at temperatures of 600 and 700 °C respectively. Visual inspection of the sample at 500 °C indicates the successful insertion of nitrogen into the TiO_2 lattice due to the yellow colour of the powders.[271] Calcination at all other temperatures did not result in nitrogen doped powders. Diffuse reflection spectra of the nitrogen doped TiO_2 powders calcined at 500 °C (figure 5.4) clearly show visible light absorption by the powders, further proof of successful insertion of nitrogen into the TiO_2 lattice.

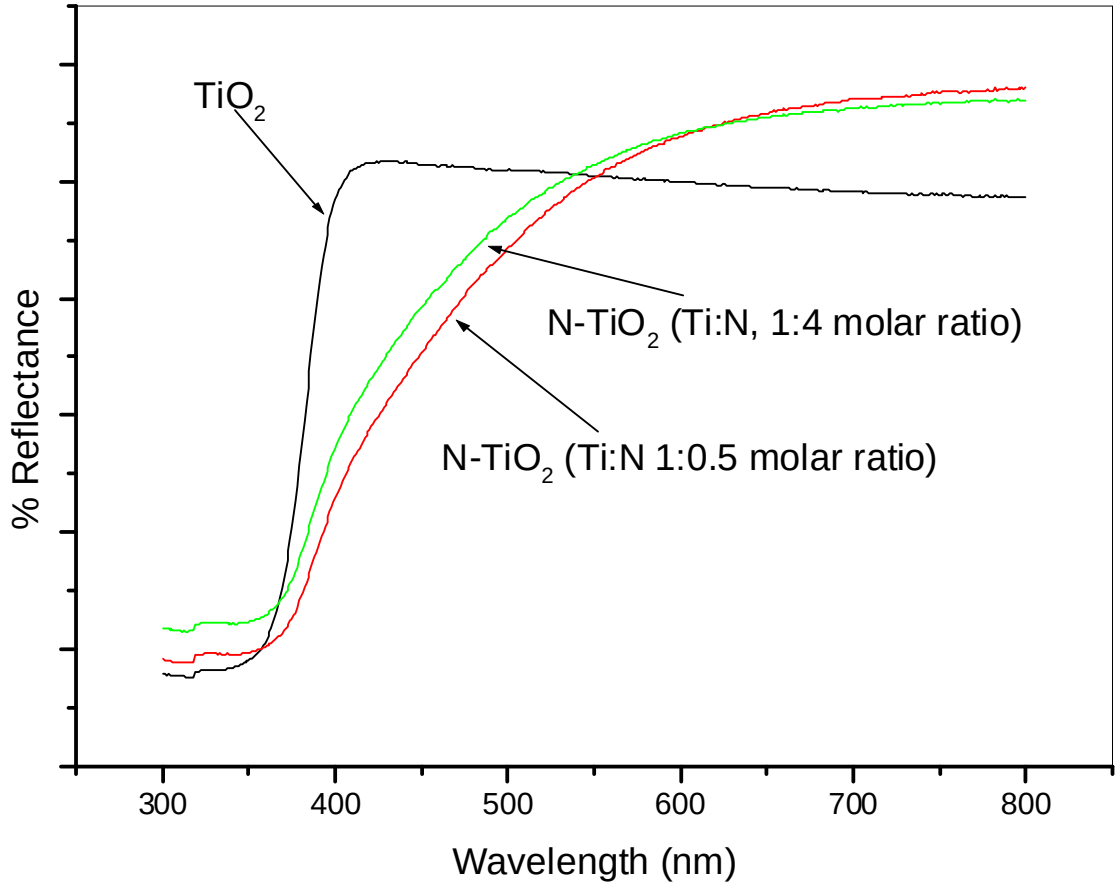

Figure 5.4. Diffuse reflectance spectra of TiO_2 and N-TiO_2

5.2.1.3 Al, N-TiO_2

Since it was shown that 1 % Al-TiO_2 delays the anatase to rutile transformation and N-TiO_2 gives visible light absorption, 1 % Al, N-TiO_2 (Ti:N, 1:0.5 and 1:4) was synthesised. The crystallisation behaviour of the TiO_2 was influenced by nitrogen more than aluminium. Aluminium alone delayed the anatase to rutile transformation up to 900 °C, but the presence of nitrogen (Ti:N, 1:0.5) with aluminium resulted in the transformation temperature being lowered to 600 °C (anatase 89 %), at 700 °C rutile was the dominant phase (60 %) and at 800 °C complete transformation had occurred. Higher ratios of nitrogen (Ti:N, 1:4) gave similar results but with higher rutile percentages. At 600 °C the sample was 16 % rutile and at 700 °C the sample was 72 % rutile. Therefore, increased amounts of nitrogen, in the presence of 1 mol % Al, lower the anatase to rutile transformation temperature. N-TiO_2 is no longer capable of visible light absorption at calcination temperatures ≥ 600 °C. Disappearance of visible

light absorption coincides with rutile formation. It can be postulated that the formation of rutile is the reason for the blue shift in the absorption properties of the materials. Di Valentin *et al* explain that a blue shift is observed with N-doped rutile because not only is the top of the TiO_2 valence band lowered (by 0.4 eV) but the inserted N 2p levels are also lower in energy than the valence band of pure rutile (0.05 eV) (figure 5.5).[271]

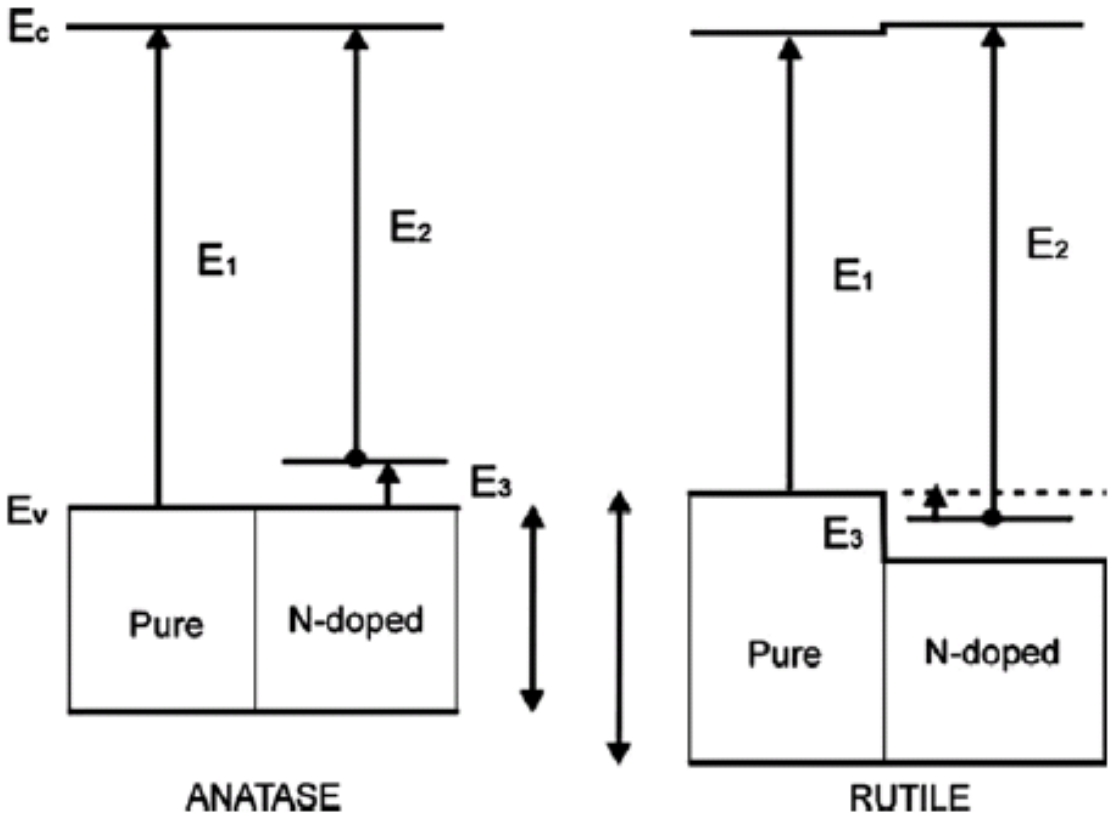

Figure 5.5. Schematic electronic structure for pure and N-doped anatase and rutile polymorphs of TiO_2[271]

Also since the anatase to rutile transformation can be dominated by effects such as defect concentration,[40] it is possible that the introduction of nitrogen increases the number of defects within the lattice, thus, lowering the anatase to rutile transformation temperature.

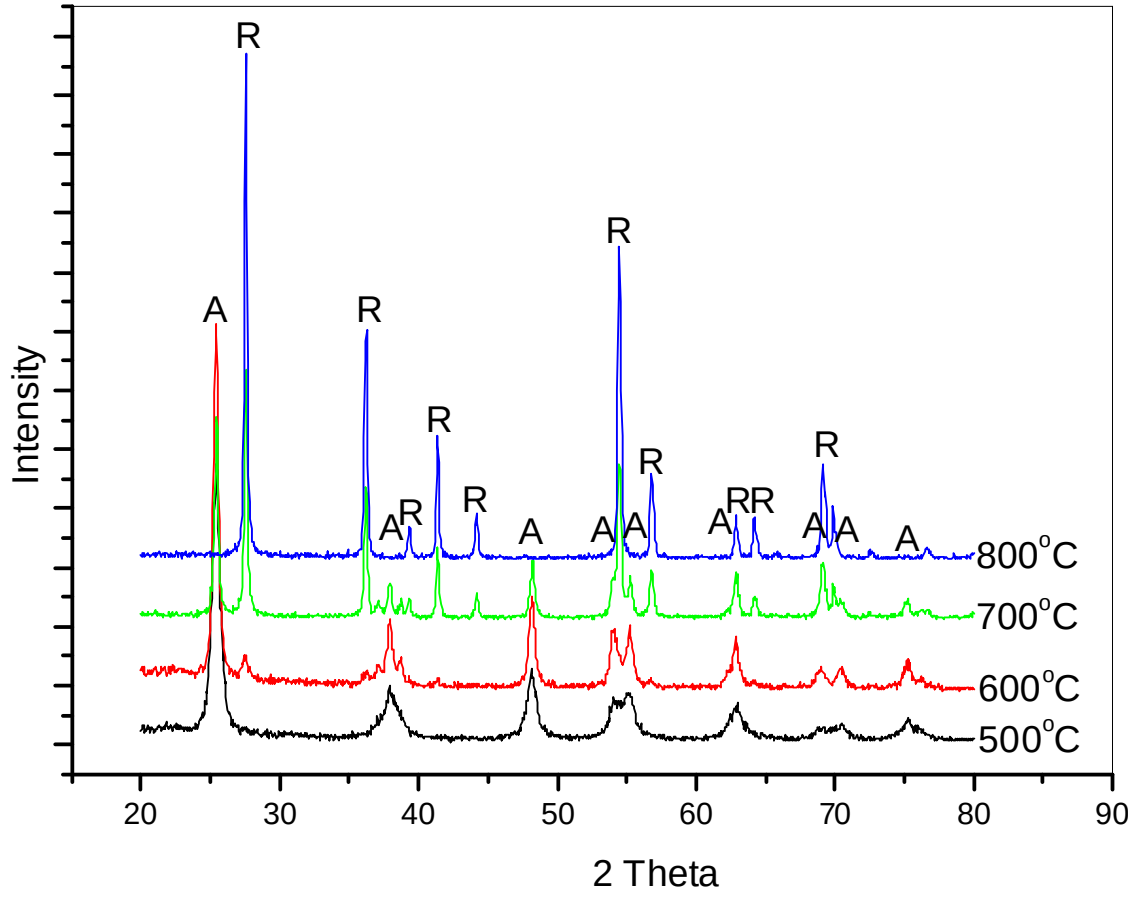

Figure 5.6. X-ray diffractogram of 1 % Al, N doped TiO_2, 1:0.5 Ti:N

Diffuse reflectance results for 1 % Al, N-TiO_2 gave similar results as were shown for N-TiO_2 (figure 5.4). It was again observed that at calcination temperatures other than 500 °C, from visual inspection, nitrogen was not inserted into the TiO_2 lattice. The formation of rutile at 600 °C coincides with the loss of visible light absorption as was noticed with N-TiO_2 previously.

To determine which of the samples was the best photocatalyst, photocatalytic degradation of methylene blue was carried out on samples calcined at 500 and 600 °C. figure 5.7 shows a typical UV-vis degradation plot and table 5.1 summarises the degradation rate constants for all samples.

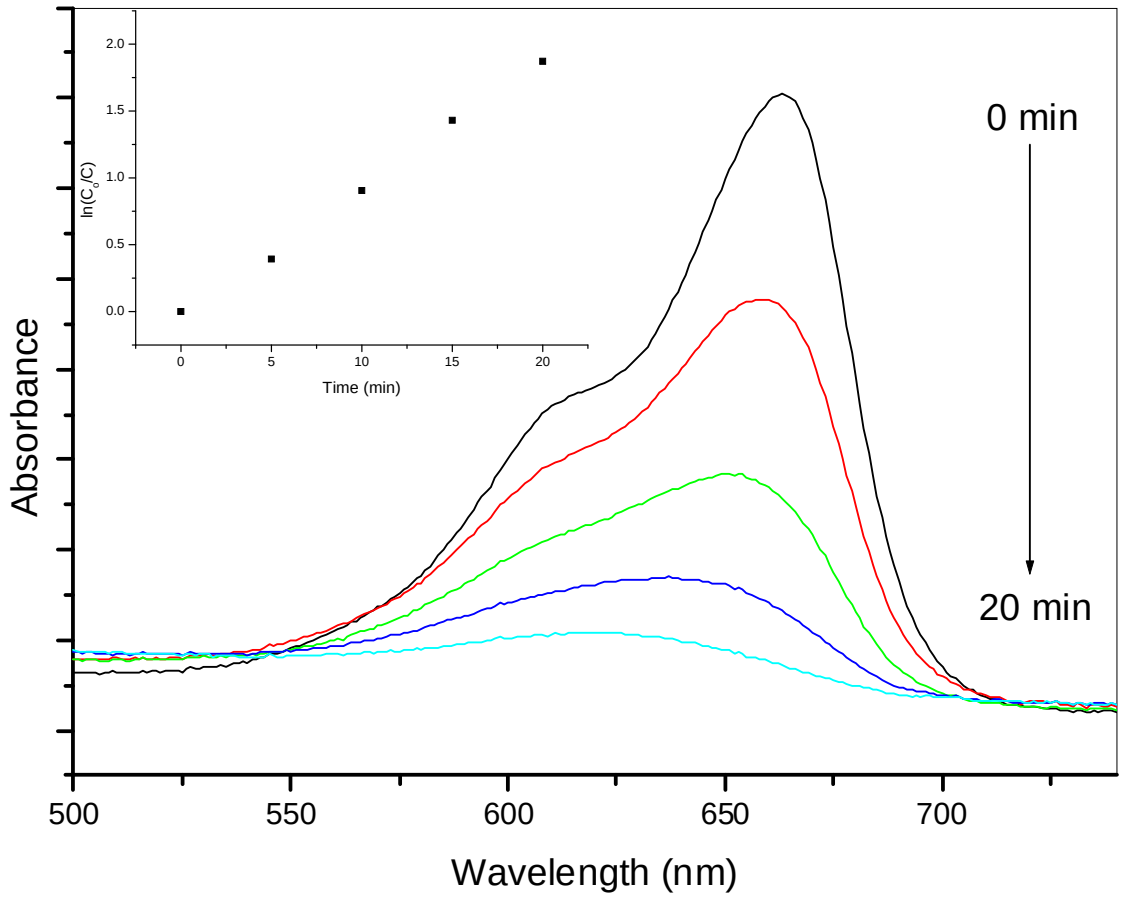

Figure 5.7. UV-vis absorption plot showing the degradation of methylene blue with N-TiO_2, Ti:N, 1:0.5 calcined at 600 °C (first order plot inset, R^2 = 0.9978)

Table 5.1. First order rate constants for methylene blue degradation with N-TiO_2

Sample	Ti:N molar ratio	Calcination Temperature (°C)	Rate Constant (min^{-1}, $x10^{-2}$)
N-TiO_2	1:0.5	500	7.2
N-TiO_2	1:0.5	600	9.6
N-TiO_2	1:4	500	3.4
N-TiO_2	1:4	600	6.5
1 % Al, N-TiO_2	1:0.5	500	3.7
1 % Al, N-TiO_2	1:0.5	600	3.1
1 % Al, N-TiO_2	1:4	500	3.8
1 % Al, N-TiO_2	1:4	600	3.1

Results from table 5.1 clearly show the negative impact of aluminium on the photocatalytic activity of N-TiO_2. The most photoactive sample had no aluminium (N-TiO_2, Ti:N, 1:0.5), and it degraded methylene blue giving a rate constant of 9.6 x 10^{-2} min^{-1}, almost three times greater than any aluminium containing sample. It has previously been reported that the addition of aluminium causes a reduction in the photocatalytic activity of TiO_2.[89] There are believed to be a number of factors regarding photocatalytic efficiency that the addition of aluminium may influence. The substitution of Ti^{4+} with Al^{3+} ions in the TiO_2 crystal lattice,[272-274] results in the formation of oxygen vacancies by charge compensation.[272] The additional oxygen vacancies can act as recombination centres therefore preventing the formation of the OH• radicals associated with the photocatalytic mechanism.[272] Comparison of Al, N-TiO_2 photocatalytic degradation results with N-TiO_2 degradation results are in agreement with Gesenhues *et al*[272,273] and it shows that the addition of aluminium causes a reduction in the photocatalytic activity of TiO_2. Adsorbed surface hydroxyl species on the TiO_2 surface are also influential on the photocatalytic activity of TiO_2, the addition of aluminium reduces the amount of adsorbed hydroxyl radicals and as such the photocatalytic efficiency of the material is also reduced.[272] A rate constant of 29.0 x 10^{-2} min^{-1} for the degradation of methylene blue was determined using the TiO_2 industrial standard, Degussa P25. This shows that although N-TiO_2 has a broader absorption spectrum, as a photocatalyst it is extremely inferior to the industrial standard under solar simulated irradiation. It is postulated that the poor photocatalytic activity of N-TiO_2 compared with Degussa P25, may be due to increased recombination caused by the insertion of N2p energy levels between the valence band and the conduction band of the TiO_2 semiconductor materials. Therefore, in order to increase the photocatalytic activity of N-TiO_2, recombination must be reduced.

5.2.1.4 Ag, N-TiO_2

This group has previously enhanced photocatalysis of TiO_2 through silver modification[130] and Kuo *et al* have shown that the addition of silver causes a reduction in photoluminescence intensity[93] indicating that silver traps excited electrons therefore reducing recombination rates.[113-117] To improve the photocatalytic activity of N-TiO_2, 3 mol % silver was added. 3 mol % silver was chosen as previous results by this group have shown it is the optimum amount.[130]

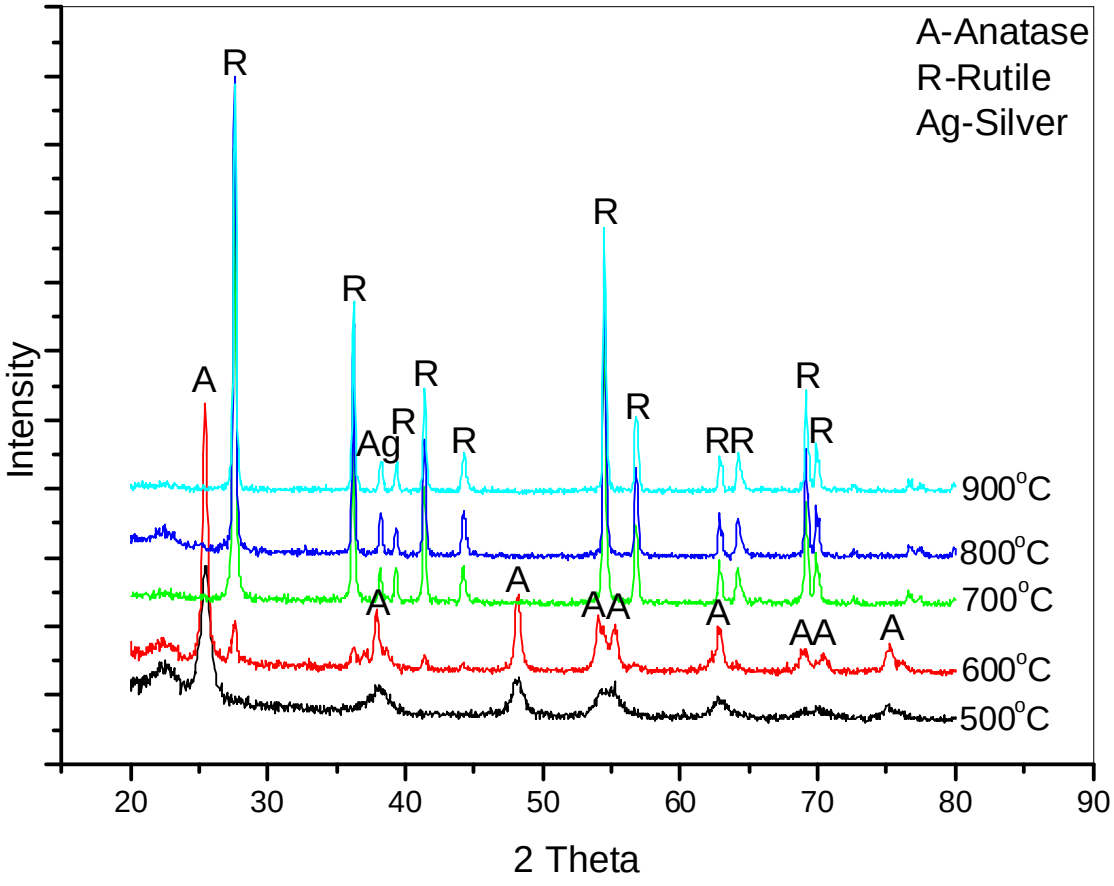

Figure 5.8. X-ray diffractogram of 3 % Ag, N doped TiO_2, 1:0.5 Ti:N

The XRD scan of 3 mol % Ag, N-TiO_2 shown in figure 5.8 is similar to that of Ag, N-TiO_2 (Ti:N, 1:4). It can be seen that silver greatly promotes the formation of rutile. At 600 °C rutile (22 %) begins to form, with complete anatase to rutile transformation occurring at 700 °C. A number of reasons for the promotion of rutile formation by silver have previously been concluded by Chao *et al*[129] including; silver causing a reduction in anatase grain size, therefore increasing the specific surface area of the TiO_2 particles

and increasing the nucleation and growth mechanism associated with the anatase to rutile transformation. Secondly, silver promotes the formation of oxygen vacancies within the TiO_2 lattice, these vacancies allow ionic and structural rearrangement to occur with greater ease thus, forming rutile.[129] In chapter 4 it was also shown that silver blocks the formation of chelating ligands to the titanium metal centre, without organic ligands binding to the metal centre, titanium isopropoxide forms a disordered network as the condensation process proceeds, this network can collapse readily upon calcination to form rutile.[275]

The electronic properties of the Ag, N-TiO_2 powders were determined by diffuse reflectance (figure 5.9).

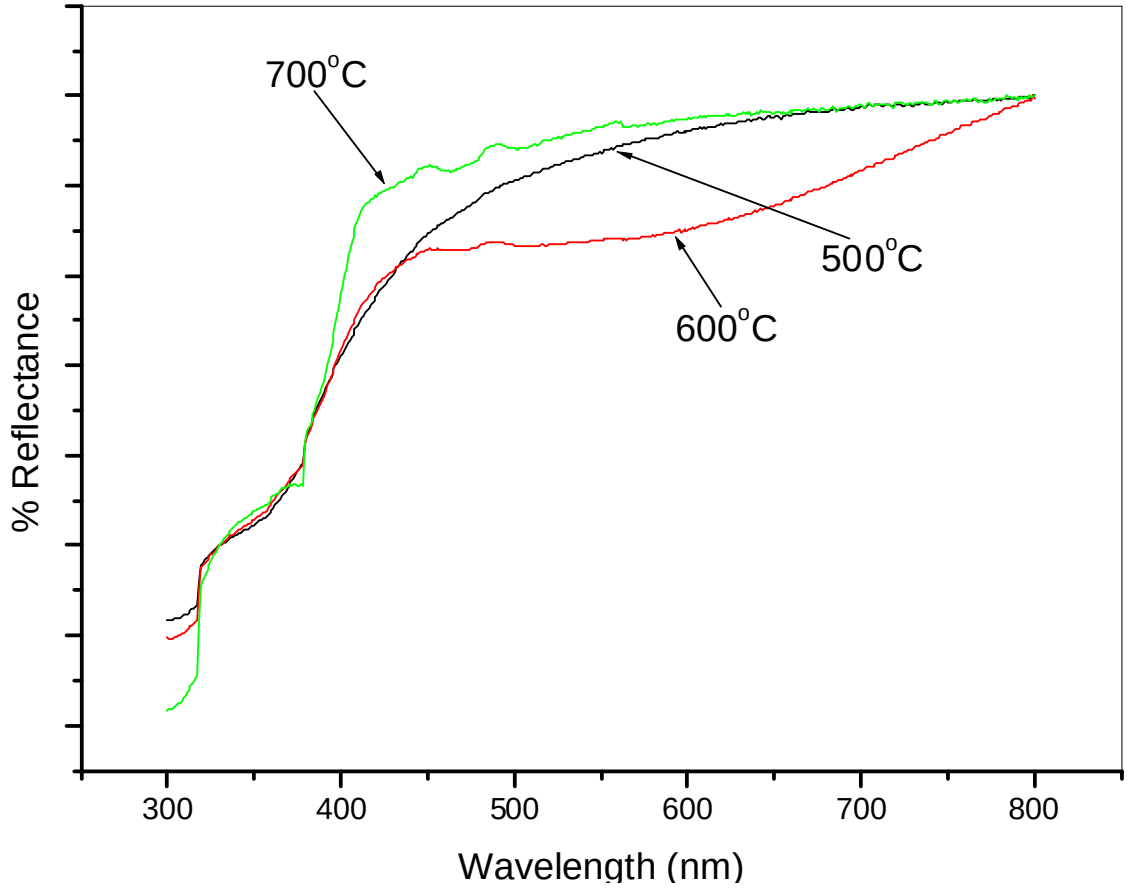

Figure 5.9. Diffuse reflectance spectra of 3 % Ag, N-TiO_2 (Ti:N, 1:4)

It can be seen from the diffuse reflectance spectra that the addition of nitrogen still enables visible light absorption. However as the calcination temperature increases up to 700 °C, rutile is formed and the sample is no longer visible light active. To determine if the photocatalytic activity of the samples has been improved, methylene blue was

again chosen as the model degradant. For consistency in the photocatalytic activity tests, degradation reactions were carried out under the same conditions as employed previously.

Table 5.2. First order rate constants for methylene blue degradation with N-TiO_2

Sample	Ti:N molar ratio	Calcination Temperature (°C)	Rate Constant (min^{-1}, x 10^{-2})
3 % Ag, N-TiO_2	1:0.5	500	8.4
3 % Ag, N-TiO_2	1:0.5	600	9.9
3 % Ag, N-TiO_2	1:0.5	700	3.8
3 % Ag, N-TiO_2	1:4	500	5.5
3 % Ag, N-TiO_2	1:4	600	3.8
3 % Ag, N-TiO_2	1:4	700	2.8

The addition of silver does cause improved photocatalytic ability with 3 % Ag, N-TiO_2 (Ti:N, 1:0.5) calcined at 600 °C being the most effective silver modified photocatalyst with a rate constant of 9.9 x 10^{-2} min^{-1} compared to 9.6 x 10^{-2} min^{-1} for the same sample without silver (table 5.2). However, this result still does not compete with Degussa P25 (29 x 10^{-2} min^{-1}). In order to improve the photocatalytic activity of TiO_2, further dopants must be investigated. From the nitrogen doping studies it was determined that ratios of Ti:N, 1:0.5 result in the most efficient photocatalyst. Therefore, the addition of increased amounts of nitrogen (Ti:N, 1:4) precursor does not result in improved photocatalytic efficiency when compared with N-TiO_2 prepared using smaller amounts of nitrogen source (Ti:N, 1:0.5). Molar ratios of 1:0.5 for Ti:N were therefore used for future synthesis.

5.2.1.5 Al, S-TiO_2

Visible light absorption has also been achieved through sulfur doping[292-294] but incorporation of anionic sulfur into the TiO_2 crystal lattice is more difficult to achieve than insertion of nitrogen because sulfur has a larger ionic radius, as shown by the larger energy of formation required for S substitution (4.1 eV) compared to that of N (1.6 eV).[252] However, insertion of cationic sulfur (S^{6+}) because of its smaller ionic radius is chemically favourable over S^{2-} insertion. Successful sulfur doping with S^{6+} was observed by this group through XPS where the presence of titanyl oxosulfate delayed the anatase to rutile transformation temperature up to 900 °C.[270]

Synthesis of sulfur doped TiO_2 was carried out using two possible sulfur sources; dimethyl sulfoxide (DMSO) and sodium thiosulfate ($Na_2S_2O_3$). Ratios of Ti:S, 1:1 and 1:16 were used for DMSO and for $Na_2S_2O_3$, ratios of 1:1 and 1:4 were chosen. X-ray diffraction of the samples showed that S-TiO_2 synthesised from DMSO gave stable anatase at increased temperatures on comparison with S-TiO_2 synthesised from $Na_2S_2O_3$ with no noticeable change observed from varying the ratio of the sulfur source. From figure 5.10 it can be seen that DMSO delays the anatase to rutile transformation. Anatase is the only phase present at 700 °C, it is the dominant phase at 800 °C (83 %) and is present in small amounts at 900 °C (3 %). On comparison, figure 5.11 shows rutile forming at 700 °C (11 % rutile) and at 800 °C the percentage rutile increases to 40 % before total transformation occurs at 900 °C.

Diffuse reflectance spectra (figure 5.12) indicated that sulfur did not cause visible light absorption, thus indicating that neither anionic nor cationic sulfur was inserted into the TiO_2 lattice. Sulfur doping may not have been achieved if the sulfur sources were not present during the condensation process. If the sulfur sources were absent after filtering and aging, then substitution of oxygen with sulfur during crystallisation could not occur. Although this result may not be conclusive it does highlight the ease at which N-doping can occur on comparison with S-doping. The photocatalytic activity of the synthesised materials was investigated through the degradation of methylene blue.

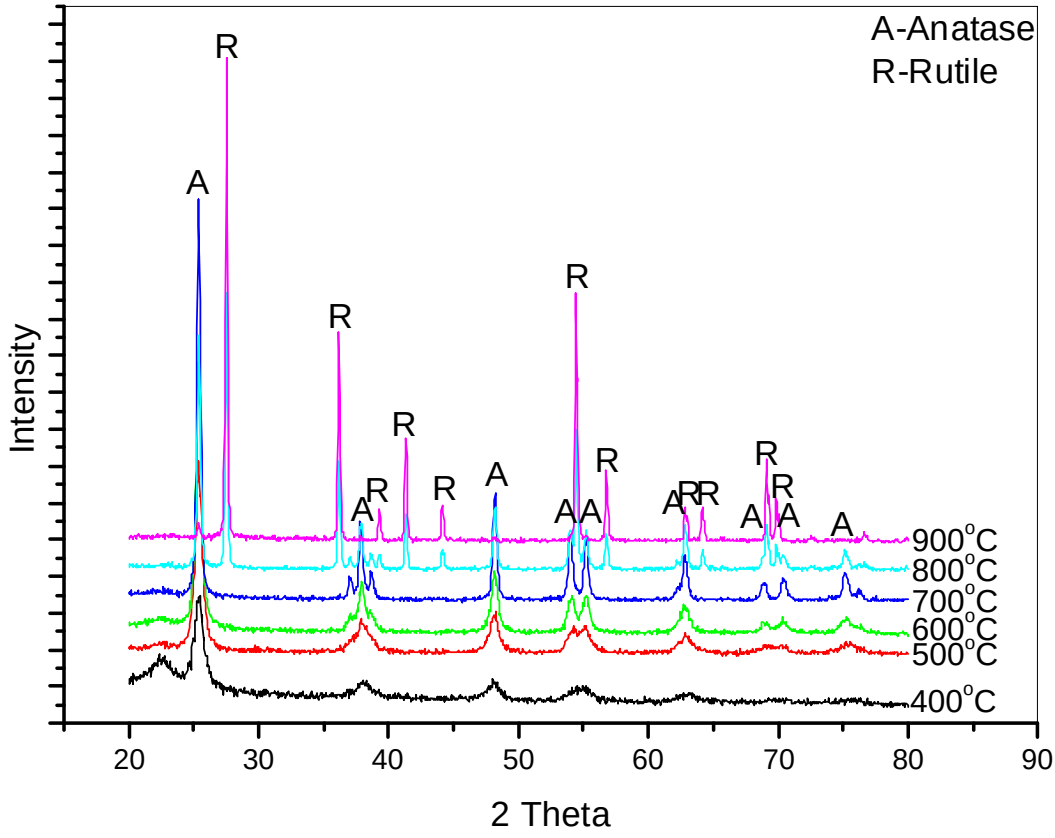

Figure 5.10. X-ray diffractogram of 1 % Al, S doped TiO_2, 1:16 Ti:S (DMSO)

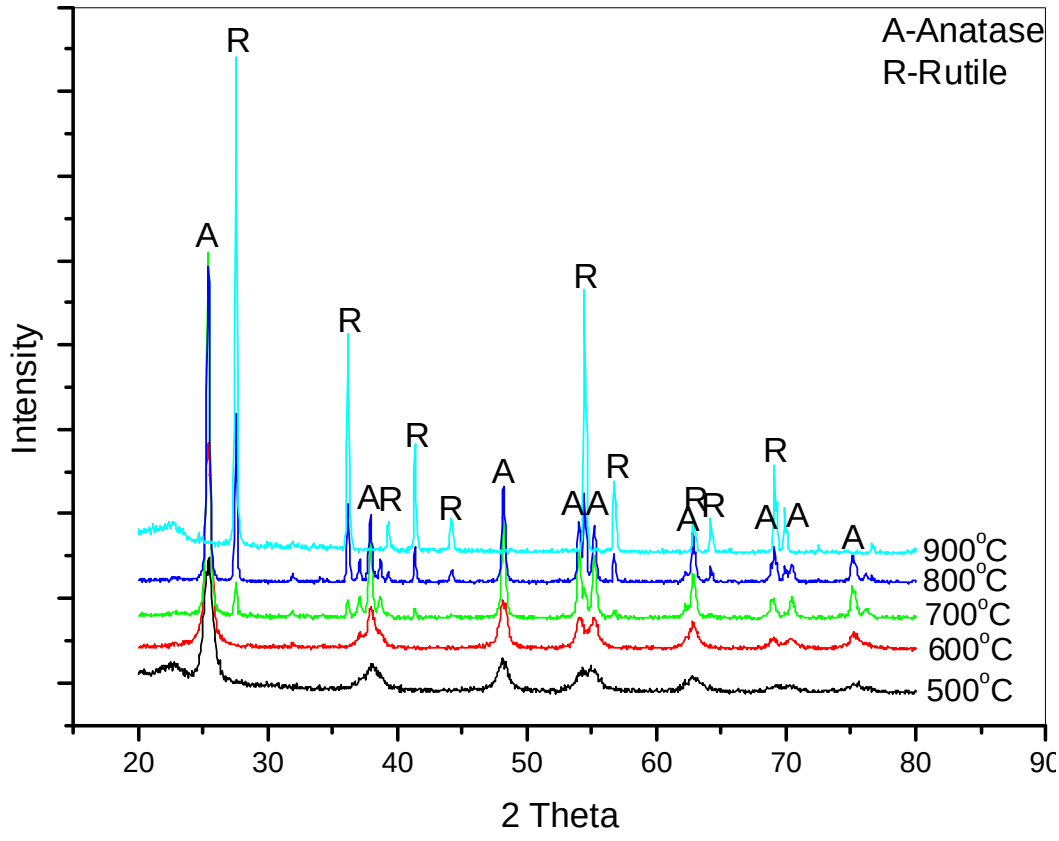

Figure 5.11. X-ray diffractogram of 1 % Al, S doped TiO_2, 1:1 Ti:S ($Na_2S_2O_3$)

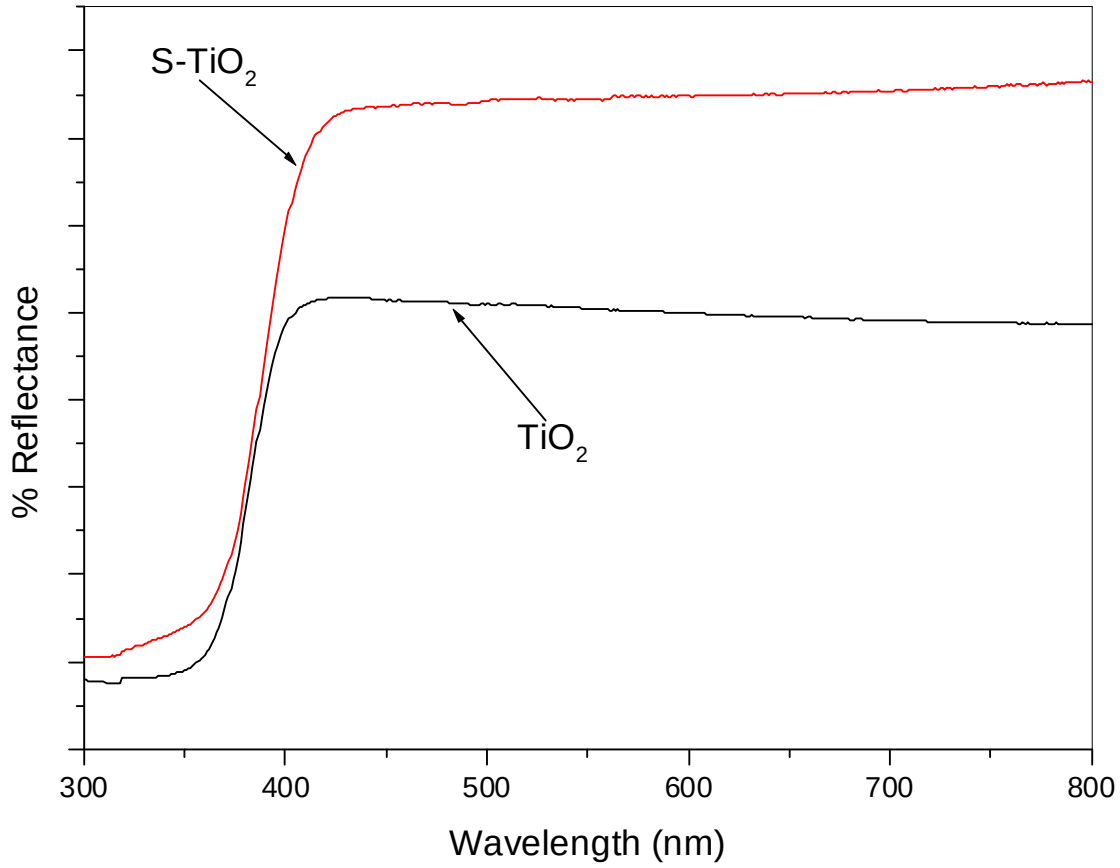

Figure 5.12. Diffuse reflectance spectra of 1 % Al, S-TiO_2 (Ti:S, 1:1, DMSO)

From the results shown in table 5.3 it can be seen that S-TiO_2 synthesised from the $Na_2S_2O_3$ source proves to be a very effective photocatalyst. On comparison with N-TiO_2 which was shown to be visible light active, S-TiO_2 is ten times more photoactive than some of the nitrogen doped samples. S-TiO_2 (1:4, $Na_2S_2O_3$) calcined at 700 °C proved to be the most efficient photocatalyst with a degradation rate constant of 43.1 x 10^{-2} min^{-1}, significantly greater than Degussa P25 (29.0 x 10^{-2} min^{-1}). S-TiO_2 synthesised from $Na_2S_2O_3$ was also more photoactive than S-TiO_2 synthesised from DMSO and as such, $Na_2S_2O_3$ was the sulfur source of choice for further synthesis. Reasons for such high photocatalytic activity may include; high surface area, reduced recombination due to excess lattice defects or reduced oxygen vacancies. The presence of Na^+ ions has previously been reported to act as a charge recombination site which would decrease the photocatalytic activity.[276,277] In fact, poisoning of TiO_2 supported on glass substrates is believed to be caused by Na contamination.[276,277] However, Bessekhouad *et al* showed that photocatalytic efficiency of alkaline-TiO_2

materials is dependant on synthesis conditions, pollutant type and alkaline concentration.[278] The results shown in table 5.3 indicate that improved photocatalytic efficiency may be caused by the synergestic effect of Na and S.

Table 5.3. First order rate constants for methylene blue degradation with S-TiO_2

Sample	Ti:S molar ratio	Calcination Temperature (°C)	Rate Constant (min^{-1}, x 10^{-2})
S-TiO_2 ($Na_2S_2O_3$)	1:1	500	7.4
S-TiO_2 ($Na_2S_2O_3$)	1:1	600	16.4
S-TiO_2 ($Na_2S_2O_3$)	1:1	700	35.9
S-TiO_2 ($Na_2S_2O_3$)	1:1	800	29.6
S-TiO_2 ($Na_2S_2O_3$)	1:4	500	32.9
S-TiO_2 ($Na_2S_2O_3$)	1:4	600	14.8
S-TiO_2 ($Na_2S_2O_3$)	1:4	700	43.1
S-TiO_2 ($Na_2S_2O_3$)	1:4	800	36.0
S-TiO_2 (DMSO)	1:1	500	3.4
S-TiO_2 (DMSO)	1:1	600	7.0
S-TiO_2 (DMSO)	1:1	700	6.8
S-TiO_2 (DMSO)	1:16	500	3.8
S-TiO_2 (DMSO)	1:16	600	6.6
S-TiO_2 (DMSO)	1:16	700	8.4

Not only have N-TiO_2 and S-TiO_2 results shown what can be achieved using the various dopants and synthesis techniques but results from N-TiO_2 and S-TiO_2 have also shown what the optimum concentrations of nitrogen/sulfur source required is. With N-TiO_2, 1:0.5 was found to be the optimum ratio and the presence of silver was shown to be of benefit to the photocatalytic ability of the material. Sodium thiosulfate produced a better photocatalyst than dimethyl sulfoxide and the optimum Ti:S molar ratio was found to be 1:4. Previous results had shown that 3 mol % silver is the ideal amount,

anymore than that acts as a physical barrier to incoming light as well as promoting recombination.[130] With the conditions optimised it was then possible to synthesise N, S-codoped TiO_2 with and without silver and aluminium.

5.2.1.6 3% Ag, 1% Al, N, S-TiO_2

Silver, aluminium, nitrogen and sulfur co-doped powders were synthesised using diaminopropane is a nitrogen source and sodium thiosulfate as a sulfur source. The doped material was synthesized in the ratio 1:0.5:4, TTIP:DAP: $Na_2S_2O_3$ with 3 mol % Ag and 1 mol % Al also present. To determine the thermal stability of the sample X-ray diffraction was carried out on the calcined powders (figure 5.13).

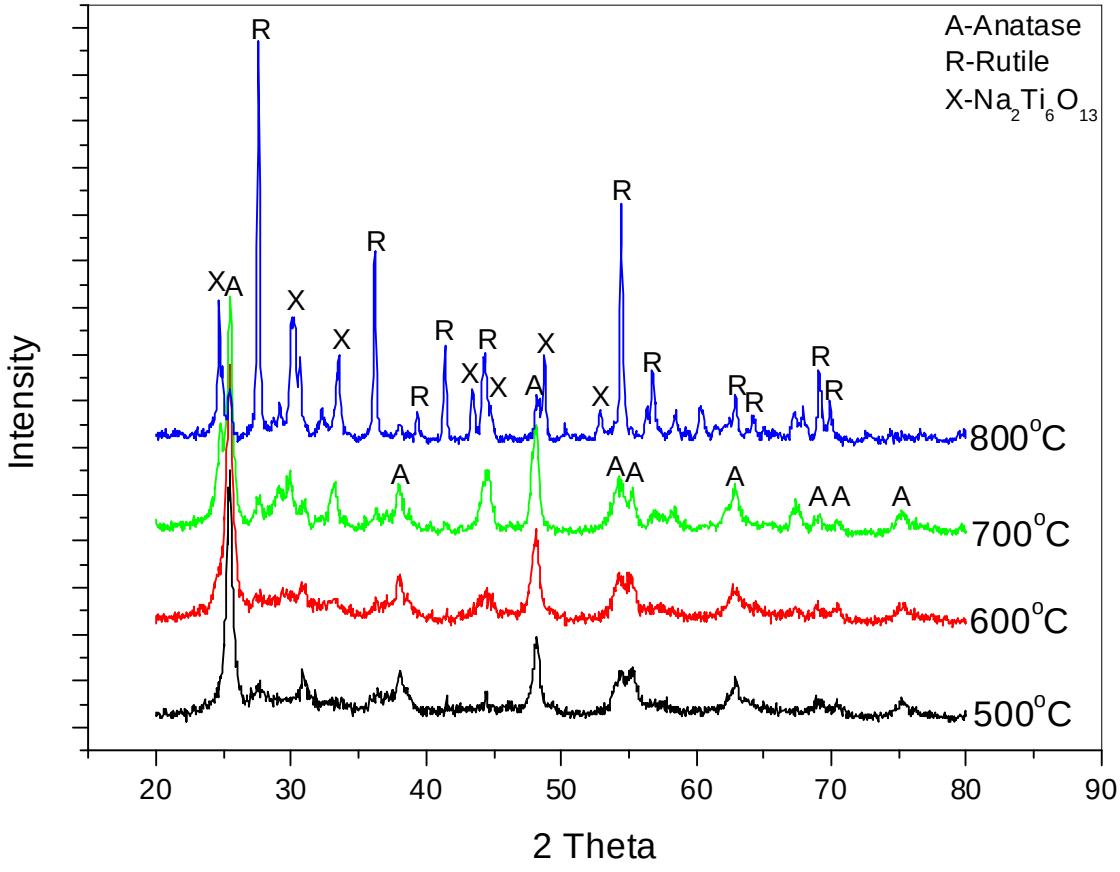

Figure 5.13. X-ray diffractogram of 3 % Ag, 1 % Al, N, S co-doped TiO_2, 1:0.5:4 Ti:N:S

When sodium thiosulfate was used alone as a sulfur source, the XRD of the calcined samples (figure 5.11) showed no evidence of the formation of any sodium titanate crystals. However, when sodium thiosulfate was used in the presence of diaminopropane, silver nitrate and aluminium nitrate, the crystalline sodium titanate

$Na_2Ti_6O_{13}$ was formed[279-281] (figure 5.13). At 500 °C the sample is anatase, as the temperature increases $Na_2Ti_6O_{13}$ begins to form. The formation of sodium titanate does not reduce the intensity of the anatase peaks indicating that sodium titanate is formed from amorphous TiO_2 and not anatase. Upon further increase in the temperature (≥ 700 °C) anatase begins to transform into rutile and the crystallinity of the sodium titanate phase increases.

5.2.1.7 Sodium titanate

To investigate why sodium titanate was formed in the co-doped powders but not in the S-doped TiO_2 powder it was necessary to eliminate additional factors and determine what was causing sodium titanate to form. Aluminium was the first dopant to be removed from the synthesis procedure. 3 % Ag, N, S co-doped TiO_2 was synthesized in the ratio 1:0.5:4, TTIP:DAP: $Na_2S_2O_3$. X-ray diffractograms of the calcined powders (figure 5.14) showed that the sodium titanate phase $Na_2Ti_6O_{13}$ still formed indicating that aluminium is not responsible for the formation of sodium titanate phase. However differences in the powders synthesized with and without aluminium were clear. Aluminium stabilized TiO_2 phases anatase and rutile which was clearly seen in figure 5.13. When aluminium was removed from the synthesis, no titanium dioxide phases were observed for the calcined powders (figure 5.14).

The sample Ag, N, S- TiO_2 calcined at 800 °C also showed peaks representative of a secondary sodium titanate phase, $Na_2Ti_3O_7$[281] which was not observed in the presence of aluminium. Finally, N, S-co doped TiO_2 (Ti:N:S, 1:0.5:4) was synthesised without any silver or aluminium. From the XRD results it was determined that synthesis of Al, S-TiO_2 (figures 5.10 & 5.11) does not result in the formation of sodium titanate. Al, Ag, N, S-TiO_2 produced both TiO_2 anatase and rutile as well as sodium titanate (figure 5.13). However, for samples Ag, N, S-TiO_2 and N, S-TiO_2, sodium titanate was the only phase present as found by XRD (figures 5.14 & 5.15). These results demonstrate that for a synthesis where 1,3-diaminopropane and $Na_2S_2O_3$ are both involved, sodium titanate is formed, but if aluminium is present, TiO_2 phases anatase and rutile exist along with

sodium titanate. Therefore, it can be deduced that the use of diaminopropane with sodium thiosulfate results in the formation of sodium titanate materials.

The basicisity of diaminopropane may facilitate the inclusion of the sodium cation from sodium thiosulfate into the TiO_2 matrix therefore promoting the formation of sodium titanates. When sodium thiosulfate was used without diaminopropane, no sodium titanates were formed. This may also explain why sulfur was not included in the TiO_2 lattice. The addition of sodium thiosulfate without the presence of a base did produce the most active photocatalyst however, since no evidence of sodium titanate was found for S-TiO_2, it may be postulated that sodium cations do not remain throughout the condensation and calcination process but instead are possibly removed through during the filtration and washing of the synthesized powders. Since sodium ions are possibly removed (through washing with deionised water) during the synthesis of S-TiO_2, the addition of 1, 3-diaminopropane must cause the retention of sodium ions around the hydrolysed titanium metal chains. The retention of the sodium ions around the hydrolysed titanium chains results in the formation of TiO_6 octahedra surrounding sodium ions. As the condensation process proceeds, sodium titanate is formed instead of TiO_2. Baliteau *et al* reported on the sol-gel synthesis of sodium titanates using titanium butoxide as the titanium precursor and sodium hydroxide (NaOH) as the sodium source.[279] In the N, S-TiO_2 system the presence of the basic 1,3-diaminopropane may have the same effect as the basic NaOH for production the of $Na_2Ti_6O_{13}$.[279] Therefore, it can be postulated that for the sol-gel synthesis of $Na_2Ti_6O_{13}$, basic conditions are required.

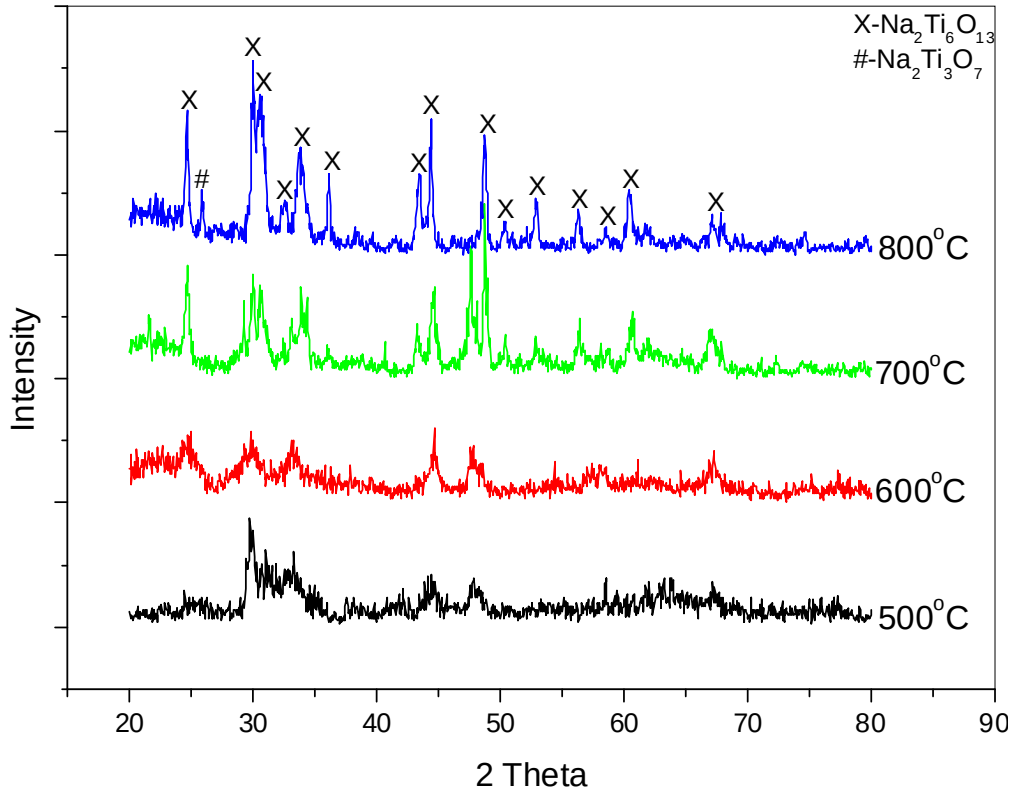

Figure 5.14. X-ray diffractogram of 3 % Ag, N, S co-doped TiO_2, 1:0.5:4 Ti:N:S

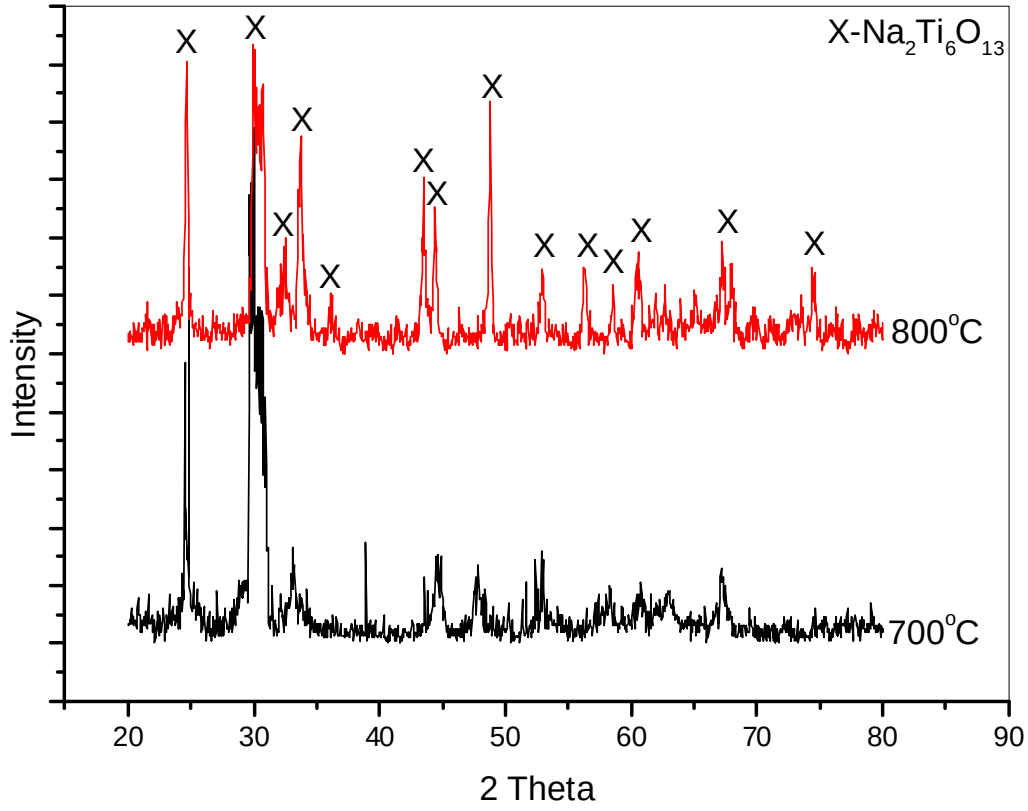

Figure 5.15. X-ray diffractogram of N, S co-doped TiO_2, 1:0.5:4 Ti:N:S

Diffuse reflectance studies of 3 % Ag, 1 % Al, S, N-TiO_2 showed that the formation of sodium titanate did not cause a significant band gap shift. However at a calcination temperature of 800 °C there was a noticeable band gap reduction as seen by the red shift in the spectra (figure 5.16). This was due to the formation of rutile.

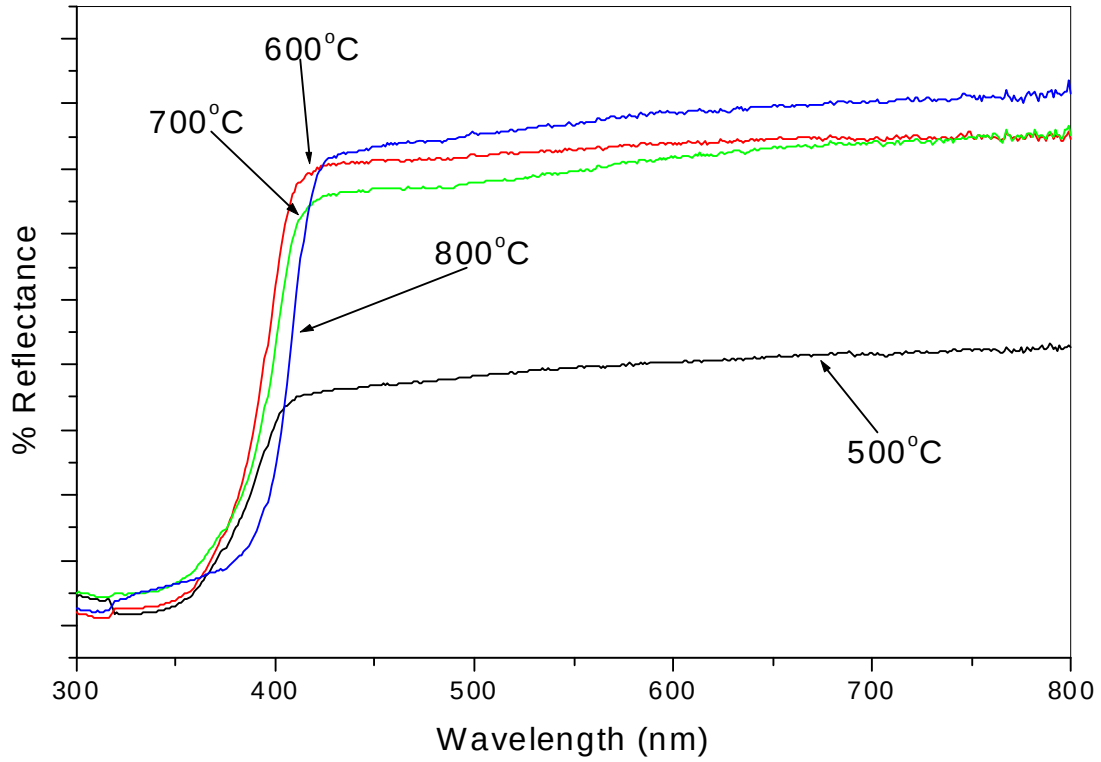

Figure 5.16. Diffuse reflectance spectra of 3 % Ag, 1 % Al, S, N-TiO_2 calcined at various temperatures

With previous samples, nitrogen was successfully inserted into the TiO_2 lattice resulting in visible light absorption as seen in figures 5.4 and 5.9. In figure 5.16 it is clear that the sample is not visible light active indicating that nitrogen is not included in the TiO_2 lattice. Therefore, the presence of additional dopants such as silver, aluminium and sulfur (from sodium thiosulfate) restrict or block nitrogen from being substituted with lattice oxygen in TiO_2. This may be due to the occurrence of additional reactions that occur between the dopant sources.

Diffuse reflectance spectra of the sample without aluminium show that nitrogen is not inserted into the TiO_2 lattice. The sample synthesized without silver and aluminium does not show visible light absorption (figure 5.17) indicating that neither aluminium nor silver block nitrogen from entering the crystal lattice.

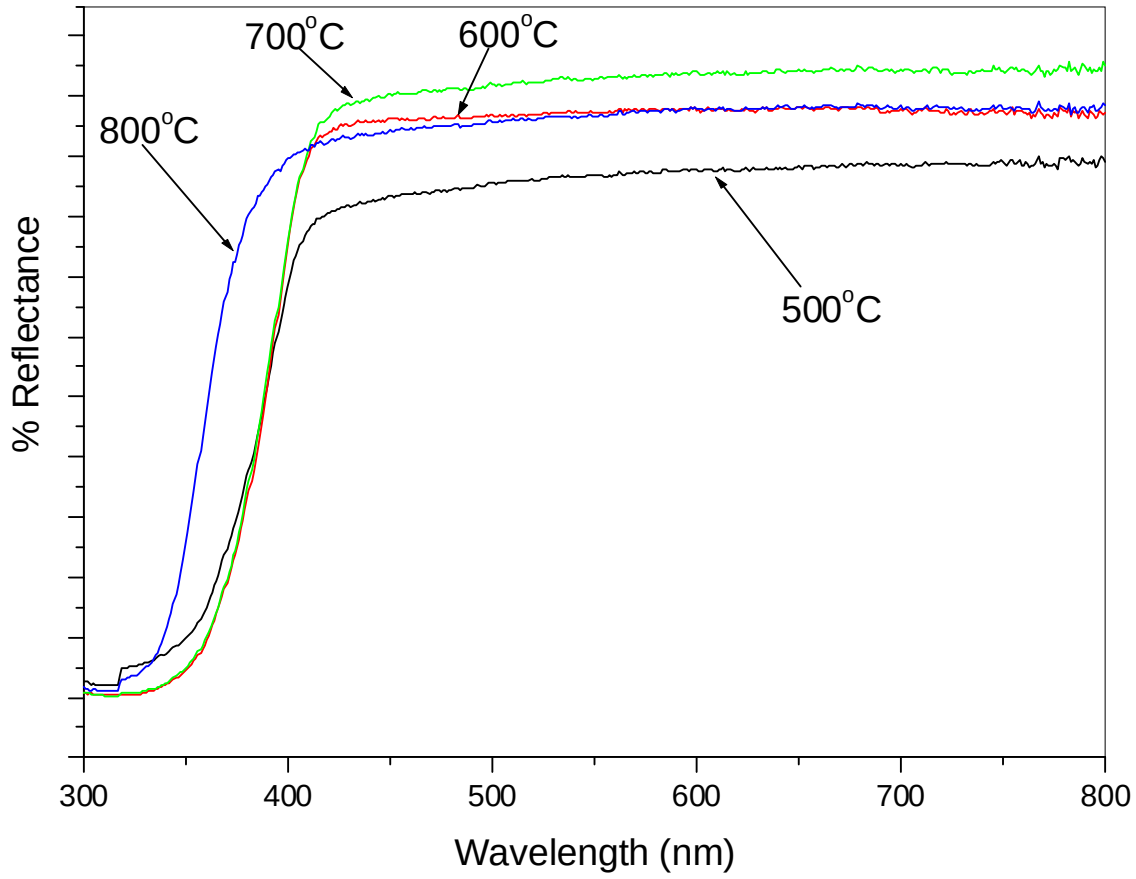

Figure 5.17. Diffuse reflectance spectra of S, N-TiO_2 calcined at various temperatures

The diffuse reflectance results indicate that sodium thiosulfate is inhibiting nitrogen insertion into the TiO_2 lattice. This result supports the findings drawn from the XRD results where it was believed that diaminopropane reacts with sodium thiosulfate allowing sodium ions to be involved in the crystallization process thus forming sodium titanates. Further evidence for sodium ions interacting with diaminopropane can be drawn from the fact that TiO_2 synthesised from diaminopropane without sodium thiosulfate resulted in nitrogen insertion into the crystal lattice and visible light absorption but in the presence of sodium thiosulfate, visible light absorption was not achieved indicating that nitrogen did not substitute lattice oxygen. In figure 5.17 it can also be seen that the sample calcined at 800 °C was significantly blue shifted indicating an increase in band gap. This may be due to the increased crystallinity of the sodium titanate phase as seen from the XRD (figure 5.15).

Applications of sodium titanates include photocatalysis[281] and the photocatalytic activity of the synthesized sodium titanates was compared with that of TiO_2 powders shown

previously. To maintain consistency methylene blue was the model pollutant used for degradation studies.

Use of multiple dopants did not cause significant improvement in the photocatalytic activity of the materials (table 5.4). On comparison of the multiple doped materials with S-TiO_2 there was a substantial reduction in the degradation rate constant. The most active S-TiO_2 sample degraded methylene blue at a rate of 43.1 x 10^{-2} min^{-1} compared with best performing co doped sample S, N-$Na_2Ti_6O_{13}$ (12.0 x 10^{-2} min^{-1}).

Table 5.4. First order rate constants for methylene blue degradation with co doped TiO_2

Sample	Ti:N:S molar ratio	Calcination Temperature (°C)	Rate Constant (min^{-1}, x 10^{-2})
3 % Ag, 1 % Al, S, N-TiO_2 & $Na_2Ti_6O_{13}$	1:0.5:4	500	4.7
3 % Ag, 1 % Al, S, N-TiO_2 & $Na_2Ti_6O_{13}$	1:0.5:4	600	6.1
3 % Ag, 1 % Al, S, N-TiO_2 & $Na_2Ti_6O_{13}$	1:0.5:4	700	4.5
3 % Ag, 1 % Al, S, N-TiO_2 & $Na_2Ti_6O_{13}$	1:0.5:4	800	2.5
3 % Ag, S, N-$Na_2Ti_6O_{13}$	1:0.5:4	500	2.2
3 % Ag, S, N-$Na_2Ti_6O_{13}$	1:0.5:4	600	2.6
3 % Ag, S, N-$Na_2Ti_6O_{13}$	1:0.5:4	700	3.8
3 % Ag, S, N-$Na_2Ti_6O_{13}$	1:0.5:4	800	4.9
S, N- $Na_2Ti_6O_{13}$	1:0.5:4	500	9.2
S, N- $Na_2Ti_6O_{13}$	1:0.5:4	600	7.9
S, N- $Na_2Ti_6O_{13}$	1:0.5:4	700	12.0
S, N- $Na_2Ti_6O_{13}$	1:0.5:4	800	3.6

Infrared spectroscopy was employed to determine the diaminopropane-titanium interactions and to find how the addition of aluminium and sodium thiosulfate affect the atomic structure of the materials before calcination occurs.

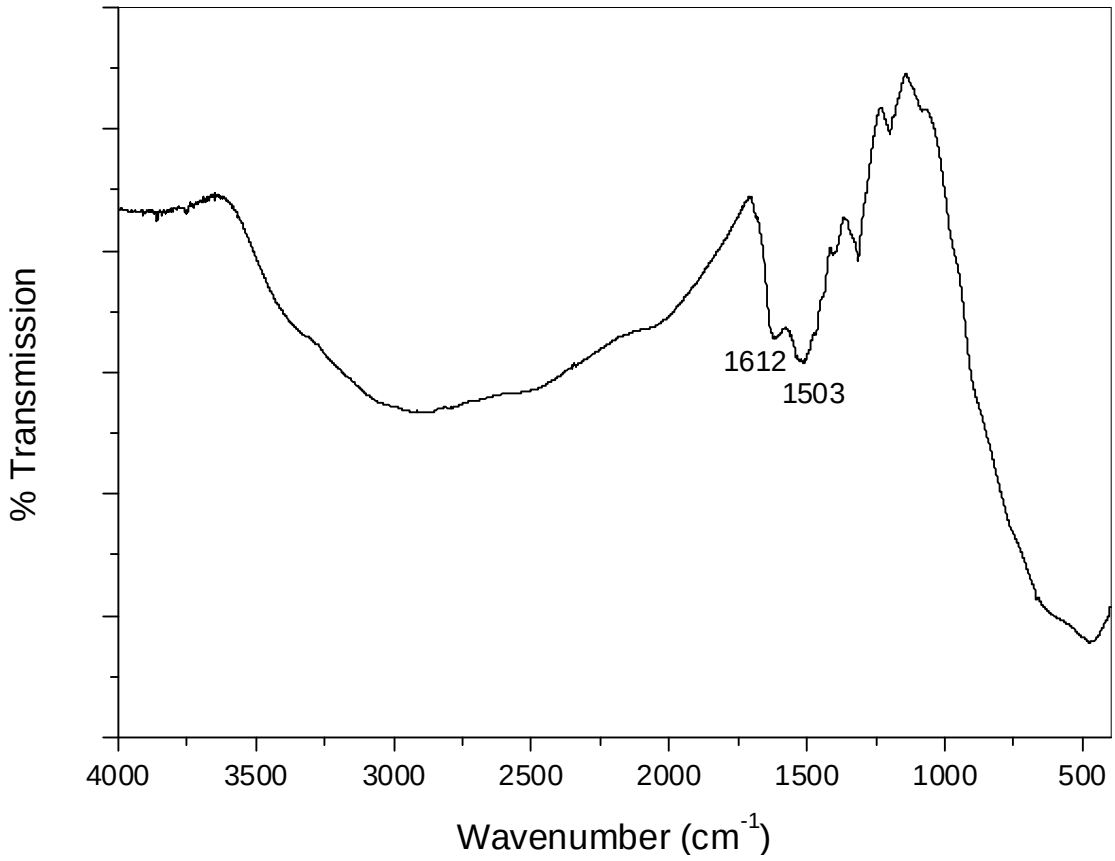

Figure 5.18. Infrared spectrum of N-TiO_2

Previously, researchers have shown through X-ray crystallography that both the nitrogen atoms from diaminopropane coordinate to metal centres to form a six membered ring.[282-285] The IR spectrum of N-TiO_2 shown in figure 5.18 shows signals at 1612 and 1503 cm^{-1} caused by NH_2 vibrations indicating that nitrogen is chelated to the titanium metal centre increasing its coordination number to six, forming a chelated complex as shown in figure 5.19.

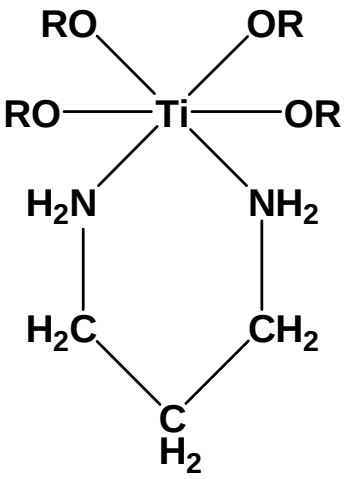

Figure 5.19. Diaminopropane chelated to titanium tetraisopropoxide

Modification of titanium alkoxides with chelating agents is known to promote thermally stable anatase phase at increased temperatures.[172] However, the employment of chelating agents for the synthesis of stable anatase typically involves the formation of bridging structures that promote the formation of polymeric chains with extensive cross linking.[217] These chains remain stable throughout much of the condensation process, resulting in extended anatase to rutile transformation temperatures.[207,220] The opposite is occurring with the addition of diaminopropane and instead of the formation of a highly branched polymeric structure, monomeric titanium amine structures are formed that may interact with neighbouring titanium amines through hydrogen bonding. During the condensation process the monomeric structures with little or no cross-linking are structurally weak and will readily collapse under calcination to form rutile as was seen through XRD. An infrared spectrum of Al, Ag, S, N-TiO_2 was identical to that shown in figure 5.18 but as was seen with XRD, once aluminium is removed from the synthesis, sodium ions become predominant in the reaction pathway thus forming sodium titanates.

The infrared spectrum of N, S-TiO_2 without the presence of aluminium (figure 5.20) shows that diaminopropane is not coordinating to titanium as was the case previously.

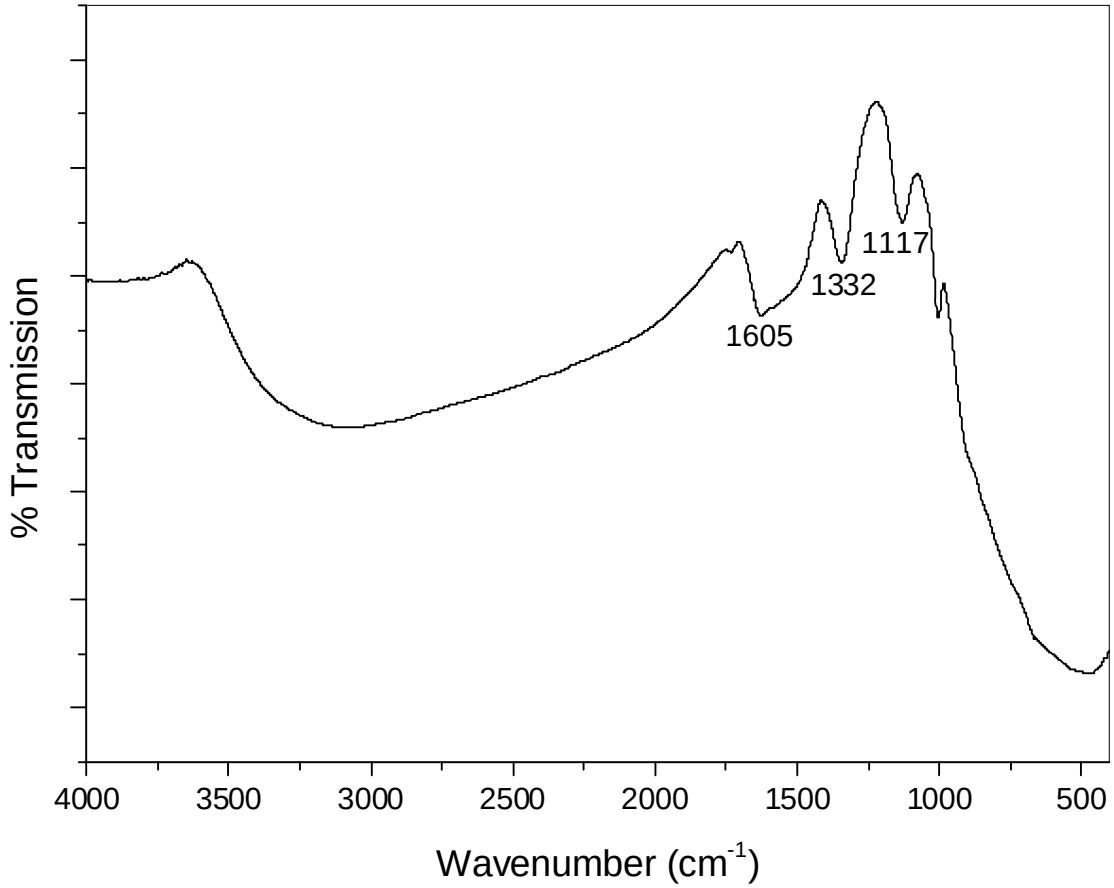

Figure 5.20. Infrared spectrum of N, S-TiO_2

The broad peak at 1605 cm^{-1} is assigned to the thiosulfate ion ($S_2O_3^{2-}$) but it most likely overlaps with NH_2 bending frequencies. Peaks at 1332 and 1117 cm^{-1} also show the presence of sodium thiosulfate. The IR spectrum shows that the thiosulfate ion has not been removed indicating that sodium ions may also be present. Diaminopropane may preferentially chelate to sodium or chelated sodium may coexist with chelated titanium. It may be the ability of diaminopropane to interact with sodium thiosulfate that causes sodium ions to participate in the reaction pathway. The retention of sodium ions during condensation results in the formation of sodium titanate.

5.3 Conclusions

A variety of dopant sources and synthesis techniques were employed for the doping of TiO_2. The resulting materials were characterised and the photocatalytic efficiency was examined. Modification with aluminium was shown to stabilise titanium dioxide as anatase at higher temperatures than TiO_2 synthesised without aluminium. Nitrogen was successfully inserted into the TiO_2 lattice through a simple sol-gel technique. Visible light absorption of N-TiO_2 was shown through diffuse reflectance spectroscopy. With optimum N and Al amounts determined, a combination of Al, N-TiO_2 materials was synthesised. N doped TiO_2 powders were modified with silver in an attempt to reduce recombination therefore increasing the photocatalytic activity. The resulting silver modified materials showed slightly improved degradation rates.

Dimethylsulfoxide and sodium thiosulfate were investigated as potential sources for the synthesis of sulfur doped TiO_2. Neither source produced visible light activated TiO_2 but S-TiO_2 synthesised from $Na_2S_2O_3$ resulted in powders that could degrade methylene blue at greater rates (0.43 min^{-1}) than the industrial standard, Degussa P25 (0.29 min^{-1}).

Optimum dopant amounts were determined and a combination of Al, Ag, N and S was used to synthesise TiO_2 materials.

It was discovered that the addition of sodium thiosulfate in the presence of diaminopropane results in the formation of sodium titanates. Aluminium was found to inhibit the influence of sodium and give TiO_2 anatase and rutile as dominant phases beside sodium titanate, but without the presence of aluminium, sodium titanates were the only phase formed indicating that aluminium stabilised TiO_2 anatase and rutile but without aluminium, the presence of 1,3-diaminopropane resulted in the retention of sodium from $Na_2S_2O_3$, therefore forming sodium titanate.

Through infrared spectroscopy it was determined that diaminopropane chelates to titanium forming a six membered ring, the chelated titanium amine results in the formation of titanium isopropoxide monomeric units that readily form rutile at low

temperatures. The inclusion of sodium thiosulfate results in the formation of a different complex that, when calcined, forms sodium titanate.

6 Sol-Gel Synthesis of Zinc Oxide/Titanium Dioxide Hybrid and the Resulting Formation of Zinc Titanates

6.1 Introduction

In the previous chapter it was shown that when sodium ions are present during the calcination of the samples, sodium titanates can form. This chapter presents results that were found when the synthesis of zinc oxide-titanium dioxide heterojunctions was attempted through a sol-gel route. Nano composites of both ZnO and TiO_2 semiconductors have been reported to show high photocatalytic activity. It is believed that high photocatalytic activity is caused by the promotion of charge separation, slowing down electron/hole recombination, therefore facilitating the photocatalytic mechanism.[286-288] Problems associated with the simultaneous synthesis of ZnO/TiO_2 composites is the formation of zinc titanates.

The simultaneous synthesis of a ZnO/TiO_2 composite usually results in the formation of one or more of the three known compounds from the ZnO-TiO_2 system. They are Zn_2TiO_4 (zinc orthotitanate) with cubic spinel crystal structure, $Zn_2Ti_3O_8$ with cubic defect spinel structure and $ZnTiO_3$ (zinc metatitanate) with rhombohedral ilmenite structure.[289-292] $Zn_2Ti_3O_8$ is the metastable, low temperature form of $ZnTiO_3$[292] but pure $ZnTiO_3$ is not easily obtained because it transforms into Zn_2TiO_4 and rutile.[290,291]

Zinc orthotitanate (Zn_2TiO_4) is an inverse spinel that has been used as a catalyst and a pigment.[293] As a catalyst it is used as sorbent for the removal of sulfur from coal gasification product gases, in hot gas desulfurization units, at temperatures in the range 400 – 700 °C. Zinc orthotitanate can easily withstand these temperatures and it is also one of the leading regenerable catalysts.[293-299] Zn_2TiO_4 may also be used for the photocatalytic splitting of water and the photocatalytic degradation of organic compounds.[300] Like other semiconductor photocatalyts, it has a wide band gap (3.1 eV) restricting its photocatalytic activity to UV light.[300,301] It is usually synthesized by solid state reaction at high temperatures and typically, when a temperature below 1000 °C is used; longer heat treatments times are required.[314,315,317,319,323] Alternative synthesis methods have been employed such as the co-precipitation method. Heat treatment at 700 °C for 2 hours resulted in the formation of zinc orthotitanate, but secondary phases

were also present.[295] A single phase material was obtained by Lew *et al* using the citrate method followed by heat treatment at 720 °C for 12 h.[297] Spinel type Zn_2TiO_4 was prepared by solid state reaction of ZnO and TiO_2 in molar ratios 3:2 at 1350 °C.[302,303]

In the present study, a range of ratios of titanium and zinc precursors have been employed for the synthesis of ZnO/TiO_2 systems. The calcined powders were investigated by XRD and in order to investigate the molecular structure of the amorphous samples, FTIR and Raman spectroscopic techniques were employed. At optimum molar ratios, pure Zn_2TiO_4 was formed under low heating temperatures for short periods of time.

6.2 Results

6.2.1 Excess of titanium precursor

Several researchers have investigated the phase changes associated with zinc titanates.[290,291,304,305] The three crystal structures known to exist in the ZnO-TiO_2 system include; Zn_2TiO_4 (zinc orthotitanate), $ZnTiO_3$ (zinc metatitanate) and $Zn_2Ti_3O_8$.[289-292,304] $Zn_2Ti_3O_8$ is widely regarded as being a metastable form of $ZnTiO_3$.[292] However, Sheinkman *et al* found that $Zn_2Ti_3O_8$ formed when anatase TiO_2 was used as the starting TiO_2 materials in a solid state synthesis but when rutile was used, $ZnTiO_3$ was formed instead.[304,305] These results were attributed to the similarity in crystal structure between anatase and $Zn_2Ti_3O_8$ in one case and similarities between rutile and $ZnTiO_3$ in the other. Much research has been carried out on the solid state synthesis of these materials, but sol-gel synthesis has received less attention.

From the sol-gel synthesised materials in this investigation, upon calcination some interesting trends were observed. It was possible to estimate the phase compositions through integration of the largest, non-overlapping peaks as was shown by Yang *et al*.[305] The calculated phase compositions of samples TZ-4:1, TZ-4:2 and TZ-4:3 are shown in figures 6.1, 6.2 and 6.3.

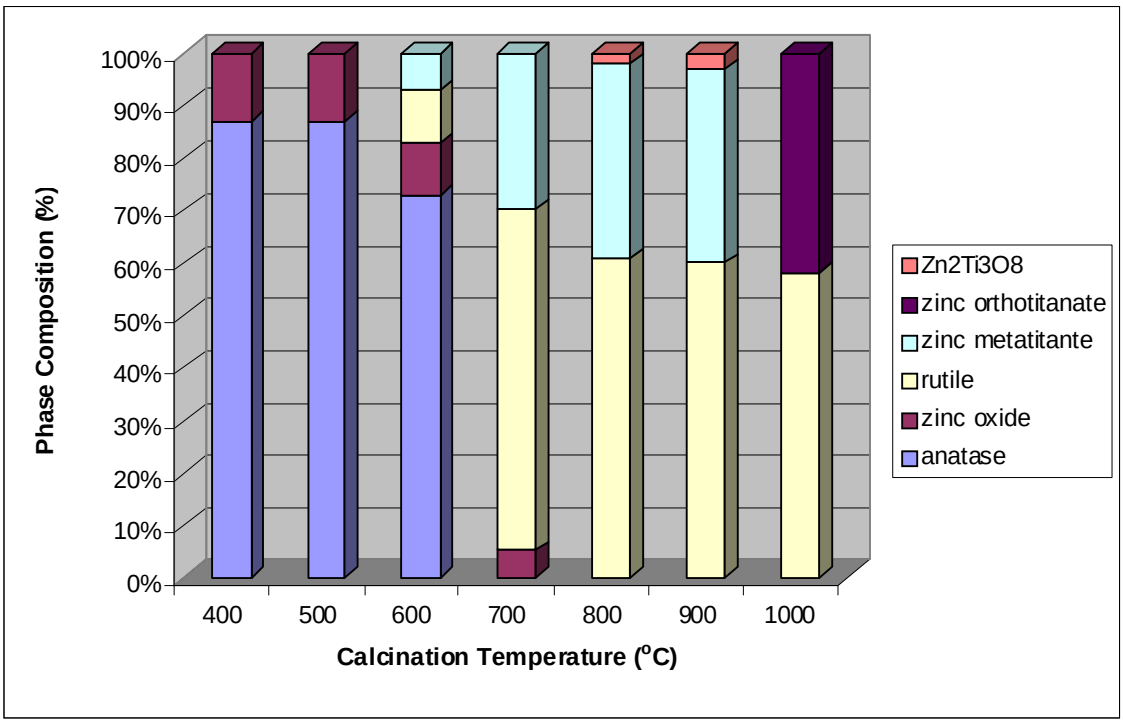

Figure 6.1. Percentage phase composition of TZ-4:1

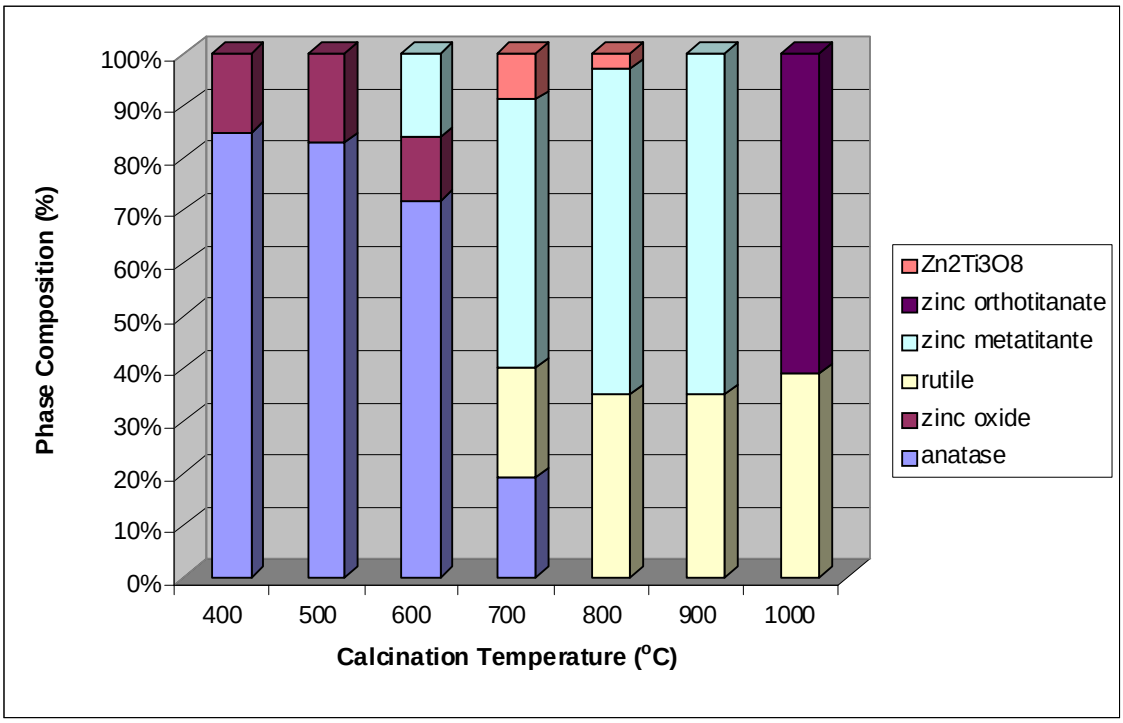

Figure 6.2. Percentage phase composition of TZ-4:2

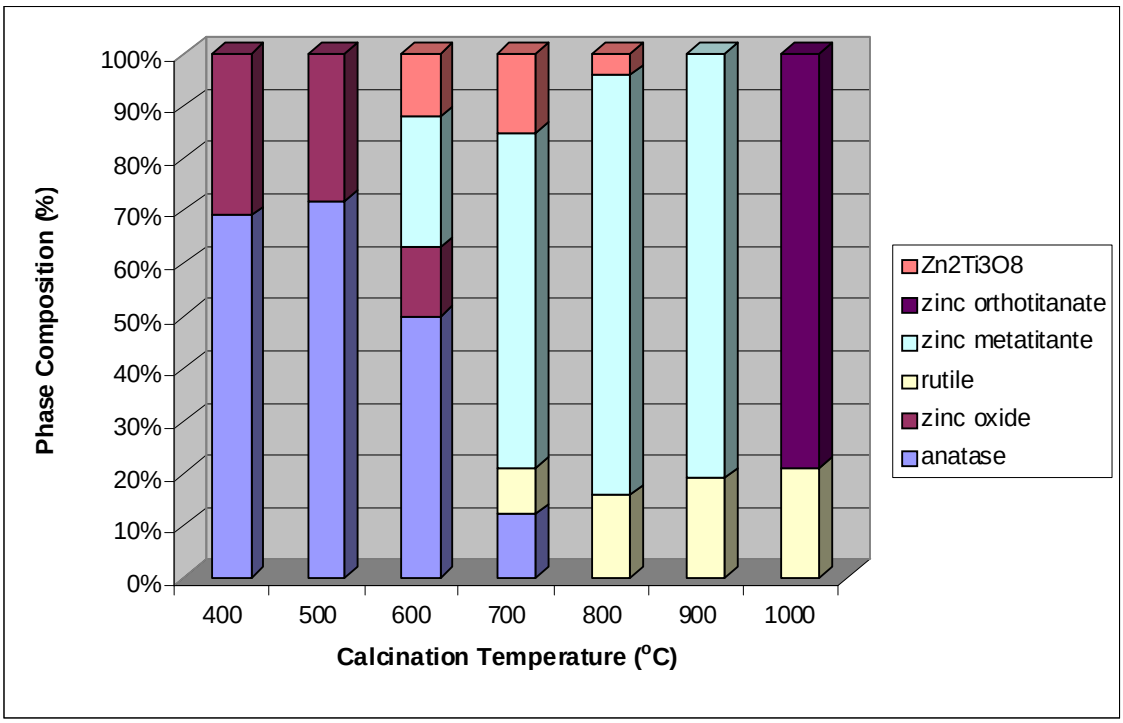

Figure 6.3. Percentage phase composition of TZ-4:3

Sample TZ-4:1 has the greatest excess of titanium precursor when compared with the other samples. This is clearly reflected in the composition of the phases. The titanium dioxide phases, anatase and rutile dominate the sample compositions at all calcination temperatures. Anatase dominates at temperatures 400 – 600 °C and from 700 – 1000 °C rutile is the predominant phase. At calcination temperatures 400 and 500 °C, TiO_2 (87 %) and ZnO (13 %) exist separately. At 600 °C the metastable[306] zinc metatitante (7 %, $ZnTiO_3$) begins to form, the crystallisation of zinc metatitante then accelerates as the temperature increases. At 700, 800 and 900 °C the sample is composed of 30 – 40 % zinc metatitante. Traces of the cubic spinel $Zn_2Ti_3O_8$ (2 – 3 %) can be found at 800 and 900 °C and at 1000 °C zinc orthotitante (42 %) and rutile are the only phases present.

As the amount of zinc precursor is increased (TZ-4:2 and TZ-4:3) the titania phase concentration is reduced and the amount of zinc titanates present increases as expected. As shown with TZ-4:1, for TZ-4:2 at 400 and 500 °C anatase (85 %) and zinc oxide are the only phases present, this is also seen for TZ-4:3 at 400 and 500 °C. As the temperature increases zinc titantes begin to form. It is interesting to note that at 600

°C, rutile is present for TZ-4:1, but rutile doesn't form until 700 °C for TZ-4:2 and TZ-4:3. Indicating that increased amounts of zinc precursor, delay the anatase to rutile transformation which is the opposite to that observed by Liu *et al*.[306] Samples TZ-4:2 and TZ-4:3 also contain anatase at 700 °C, TZ-4:1 does not, providing further evidence that increased amounts of zinc precursor delay the anatase to rutile transformation. Increased amounts of zinc precursor also promote formation of the cubic spinel $Zn_2Ti_3O_8$ structure. For TZ-4:1, it forms at 800 °C (3 %), it is seen at 700 °C with TZ-4:2 (9 %) and it forms at 600 °C for TZ-4:3 (12 %). Also, as can be expected, at 1000 °C all samples consist of only zinc orthotitanate and rutile. As the amount of zinc precursor is increased, the amount of zinc orthotitanate is also increased in an almost linear manner. Titanium:zinc ratios of 4:1 give 60/40 rutile/zinc orthotitante, ratios of 4:2 give 40/60 and a ratio of titanium:zinc 4:3 gives 80 % zinc orthotitante and 20 % rutile. A similar pattern is also observed for zinc metatitante but with other phases (such as $Zn_2Ti_3O_8$ and rutile) also present. For all samples, the percentage of zinc metatitante at 800 and 900 °C was almost identical to the amount of zinc orthotitanate at 1000 °C indicating a direct transformation zinc metatitanate to zinc orthotitanate.

6.2.2 Excess of zinc precursor

The X-ray diffractogram of TZ-1:4 (figure 6.4) shows that ZnO is the only crystal structure present at temperatures 400 and 500 °C. $Zn_2Ti_3O_8$ begins to form at 600 °C, and from 700 – 1000 °C, Zn2Ti3O8 and zinc oxide peak intensity grows stronger, indicating an increase in crystallinity for both phases. There are no TiO_2 phases present at any temperature.

As the titanium precursor was increased, TZ-3:4, anatase is present along with zinc oxide at calcination temperatures 400 and 500 °C (figure 6.5). At 600 and 700 °C the metastable $Zn_2Ti_3O_8$ is the only phase present. At 800 °C zinc metatitanate forms along with $Zn_2Ti_3O_8$ and at 900 °C the sample consists of zinc metatitante and either $Zn_2Ti_3O_8$ or zinc orthotitanate which is unclear due to similarities in the X-ray inflections. At 1000 °C zinc orthotitanate is the dominant phase with trace amounts of rutile present.

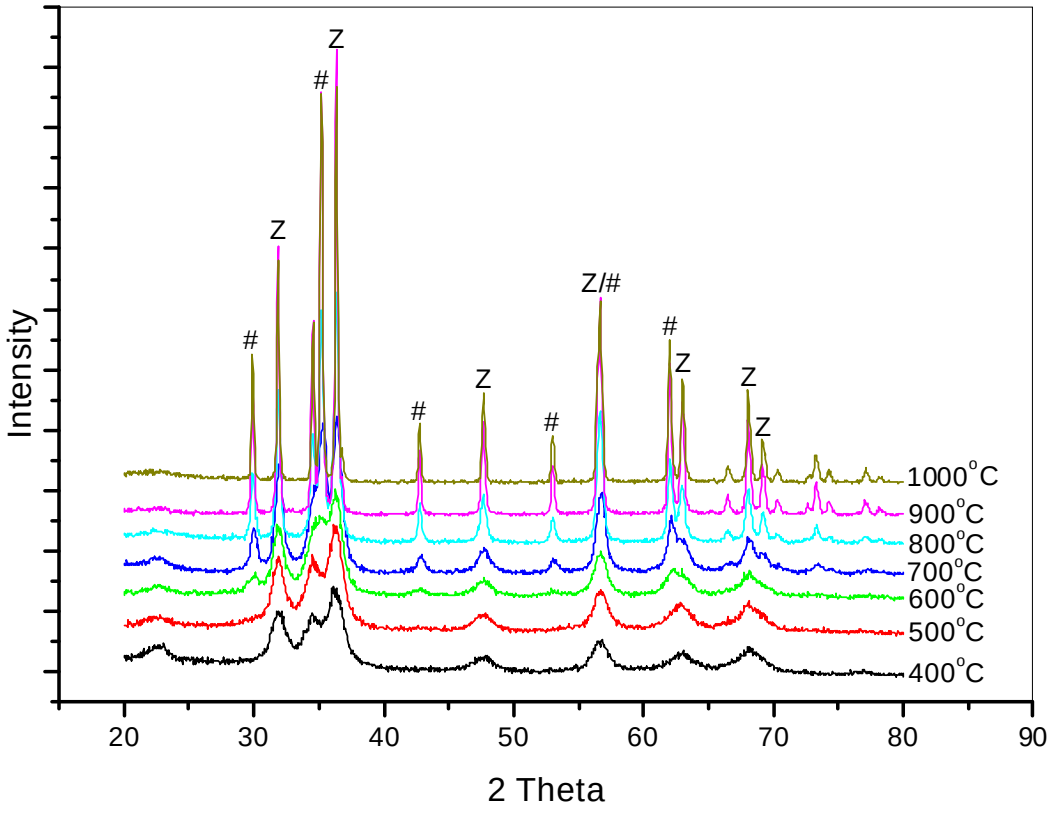

Figure 6.4. XRD of TZ-1:4, Z-ZnO and #-$TiZn_2O_4$

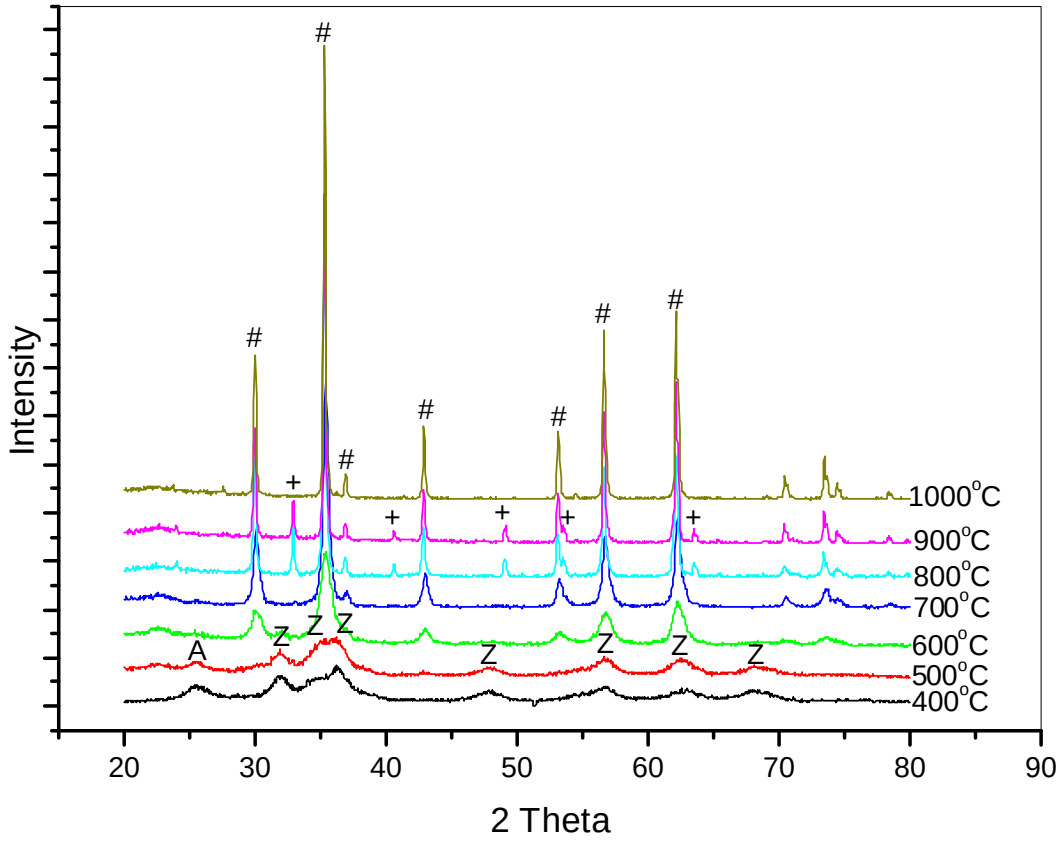

Figure 6.5. XRD of TZ-3:4, R-rutile, Z-ZnO, +-$ZnTiO_3$ and #-$TiZn_2O_4$

Figures 6.6, 6.7 and 6.8 summarises the compositions for samples TZ-1:4, TZ-2:4 and TZ-3:4. For lower calcination temperatures the primary zinc oxide peak was overlapping with $Zn_2Ti_3O_8$ (and zinc orthotitanate) peak and as such the composition percentages could not be determined at temperatures 400 – 600 °C. However, from the XRD diffractograms (figure 6.4 and 6.5) it can be seen that zinc oxide is the only phase present at temperatures 400 and 500 °C for TZ-1:4 (figure 6.4) and the same was seen for TZ-2:4, however, figure 6.5 (TZ-3:4) shows that both anatase and zinc oxide are present at 400 and 500 °C, while at 600 and 700 °C the only the metastable $Zn_2Ti_3O_8$ exists. From figures 6.6, 6.7 and 6.8, it is clear that the amount of $Zn_2Ti_3O_8$ increases with increasing amounts of titanium precursor at temperatures 700 – 900 °C. The same trend is also noticed for zinc orthotitanate. Results infer that $Zn_2Ti_3O_8$ directly transforms into zinc orthotitanate without affecting the zinc oxide crystal as can be seen for samples TZ-1:4 and TZ-2:4 (figure 6.6 and 6.7). Results for sample TZ-3:4 (figure 6.8) indicate the same direct $Zn_2Ti_3O_8$ to zinc orthotitanate transformation with the minor phase, zinc metatitanate transforming to rutile.

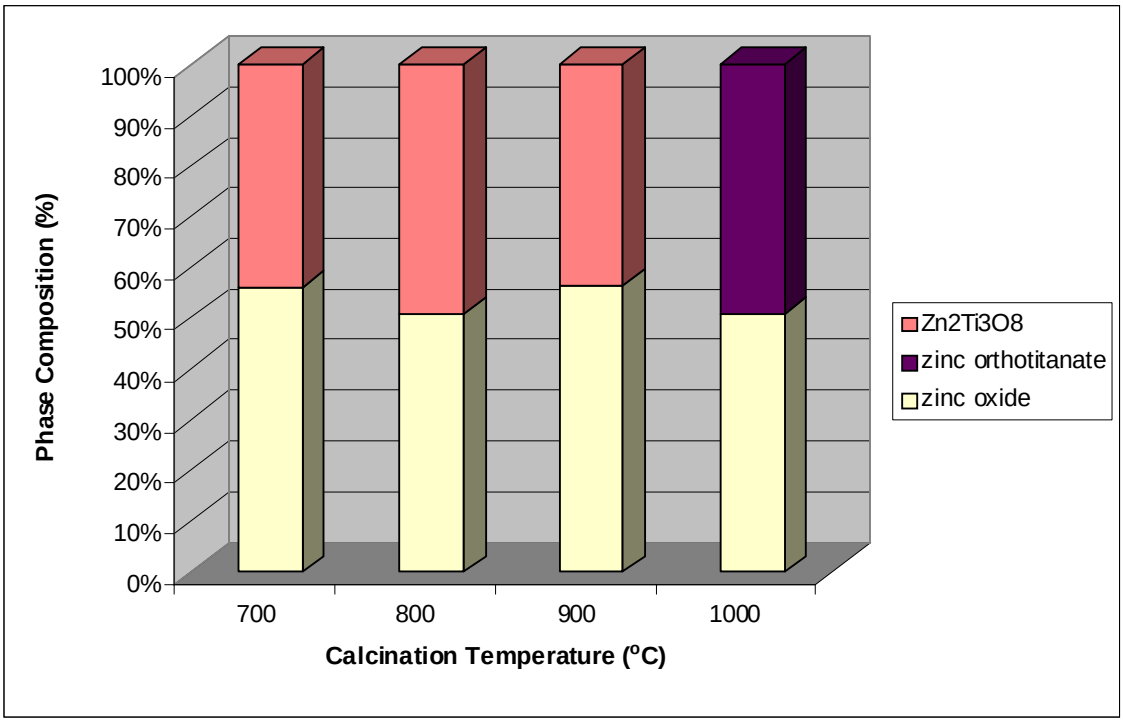

Figure 6.6. Phase composition of TZ-1:4

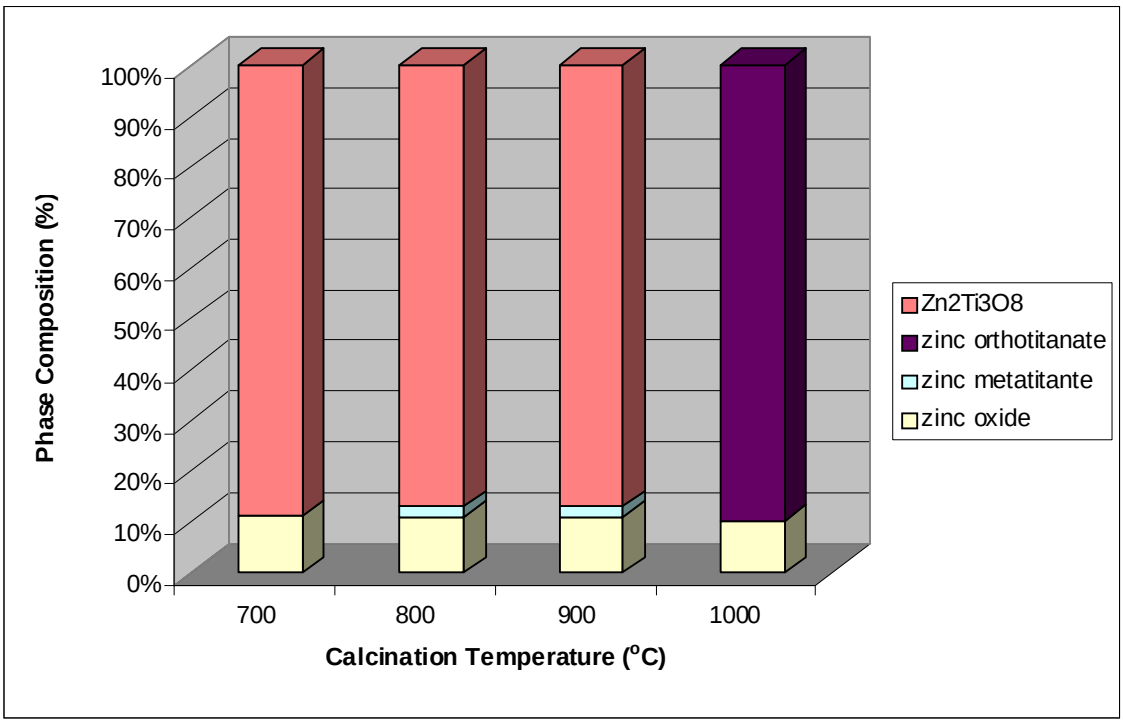

Figure 6.7. Phase composition of TZ-2:4

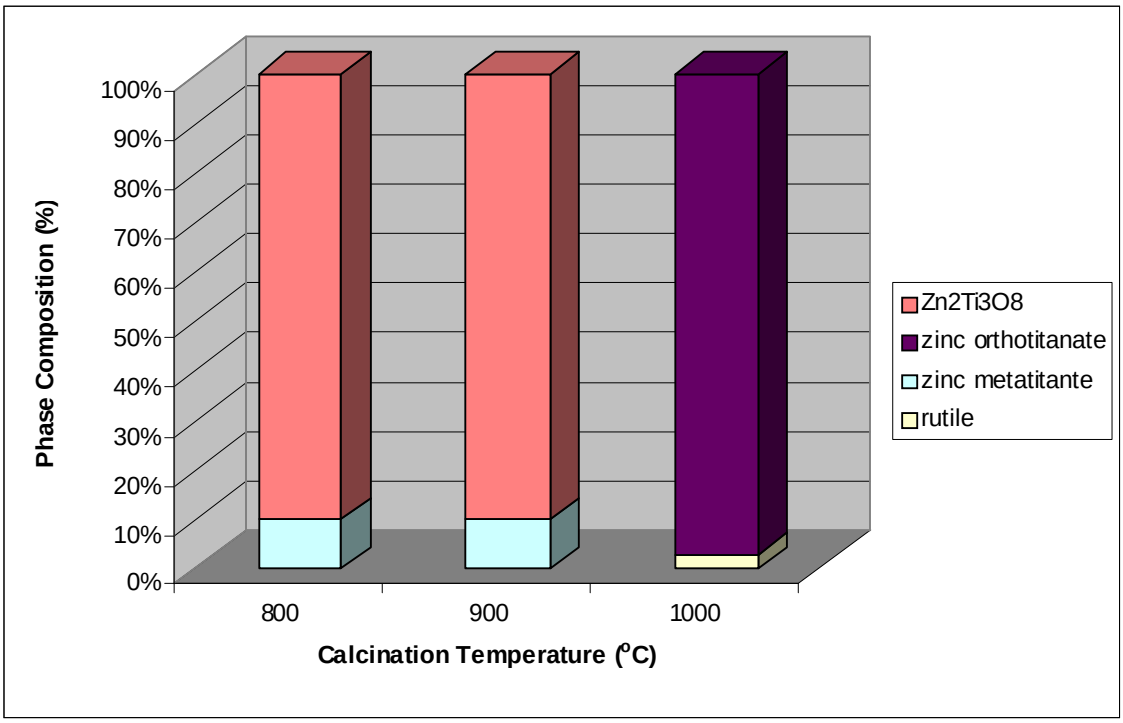

Figure 6.8. Phase composition of TZ-3:4

The results show that near identical amounts of $Zn_2Ti_3O_8$ transform to zinc orthotitanate when zinc precursor is in excess over titanium, this behaviour is distinctly different to the excess titanium system where results showed that zinc metatitanate transformed to

zinc orthotitanate. Since this synthesis is not a typical solid state reaction but a sol-gel reaction of titanium and zinc precursors, it is necessary to understand if the amorphous metal oxide structure influences the final crystalline structure. Therefore, to determine what is happening with the metal oxide system in the early stages of the reaction, FTIR and Raman spectroscopic techniques were carried out on the samples before calcination to determine the structure of the amorphous metal-oxide frameworks.

6.2.3 Infrared spectroscopy

6.2.3.1 Excess titanium precursor

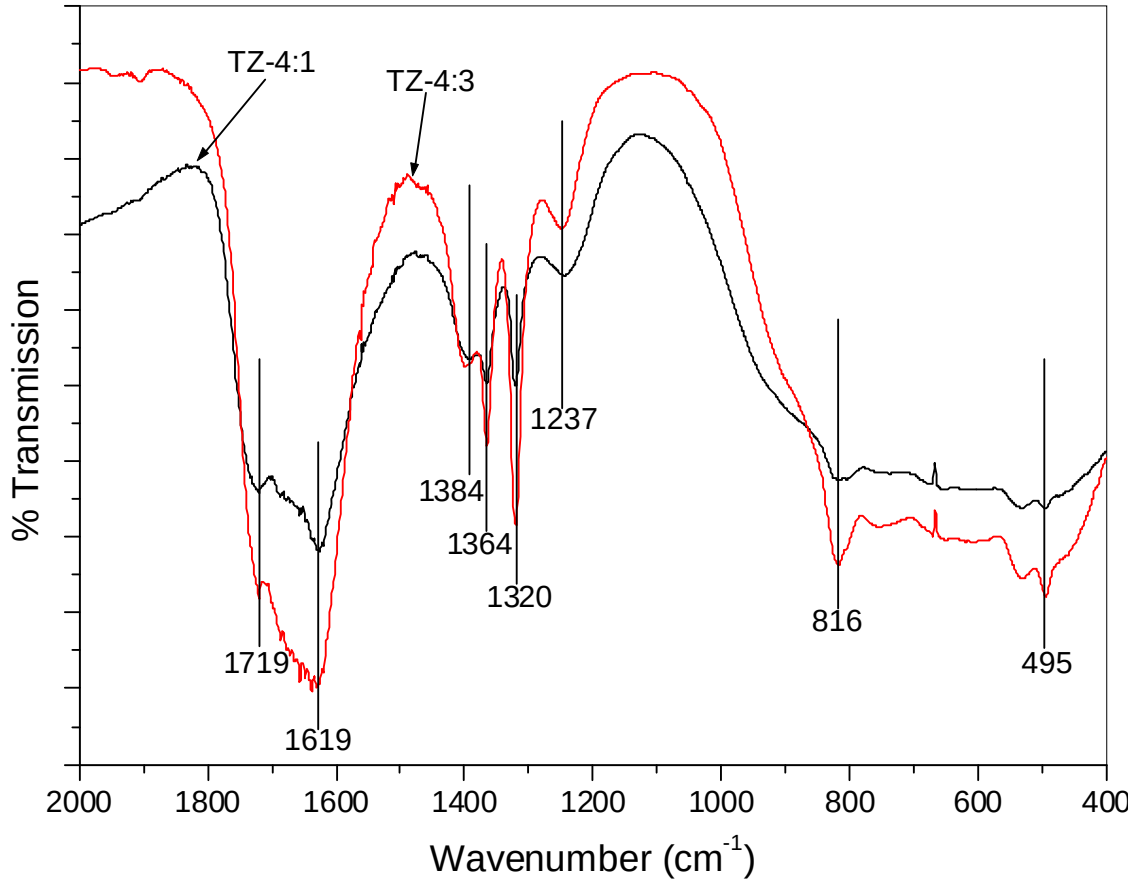

Figure 6.9. IR spectra of TZ-4:1 and TZ-4:3

Table 6.1. Assigned frequencies for IR spectra of TZ-4:1 and TZ-4:3.

Observed frequency (cm^{-1})	Assignments
1719	$\nu_{asym}(COO^-)$ titanium oxalate
1619	$\nu_{asym}(COO^-)$ zinc oxalate
1384	$\nu_{sym}(COO^-)$ titanium oxalate
1364	$\nu_{sym}(COO^-)$ zinc oxalate
1320	$\nu_{sym}(COO^-)$ zinc oxalate
1237	$\nu_{sym}(COO^-)$ titanium oxalate
816	δ_{asym}(O-C-O) zinc oxalate
495	ν(M-O) and δ_{asym}(C-C-O) zinc oxalate

Figure 6.9 shows the IR spectra of samples TZ-4:1 and TZ-4:3 before calcination. The assigned signals are summarized in table 6.1. The zinc oxalate signals are in agreement with Gabal *et al*.[307] Asymmetric (1719 cm^{-1}) and symmetric carboxylate stretches (1384 and 1237 cm^{-1}) are assigned to titanium oxalate. Comparing the IR spectra shown in figure 6.9 it can be seen that the presence of additional amounts of zinc cause an increase in the zinc oxalate $\nu_{asym}(COO^-)$ stretch at 1619 cm^{-1} relative to its titanium oxalate equivalent at 1719 cm^{-1}. There is also an increase in the $\nu_{sym}(COO^-)$ stretches of zinc oxalate (1364 and 1320 cm^{-1}) compared to their titanium counterpart (1384 and 1237 cm^{-1}). These results are to be expected as an increase in zinc oxalate is going to provide an increase in the resulting peak intensities. The initial amounts of titanium and zinc will therefore control the composition of the metal oxalate chain. Any infrared features typical of Ti-OR coordination bonds[308] are not present in figure 6.9, suggesting that a polymeric zinc/titanium oxalate exists where OR groups have been removed through hydrolysis/condensation reactions from the sol-gel synthesis.[308]

6.2.3.2 Excess zinc precursor

When excess titanium is present XRD has shown that at low calcination temperatures (400 – 600 °C) anatase TiO_2 is favoured over zinc oxide and at higher temperatures (700 – 1000 °C) rutile TiO_2 dominates while zinc metatitanate transforms into zinc orthotitanate between 900 and 1000 °C.

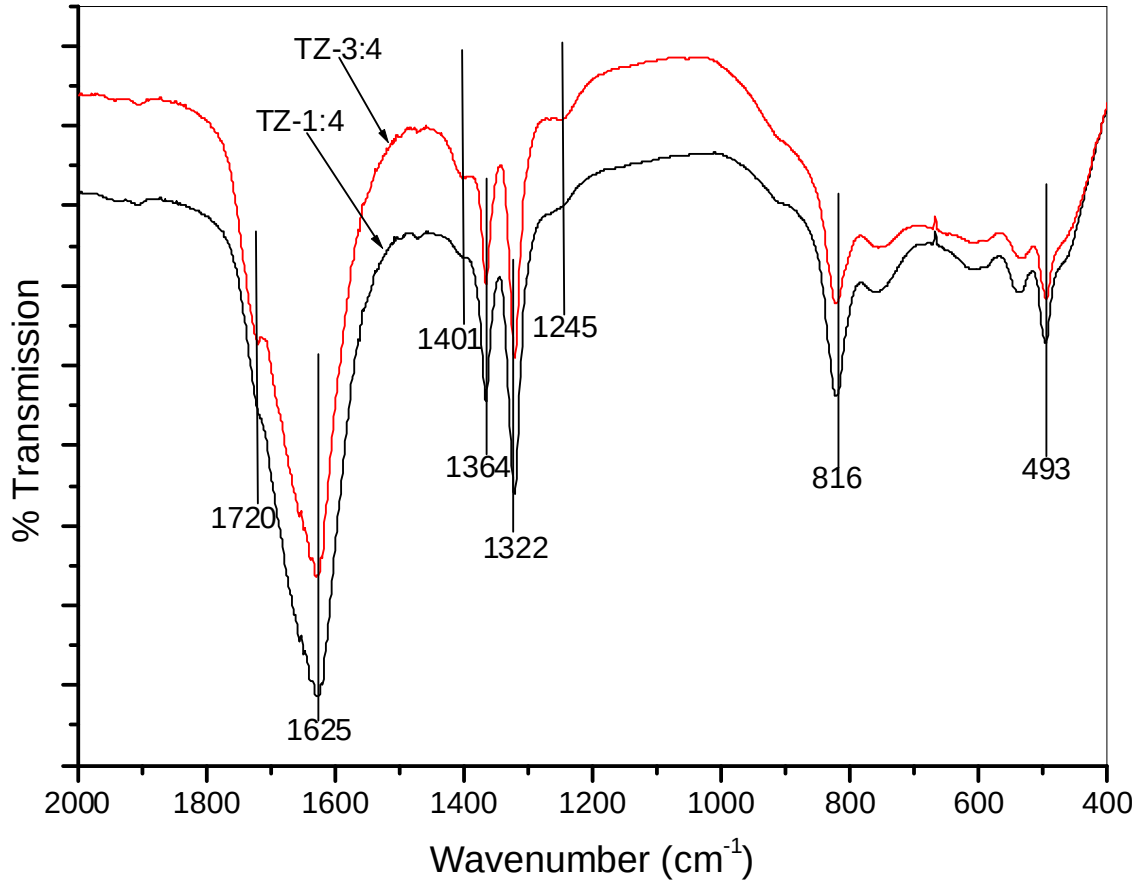

Figure 6.10. IR spectra of TZ-1:4 and TZ-3:4

The IR spectra of samples TZ-1:4 and TZ-3:4 are shown in figure 6.10 with peaks of interest labelled. For TZ-1:4 peaks at 1720, 1401 and 1245 cm^{-1} which represent COO^-_{asym} and COO^-_{sym} of titanium oxalate respectively are significantly decreased when compared with the IR spectrum of TZ-4:1 (figure 6.9). However, as the titanium ratio increases (TZ-3:4), peaks at 1720, 1401 and 1245 cm^{-1} appear, indicating the presence of titanium oxalate in the metal oxalate chain. Peaks at 816 and 493 cm^{-1} representing δ_{asym}(O-C-O) and ν(M-O), δ_{asym}(C-C-O) respectively are more intense for sample TZ-

1:4 than for TZ-3:4. Again this shows that with greater amounts of zinc precursor, zinc oxalate dominates the metal oxalate chain network.

Symmetric and asymmetric carboxylate stretches from titanium and zinc oxalate are clearly present in shown IR spectra. As expected when the zinc precursor is in excess, carboxylate stretches of titanium oxalate are weak. However, when titanium is in excess, strong signals representative of zinc oxalate are still clear. This can be explained through the synthesis where zinc acetate is first reacted with oxalic acid to give zinc oxalate before titanium isopropoxide is added. Therefore, TTIP can chelate with unreacted oxalic acid.

6.2.4 Raman spectroscopy

6.2.4.1 Excess titanium precursor

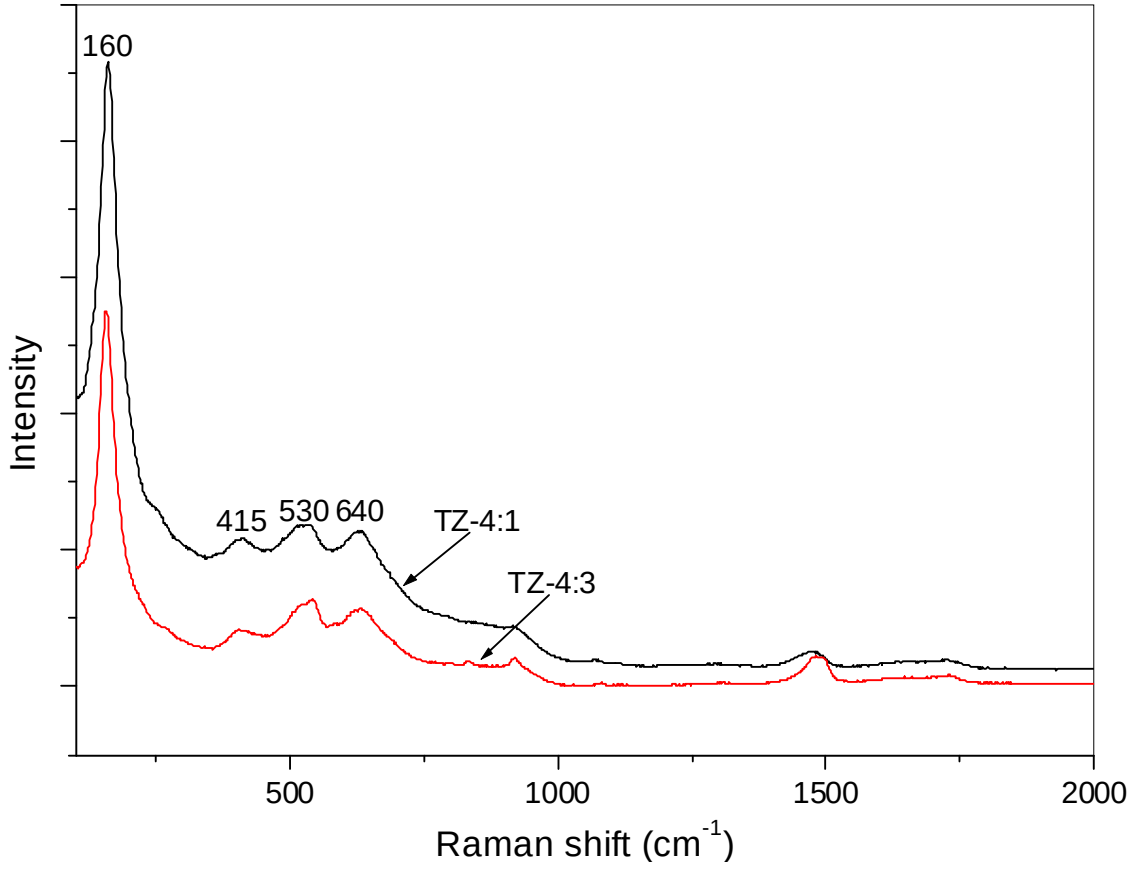

Figure 6.11. Raman spectra of TZ-4:1 and TZ-4:3

Figure 6.11 shows the Raman spectra of the samples TZ-4:1 and TZ-4:3 where titanium is in excess. The range 0-1000 cm^{-1} represents the M-O stretches of the

material. Peaks at 158, 418, 540 and 643 cm^{-1} are similar to those of the anatase four peak pattern.[222-224] It has been previously reported that during the crystallization process, titanium hydrolysate forms anatase/rutile like structures that can be detected by Raman. These Raman spectral patterns then disappear before the material crystallizes into anatase.[224] Raman studies show that Ti-O structures are dominating the metal oxide framework during the early processes of the reaction. This is expected as the titanium precursor is in excess over that of the zinc precursor. When the zinc precursor exceeds the titanium precursor, Raman spectra with different spectral profiles are obtained.

6.2.4.2 Excess zinc precursor

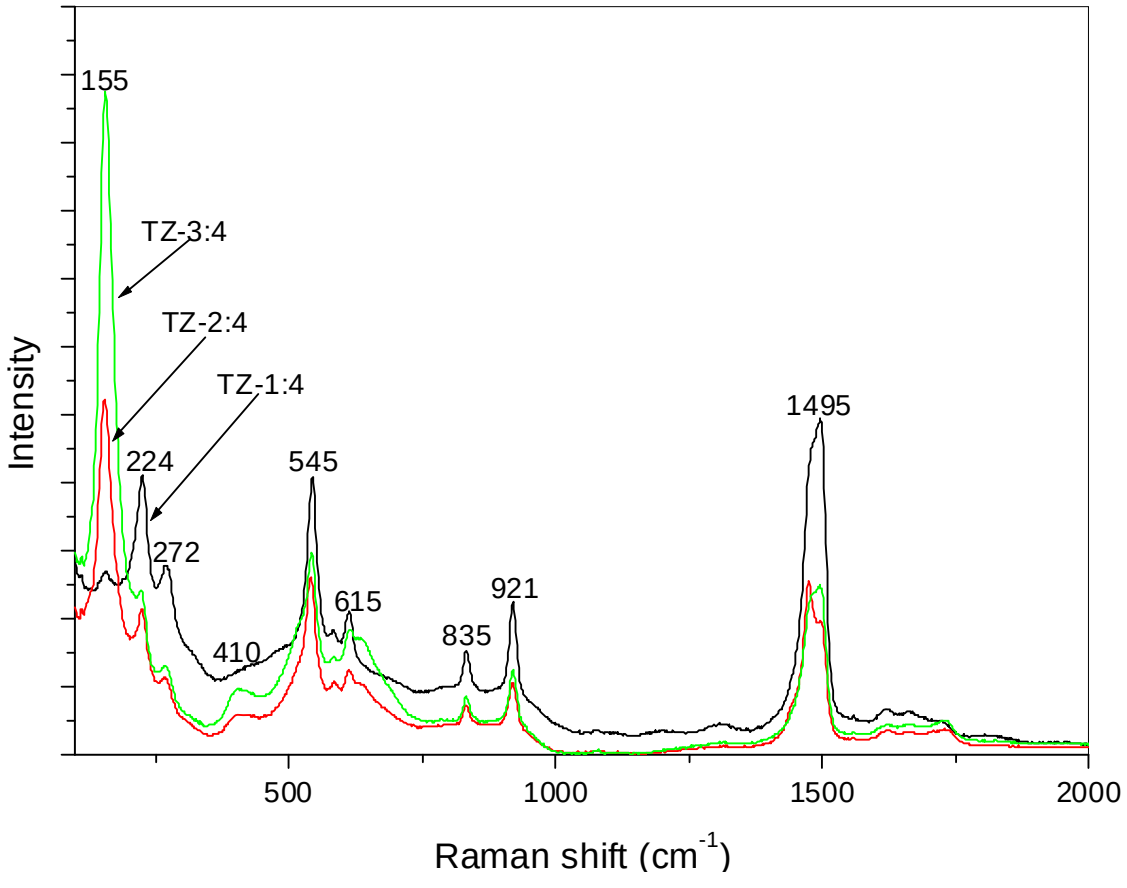

Figure 6.12. Raman spectra of TZ-1:4, TZ-2:4 and TZ-3:4

The Raman spectra of excess zinc samples TZ-1:4, TZ-2:4 and TZ-3:4 is shown in figure 6.12. Peaks representative of the anatase four peak pattern[222-224] are present at 155, 415, 545 and 615 cm^{-1} for samples TZ-2:4 and TZ-3:4. All other signals in the

region 0 – 1000 cm^{-1} are believed to be caused by Zn-O contributions. There is a large signal at 1495 cm^{-1} due to $(COO^-)_{sym}$ stretching of the oxalate group. Comparing peak intensities of 1495 cm^{-1} with M-O peaks it is clear that this signal is largest relative to its surrounding peaks for TZ-1:4 and as the titanium ratio increases, the carboxylate peak decreases. Again, this is evidence of the dominant effect of zinc oxalate in the metal oxalate chain. The Raman spectra of TZ-2:4 and TZ-3:4 give similar peak positions to each other but on comparison of the profile of TZ-1:4, it can be seen that TZ-1:4 gives a spectrum that contains no similarities with either TZ-2:4 and TZ-3:4. In the spectra of TZ-2:4 and TZ-3:4 the increased levels of titanium lead to signals at 155, 415, 545 and 615 cm^{-1}, but the spectrum of TZ-1:4 does not display these peaks. It was therefore speculated that all peaks shown in the spectrum of TZ-1:4 (figure 6.12) arise from Zn-O stretches.

The presence of the highlighted peaks show the dominant influence of the titanium as the ratio is increased. Comparison of figure 6.11 with figure 6.12 also shows that Ti-O bonds give exceptionally higher Raman signals than Zn-O. It can also be shown upon comparison of both IR and Raman spectra that there is no coincidence between the peak profiles of either. This suggests that the rule of mutual exclusion may be applied to the titanium-zinc oxalate structures.[309] Applying the rule of mutual exclusion would indicate a centrosymmetric structure, where the metal atoms occupy a position equidistant from the coordinating oxygens.[309] Summarising the spectroscopic results it has been demonstrated that:

- Oxalic acid chelates to titanium to form titanium oxalate
- Increasing zinc oxalate causes reduction in asymmetric and symmetric carboxylate stretches from titanium oxalate and an increase in the symmetric stretch in Raman
- When Ti is in excess, the anatase four peak pattern dominates the Raman spectra and there is a broad signal without significant individual peak contributions in IR (400 – 1000 cm^{-1})
- When Zn is in excess, the four peak pattern is reduced in Raman and the IR spectra show individual peaks representative of O-C-O and M-O from zinc oxalate

- There is a metal oxalate chain composed of titanium and zinc
- Asymmetric and symmetric carboxylate stretches for zinc oxalate are always present in the IR spectra, but carboxylate stretches are only present for titanium oxalate at high ratios of the titanium precursor
- The rule of mutual exclusion can be applied, indicating the presence of a symmetric molecule

6.3 Discussion

The structure of zinc acetate was previously reported by Niekerk *et al*, they found that zinc was six-coordinated to acetate ligands and water. The acetate ligands were found to have chelating bidentate coordination, with two water molecules also coordinated to the zinc atom (figure 6.13).[310] Ishioka *et al* also showed the structure of zinc acetate dihydrate (figure 6.13) through X-ray crystallography.[311]

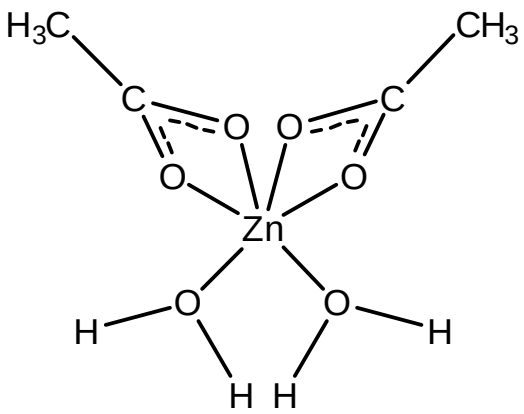

Figure 6.13. Molecular structure of zinc acetate dihydrate.

Reacting oxalic acid with zinc acetate forms the intermediate zinc oxalate (eqn. 6.1) as presented by Kanade *et al*.[312]

$Zn(CH_3COO)_2.2H_2O + H_2C_2O_4 \rightarrow ZnC_2O_4.2H_2O + 2HOAc + 2H_2O$ Equation 6.1

X-ray crystallographic studies of zinc oxalate show that zinc is octahedrally coordinated to six oxygen atoms[313,314] as shown in figure 6.14a. It is also been shown that divalent metal cations and oxalate groups generate an infinite chain arrangement as depicted in figure 6.14b.[315,316]

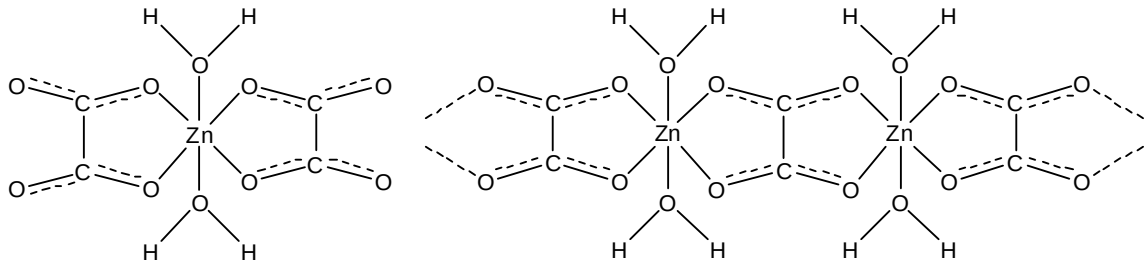

(a) (b)

Figure 6.14. Molecular structure of zinc oxalate dihydrate (a) and the infinite chain arrangement (b).

Thermal treatment of zinc oxalate leads to the formation of zinc oxide. TGA/DTA studies have shown the removal of water at 120 °C and the decomposition of zinc oxalate at 400 °C as shown in equation 6.2.[312]

$ZnC_2O_4.2H_2O + ½O_2 \rightarrow ZnO + 2CO_2 + 2H_2O$ Equation 6.2

The system under investigation in this study is not zinc oxalate alone but it also includes varying ratios of titanium isopropoxide (figure 6.15a) which consists of monomeric units.[179] It has been previously reported that acetic acid,[172,207] formic acid[317] and acetyl acetone[200] chelate to titanium isopropoxide. As was shown with zinc oxalate,[315,316] titanium isopropoxide also forms chains upon reaction with a chelating agent figure 6.15b.[192-194]

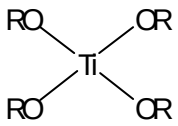

(a)

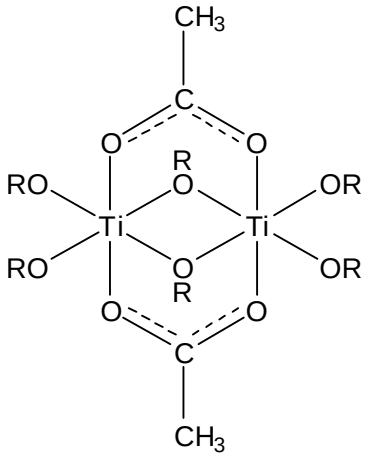

(b)

Figure 6.15. Molecular structure of titanium isopropoxide (a) and chelated titanium isopropoxide, titanium acetate (b)

During the sol-gel reaction of titanium alkoxides, the OR groups are preferentially hydrolysed while the ligands remain tightly bound throughout much of the condensation process. This promotes the formation of linear chains of Ti-O polymers composed of edge sharing octahedra.[207,220] The formation of these octahedra stabilises TiO_2 as anatase, lowering the anatase to rutile transformation temperature.[207,220]

Previous research has shown the structure of zinc oxalate[313,314] and titanium carboxylates.[172,207,317] However, to the best of the author's knowledge a combination of structures has not previously been investigated. From the results shown through IR and Raman it is known that titanium and zinc oxalate are present (figure 6.16), but it can not be shown if titanium oxalate chains exist separately from zinc oxalate chains or do they combine. X-ray diffraction results showed that initially crystalline ZnO or TiO_2 anatase formed separately and at higher calcination temperatures, zinc titanates were formed. This indicates that there were two separate metal oxalate chains formed during the synthesis (figure 6.16a & b).

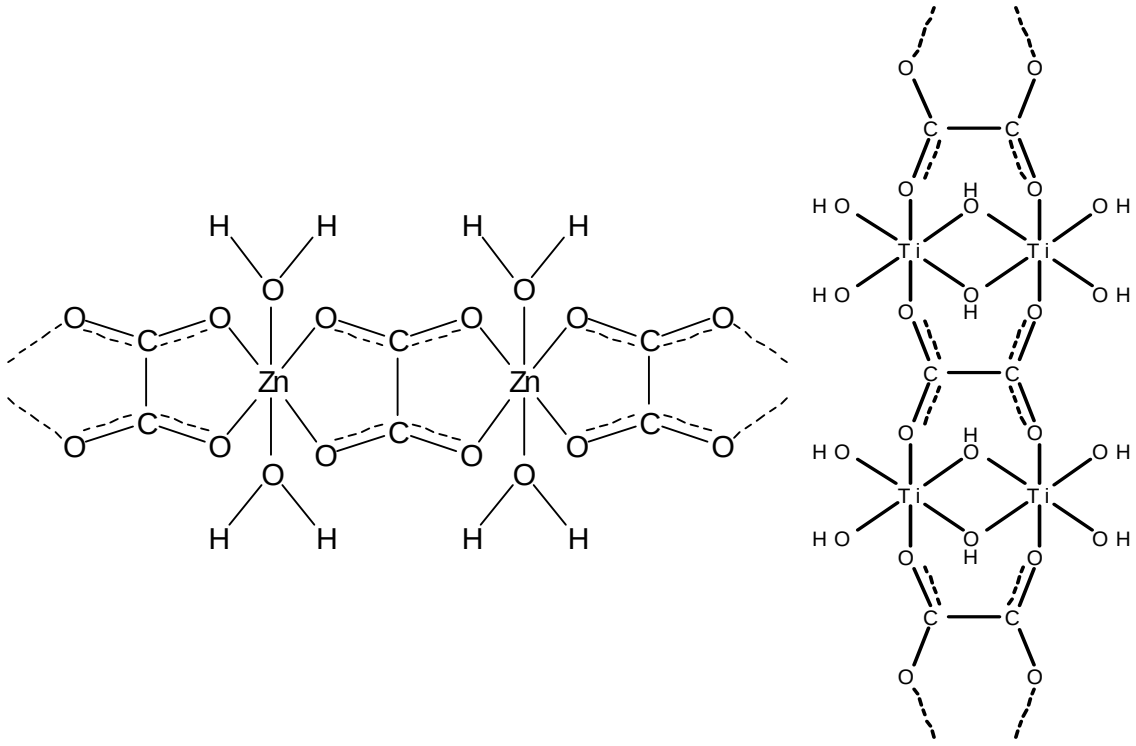

(a) (b)

Figure 6.16. Proposed structures of metal oxalate chains formed, zinc oxalate (a) and titanium oxalate (b)

As the condensation process proceeds with excess titanium (TZ-4:1), TiO_6 octahedra form TiO_2 anatase and ZnO_4 tetrahedra form ZnO (wurtzite). As the calcination temperature becomes more intense (≥ 600 °C), the TiO_6 octahedra and ZnO_4 tetrahedra undergo molecular rearrangement and phase transformation occurs. Zinc oxide tetrahedral and TiO_6 octahedra undergo further atomic movement and combine to form zinc titanates and rutile. The metastable zinc metatitanate and stable rutile exist at 800 and 900 °C with trace amounts of $Zn_2Ti_3O_8$ also present. At 1000 °C zinc metatitanate and $Zn_2Ti_3O_8$ decompose to form zinc orthotitanate, rutile remains the dominant phase. As the amount of zinc precursor increases (TZ-4:2 and TZ-4:3), the materials behave in a similar manner but with increasing amounts of zinc oxide at early calcination temperatures (400 and 500 °C) and greater amounts of zinc titanates at temperatures ≥ 700 °C. It is clear from the results (figure 6.1, 6.2 and 6.3), that the percentage of zinc titanate at 700 °C is very similar to the final percentage of zinc orthotitanate. The results have shown that at temperatures 700 – 900 °C for samples with excess titanium precursor, zinc metatitante is the dominant zinc titanate phase and is stable up to 900 °C, it then undergoes complete transformation to form zinc orthotitanate. Phase transformation is almost 100 % zinc metatitante to zinc orthotitanate, however, results do show that rutile is also formed. Calculated values for percentage conversion are 90 % for TZ-4:1, 93 % for TZ-4:2 and 98 % for TZ-4:3 reflecting an increase in conversion in line with increasing zinc precursor ratio.

Three different molar ratios where zinc precursors are in excess over titanium were also prepared. All three behaved differently to those where titanium was in excess. For all samples where zinc is in excess, accurate compositions at calcination temperatures 400 – 600 °C could not be obtained from the X-ray diffractograms as the peaks were not resolved but from the diffractograms it was clear that zinc oxide was the dominant phase at early temperatures with anatase also present in small amounts. However, the percentage composition was calculated from results of temperatures 700 °C onwards (figure 6.6, 6.7 and 6.8). When titanium was in excess a clear transformation of large compositions of zinc metatitanate to zinc orthotitanate was noticed. With excess zinc,

zinc metatitanate is not present in TZ-1:4, for TZ-2:4, trace amounts of zinc metatitanate are present at 800 and 900 °C and as the titanium ratio increases (TZ-3:4), larger amounts of zinc metatitanate are present at calcination temperatures 800 and 900 °C. With excess zinc, $Zn_2Ti_3O_8$ was the dominant, metastable phase formed at temperatures 700 – 900 °C, total phase transformation occurred at temperatures > 900 °C and zinc orthotitanate was formed. Unlike the excess titanium system where zinc metatitanate transformed to zinc orthotitanate and rutile with conversion percentages of between 90 – 98 %, when zinc was in excess it was $Zn_2Ti_3O_8$ combining with zinc oxide transforming into zinc orthotitanate. Conversion percentages of $Zn_2Ti_3O_8$ of greater than 100 % were calculated for TZ-1:4 (104 %), TZ-2:4 (101 %) and TZ-3:4 (107 %), values greater than 100 % are achieved because unlike zinc metatitanate that transforms to zinc orthotitanate and rutile, it appears that when zinc precursor is used in excess, $Zn_2Ti_3O_8$ is the favoured phase and it combines with zinc oxide to form zinc metatitanate.

The structures of all zinc titanates studied here share common features; they all consist of TiO_6 octahedra that are connected over common edges.[306] Anatase displays similarities with the spinel structures of Zn_2TiO_4 and $Zn_2Ti_3O_8$ but $ZnTiO_3$ shares its structure with rutile.[306,318] As such, it has previously been suggested that the formation of Zn_2TiO_4 and $Zn_2Ti_3O_8$ is limited by the presence of anatase and $ZnTiO_3$ only forms in the presence of rutile.[289,319] However, subsequent researchers have shown that this is not necessarily the case.[305,306,319] Results from the present study show that for samples where titanium is in excess (TZ-4:1, TZ-4:2 and TZ-4:3) anatase and zinc oxide are present during the early stages of crystallisation (400 – 600 °C) and as the calcination temperature increases, zinc metatitanate is formed, greater amounts of metatitanate are formed with an increased percentage of zinc oxide. These results suggest that in a sol-gel synthesis, the formation of zinc metatitanate is determined by the not only the presence of titanium dioxide (anatase or rutile) but also on the presence of zinc oxide. With excess zinc precursor (TZ-1:4, TZ-2:4 and TZ-3:4), zinc oxide was the dominant crystalline phase for calcination temperatures 400 – 600 °C and as the temperature

increased, $Zn_2Ti_3O_8$ became the dominant phase, transforming to zinc orthotitanate at 1000 °C. Again this result shows that anatase is not necessary for the formation of $Zn_2Ti_3O_8$ and that the percentage of zinc oxide influences what zinc titanate phase is formed. Photocatalytic studies of the synthesised materials displayed extremely weak photocatalytic activity.

6.4 Conclusions

A series of different phases of zinc titanate powders were successfully synthesised using a simple sol-gel technique. The effect of varying ratios of zinc/titanium precursors was investigated. The powders were calcined at temperatures ranging from 400 – 1000 °C and the crystalline phases of the powders were determined using X-ray diffraction.

To determine the molecular structures of the samples before they underwent calcination, infrared and Raman spectroscopy were employed. Possible structures of zinc oxalate and titanium oxalate were proposed, based on spectroscopic results obtained and from what is known from the literature. It was suggested that both the titanium oxalate and the zinc oxalate remain separate throughout the reaction which may be shown through XRD results of the powders calcined at low temperatures.

It was shown that low percentages of zinc oxide result in the formation of the metastable zinc metatitanate which ultimately transforms (90 – 98 % conversion) to zinc orthotitanate (< 900 °C) with rutile from 700 °C onwards. When zinc oxide is the dominant structure during the early stages of crystallisation (400 and 500 °C), $Zn_2Ti_3O_8$ is the zinc titanate phase preferentially formed as the calcination temperature increases. It transforms to zinc orthotitanate at 1000 °C.

7 Future Work

7.1 Investigate Alternative Carboxylate Chelating Agents

Much work has been carried out on the effect of organic chelating groups to titanium isopropoxide. Acetyl acetone,[200] alkanolamines,[201] and diols[202] are some of the organic chelating agents that have been investigated. Throughout chapters 3 and 4, this thesis focused on how the simplest carboxylic acid, formic acid interacts with titanium isopropoxide. Previous work carried out in our laboratory also looked at another simple carboxylic acid, acetic acid as a chemical modifier. Both were shown to result in the formation of anatase TiO_2 that is stable at increased temperature. However, there is a wide range of more complex carboxylic acids that need to be investigated. For example zinc oxide is synthesised using oxalic acid and although chapter 6 presented results showing that titanium oxalate may be formed when titanium isopropoxide is reacted with oxalic acid, this was part of a composite system and a more thorough study of the synthesis of TiO_2 when chelated with oxalic acid is necessary.

Carboxylic acids such as malic acid or tartaric acid (figure 7.1) could also delay the anatase to rutile transformation as well as producing nanomaterials of different shapes.

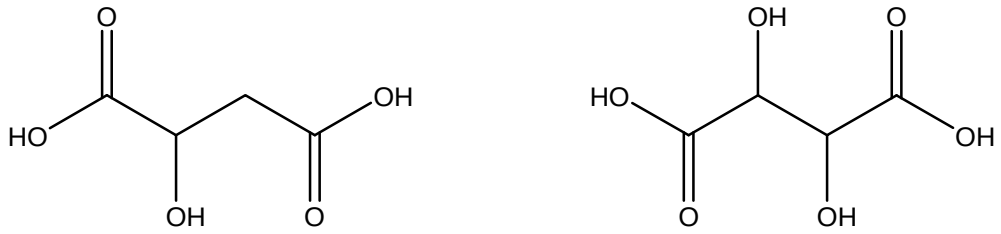

(a) (b)

Figure 7.1. Chemical structure of malic acid (a) and tartaric acid (b)

Dicarboxylates such as malic or tartaric acid may promote the formation of linear metal oxide chains by acting as a branch between parallel rows of the metal oxide framework (figure 7.2). The formation of such a network may promote the formation of edge sharing octahedra because as upon calcination, the organic groups will be removed from the network to leave TiO_6 octahedra (scheme 7.1).

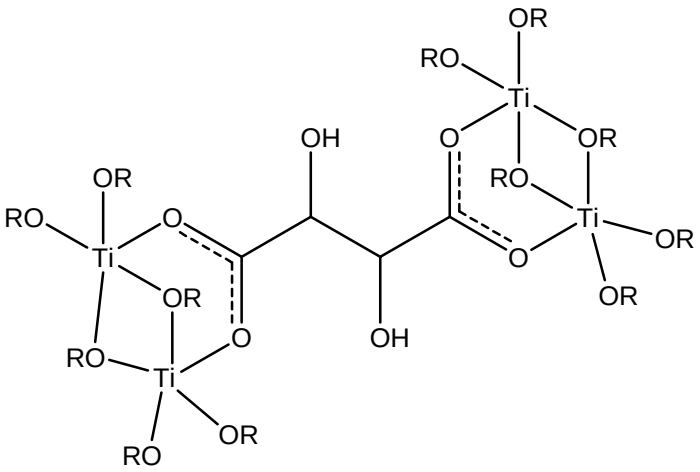

Figure 7.2. Possible structure of malic acid chelated to titanium isopropoxide

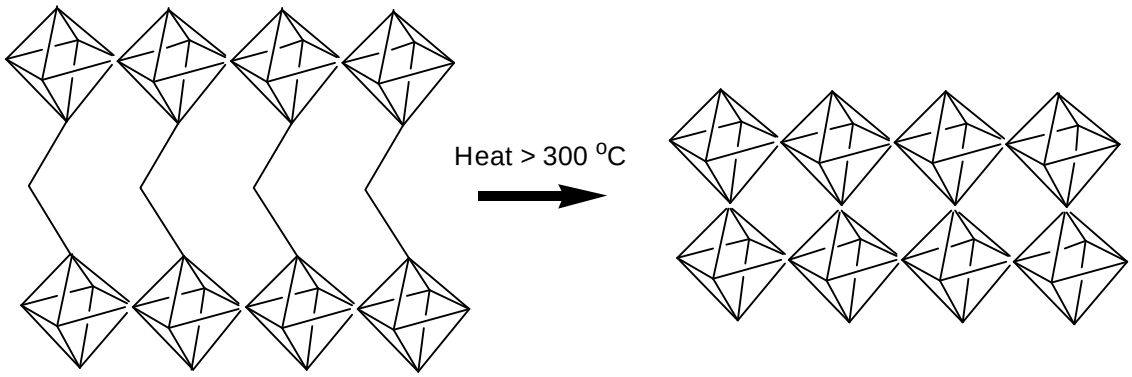

Scheme 7.1. Schematic showing the removal of organic modifier under heat action to leave edge sharing octahedra

Nitrogen doped TiO_2 that remains stable as anatase may also be produced from chelation of amino carboxylates such as 3-amino-2-(hydroxymethyl)propionic acid or 4-amino-3-hydroxybutyric acid (figure 7.3 a and b).

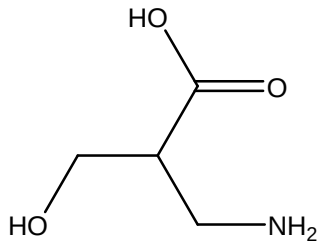

(a)

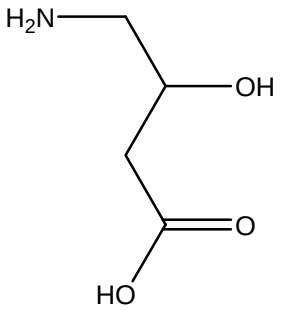

(b)

Figure 7.3. Chemical structure of 3-amino-2-(hydroxymethyl)propionic acid (a) and 4-amino-3-hydroxybutyric acid (b)

7.2 Incorporation of Powders into Thin Film Coatings

Schmidt *et al* have incorporated TiO_2 powders into thin films through the creation of a silane binder sol.[320] To create clear coatings they ensured that the TiO_2 particles were of small enough size (< 20 nm) so that they would not scatter light to give white coatings. The addition of a fluoro-organic silane modified the surface and reduced the polarity of the nano particles (figure 7.4).

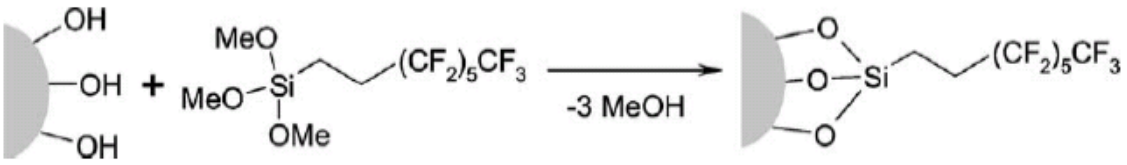

Figure 7.4. Scheme of the surface modification of the nanoparticulate TiO_2[320]

Redispersion of the modified sols into inorganic-organic matrix sols (binders) resulted in a suspension that could be used to dip coat or spray coat onto a substrate. Upon application of the sol coatings, solvent evaporation proceeds causing a change in the balance between polar and non-polar compounds in the film. This destabilises the thermodynamic equilibrium between the modified particles and the matrix system, allowing the functionalised, photocatalytic nanoparticles diffuse to the surface of the coating (figure 7.5).

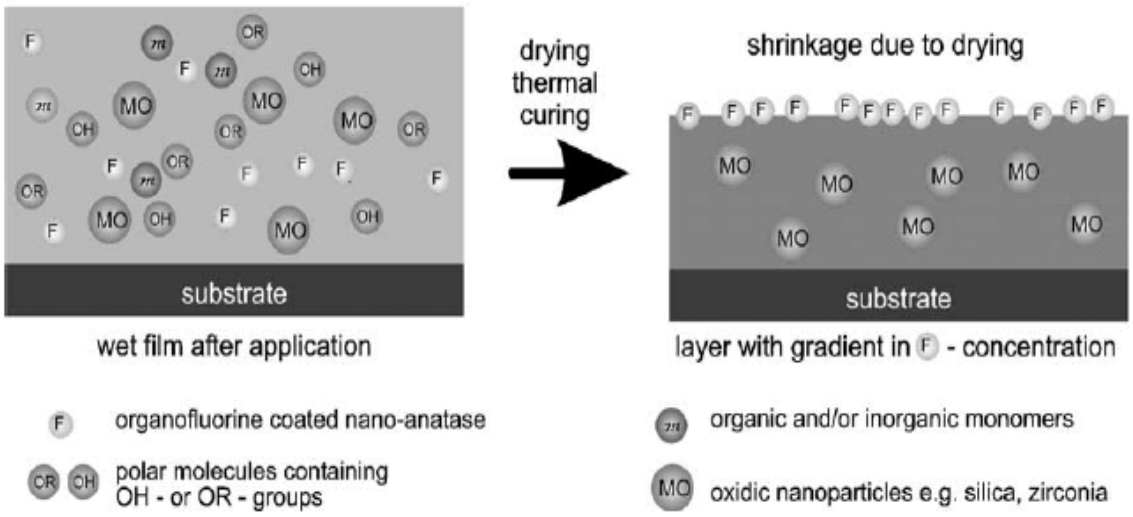

Figure 7.5. Proposed mechanism of the formation of thin film coating[320]

Exposure to sunlight activates the TiO_2 photocatalytic process and the organic side chains absorbed to the TiO_2 surface are oxidised, revealing the photocatalytically active

nanoparticles on the substrate-air interface. Titanium dioxide particles also photocatalytically oxidise the surrounding matrix leading to an intrinsic barrier (SiO_2) which protects the substrate from the photocatalytic reactions associated with TiO_2 (figure 7.6).

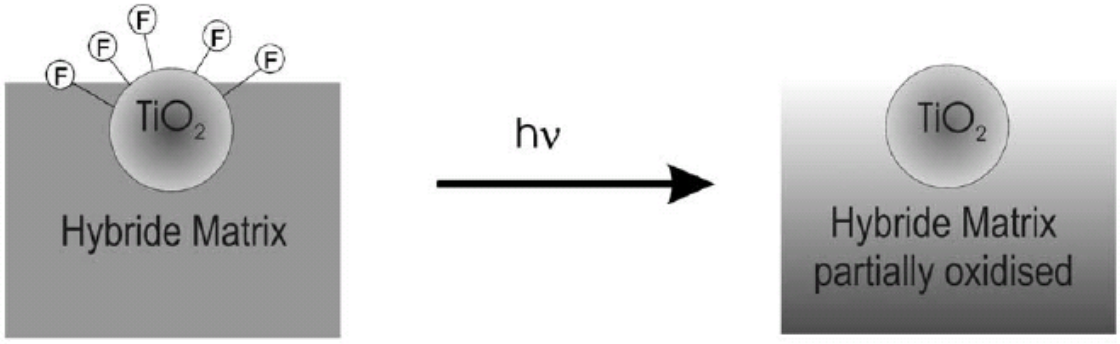

Figure 7.6. Scheme of photoactivation of the protective coating[320]

Fluorination of TiO_2 has also shown increased photocatalytic activity. Choi *et al* have carried out extensive investigations on fluorinated TiO_2 photocatalysis.[321-323] Fluorine adsorption onto TiO_2 is known to replace surface hydroxyl groups with Ti–F (equation 7.1).

$Ti–OH + F^- \leftrightarrow Ti–F + OH^-$ Equation 7.1

Increased photocatalytic activity of F-TiO_2 has been attributed to the production of mobile OH• radicals as opposed to adsorbed OH• radicals that are formed in a typical photocatalytic reaction.[322]

Taking these results into account it may be possible to produce a range of thin film coatings from the powders synthesised throughout this thesis. The resulting fluorinated-TiO_2 thin films may provide highly effective photocatalytic materials.

7.3 Synthesis of Visible Light Active, High Temperature Anatase

The addition of aluminium showed that anatase can be stabilised at increased temperatures. However, a decrease in the photocatalytic activity was also caused by the addition of aluminium. Titanium dioxide doped with Fe^{3+} has also shown great promise for the facilitation of visible light absorbance.[324] Substitution of Ti^{4+} in the TiO_2 lattice by Fe^{3+} creates additional energy states in the band gap. These additional

energy levels cause a reduction in the band gap, allowing visible light absorption to occur. Visible light absorption was achieved through nitrogen doping (chapter 5) but the sample was not as effective a photocatalyst as Degussa P25 for the degradation of methylene blue under simulated solar radiation. Metal doping may improve the photocatalytic activity of the materials and it might also be possible to create anatase that is stable at increased temperatures.

7.4 Antibacterial Testing

Much work is being carried out on the development of antibacterial coatings for both the home but also for hospitals where highly sterile facilities are essential in order to provide the necessary patient care. Our lab has investigated the photocatalytic elimination of MRSA using visible light active materials coated onto tiles[11] and we have also studied the antibacterial effect of silver nanoparticles.[325] Chapter 5 highlighted the results of Ag-N co-doped TiO_2. The materials synthesised in chapter 5 may prove to be highly effective, indoor antibacterial agents due to not only the presence of silver, but also the visible light activity of the N-TiO_2. Further investigations of this material are necessary using indoor lighting as an illumination source.

7.5 Nitric Oxide Degradation

Research pertaining to the photocatalytic activity of TiO_2 is currently a huge area of interest. However, in order for researchers to be able to accurately evaluate the photocatalytic effectiveness of the materials they produce, the semiconductor photocatalyst community must all carry out degradation reactions under identical conditions.

Over the past three years apparatus has been gathered for the assembly of the international standard ISO 22197-1. This is the test method for semiconducting photocatalytic nanomaterials. It involves the photocatalytic degradation of nitric oxide from air in a continuous flow reactor. For future photocatalytic degradation studies concerning materials developed by this lab to be recognised for commercial

applications, degradation studies must be carried out following an internationally recognised procedure such as ISO 22197-1. The experimental set up which will be assembled in the near future is outlined in figure 7.7.

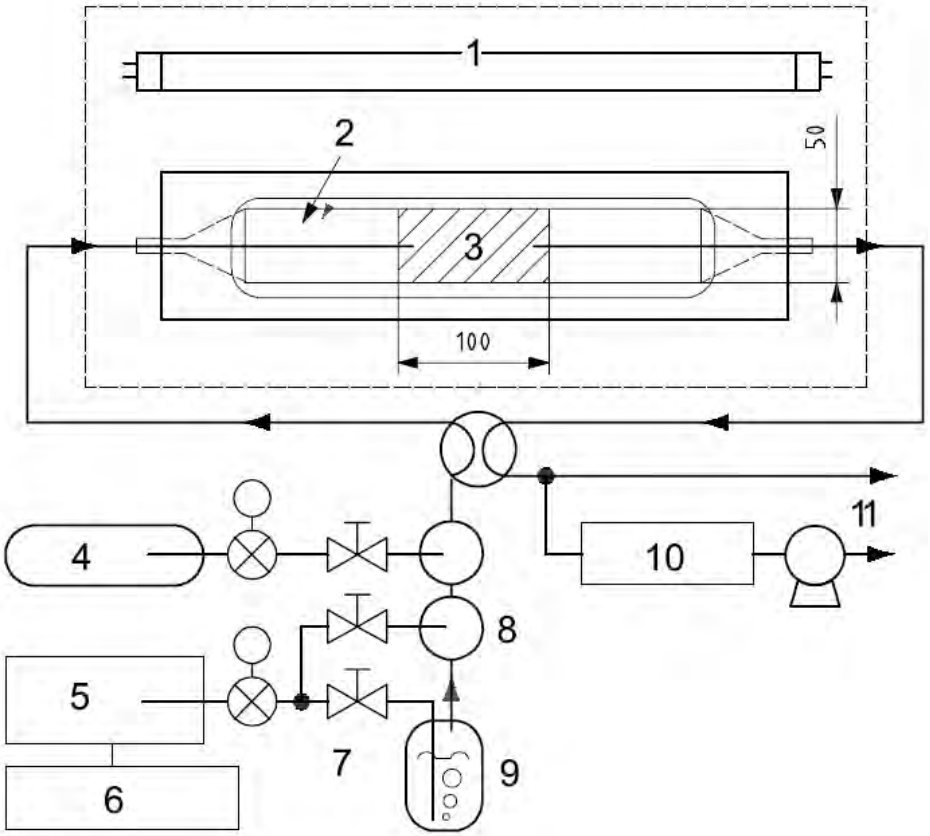

Key

1	light source	7	mass-flow controllers
2	optical window	8	gas mixers
3	test piece	9	humidifier
4	standard gas (pollutant)	10	analyser
5	air-purification system	11	vent
6	air compressor		

Figure 7.7. A schematic of the test equipment (dimensions in millimetres)

7.6 Conclusions

The effect of chelation on phase transformation was systematically investigated and it was shown through IR and Raman spectroscopy that there are two possible bridging structures for formic acid chelated to titanium isopropoxide (*syn-syn* and *syn-anti*). It was shown that the *syn-anti* bridging structure was structurally weak and could readily collapse upon calcination to form rutile.

Addition of silver was shown to block the formation of the chelated bridging structure as shown through a reduction in the COO^- peak intensity found through IR, Raman and XPS. Without the formation of a chelated complex, anatase readily transformed to rutile under calcination.

Aluminium doped TiO_2 resulted in the formation of anatase that was stable at temperatures up to 1000 °C. Visible light absorbing N-TiO_2 materials were successfully synthesised through a simple sol-gel process. The photocatalytic activity of the materials was increased through the addition of silver which was accredited to reduced recombination. Sulfur doped materials were investigated using two different sulfur sources. Highly photoactive materials were produced from the synthesis of S-TiO_2 with sodium thiosulfate.

Sol-gel synthesis of ZnO/TiO_2 hybrids from zinc acetate and titanium isopropoxide precursors resulted in the formation of zinc titanates. Differences between the phase transformations of the zinc titanates were observed with varying precursor ratios. When titanium precursor was in excess over zinc precursor, zinc metatitanate was the favoured zinc titanate phase which transformed to zinc orthotitanate (in an almost 1:1 ratio) upon calcination at 1000 °C. When zinc precursor was in excess over titanium precursor, $Zn_2Ti_3O_8$ was the favoured zinc titanate phase. It transformed to zinc orthotitanate at 1000 °C (in an almost 1:1 ratio).

References

(1) Fujishima, A.; Honda, K. *Nature* **1972**, *238*.
(2) Frank, S. N.; Bard, A. J. *J. Am. Chem. Soc.* **1977**, *99*.
(3) Frank, S. N.; Bard, A. J. *J. Phys. Chem.* **1977**, *81*.
(4) Hsiav, C. Y.; Lee, C. L.; Ollis, D. F. *J. Catal.* **1983**, *82*.
(5) Pruden, A. L.; Ollis, D. F. *J. Catal.* **1983**, *82*.
(6) O'Regan, B.; Gratzel, M. *Nature* **1991**, *238*, 37.
(7) Carp, O.; Huisman, C. L.; Reller, A. *Progress in Solid State Chem.* **2004**, *32*, 33.
(8) Chen, X.; Mao, S. S. *Chem. Rev.* **2007**, *107*, 2891
(9) Kudo, A. *Catal. Surv. Asia* **2003**, *7*.
(10) http://www.pilkingtonselfcleaningglass.co.uk/trade/; 28-May-2010
(11) http://www.dit.ie/hothouse/technologiestolicence/availableforlicense/industrialtechnology/anti-bacterial%20powder/; 28-May-2010
(12) Kato, N.; Higuchi, K.; Tanaka, H.; Nakajima, J.; Sano, T.; Toyoda, T. *Sol. Energy Mater. Sol. Cells* **2010**.
(13) http://www.solarisnano.com/images/handheldcell.png; 28-May-2010
(14) http://www.sikantis.org/sikantis.org/site/pix/content/dyesolar.jpg; 28-May-2010
(15) http://photochemistryportal.net/home/index.php/tag/dye-sensitized-solar-cells/; 28-May-2010
(16) Pagliaro, M.; Palmisano, G.; Ciriminna, R.; Loddo, V. *Energy Environ. Sci.* **2009**, *2*, 838
(17) Miessler, G. L.; Tarr, D. A. *Inorganic Chemistry*; Prentice-Hall Inc.: New Jersey, 1999.
(18) Shriver, D. F.; Atkins, P. W. *Inorganic Chemistry*; Oxford University Press: Oxford, 1999.
(19) Mills, A.; Le Hunte, S. *J. Photochem. Photobiol. A* **1997**, *108*, 1
(20) Asahi, R.; Taga, Y.; Mannstadt, W.; Freeman, A. J. *J. Phys. Rev. B* **2000**, *33*.
(21) Hu, Y.; Tsai, H.-L.; Huangk, C.-L. *Eur. Ceram. Soc.* **2003**, *23*, 691.
(22) Shao, Y.; Tang, D.; Sun, J.; Lee, Y.; Xiong, W. *China Particuology* **2004**, *2*, 119.
(23) Nicholls, D. *Complexes and First-Row Transition Elements*; MacMillan Education: Hong Kong, 1974.
(24) http://staff.aist.go.jp/nomura-k/common/STRUCIMAGES/Anatase.gif&imgrefurl=http://staff.aist.go.jp/nomura; 27-May-2010
(25) Wisitsoraat, A.; Tuantranont, A.; Comini, E.; Sberveglieri, G.; Wlodarski, W. *Thin Solid Films* **2009**, *517*, 2775
(26) Asahi, R.; Taga, Y.; Mannstadt, W.; Freeman, A. J. *Phys. Rev. B* **2000**, *61*.
(27) Hosaka, N.; Sekiya, T.; Aatoko, C.; Kurita, S. *J. Phys. Soc. Japan* **1997**, *66*.
(28) Hosaka, N.; Sekiya, T.; Fujisawa, M.; Satokob, C.; Kurita, S. *J. Electron Spectrosc. Relat. Phenom.* **1996**, *78*.
(29) Kavan, L.; Gratzel, M.; Gilbert, S. E.; Klemenz, C.; Scheel, H. J. *J. Am. Chem. Soc.* **1996**, *118*.
(30) Amtout, A.; Leonelli, R. *Phys. Rev. B* **1995**, *51*.
(31) Glassford, K. M.; Chelikowsky, J. R. *Phys. Rev. B* **1992**, *45*.
(32) Pascual, J.; Camassel, J.; Mathieu, H. *Phys. Rev. B* **1978**, *18*.
(33) Koelsch, M.; Cassaignon, S.; Thanh Minh, C. T.; Guillemoles, J.-F.; Jolivet, J.-P. *Thin Solid Films* **2004**, *451*.
(34) Li, J.-G.; Ishigaki, T.; Sun, X. *J. Phys. Chem. C* **2007**, *111*.
(35) Reyes-Coronado, D.; Rodriguez-Gattorno, G.; Espinosa-Pesqueira, M. E.; Cab, C.; de Coss, R.; Oskam, G. *Nanotechnology* **2008**, *19*, 1

(36) Hoffmann, M. R.; Martin, S. T.; Choi, W.; Bahnemann, D. W. *Chem. Rev.* **1995**, *95*, 69
(37) Wang, Y.; Huang, Y.; Ho, W.; Zhang, L.; Zou, Z.; Lee, S. *J. Hazard. Mater.* **2009**, *169*, 77
(38) Su, C.; Tseng, C.-M.; Chen, L.-F.; You, B.-H.; Hsu, B.-C.; Chen, S.-S. *Thin Solid Films* **2006**, *498*, 259
(39) Fox, M. A.; Dulay, M. T. *Chem. Rev.* **1993**, *93*, 341
(40) Liu, H.; Cheng, S.; Wu, M.; Zhang, J.; Li, W.; Cao, C. *J. Phys. Chem., A* **2000**, *104*, 7016.
(41) Tada, H.; Yamamoto, M.; Ito, S. *Langmuir* **1999**, *15*, 3699.
(42) Xu, Y. M.; Langford, C. H. *Langmuir* **2001**, *17*, 897.
(43) Yu, J.; Yu, H.; Ao, C. H.; Lee, S. C.; Yu, J. C.; Ho, W. *Thin Solid Films* **2006**, *496*, 273
(44) Yu, J. G.; Yu, H. G.; Cheng, B.; Zhao, X. J.; Yu, J. C.; Ho, W. K. *J. Phys. Chem., B* **2003**, *107*, 13871.
(45) Yu, J. G.; Yu, J. G.; Ho, W. K.; Zhang, L. Z. *Chem. Commun.* **2001**, 1942.
(46) Zhao, J.; Wu, T.; Wu, K.; Oikawa, K.; Hidaka, H.; Serpone, N. *Environ. Sci. Technol.* **1998**, *32*, 2394
(47) Wang, R.; Hashimoto, K.; Fujishima, A.; Chikuni, M.; Kojima, E.; Kitamura, A. *Nature* **1997**, *388*.
(48) Suresh, C.; Biju, V.; Mukundan, P.; Warrier, K. G. K. *Polyhedron* **1998**, *17*, 3131.
(49) Zhang, Q.; Gao, L.; Guo, J. *Appl. Catal., B.* **2000**, *26*, 207.
(50) Yoganarasimhan, S. R.; Rao, C. N. R. *Trans. Faraday Soc.* **1962**, *58*, 1579.
(51) MacKenzie, K. J. D. *Trans. J. Br. Ceram. Soc.* **1975**, *74*, 29.
(52) Byun, C.; Wang, J. W.; Kim, L. T.; Hong, K. S.; Lee, B. W. *Mater. Res. Bull.* **1997**, *32*, 431.
(53) MacKenzie, K. J. D. *Trans. J. Br. Ceram. Soc.* **1975**, *74*, 121.
(54) Li, Y.; White, T. J.; Lim, S. H. *J. Solid State Chem.* **2004**, *177*, 1372.
(55) Ding, X.-Z.; Liu, X.-H. *J. Mater. Res.* **1998**, *13*, 2556.
(56) Gribb, A. A.; Banfield, J. F. *Am. Mineral.* **1977**, *82*, 717.
(57) Zhang, H.; Banfield, J. F. *J. Mater. Chem.* **1998**, *8*, 2073.
(58) Ahn, Y. U.; Kim, E. J.; Kim, H. T.; Hahn, S. H. *Mater. Lett.* **2003**, *57*, 4660.
(59) Kumar, K. P.; Keizer, K.; Burggraaf, A. J.; Okubo, T.; Nagamoto, H. *J. Mater. Chem.* **1993**, *3*, 1151.
(60) Aguado, J.; van Grieken, R.; Lopez-Munoz, M. J.; Marugan, J. *Catal. Today* **2002**, *75*, 95.
(61) Diebold, U. *Surf. Sci. Reports* **2003**, *48*, 53.
(62) Czanderna, A. W.; Rao, C. N. R.; Honig, J. M. *Trans. Faraday Soc.* **1958**, *54*.
(63) Kumar, K. N. P.; Keizer, K.; Burggraaf, A. J. *Nature* **1992**, *358*.
(64) Rao, C. N. R.; Rao, K. J. *Phase Transition in Solids*; McGraw-Hill: New York, 1978.
(65) MacKenzie, J. D. *Trans. J. Br. Ceram. Soc.* **1975**, *74*.
(66) Yoganarasimhan, S. R.; Rao, C. N. R. *Trans. Faraday Soc.* **1962**, *58*, 1579.
(67) Suppan, P. *Chemistry and Light*; Roral Society of Chemistry: Cambridge, 1994.
(68) Testino, A.; Bellobono, I. R.; Buscaglia, V.; Canevali, C.; D'Arienzo, M.; Polizzi, S.; Scotti, R.; Morazzoni, F. *J. Am. Chem. Soc.* **2007**, *129*, 3564
(69) Tachikawa, T.; Fujitsuka, M.; Majima, T. *J. Phys. Chem. C* **2007**, *111*, 5259
(70) Cozzoli, P. D.; Comparelli, R.; Fanizza, E.; Curri, M. L.; Agostiano, A. *Mat. Sci. Engg. C* **2003**, *23*, 707
(71) Hoffman, A.; Carraway, E. R.; Hoffman, M. *Environ. Sci. Technol.* **1994**, *28*.
(72) Mahdavi, F.; Burton, T. C.; Li, Y. *J. Org. Chem.* **1993**, *58*.
(73) Liqiang, J.; Yichun, Q.; Baiqi, W.; Shudan, L.; Baojiang, J.; Libin, Y.; Wei, F.; Honggang, F.; Jiazhong, S. *Solar Energy Materials & Solar Cells* **2006**, *90*, 1773
(74) Choi, W.; Termin, A.; Hoffmann, M. R. *J. Phys. Chem. B* **1994**, *98*.
(75) Soria, J.; Conesa, J. C.; Augugliaro, V.; Palmisano, L.; Schiavello, M.; Sclafani, A. *J. Phys. Chem.* **1991**, *95*.

(76) Yu, J. C.; Yu, J. G.; Ho, K. W.; Jiang, Z. T.; Zhang, L. Z. *Chem. Mater.* **2002**, *14*.
(77) Do, Y. R.; Lee, K.; Dwight, K.; Wold, W. *J. Sol. State Chem.* **1994**, *108*.
(78) Engweiler, J.; Harf, J.; Baiker, A. *J. Catal.* **1996**, *159*.
(79) Vinodgopal, K.; Kamat, P. V. *Environ. Sci. Technol.* **1995**, *29*.
(80) Maira, A. J.; Yeung, K. L.; Lee, C. Y.; Yue, P. L.; Chan, C. K. *J. Catal.* **2000**, *192*.
(81) Xu, Z. L.; Shang, J.; Liu, C. M.; Kang, C.; Guo, H. C.; Du, Y. G. *Mater. Sci. Eng. B* **1999**, *63*.
(82) Li, Y.; Hwang, D.-S.; Lee, N. H.; Kim, S.-J. *Chem. Phys. Lett.* **2005**, *404*.
(83) Sclafani, A. *J. Phys. Chem.* **1996**, *100*.
(84) Emilio, C. A.; Litter, M. I.; Kunst, M.; Bouchard, M.; Colbeau-Justin, C. *Langmuir* **2006**, *22*.
(85) Serpone, N. *J. Photochem. Photobiol. A* **1997**, *104*.
(86) Serpone, N.; Lawless, D.; Khairutdinov, R. *J. Phys. Chem.* **1995**, *99*, 16646
(87) Wang, R.; Hashimoto, K.; Fujishima, A.; Chikuni, M.; Kitamura, A.; Shimohigoshi, M.; Watanabe, T. *Adv. Mater.* **1998**, *2*, 135.
(88) Wang, R.; Hashimoto, K.; Fujishima, A.; Cjikuni, M.; Kojima, E.; Kitamura, A.; Shimohigoshi, M.; Watanabe, T. *Nature* **1997**, *388*, 431.
(89) Lee, Y. C.; Hong, Y. P.; Lee, H. Y.; Kim, H.; Jung, Y. J.; Ko, K. H.; Jung, H. S.; Hong, K. S. *J. Colloid and Interface Science* **2003**, *267*, 127
(90) Watanabe, T.; Fukayama, S.; Miyauchi, M.; Fujishima, A.; Hashimoto, K. *J. Sol-Gel Sci. Technol.* **2000**, *19*, 71.
(91) Misook, K. *Mat. Lett.* **2005**, *59*, 3122
(92) Hamal, D. B.; Klabunde, K. J. *J. Colloid Interface Sci.* **2007**, *311*, 514
(93) Kuo, Y.-L.; Chen, H.-W.; Ku, Y. *Thin Solid Films* **2007**, *515*, 3461
(94) Luo, H.; Takata, T.; Lee, Y.; Zhao, J.; Domen, K.; Yan, Y. *Chem. Mater.* **2004**, *16*, 846
(95) Asahi, R.; Morikawa, T.; Oikawa, K.; Aoki, K.; Taga, Y. *Science* **2001**, *293*, 269.
(96) Ihara, T.; Miyoshi, M.; Iriyama, Y.; Matsumoto, O.; Sugihara, S. *Appl. Catal., B* **2003**, *42*, 403
(97) Martyanov, I. N.; Uma, S.; Rodrigues, S.; Klabunde, K. J. *Chem. Commun.* **2004**, *7*, 2476
(98) Irie, H.; Watanabe, Y.; Hashimoto, K. *J. Phys. Chem. B* **2003**, *107*, 5483
(99) Nakamura, R.; Tanaka, T.; Nakoto, Y. *J. Phys. Chem. B* **2004**, *108*, 10617
(100) Li, D.; Ohashi, N.; Hishita, S.; Kolodiazhnyi, T.; Haneda, H. *J. Sol. State Chem.* **2005**, *178*.
(101) Irie, H.; Watanabe, Y.; Hashimoto, K. *Chem. Lett.* **2003**, *32*.
(102) Sakthivel, S.; Kisch, H. *Angew. Chem. Int. Ed.* **2003**, *42*.
(103) Morikawa, T.; Asahi, R.; Ohwaki, T.; Aoki, K.; Taga, Y. *Jpn. J. Appl. Phys.* **2001**, *40*.
(104) Nagaveni, K.; Hedge, M. S.; Ravishankar, N.; Subbanna, G. N.; Madras, G. *Langmuir* **2004**, *20*.
(105) Umebayashi, T.; Yamaki, T.; Itoh, H.; Asai, K. *Appl. Phys. lett.* **2002**, *81*.
(106) Borgarello, E.; Kiwi, J.; Gratzel, M.; Pelizzetti, E.; Visca, M. *J. Am. Chem. Soc.* **1982**, *104*.
(107) Iwasaki, M.; Hara, M.; Kawada, H.; Tada, H.; Ito, S. *J. Colloid Interface Sci.* **2000**, *224*.
(108) Klosek, S.; Raftery, D. *J. Phys. Chem. B* **2001**, *105*.
(109) Zhu, J.; Chen, F.; Zhang, J.; Chen, H.; Anpo, M. *J. Photochem. Photobiol. A* **2006**, *180*.
(110) Kang, M. *Mat. Lett.* **2005**, *59*, 3122
(111) Szczepankiewicz, S. H.; Colussi, A. J.; Hoffmann, M. R. *J. Phys. Chem. B* **2000**, *204*.
(112) Serpone, N.; Lawless, D.; Khairutdinov, R.; Pelizetti, E. *J. Phys. Chem.* **1995**, *99*.
(113) Behar, D.; Rabani, J. *J. Phys. Chem. B* **2006**, *110*, 8750.

(114) Kim, S. K.; Hwang, S. J.; Choi, W. *Sci. Technol.* **2005**, *35*, 2381.
(115) Li, X. Z.; Li, F. B. *Environ. Sci. Technol.* **2001**, *35*, 2381.
(116) Wang, W.; Zhang, J.; Chen, F.; He, D.; Anpo, M. *J. Colloid Interface Sci.* **2008**, *323*, 182
(117) You, X.; Chen, F.; Zhang, J.; Anpo, M. *Catal. Lett.* **2005**, *102*, 247.
(118) Hwang, S.; Lee, M. C.; Choi, W. *Appl. Catal. B Environ.* **2003**, *46*.
(119) Morikawa, T.; Irokawa, Y.; Ohwaki, T. *Appl. Catal. A Gen.* **2006**, *314*.
(120) Demeestre, K.; Dewulf, J.; Ohno, T.; Salgado, P. H.; Langenhove, H. V. *Appl. Catal. B Environ.* **2005**, *61*.
(121) Dvoranova, D.; Brezova, V.; Mazur, M.; Malati, M. A. *Appl. Catal. B: Environ.* **2002**, *37*, 91
(122) Fuerte, A.; Hernandez-Alonso, M. D.; Maira, A. J.; Martinez-Arias, A.; Fernandez-Garcia, M.; Conesa, J. C.; Soria, J. *Chem. Commun.* **2001**, 2718
(123) Iketani, K.; Sun, R.-D.; Toki, M.; Hirota, K.; Yamaguchi, O. *Mater. Sci. Eng. B* **2004**, *108*, 187
(124) Li, F. B.; Li, X. Z. *Chemosphere* **2002**, *48*, 1103
(125) Ohno, T.; Tanigawa, F.; Fujihara, K.; Izumi, S.; Matsumara, M. *J. Photochem. Photobiol. A* **1999**, *127*, 107
(126) Wu, J. C.-S.; Chen, C.-H. *J. Photochem. Photobiol. A* **2004**, *293*, 509
(127) Yamashita, H.; Harada, M.; Misaka, J.; Takeuchi, M.; Ikeue, K.; Anpo, M. *J. Photochem. Photobiol. A* **2002**, *148*, 257
(128) Yamashita, H.; Harada, M.; Misaka, J.; Takeuchi, M.; Neppolian, B.; Anpo, M. *Catal. Today* **2003**, *84*, 191
(129) Chao, H. E.; Yun, Y. U.; Xingfang, H. U.; Larbot, A. *ECERS* **2003**, *23*, 1457
(130) Seery, M. K.; George, R.; Floris, P.; Pillai, S. C. *J. Photochem. Photobiol. A* **2007**, *189*, 258
(131) Yu, J.; Yu, H.; Cheng, B.; Zhou, M.; Zhao, X. *J. Mol. Catal. A* **2006**, *253*.
(132) Zhang, L.; Yu, J. C. *Catal. Comm.* **2005**, *6*, 684
(133) Cao, L. X.; Cao, Z.; Suib, S. L.; Obee, T. N.; Hay, S. O.; Freihauty, J. D. *J. Catal.* **2000**, *196*.
(134) Piera, E.; Ayllon, J. A.; Domenach, X.; Peral, J. *Catal. Today* **2002**, *76*.
(135) Peral, J.; Ollis, D. F. *Photocatalytic Purification and Treatment of Water and Air*; Elsevier: New York, 1993.
(136) Pillai, U. R.; Sahle-Demessie, E. *J. Catal.* **2002**, *211*.
(137) Shang, J.; Zhu, Y. F.; Du, Y. G.; Xu, Z. L. *J. Sol. State Chem.* **2002**, *166*.
(138) Ameen, M. M.; Raupp, G. B. *J. Catal.* **1999**, *184*.
(139) Keshmiri, M.; Troczynski, T.; Mohseni, M. *J. Hazard. Mater.* **2006**, *B128*, 130
(140) Kraeutler, B.; Bard, A. J. *J. Am. Chem. Soc.* **1978**, *100*.
(141) Lindner, M.; Theurich, J.; Bahnemann, D. W. *Water Sci. Technol.* **1997**, *35*.
(142) Martin, C. A.; Baltanas, M. A.; Cassano, A. E. *Catal. Today* **1996**, *27*.
(143) Muggli, D. S.; McCue, J. T.; Falconer, J. L. *J. Catal.* **1998**, *173*.
(144) Nishimoto, S.-I.; Ohtani, B.; Kajiwara, H.; Kagiya, T. *J. Chem. Soc., Faraday Trans.* **1985**, *81*.
(145) Ohko, Y.; Tryk, D. A.; Hashimoto, K.; Fujishima, A. *J. Phys. Chem. B* **1998**, *102*.
(146) Walker, S. A.; Christensen, P. A.; Shaw, K. E.; Walker, G. M. *J. Electroanal. Chem.* **1995**, *393*.
(147) Cheng, H.; Ma, J.; Zhao, Z.; Qi, L. *Chem. Mater.* **1995**, *7*.
(148) Yin, H.; Wada, Y.; Kitamura, T.; Kambe, S.; Murasawa, S.; Mori, H.; Sakata, T.; Yanagida, S. *J. Mater. Chem.* **2001**, *11*.
(149) Nagaveni, K.; Sivalingam, G.; Hegde, M. S.; Madras, G. *Appl. Catal. B* **2004**, *48*.
(150) Jones, A. C.; Chalker, P. R. *J. Phys. D: Appl. Phys.* **2003**, *36*, R80.
(151) Wang, W.-N.; Lenggoro, I. W.; Terashi, Y.; Kim, T. O.; Okuyama, K. *Mat. Sci. Eng. B* **2005**, *123*.
(152) Watson, S.; Beydoun, D.; Scott, J.; Amal, R. *J. Nanopart. Res.* **2004**, *6*.
(153) Yang, J.; Mei, S.; Ferreira, J. M. F. *Mater. Sci. Eng. B* **2001**, *C15*.
(154) Choy, K. L. *Prog. Mater. Sci.* **2003**, *48*.

(155) van de Krol, R.; Goossens, A.; Schoonman, J. *J. Electrochem. Soc.* **1997**, *144*.
(156) Corradi, A. B.; Bondioli, F.; Focher, B.; Ferrari, A. M.; Grippo, C.; Mariani, E.; Villa, C. *J. Am. Ceram. Soc.* **2005**, *88*.
(157) Ma, G.; Zhao, X.; Zhu, J. *Int. J. Mod. Phys. B* **2005**, *19*.
(158) Wu, X.; Jiang, Q. Z.; Ma, Z. F.; Fu, M.; Shangguan, W. F. *Sol. State Comm.* **2005**, *136*.
(159) Chan, C. K.; Chu, I.-M. *Polymer* **2001**, *42*.
(160) Corriu, R. J. P.; Leclerq, D. *Angew. Chem. Int. Ed. Engl.* **1996**, *35*.
(161) Hsu, Y. G.; Chiang, I. L.; Lo, J. F. *J. Appl. Polym. Sci.* **2000**, *78*.
(162) Mark, J. E. *Heterogenous Chem. Rev.* **1996**, *3*.
(163) Perrin, F. X.; Nguyen, V.; Vernet, J. L. *J. Sol-Gel Sci. Technol.* **2003**, *28*, 205
(164) Sanchez, C.; Livage, J.; Henry, M.; Babonneau, F. *J. Non-Cryst. Solids* **1988**, *100*.
(165) Sanchez, C.; Ribot, F. *New J. Chem.* **1994**, *18*.
(166) Sanchez, C.; Ribot, F.; Lebeau, B. *J. Mater. Chem.* **1999**, *9*.
(167) Schubert, H.; Husing, N.; Lorenz, N. *Chem. Mater.* **1995**, *7*.
(168) Wen, J.; Wilkes, G. L. *Chem. Mater.* **1996**, *8*.
(169) Ershad-Langroudi, A.; Mai, C.; Vigier, G.; Vassoile, R. *J. Appl. Polym. Sci.* **1997**, *65*.
(170) Verma, A.; Samanta, S. B.; Bakhshi, A. K.; Agnihotry, S. A. *Sol. Energy Mater. Sol. Cells* **2005**, *88*, 47
(171) Barboux-Doeuff, S.; Sanchez, C. *Mat. Res. Bull.* **1994**, *29*, 1
(172) Brinker, C. J.; Scherer, G. W. *The Physics and Chemistry of Sol-Gel Science*; Academic Press: New York, 1990.
(173) Sanderson, R. T. *Science* **1951**, *114*.
(174) Livage, J.; Henry, M.; Sanchez, C. *Prog. Sol. State Chem.* **1988**, *18*, 259
(175) Barringer, E. A.; Bowen, H. K. *Langmuir* **1985**, *1*.
(176) Ingebrethsen, B. J.; Matijevic, E. *J. Colloid Interface Sci.* **1984**, *100*.
(177) Winter, G. *Oil Colour Chem. Assoc.* **1953**, *34*.
(178) Adams, R. W.; Bishop, E.; Martin, R. L.; Winter, G. *Aust. J. Chem.* **1966**, *19*.
(179) Bradley, D. C.; Mehrotra, R. C.; Gaur, D. P. *Metal Alkoxides*; Academic Press: London, 1978.
(180) Kundu, D.; Ganguli, D. *J. Mater. Sci. Lett.* **1986**, *5*.
(181) Bistan, E.; Gomory, I. *Chem. Zvesti.* **1956**, *10*.
(182) Boyd, T. *J. Polym. Sci.* **1951**, *7*.
(183) Minami, S.; Ishino, T. *Technol. Rept. Osaka Univ.* **1953**, *3*.
(184) Springer, L.; Yan, M. F. *Ultrastructure Processing of Ceramics, Glasses and Composites*; Wiley: New York, 1984.
(185) Vallet-Regi, M.; Veiga-Blanco, M. L.; Mata-Arjon, A. *Ann. Quim.* **1980**, *76B*.
(186) Hench, L. L.; Ulrich, D. R. *Ann. Quim.* **1980**, *76B*.
(187) Yoldas, B. E. *J. Mater. Sci.* **1986**, *21*.
(188) Kamiya, K.; Tanimoto, K.; Yoko, T. *J. Mater. Sci. Lett.* **1986**, *5*.
(189) Sakka, S.; Kamiya, K. *J. Non-Cryst. Solids* **1980**, *42*.
(190) Bradley, D. C. *Adv. Chem. Ser.* **1959**, *23*.
(191) Pouxviel, J. C.; Boilot, J. P.; Beloeil, J. C.; Lallemand, J. Y. *J. Non-Cryst. Solids* **1987**, *89*.
(192) Mehrotra, R. C.; Bohra, R. *Metal Carboxylates*; Academic Press: London, 1983.
(193) Yoldas, B. E. *Amer. Ceram. Soc. Bull.* **1975**, *54*.
(194) Doeuff, S.; Henry, M.; Sanchez, C.; Livage, J. **1987**, *89*.
(195) Livage, J.; Sanchez, C.; Henry, M.; Doeuff, S. *Solid State Ionics* **1989**, *32/33*, 633
(196) Nguyen, T.-V.; Choi, D.-J.; Yang, O.-B. *Res. Chem. intermed.* **2005**, *31*, 483
(197) Scherrer, P. *Gottinger Nachrichten* **1918**.
(198) Spurr, R.; Myers, H. *Anal. Chem.* **1957**, *29*, 760.
(199) Verma, A.; Samant, S. B.; Bakhshi, A. K.; Agnihotry, S. A. *Sol. Energy Mat. Sol. Cells* **2005**, *88*, 47.
(200) Phule, P. P.; Risbud, S. H. *J. Mater. Sci.* **1990**, *25*, 1169.

(201) Takahaschi, Y.; Matsuoka, Y. *J. Mater. Sci.* **1988**, *23*, 2259.
(202) Takahaschi, Y.; Kiwa, K.; Kobayashi, K.; Matsuki, M. *J. Am. Ceram. Soc.* **1991**, *74*, 67.
(203) Sanchez, C.; Livage, J.; Henry, M.; Babonneau, F. *J. Non-Cryst. Solids* **1988**, *100*, 65.
(204) Guilment, J.; Pencelot, O.; Rigola, J.; Truchet, S. *Vib. Spectrosc.* **1996**, *11*, 37.
(205) Pillai, S. C.; Periyat, P.; George, R.; McCormack, D. E.; Seery, M. K.; Hayden, H.; Colreavy, J.; Corr, D.; Hinder, S. J. *J. Phys. Chem. C* **2007**, *111*, 1605.
(206) Guillard, C.; Beaugiraud, B.; Dutriez, C.; Herrmann, J.-M.; Jaffrezic, H.; Jaffrezic-Renault, N.; Lacroix, M. *Appl. Catal., B.* **2002**, *39*, 331.
(207) Nguyen, T.-V.; Choi, D.-J.; Yang, O.-B. *Res. Chem. Intermed.* **2005**, *31*, 483.
(208) Zelenak, V.; Vargova, Z.; Gyoryova, K. *Spectrochim. Acta* **2007**, *66*, 262.
(209) Ivanda, M.; Music, S.; Popovic, S.; Gotic, M. *J. Mol. Struct.* **1999**, *480 - 481*, 645
(210) Nakamoto, K. *Infrared and Raman Spectra of Inorganic and Coordinated Compounds, Part B*; John Wiley: New York, 1997.
(211) Nara, M.; Tasumi, M.; Tanokura, M.; Hiraoki, T.; Yazawa, M.; Tsutsumi, A. *FEBS Lett.* **1994**, *349*, 84.
(212) Czakis-Sulikowska, D.; Czylkowska, A.; Malinowska, A. *J. Therm. Anal. Cal.* **2002**, *67*, 667.
(213) Deacon, G. B.; Phillip, R. J. *Coord. Chem. Rev.* **1980**, *33*, 227.
(214) Lewandowski, W.; Fuks, L.; Lewandowski, H. *J. Inorg. Biochem.* **2005**, *99*, 1407.
(215) Manhas, B. S.; Trikha, A. K. *J. Indian Chem. Soc.* **1982**, *59*, 315.
(216) Rardin, R. L.; Tolman, W. B.; Lippard, S. J. *New. J. Chem.* **1991**, *15*, 417.
(217) Kung, H. H.; Ko, E. I. *The Chem. Eng. J.* **1996**, *64*, 203.
(218) Sahni, S.; Bhaskar Reddy, S.; Murty, B. S. *Mater. Sci. & Eng.* **2007**, *452 - 453*, 758
(219) Urlaub, R.; Posset, U.; Thull, R. *J. Non-Cryst. Solids* **2000**, *265*, 276.
(220) Livage, J.; Sanchez, C.; Henry, M.; Doeuff, S. *Solid State Ionics* **1989**, *32/33*, 633.
(221) Ishioka, T.; Shibata, Y.; Takahaski, M.; Kaneska, I.; Kitagawa, Y.; Nakamura, K. T. *Spectrochim. Acta, Part A* **1998**, *54*, 1827.
(222) Hwang, D. S.; Lee, N. H.; Lee, D. Y.; Song, J. S.; Shin, S. H.; Kim, S. J. *Smart Mater. Struct.* **2006**, *15*, S74.
(223) Kittaka, S.; K., M.; Takahara, S. *J. Solid State Chem.* **1997**, *132*, 447.
(224) Yoshitake, H.; Abe, D. *Microporous Mesoporous Mater.* **2009**, *119*, 267.
(225) Bickley, R. I.; Gonzalez-Carreno, T.; Lees, J. S.; Palmisano, L.; Tilley, R. J. D. *J. Solid State Chem.* **1991**, *92*, 178
(226) Hurum, D. C.; Agrios, A. G.; Gray, K. A.; Rajh, T.; Thurnauer, M. C. *J. Phys. Chem. B* **2003**, *107*, 4545
(227) Yu, J.; Yu, H.; Cheng, B.; Zhou, M.; Zhao, X. *J. Mol. Catal. A: Chem.* **2006**, *253*, 112
(228) Datye, A. K.; Riegel, G.; Bolton, J. R.; Huang, M.; Prairie, M. R. *J. Solid State Chem.* **1995**, *115*, 236
(229) Fujishima, A.; Rao, T. N.; Tryk, D. A. *J. Photochem. Photobiol. A* **2000**, *1*.
(230) Gunawan, C.; Teoh, W. Y.; Marquis, C. P.; Lifia, J.; Amal, R. *Small* **2009**, *5*, 341.
(231) Hishita, S.; Mutoh, I.; Koumoto, K.; Yanagida, H. *Ceram. Intern.* **1982**, *9*, 61
(232) MacKenzie, K. J. D. *J. Brit. Ceram. Soc.* **1975**, *74*, 77
(233) Oliveri, G.; Ramis, G.; Busca, G.; Sanchez Escribano, V. *J. Mater. Chem.* **1993**, *3*, 1239
(234) Henglein, A.; Bunsenges, B. *Phys. Chem.* **1977**, *81*.
(235) Mallick, K.; Witcomb, M.; Scurrell, M. *Mat. Chem. Phys.* **2006**, *97*, 283
(236) Epifani, M.; Giannini, C.; Tapfer, L.; Vasanelli, L. *J. Am. Ceram. Soc.* **2000**, *85*, 2385
(237) Litter, M. I. *Appl. Catal. B* **1999**, *23*, 89

(238) Ben Amor, S.; Baud, G.; Jacquet, M.; Nanse, G.; Fioux, P.; Nardin, M. *Appl. Surf. Sci.* **2000**, *153*, 172
(239) Korosi, L.; Papp, S.; Menesi, J.; Illes, E.; Zollmer, V.; Richardt, A.; Dekany, I. *Colloids and Surfaces A* **2008**, *319*, 136
(240) Xu, W.-X.; Zhu, S.; Fu, X.-C. *Appl. Surf. Sci.* **1998**, *136*, 194
(241) Barlier, V.; Bounor-Legare, V.; Boiteux, G.; Davenas, J.; Leonard, D. *Appl. Surf. Sci.* **2008**, *254*, 5408
(242) Henderson, M. A. *Surf. Sci.* **1999**, *419*, 174
(243) G. F. Hoflund; H-L. Yin; A. L. Grogan Jr.; D. A. Asbury *Langmuir* **1988**, *4*, 346
(244) Xu, J.; Chang, Y.; Zhang, Y.; Ma, S.; Qu, Y.; Xu, C. *Appl. Surf. Sci.* **2008**, *255*, 1996
(245) Akyol, A.; Yatmaz, H. C.; Bayramoglu, M. *Appl. Catal. B.* **2004**, *54*, 19
(246) Spojakina, A.; Kraleva, E.; Jiratova, K.; Petrov, L. *Appl. Catal. A.* **2005**, *288*, 10
(247) He, C.; Xiong, Y.; Chen, J.; Zha, C.; Zhu, X. *J. Photochem. Photobiol. A* **2003**, *157*, 71
(248) Sen, S.; Mahanty, S.; Roy, S.; Heintz, O.; Bourgeois, S.; Chaumont, D. *Thin Solid Films* **2005**, *474*, 245
(249) Kumar, K. M. P.; Keizer, K.; Burggraff, T. J.; Okubo, T.; Nagomoto, H.; Naroooka, S. *Nature* **1992**, *358*.
(250) Yang, J.; Ferreira, J. M. F. *36* **1998**.
(251) Lee, B.-Y.; Park, S.-H.; Kang, M.; Lee, S.-C.; Choung, S.-K. *Appl. Catal. A* **2003**, *253*, 371
(252) Asahi, R.; Morikawa, T.; Ohwaki, T.; Aoki, K.; Taga, Y. *Science* **2001**, *293*, 269.
(253) Khan, S. U. M.; Al-Shahry, M.; Ingler Jr., W. B. *Science* **2002**, *297*, 2243.
(254) Lee, D. H.; Cho, Y. S.; Yi, W. I.; Kim, T. S.; Lee, J. K.; Jung, H. J. *Appl. Phys. Lett.* **1995**, *66*, 815.
(255) Wu, P.-G.; Ma, C.-H.; Shang, J. K. *Appl. Phys. A* **2005**, *81*.
(256) Ihara, T.; Miyoshi, M.; Iriyama, Y.; Matsumoto, O.; Sugihara, S. *Appl. Catal. B: Environ.* **2003**, *42*.
(257) Martyanov, I. N.; Uma, S.; Rodrigues, S.; Klabunde, K. J. *Chem. Comm.* **2004**.
(258) Irie, H.; Watanabe, W.; Hashimoto, K. *J. Phys. Chem. B* **2003**, *107*.
(259) Lee, J.; Park, J.; Cho, J. *Appl. Phys. Lett.* **2005**, *87*.
(260) Lindgren, T.; Mwabora, J. M.; Avendano, E.; Jonsson, J.; Hoel, A.; Granqvist, C.; Lindquist, S. *J. Phys. Chem. B* **2003**, *107*.
(261) Ohno, T. *Water Sci. Technol.* **2004**, *49*, 159.
(262) Ohno, T.; Akiyoshi, M.; Umebayashi, T.; Asai, K.; Mitsui, T.; Matsumura, M. *Appl. Catal. A* **2004**, *265*, 115.
(263) Ohno, T.; Mitsui, T.; Matsumura, M. *Chem. Lett.* **2003**, *32*, 364.
(264) Gole, J. L.; Stout, J. D.; Burda, C.; Lou, Y.; Chen, X. *J. Phys, Chem. B* **2004**, *108*, 1230.
(265) Wang, Y.; Li, J.; Peng, P.; Lu, T.; Wang, L. *Appl. Surf. Sci.* **2008**, *254*, 5276
(266) Li, D.; Haneda, H.; Hishita, S.; Ohashi, N. *Chem. Mater.* **2005**, *17*.
(267) Cong, Y.; Chen, F.; Zhang, J.; Anpo, M. *Chem. Lett.* **2006**, *35*.
(268) Sun, H. Q.; Bai, Y.; Cheng, Y. P.; Jin, W. Q.; Xu, N. P. *Ind. Eng. Chem. Res.* **2006**, *45*.
(269) Zhou, M. H.; Yu, Y. G. *J. Hazard. Mater.* **2007**, *7*.
(270) Periyat, P.; Pillai, S. C.; McCormack, D. E.; Colreavy, J.; Hinder, S. J. *J. Phys. Chem. C* **2008**, *112*, 7644
(271) Di Valentin, C.; Finazzi, E.; Pacchioni, G.; Selloni, A.; Livraghi, S.; Paganini, M. C.; Giamello, E. *Chem. Phys.* **2007**, *339*, 44
(272) Gesenhues, U. *J. Photochem. Photobiol. A* **2001**, *139*, 243
(273) Gesenhues, U.; Rentschler, T. *J. Sol. State Chem.* **1999**, *143*.
(274) Stebbins, J. F.; Farnan, I.; Klabunde, U. *J. Am. Ceram. Soc.* **1989**, *72*.
(275) Nolan, N. T.; Seery, M. K.; Hinder, S. J.; Healy, L. F.; Pillai, S. C. *J. Phys. Chem. C* **2010**, *ASAP*.
(276) Fernandez, A.; Lassaletta, G.; Jimenez, V. M.; Justo, A.; Gonzalez-Elipe, A. R.; Herrmann, J.-M.; Tahiri, H.; Ait-Ichou, Y. *Appl. Catal. B: Environ.* **1995**, *7*.

(277) Paz, Y.; Luo, Z.; Rabenberg, L.; Heller, A. *J. Mater. Res.* **1995**, *10*.
(278) Bessekhouad, Y.; Robert, D.; Weber, J.-V.; Chaoui, N. *J. Photochem. Photobiol. A* **2004**, *167*, 49
(279) Baliteau, S.; Sauvet, A.-L.; Lopez, C.; Fabry, P. *Solid State Ionics* **2007**, *178*, 1517
(280) Zhang, H.; Gao, X. P.; Li, G. R.; Yan, T. Y.; Zhu, H. Y. *Electrochimica Acta* **2008**, *53*, 7061.
(281) Stengl, V.; Bakardjieva, S.; Subrt, J.; Vecernikova, E.; Szatmary, L.; Klementova, M.; Balek, V. *Appl. Catal. B* **2006**, *63*, 20
(282) Bazzicalupi, C.; Bencini, A.; Bianchi, A.; Fusi, V.; Paoletti, P.; Valtancoli, B. *Inorganica Chimica Acta* **1996**, *244*, 255
(283) Cernak, J.; Abboud, K. A.; Chomic, J.; Meisel, M. W.; Orendac, M.; Orendacova, A.; Feher, A. *Inorganica Chimica Acta* **2000**, *311*, 126
(284) Legendre, A. d. O.; Mauro, A. E.; de Oliveira, M. A. R.; do Prado Gambardella, M. T. *Inorg. Chem. Comm.* **2008**, *11*, 896
(285) Lloyd, J.; Vatsadze, S. Z.; Robson, D. A.; Blake, A. J.; Mountford, P. *J. Organometallic Chem.* **1999**, *591*, 114
(286) Mane, R. S.; Lee, W. J.; Pathan, H. M.; Han, S.-H. *J. Phys. Chem. B.* **2005**, *109*, 24254
(287) Marci, G.; Augugliaro, V.; Lopez-Munoz, M. J.; Martin, C.; Palmisano, L.; Rives, V.; Schiavello, M.; Telly, R. J. D.; Venezia, A. M. *J. Phys. Chem. B.* **2001**, *105*, 1026
(288) Zhang, Z.; Yuan, Y.; Fang, Y.; Liang, L.; Ding, H.; Jin, L. *Talanta* **2007**, *73*, 523
(289) Bartram, S. F.; Slepetys, R. A. *J. Am. Ceram. Soc.* **1961**, *44*, 493
(290) Dulin, F. H.; Rase, D. E. *J. Am. Ceram. Soc.* **1960**, *43*, 125
(291) Mohammadi, M. R.; Fray, D. J. *ECERS* **2010**, *30*, 947
(292) Yamaguchi, O.; Morimi, M.; Kawabata, H.; Shimizu, K. *J. Am. Ceram. Soc.* **1987**, *70*, C97
(293) Chaves, A. C.; Lima, S. J. G.; Araujo, R. C. M. U.; Maurera, M. A. M. A.; Longo, E.; Pizani, P. S.; Simoes, L. G. P.; Soledade, L. E. B.; Souza, A. G.; dos Santos, I. M. G. *J. Solid State Chem.* **2006**, *179*, 985
(294) Alonso, L.; Palacios, J. M.; Moliner, R. *Energy Fuel* **2001**, *15*, 1396
(295) Jothimurugesan, K.; Gangwal, S. K. *Ind. Eng. Chem. Res.* **1998**, *37*, 1929
(296) Jun, H. K.; Lee, T. J.; Ryu, S. O.; Kim, J. C. *Ind. Eng. Chem. Res.* **2001**, *40*, 3547
(297) Lew, S.; Sarofim, A. F.; Flytzani-Stephanipoulos, M. *Chem. Eng. Sci.* **1992**, *47*, 1421
(298) Pineda, M.; Fierro, J. L. G.; Palacios, J. M.; Cilleruelo, C.; Garcia, E.; Ibarra, J. V. *Appl. Surf. Sci.* **1997**, *119*, 1
(299) Slimane, R. B.; Abbasian, J. *Adv. Environ. Res.* **2000**, *4*, 147
(300) Jang, J. S.; Borse, P. H.; Lee, J. S.; Lim, K. T.; Jung, O.-S.; Jeoung, E. D.; Bae, J. S.; Won, M. S.; Kim, H. G. *Bull. Korean Chem. Soc.* **2009**, *30*, 3021
(301) Matsumoto, Y. *J. Solid State Chem.* **1996**, *126*.
(302) Li, C.; Bando, M.; Nakamura, M.; Kimizuka, N.; Kito, H. *Mater. Res. Bull.* **2000**, *35*, 351
(303) Sedpho, S.; Wongratanaphisan, D.; Mangkorntong, P.; Mangkorntong, N.; Choopun, S. *J. Nat. Sci.* **2008**, *7*, 99
(304) Sheinkman, A. I.; Sheinkman, F. P.; Dobrovol'skii, I. P.; Zvyagina, G. R. *Izv, Akad, Nauk SSSR Neorg, Mater.* **1977**, *13*, 1447
(305) Yang, J.; Swisher, J. H. *Mater. Charac.* **1996**, *37*, 153
(306) Liu, Z.; Dongxiang, Z.; Gong, S.; Li, H. *J. Alloys Compd.* **2009**, *475*, 840
(307) Gabal, M. A.; El-Bellihi, A. A.; El-Bahnasaway, H. H. *Mater. Chem. Phys.* **2003**, *81*, 174
(308) Doeuff, S.; Henry, M.; Sanchez, C.; Livage, J. *J. Non-Cryst. Solids* **1987**, *89*, 206
(309) Edwards, H. G. M.; Russell, N. C. *J. Molec. Struct.* **1998**, *443*, 223
(310) Van Niekerk, J. N.; Schoening, F. R. L.; Talbot, J. H. *Acta Crystallogr.* **1953**, *6*.

(311) Ishioka, T.; Shibata, Y.; Takahashi, M.; Kanesaka, I.; Kitagawa, Y.; Nakamura, K. T. *Spectrochimica Acta Part A* **1998**, *54*, 1827
(312) Kanade, K. G.; Kale, B. B.; Aiyer, R. C.; Das, B. K. *Mater. Res. Bull.* **2006**, *41*, 590
(313) Natarajan, S. *Solid State Sci.* **2002**, *4*, 1331
(314) Vaidhyanathan, R.; Natarajan, S.; Rao, C. N. R. *J. Chem. Soc., Dalton Trans.* **2001**, 699
(315) D'Antonio, M. C.; Mancilla, N.; Wladimirsky, A.; Palacios, D.; Gonzalez-Baro, A. C.; Baran, E. J. *Vib. Spec.* **2010**, *53*, 218
(316) Lagier, J. P.; Pezerat, H.; Dubernat, J. *Rev. Chim. Miner.* **1969**, *6*, 1081
(317) Nolan, N. T.; Seery, M. K.; Pillai, S. C. *J. Phys. Chem. C* **2009**, *113*, 16151
(318) Sugiura, M.; Ikeda, K. *J. Jpn. Ceram. Assoc.* **1947**, *55*, 62
(319) Kim, H. T.; Kim, S. H.; Nahm, S.; Byun, J. D.; Kim, Y. *J. Am. Ceram. Soc.* **1999**, *82*, 3043
(320) Schmidt, H.; Naumann, M.; Muller, T. S.; Akarsu, M. *Thin Solid Films* **2006**, *502*, 132
(321) Kim, H.; Choi, W. *Appl. Catal. B Environ.* **2007**, *69*, 127
(322) Park, H.; Choi, W. *J. Phys. Chem. B* **2004**, *108*, 4086
(323) Vohra, M. S.; Kim, S.; Choi, W. *J. Photochem. Photobiol. A* **2003**, *160*, 55
(324) Alam Khan, M.; Ihl Woo, S.; Bong Yang, O. *Int. J. Hydrogen Energy* **2008**, *33*, 5345
(325) Stobie, N.; Duffy, B.; Colreavy, J.; Hidalgo, M.; McHale, P.; Hinder, S. J. *Biomaterials* **2008**, *29*, 963

Publications by the Author

1. N. T. Nolan, M. K. Seery and S. C. Pillai, *J. Phys. Chem. C*, **2009**, *113*, 16151

2. N. T. Nolan, M. K. Seery, S. J. Hinder, L. F. Healy and S. C. Pillai, *J. Phys. Chem. C*, **2010**, *114*, 13026

Presentations by the Author

1. DRIFTS Investigation of CO Adsorbed on Pd Aggregates Deposited on an Alumina Model Support, (Poster Presentation) N. T. Nolan, M. K. Seery, S. C. Pillai and M. S. Wong, June 2008, 60th Irish Universities Chemistry Research Colloquium, UCC, Cork.
2. The Effect of Silver on the Crystalline Properties of TiO_2, (Poster Presentation) N. T. Nolan, L. F. Healy, S. J. Hinder, M. K. Seery, S. C. Pillai, December 2009, Materials Ireland, Cork.

Appendices

Appendix A: Gaussian fit of Ti2p XPS spectra with increasing amounts of silver

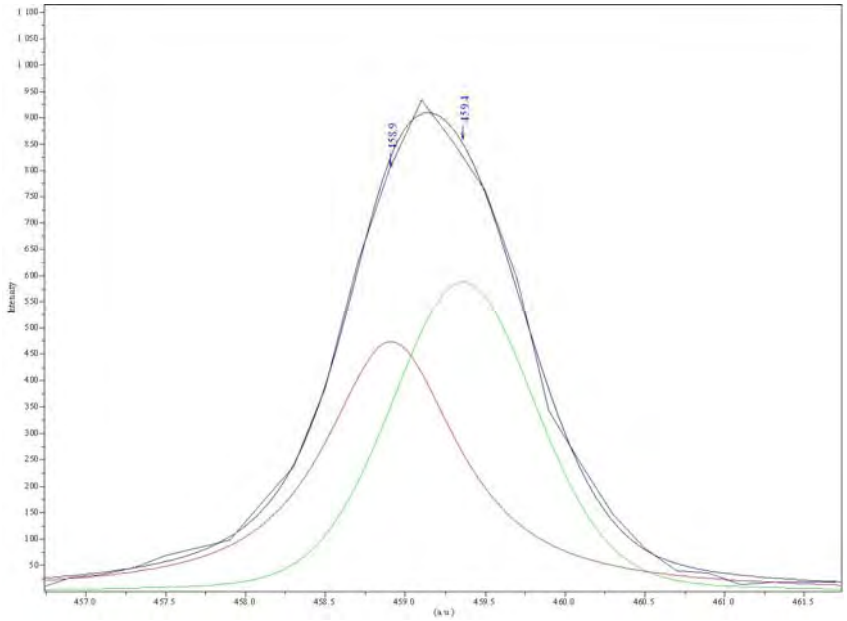

Figure A.1. Ti2p XPS spectrum of 0% Ag before calcination

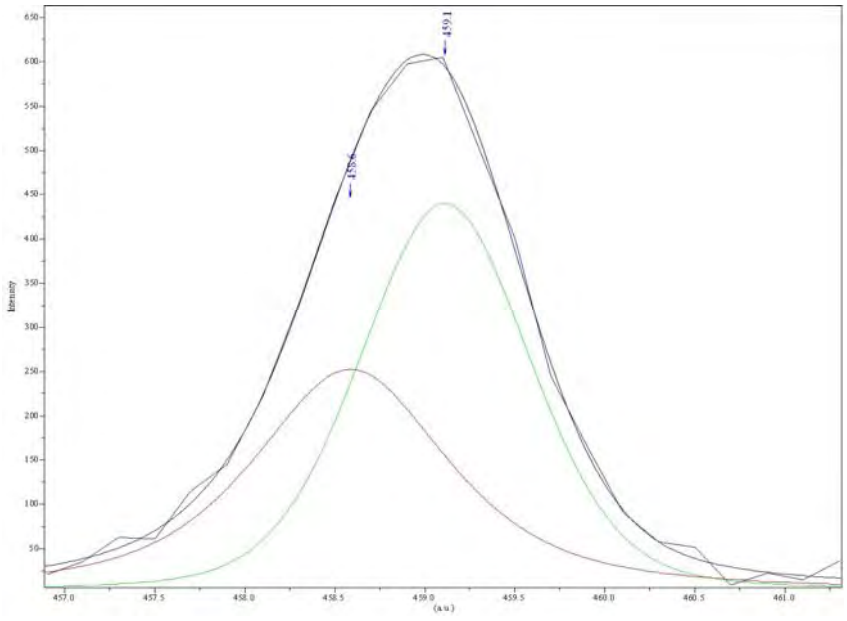

Figure A.2. Ti2p XPS spectrum of 1% Ag before calcination

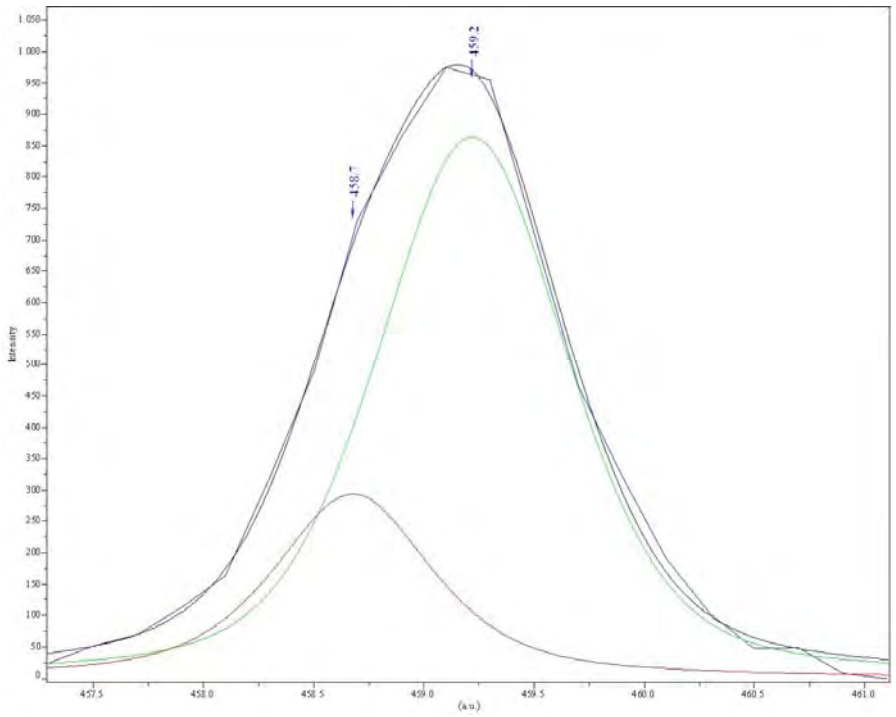

Figure A.3. Ti2p XPS spectrum of 3% Ag before calcination

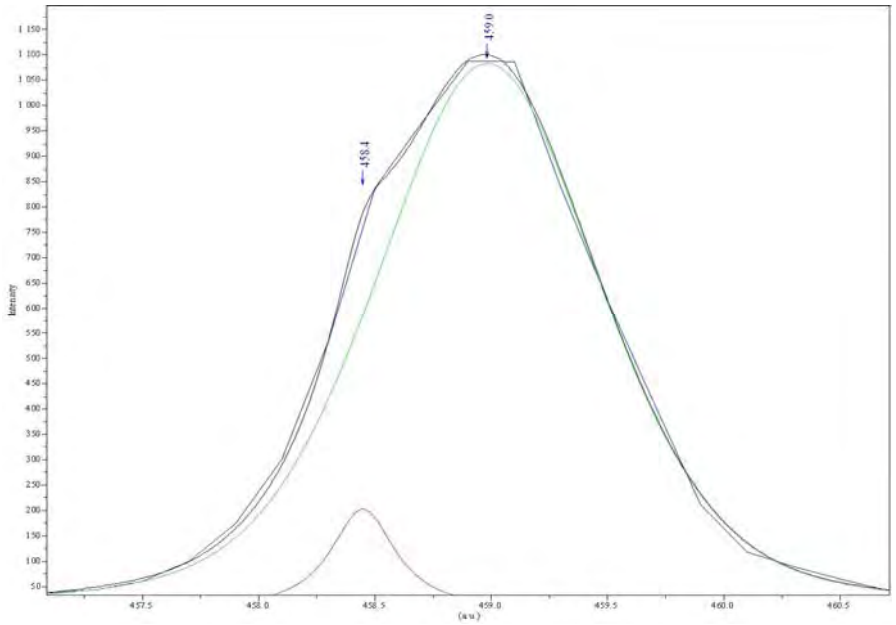

Figure A.4. Ti2p XPS spectrum of 5% Ag before calcination

Appendix B: EDX analysis of Ag-TiO_2

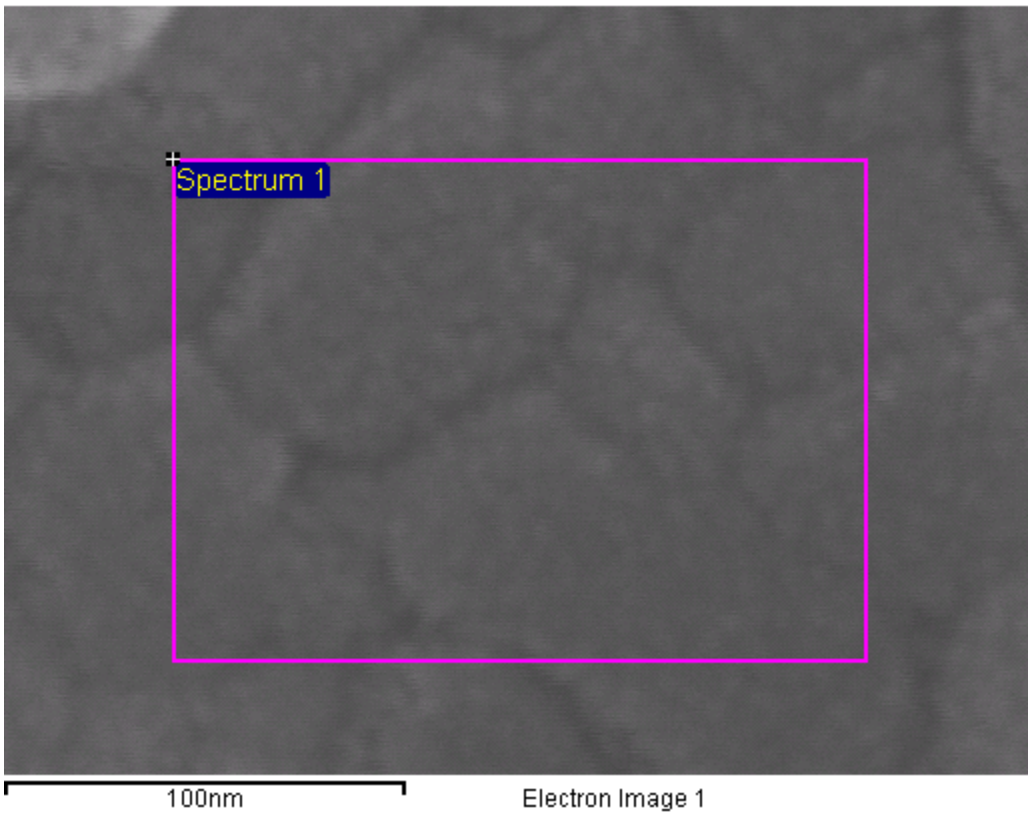

Figure A.5. Analysis area for EDX spectrum of 5% Ag-TiO_2 calcined at 700 °C

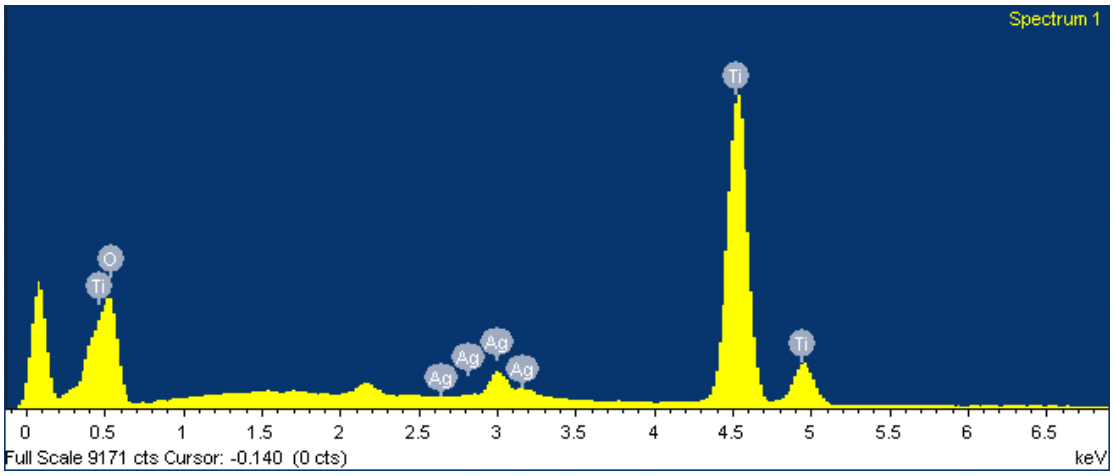

Figure A.6. EDX spectrum of 5% Ag-TiO_2 calcined at 700 °C

Table A1. Atomic weight percentages calculated from EDX of 5% Ag-TiO_2 calcined at 700 °C

Element	Weight%	Atomic%	Compd%	Formula
Ti K	56.51	32.65	94.26	TiO_2
Ag L	5.34	1.37	5.74	Ag_2O
O	38.15	65.98		
Totals	100.00			

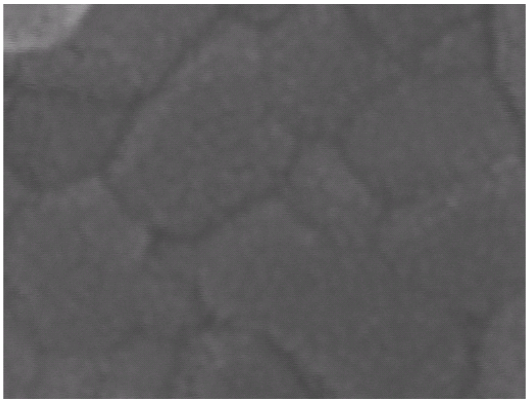

Electron Image 1

(a)

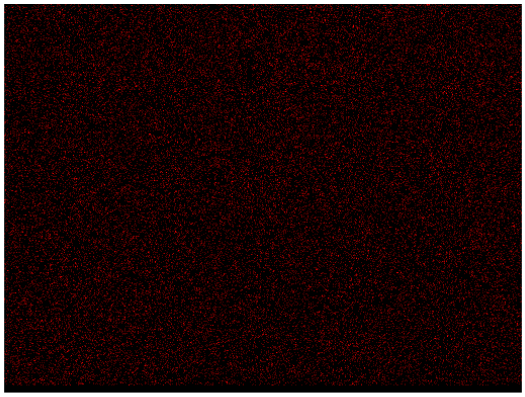

O Ka1

(b)

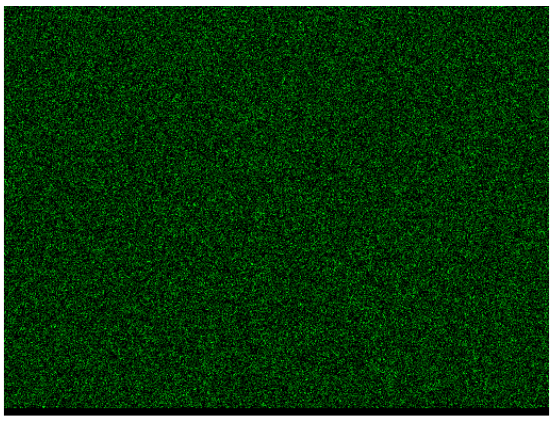

Ti Ka1

(c)

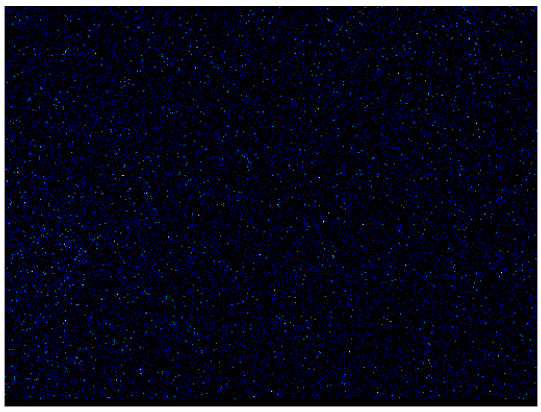

Ag La1

(d)

Figure A.7. Elemental mapping of 5% Ag-TiO_2 calcined at 700 °C, mapping area (a), oxygen profile (b), titanium profile (c) and silver profile (d)

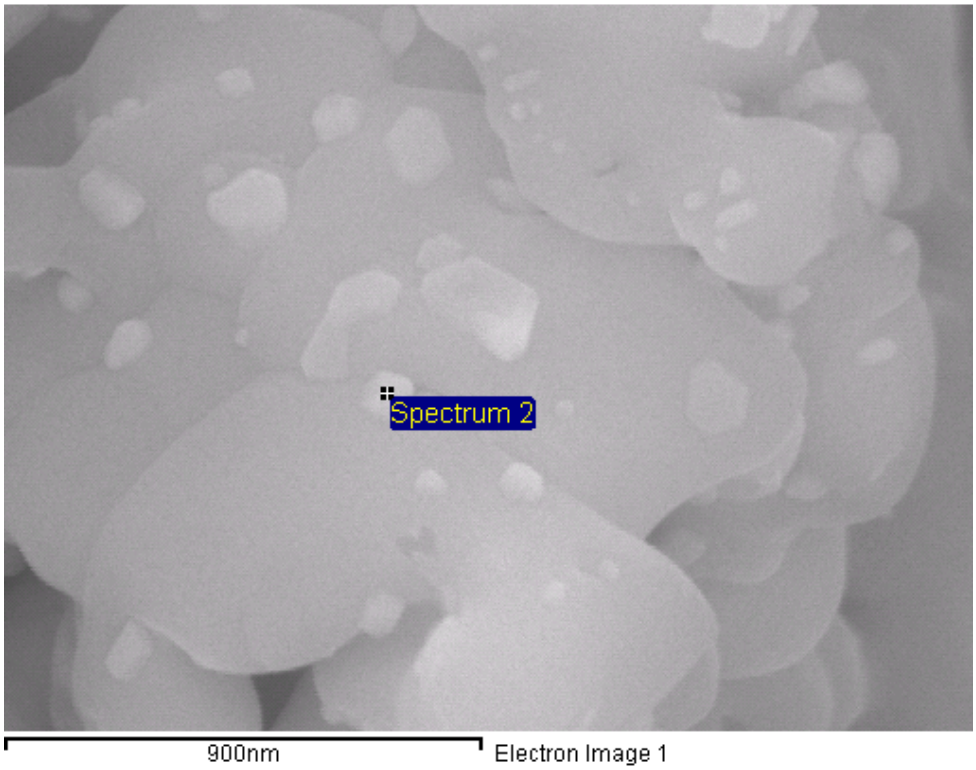

Figure A.8. Analysis area for EDX spectrum of 5% Ag-TiO_2 calcined at 800 °C

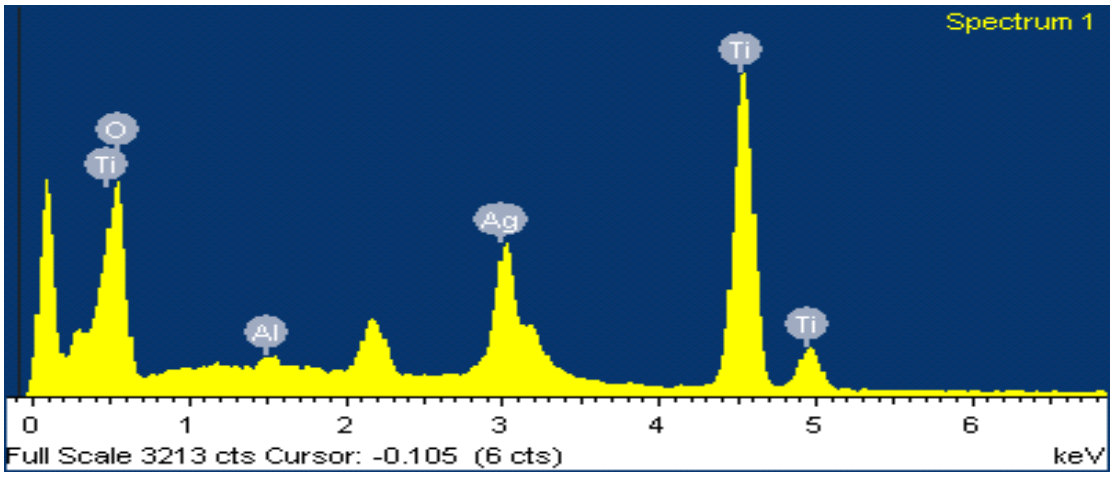

Figure A.9. EDX spectrum of 5% Ag-TiO_2 calcined at 800 °C

Table A2. Atomic weight percentages calculated from EDX of 5% Ag-TiO_2 calcined at 800 °C

Element	Weight%	Atomic%	Compd%	Formula
Al K	0.52	0.60	0.99	Al_2O_3
Ti K	46.21	30.01	77.08	TiO_2
Ag L	13.52	3.90	14.52	Ag_2O
Au M	6.61	1.04	7.41	Au_2O_3
O	33.14	64.44		
Totals	100.00			

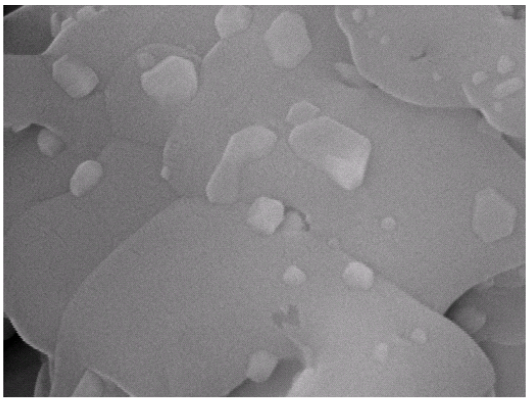

(a)

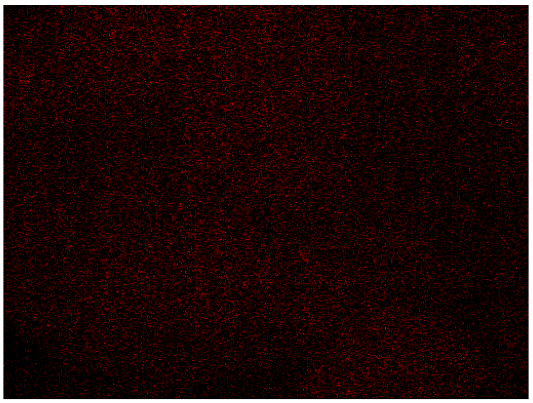

(b)

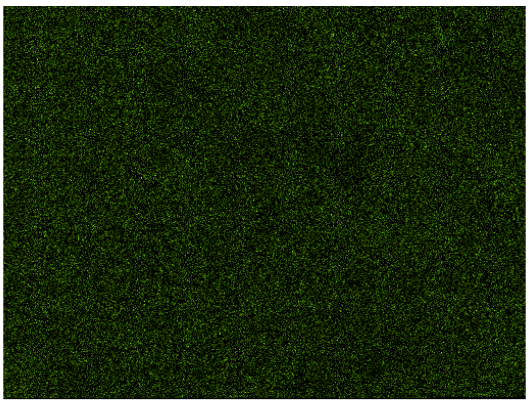

(c)

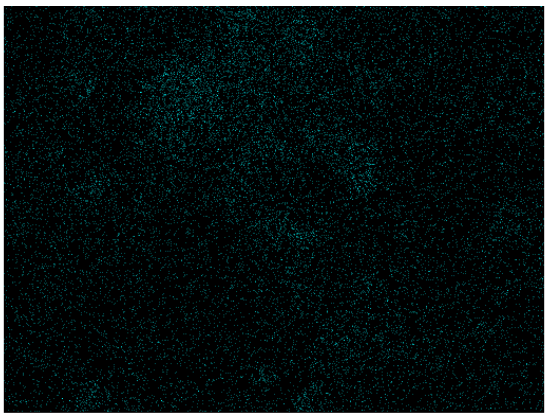

(d)

Figure A.10. Elemental mapping of 5% Ag-TiO_2 calcined at 800 °C, mapping area (a), oxygen profile (b), titanium profile (c) and silver profile (d)